

NextGen Voices: Imagining  
a postpandemic world p. 26

Young and breeding fishes more  
susceptible to warming pp. 35 & 65

An ultracold Josephson  
junction pp. 84 & 89

# Science

\$15  
3 JULY 2020

AAAS

## MICROBIAL HOTSPOT

Stunning diversity at  
Mexico's Cuatro Ciénegas p. 20

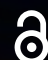




CALL FOR PAPERS



# Advanced Devices & Instrumentation

 OPEN ACCESS

*Advanced Devices & Instrumentation* is an online-only open access journal published in affiliation with **Beijing Institute of Aerospace Control Devices (BIACD)** and distributed by the **American Association for the Advancement of Science (AAAS)**. *Advanced Devices & Instrumentation* aims to publish the latest investigations on novel ideas, methods, and techniques for the development and manufacture of advanced devices and instrumentation, as well as novel and practical solutions for existing applications.

**Submit your research to *Advanced Devices & Instrumentation* today!**

Learn more at [spj.sciencemag.org/adi](https://spj.sciencemag.org/adi)

The Science Partner Journals (SPJ) program was established by the American Association for the Advancement of Science (AAAS), the non-profit publisher of the *Science* family of journals. The SPJ program features high quality, online-only, editorially independent open-access publications produced in collaboration with international research institutions, foundations, funders and societies. Through these collaborations, AAAS expands its efforts to communicate science broadly and for the benefit of all people by providing a top-tier international research organization with the technology, visibility, and publishing expertise that AAAS is uniquely positioned to offer as the world's largest. Visit us at [spj.sciencemag.org](https://spj.sciencemag.org)



@SPJournals



@SPJournals

ARTICLE PROCESSING CHARGES WAIVED UNTIL 2023



## Neuroscience professors open the minds of Hong Kong's science community

**T**he doors of the Hong Kong Institute for Advanced Study (HKIAS) at City University of Hong Kong (CityU) were reopened in May for the launch of the institute's first series of lectures since the outbreak of the novel coronavirus.

Made possible by a generous grant from the Kwang Hua Education Foundation, the HKIAS Distinguished Lecture Series on Life Sciences aims to identify and showcase the work of life scientists and neuroscientists at CityU whose research cuts across traditional disciplinary boundaries.

Over the past 5 years, HKIAS has become internationally recognized for its high-profile lectures, many of which are given by the institute's rapidly expanding international faculty.

Bruce Ransom, chair professor and head of the Department of Neuroscience at CityU and professor emeritus of neurology at the University of Washington in the United States, introduced the lecture series on May 4 with his talk titled "Acute Ischemic Stroke: Why Don't We Have Better Treatments?" Ransom revealed why stroke researchers and pharmaceutical companies have spent billions of dollars on therapies for stroke victims, but still have nothing to show for it.

He was followed by Sir Colin Blakemore, Yeung Kin Man Chair Professor of Neuroscience at CityU and a senior fellow at HKIAS. In his May 8 talk, "The Past, Present, and Future of the Human Brain," Blakemore suggested that given the plasticity of the brain and its ability to change over time, it might be time to teach our brains new ways to find solutions to problems created by humans, such as climate change.



Bruce Ransom

Sir Colin Blakemore

## Academic discussion has a bright future

HKIAS intends to organize monthly lectures covering the institute's full range of specialist research areas, which include mathematics, natural sciences, materials science, and biomedical sciences.

All of these intellectual forums have been made possible by a USD 2 million (HKD 15 million) donation from the estate of one of Hong Kong's most influential figures, the late Chung Sze-yuen, an engineer and politician who died in 2018 at the age of 101. This generous financial support will enable HKIAS to recruit established first-class academicians as well as talented early-career scholars from around the world.

"We cherish and always remember the kindness of Chung Sze-yuen," says Jacob Huang, executive director of HKIAS and chair professor of the Department of Materials Science and Engineering at CityU. "It is a powerful endorsement of our future."

## HKIAS continues to grow

To prepare for future development, in August 2019 HKIAS relocated to a new office that is better equipped to provide a stimulating environment for intellectual discussion. The new facility has a lecture theater with cutting-edge facilities that will enable a wide range of academic activities.

HKIAS also continues to expand its team. The institute recently welcomed two new senior female fellows: Alison Noble and Evelyn Hu.

Noble is a biomedical engineering scientist at the University of Oxford, United Kingdom, who is a member of many distinguished British academic institutions, including the Royal Society.

Hu is a renowned scholar in the field of applied physics and electrical engineering; a member of multiple high-profile science organizations, such as the U.S. National Academy of Sciences; and currently the Tarr-Coyne Professor of Electrical Engineering and Applied Science at Harvard University in Boston, Massachusetts.

Huang says that such high-caliber scholars bring with them a vast store of experience, insight, and knowledge, and will add new dimensions to CityU's academic community.

At a time when the world faces an external threat from the spread of the novel coronavirus, scientific collaboration has never been more important. In Hong Kong, HKIAS is a center for scientific discussion that will help researchers face such challenges together.

**Hong Kong Institute for Advanced Study**

Phone: +852 3442 6611

Email: [hkias@cityu.edu.hk](mailto:hkias@cityu.edu.hk)





THE NORWEGIAN ACADEMY OF SCIENCE AND LETTERS  
ANNOUNCES THE 2020 LAUREATES OF

# THE KAVLI PRIZE

## THE KAVLI PRIZE IN ASTROPHYSICS

Selection Committee: Viggo Hansteen (Chair), University of Oslo, Norway; Alessandra Buonanno, Max Planck Institute for Gravitational Physics, Germany; Andrea Ghez, University of California, Los Angeles, USA; Robert C. Kennicutt, Jr, University of Arizona, US; Irwin I. Shapiro, Harvard University, USA

for groundbreaking research in the field of observational X-ray astronomy, covering a wide range of topics from gas flows in clusters of galaxies to supermassive black holes at the heart of galaxies

**ANDREW FABIAN**, University of Cambridge, UK

## THE KAVLI PRIZE IN NANOSCIENCE

Selection Committee: Bodil Holst (Chair), University of Bergen, Norway; Gabriel Aeppli, Paul Scherrer Institut, Switzerland; Susan Coppersmith, University of New South Wales, Australia; Shuit-Tong Lee, Soochow University, China; Joachim Spatz, Max Planck Institute for Medical Research, Germany

for sub-ångström resolution imaging and chemical analysis using electron beams

**HARALD ROSE** Universität Ulm, Germany  
**MAXIMILIAN HAIDER** CEOS GmbH, Germany  
**KNUT URBAN** Forschungszentrum Jülich, Germany  
**ONDREJ L. KRIVANEK** Nion Co, USA

## THE KAVLI PRIZE IN NEUROSCIENCE

Selection Committee: Kristine B. Walhovd (Chair), University of Oslo, Norway; Alexander Borst, Max Planck Institute of Neurobiology, Germany; Catherine Dulac, Harvard University, USA; Mary E. Hatten, The Rockefeller University, USA; Denis Le Bihan, NeuroSpin, CEA, France

for the transformative discovery of receptors for temperature and pressure

**DAVID JULIUS** UC San Francisco, USA  
**ARDEM PATAPOUTIAN** Scripps Research, USA



[kavliprize.org](https://kavliprize.org)

The Kavli Prize is a partnership among The Norwegian Academy of Science and Letters, The Norwegian Ministry of Education and Research, and The Kavli Foundation (USA).



# CONTENTS

3 JULY 2020 • VOLUME 369 • ISSUE 6499

20

## NEWS

### IN BRIEF

**12** News at a glance

### IN DEPTH

**14 Officials gird for a war on vaccine misinformation**

Fears of a rushed COVID-19 vaccine and rise of social media demand new messaging strategy  
*By W. Cornwall*

**15 The line starts to form for a coronavirus vaccine**

U.S. and others debate who should get priority if vaccine doses are scarce  
*By J. Cohen*

**17 Rock seen inside Venus's orbit could solve puzzle**

Mineral in first object so close to the Sun may be a clue to missing "mantle" asteroids  
*By N. Redd*

**18 A colorful chemotherapy agent could be made less toxic**

Safer forms of doxorubicin, which kill tumor cells without damaging DNA, could spare hearts of cancer patients  
*By J. Kaiser*

**19 Greenland rock cores to trace ice's past melting**

U.S. drilling campaign could also date controversial Hiawatha impact crater  
*By P. Voosen*

### FEATURES

**20 Improbable oasis**

Pools in the Mexican desert are a hot spot of microbial diversity—and a window into early life  
*By R. P. Ortega*

PODCAST; VIDEO

## INSIGHTS

### LETTERS

**26 Nextgen voices: News from a postpandemic world**

### PERSPECTIVES

**30 Tracing cell trajectories in a biofilm**

Single bacterial cells are programmed to form multicellular structures

*By A. Dal Co and M. P. Brenner*

RESEARCH ARTICLE p. 71

**31 Shutting down RNA-targeting CRISPR**

The discovery of an anti-CRISPR reveals viral escape from CRISPR immunity

*By R. Barrangou and E. J. Sontheimer*

RESEARCH ARTICLE p. 54

**33 The secret life of histones**

Histone H3 leads a double life as a copper reductase  
*By J. Rudolph and K. Luger*

RESEARCH ARTICLE p. 59

**34 Stronger bonds bring bigger challenges**

A polyoxometalate photocatalyst enables selective bond activation of light alkanes  
*By G. Oksdath-Mansilla*

REPORT p. 92

**35 When do fish succumb to heat?**

Greater sensitivity in fish reproductive stages reveals vulnerability to climate change  
*By J. Sunday*

RESEARCH ARTICLE p. 65

**37 Rewilding immunology**

Integrating comparative immunology can improve human, animal, and ecosystem health

*By A. S. Flies and Wild Comparative Immunology Consortium*

### POLICY FORUM

**39 Improve alignment of research policy and societal values**

The EU promotes Responsible Research and Innovation in principle, but implementation leaves much to be desired  
*By P. Novitzky et al.*

### BOOKS ET AL.

**42 Better homes and safer spaces**

Evidence-based indoor design is more important than ever  
*By B. Brown*

**43 Physics meets America's defense agenda**

War transformed 20th-century physics in sometimes subtle ways  
*By M. Frappier*

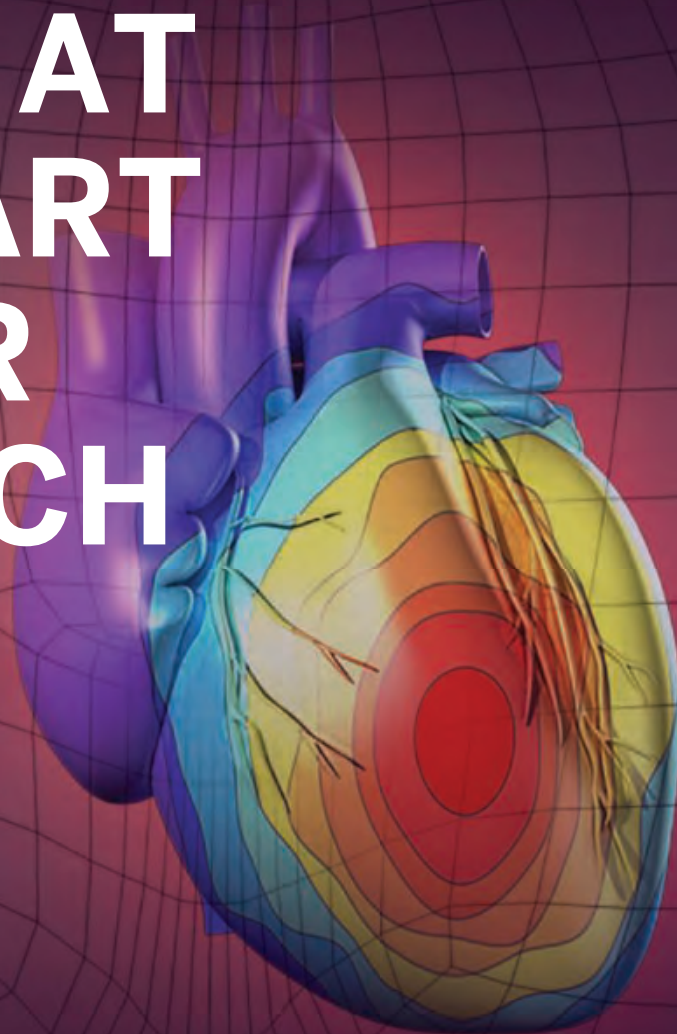


CREDITS: (PHOTO) DAVID JARAMILLO; (IMAGE) EQUINOX GRAPHICS/SCIENCE SOURCE





# PUT HUMAN HEALTH AT THE HEART OF YOUR RESEARCH

Submit your research:  
**cts.ScienceMag.org**



Science  
Translational  
Medicine  
 AAAS

 Twitter: @ScienceTM  
 Facebook: @ScienceTranslationalMedicine



# RESEARCH

## IN BRIEF

**45** From *Science* and other journals

## REVIEW

### 48 Microbiology

Sharing vitamins: Cobamides unveil microbial interactions

*O. M. Sokolovskaya et al.*

REVIEW SUMMARY; FOR FULL TEXT:

DX.DOI.ORG/10.1126/SCIENCE.ABA0165

## RESEARCH ARTICLES

### 49 Cancer

Feasibility of blood testing combined with PET-CT to screen for cancer and guide intervention *A. M. Lennon et al.*

RESEARCH ARTICLE SUMMARY; FOR FULL TEXT:

DX.DOI.ORG/10.1126/SCIENCE.ABB9601

### 50 Coronavirus

SARS-CoV-2 productively infects human gut enterocytes

*M. M. Lamers et al.*

### 54 CRISPR biology

A phage-encoded anti-CRISPR enables complete evasion of type VI-A CRISPR-Cas immunity *A. J. Meeske et al.*

PERSPECTIVE p. 31

### 59 Histone function

The histone H3-H4 tetramer is a copper reductase enzyme *N. Attar et al.*

PERSPECTIVE p. 33

### 65 Climate responses

Thermal bottlenecks in the life cycle define climate vulnerability of fish *F. T. Dahlke et al.*

PERSPECTIVE p. 35

### 71 Biofilms

Cell position fates and collective fountain flow in bacterial biofilms revealed by light-sheet microscopy *B. Qin et al.*

PERSPECTIVE p. 30

## REPORTS

### 77 Coronavirus

Development of an inactivated vaccine candidate for SARS-CoV-2 *Q. Gao et al.*

### 81 Dielectrics

Ultrahigh capacitive energy density in ion-bombarded relaxor ferroelectric films *J. Kim et al.*



Fish embryos, like these cod, are especially sensitive to warming.

## Quantum gases

**84** Strongly correlated superfluid order parameters from dc Josephson supercurrents *W. J. Kwon et al.*

**89** An ideal Josephson junction in an ultracold two-dimensional Fermi gas *N. Luick et al.*

## 92 Organic chemistry

C(sp<sup>3</sup>)-H functionalizations of light hydrocarbons using decatungstate photocatalysis in flow *G. Laudadio et al.*

PERSPECTIVE p. 34

## 96 Solar cells

A piperidinium salt stabilizes efficient metal-halide perovskite solar cells *Y.-H. Lin et al.*

## 103 HIV

Number of HIV-1 founder variants is determined by the recency of the source partner infection *Ch. J. Villabona-Arenas et al.*

## DEPARTMENTS

### 11 Editorial

Surviving the trauma of COVID-19  
*By Roxane Cohen Silver*

### 110 Working Life

A child of the slums *By Shalini Arya*

## ON THE COVER



Tinged blue with minerals, La Poza Azul II is one of hundreds of spring-fed pools in Cuatro Ciénegas, an oasis in the desert of northern Mexico that preserves a vast diversity of microbes resembling those in ancient oceans. Drainage for agriculture threatens the unique ecosystems of this oasis. See page 20. Photo: Miguel Angel de la Cueva

Science Staff ..... 8  
Science Careers ..... 109

SCIENCE (ISSN 0036-8075) is published weekly on Friday, except last week in December, by the American Association for the Advancement of Science, 1200 New York Avenue, NW, Washington, DC 20005. Periodicals mail postage (publication No. 484460) paid at Washington, DC, and additional mailing offices. Copyright © 2020 by the American Association for the Advancement of Science. The title SCIENCE is a registered trademark of the AAAS. Domestic individual membership, including subscription (12 months): \$165 (\$74 allocated to subscription). Domestic institutional subscription (51 issues): \$2148; Foreign postage extra: Air assist delivery: \$98. First class, airmail, student, and emeritus rates on request. Canadian rates with GST available upon request. GST #125488122. Publications Mail Agreement Number 1069624. Printed in the U.S.A.

Change of address: Allow 4 weeks, giving old and new addresses and 8-digit account number. Postmaster: Send change of address to AAAS, P.O. Box 96178, Washington, DC 20090-6178. Single-copy sales: \$15 each plus shipping and handling available from backissues.science.org; bulk rate on request. Authorization to reproduce material for internal or personal use under circumstances not falling within the fair use provisions of the Copyright Act can be obtained through the Copyright Clearance Center (CCC), www.copyright.com. The identification code for Science is 0036-8075. Science is indexed in the Reader's Guide to Periodical Literature and in several specialized indexes.



Editor-in-Chief Holden Thorp, hthorp@aaas.org

Executive Editor Monica M. Bradford

Editors, Research Valda Vinson, Jake S. Yeston Editor, Insights Lisa D. Chong

**DEPUTY EDITORS** Julia Fahrenkamp-Uppenbrink (UK), Stella M. Hurlley (UK), Phillip D. Szurmi, Sacha Vignieri **SR. EDITORIAL FELLOW** Andrew M. Sugden (UK) **SR. EDITORS** Gemma Alderton (UK), Caroline Ash (UK), Brent Grocholski, Pamela J. Hines, Marc S. Lavine (Canada), Ian S. Osborne (UK), Beverly A. Purnell, L. Bryan Ray, H. Jesse Smith, Keith T. Smith (UK), Jelena Stajic, Peter Stern (UK), Valerie B. Thompson, Brad Wible, Laura M. Zahn **ASSOCIATE EDITORS** Michael A. Funk, Priscilla N. Kelly, Tage S. Rai, Seth Thomas Scanlon (UK), Yury V. Suleymanov **LETTERS EDITOR** Jennifer Sills **LEAD CONTENT PRODUCTION EDITORS** Harry Jach, Lauren Kmeck **CONTENT PRODUCTION EDITORS** Amelia Belya, Jeffrey E. Cook, Chris Filiatreau, Julia Katris, Nida Masulis, Suzanne M. White **SR. EDITORIAL COORDINATORS** Carolyn Kyle, Beverly Shields **EDITORIAL COORDINATORS** Aneera Dobbins, Joi S. Granger, Jeffrey Hearn, Lisa Johnson, Maryrose Madrid, Ope Martins, Shannon McMahon, Jerry Richardson, Hilary Stewart (UK), Alana Wanke, Alice Whaley (UK), Anita Wynn **PUBLICATIONS ASSISTANTS** Jeremy Dow, Alexander Kief, Ronnel Navas, Brian White **EXECUTIVE ASSISTANT** Jessica Slater **ASI DIRECTOR, OPERATIONS** Janet Clements (UK) **ASI SR. OFFICE ADMINISTRATOR** Jessica Waldo (UK)

News Editor Tim Appenzeller

**NEWS MANAGING EDITOR** John Travis **INTERNATIONAL EDITOR** Martin Enserink **DEPUTY NEWS EDITORS** Elizabeth Culotta, Lila Guterman, David Grimm, Eric Hand (Europe), David Malakoff **SR. CORRESPONDENTS** Daniel Cley (UK), Jon Cohen, Jeffrey Mervis, Elizabeth Pennisi **ASSOCIATE EDITORS** Jeffrey Brainard, Catherine Maticos **NEWS REPORTERS** Adrian Koh, Jennifer Couzin-Frankel, Jocelyn Kaiser, Kelly Servick, Robert F. Service, Erik Stokstad, Paul Voosen, Meredith Wadman **INTERNS** Eva Frederick, Rodrigo Perez Ortega **CONTRIBUTING CORRESPONDENTS** Warren Cornwall, Ann Gibbons, Mara Hvistendahl, Sam Kean, Eli Kintisch, Kai Kupferschmidt (Berlin), Andrew Lawler, Mitch Leslie, Eliot Marshall, Virginia Morell, Dennis Normile (Shanghai), Elisabeth Pain (Careers), Charles Pillar, Michael Price, Tania Rabesandratana (Barcelona), Emily Underwood, Gretchen Vogel (Berlin), Lizzie Wade (Mexico City) **CAREERS** Donisha Adams, Rachel Bernstein (Editor), Katie Langin (Acting Editor) **COPY EDITORS** Julia Cole (Senior Copy Editor), Cyra Master (Copy Chief) **ADMINISTRATIVE SUPPORT** Meagan Weiland

Creative Director Beth Rakouskas

**DESIGN MANAGING EDITOR** Marcy Atard **GRAPHICS MANAGING EDITOR** Alberto Cuadra **PHOTOGRAPHY MANAGING EDITOR** William Douthitt **WEB CONTENT STRATEGY MANAGER** Kara Estelle-Powers **DESIGN EDITOR** Chrystal Smith **DESIGNER** Christina Aycock **GRAPHICS EDITOR** Nirja Desai **INTERACTIVE GRAPHICS EDITOR** Xing Liu **SENIOR SCIENTIFIC ILLUSTRATORS** Valerie Altounian, Chris Bickel **SCIENTIFIC ILLUSTRATOR** Alice Kitterman **SENIOR GRAPHICS SPECIALISTS** Holly Bishop, Nathalie Cary **SENIOR PHOTO EDITOR** Emily Petersen **PHOTO EDITOR** Kaitlyn Dolan

Chief Executive Officer and Executive Publisher Sudip Parikh

Publisher, Science Family of Journals Bill Moran

**DIRECTOR, BUSINESS SYSTEMS AND FINANCIAL ANALYSIS** Randy Yi **DIRECTOR, BUSINESS OPERATIONS & ANALYSIS** Eric Knott **DIRECTOR OF ANALYTICS** Enrique Gonzales **MANAGER, BUSINESS OPERATIONS** Jessica Tierney **SENIOR BUSINESS ANALYST** Cory Lipman, Meron Kebede **FINANCIAL ANALYST** Alexander Lee **ADVERTISING SYSTEM ADMINISTRATOR** Tina Burks **SENIOR SALES COORDINATOR** Shirley Young **DIGITAL/PRINT STRATEGY MANAGER** Jason Hillman **QUALITY TECHNICAL MANAGER** Marcus Spiegler **ASSISTANT MANAGER DIGITAL/PRINT** Rebecca Doshi **SENIOR CONTENT SPECIALISTS** Steve Forrester, Jacob Hedrick, Antoinette Hodal, Lori Murphy **PRODUCTION SPECIALIST** Kristin Wovk **DIGITAL PRODUCTION MANAGER** Lisa Stanford **CONTENT SPECIALIST** Kimberley Oster **ADVERTISING PRODUCTION OPERATIONS MANAGER** Deborah Tompkins **DESIGNER, CUSTOM PUBLISHING** Jeremy Huntsinger **SR. TRAFFIC ASSOCIATE** Christine Hall **SPECIAL PROJECTS ASSOCIATE** Sarah Dhore

**ASSOCIATE DIRECTOR, BUSINESS DEVELOPMENT** Justin Sawyers **GLOBAL MARKETING MANAGER** Allison Pritchard **DIGITAL MARKETING MANAGER** Aimee Aponte **JOURNALS MARKETING MANAGER** Shawana Arnold **MARKETING ASSOCIATES** Tori Velasquez, Mike Romano, Ashley Hylton **DIGITAL MARKETING SPECIALIST** Asleigh Rojanavongse **SENIOR DESIGNER** Kim Huynh

**DIRECTOR AND SENIOR EDITOR, CUSTOM PUBLISHING** Sean Sanders **ASSISTANT EDITOR, CUSTOM PUBLISHING** Jackie Oberst

**DIRECTOR, PRODUCT & PUBLISHING DEVELOPMENT** Chris Reid **DIRECTOR, BUSINESS STRATEGY AND PORTFOLIO MANAGEMENT** Sarah Whalen **ASSOCIATE DIRECTOR, PRODUCT MANAGEMENT** Kris Bishop **SR. PRODUCT ASSOCIATE** Robert Koepeke **DIGITAL PRODUCT STRATEGIST** Michael Hardesty **SPI ASSOCIATE** Samantha Bruno Fuller

**DIRECTOR, INSTITUTIONAL LICENSING** Iquo Edim **ASSOCIATE DIRECTOR, RESEARCH & DEVELOPMENT** Elisabeth Leonard **MARKETING MANAGER** Kess Knight **SENIOR INSTITUTIONAL LICENSING MANAGER** Ryan Rexroth **INSTITUTIONAL LICENSING MANAGER** Marco Castellan **MANAGER, AGENT RELATIONS & CUSTOMER SERVICE** Judy Lillibridge **SENIOR OPERATIONS ANALYST** Lana Guz **FULFILLMENT COORDINATOR** Melody Stringer **SALES COORDINATOR** Josh Haverlock

**DIRECTOR, GLOBAL SALES** Tracy Holmes **US EAST COAST AND MID WEST SALES** Stephanie O'Connor **US WEST COAST SALES** Lynne Stickrod **US SALES MANAGER, SCIENCE CAREERS** Claudia Paulsen-Young **US SALES REP, SCIENCE CAREERS** Tracy Anderson **ASSOCIATE DIRECTOR, ROW** Roger Gonçalves **SALES REP, ROW** Sarah LeLarge **SALES ADMIN ASSISTANT, ROW** Bryony Cousins **DIRECTOR OF GLOBAL COLLABORATION AND ACADEMIC PUBLISHING RELATIONS, ASIA** Xiaoying Chu **ASSOCIATE DIRECTOR, INTERNATIONAL COLLABORATION** Grace Yao **SALES MANAGER** Danny Zhao **MARKETING MANAGER** Kilo Lan **ASCA CORPORATION, JAPAN** Kaoru Sasaki (Tokyo), Miyuki Tani (Osaka) **COLLABORATION/CUSTOM PUBLICATIONS/JAPAN** Adarsh Sandhu

**DIRECTOR, COPYRIGHT, LICENSING AND SPECIAL PROJECTS** Emilie David **RIGHTS AND LICENSING COORDINATOR** Jessica Adams **RIGHTS AND PERMISSIONS ASSOCIATE** Elizabeth Sandler **CONTRACTS AND LICENSING ASSOCIATE** Lili Catlett

## MAIN HEADQUARTERS

Science/AAAS  
1200 New York Ave. NW  
Washington, DC 20005

## SCIENCE INTERNATIONAL

Clarendon House  
Clarendon Road  
Cambridge, CB2 8FH, UK

## SCIENCE CHINA

Room 1004, Culture Square  
No. 59 Zhongguancun St.  
Haidian District, Beijing, 100872

## SCIENCE JAPAN

ASCA Corporation  
Sibaura TY Bldg. 4F, 1-14-5  
Shibaura Minato-ku  
Tokyo, 108-0073 Japan

## EDITORIAL

science\_editors@aaas.org

## NEWS

science\_news@aaas.org

## INFORMATION FOR AUTHORS

sciencemag.org/authors/  
science-information-authors

## REPRINTS AND PERMISSIONS

sciencemag.org/help/  
reprints-and-permissions

## MEDIA CONTACTS

scipak@aaas.org

## MULTIMEDIA CONTACTS

SciencePodcast@aaas.org  
ScienceVideo@aaas.org

## INSTITUTIONAL SALES

AND SITE LICENSES  
sciencemag.org/librarian

## PRODUCT ADVERTISING

& CUSTOM PUBLISHING  
advertising.sciencemag.org/  
products-services

science\_advertising@aaas.org

## CLASSIFIED ADVERTISING

advertising.sciencemag.org/  
science-careers

advertise@sciencecareers.org

## JOB POSTING CUSTOMER SERVICE

employers.sciencemag.org  
support@sciencecareers.org

## MEMBERSHIP AND INDIVIDUAL

SUBSCRIPTIONS  
sciencemag.org/subscriptions

## MEMBER BENEFITS

aaas.org/membercentral

## AAAS BOARD OF DIRECTORS

**CHAIR** Steven Chu  
**PRESIDENT** Claire M. Fraser  
**PRESIDENT-ELECT** Susan G. Amara  
**TREASURER** Carolyn N. Ainslie  
**CHIEF EXECUTIVE OFFICER** Sudip Parikh  
**BOARD** Cynthia M. Beall  
Rosina M. Bierbaum  
Ann Bostrom  
Stephen P.A. Fodor  
S. James Gates, Jr.  
Laura H. Greene  
Kaye Husbands Fealing  
Maria M. Klawe  
Robert B. Millard  
Alondra Nelson  
William D. Provine

## BOARD OF REVIEWING EDITORS (Statistics board members indicated with \$)

Adriano Aguzzi, U. Hospital Zürich  
Takuzo Aida, U. of Tokyo  
Leslie Aiello, Wenner-Gren Foundation  
Judith Allen, U. of Manchester  
Sebastian Amigorena, Institut Curie  
James Analytis, U. of California, Berkeley  
Paola Ariotta, Harvard U.  
Johan Auwerx, EPFL  
David Awschalom, U. of Chicago  
Clare Baker, U. of Cambridge  
Nenad Ban, ETH Zürich  
Franz Bauer, Pontificia Universidad Católica de Chile  
Ray H. Baughman, U. of Texas at Dallas  
Peter Bearman, Columbia U.  
Carlo Beenakker, Leiden U.  
Yasmine Belkaid, NIAID, NIH  
Philip Benfey, Duke U.  
Gabriele Bergers, VIB  
Bradley Bernstein, Mass. General Hospital  
Alessandra Biffi, Harvard Med. School  
Peer Bork, EMBL  
Chris Bowler, École Normale Supérieure  
Ian Boyd, U. of St. Andrews  
Emily Brodsky, U. of California, Santa Cruz  
Ron Brookmeyer, U. of California, Los Angeles (\$) **Christian Büchel, UKE Hamburg**  
Dennis Burton, Scripps Research  
Carter Tribble Butts, U. of California, Irvine  
György Buzsáki, New York U. School of Med.  
Blanche Capel, Duke U.  
Annmarie Carlton, U. of California, Irvine  
Nick Chater, U. of Warwick  
Zhijian Chen, UT Southwestern Med. Ctr.  
Ib Chorkendorff, Denmark TU  
James J. Collins, MIT  
Robert Cook-Deegan, Arizona State U.  
Alan Cowman, Walter & Eliza Hall Inst.  
Carolyn Coyne, U. of Pittsburgh  
Roberta Croce, VU Amsterdam  
Jeff L. Dangi, U. of North Carolina  
Tom Daniel, U. of Washington  
Chiara Daraio, Caltech  
Nicolas Daughas, U. of Chicago  
Frans de Waal, Emory U.  
Claude Desplan, New York U.  
Sandra Díaz, Universidad Nacional de Córdoba  
Ulrike Diebold, TU Wien  
Hong Ding, Inst. of Physics, CAS  
Jennifer Dionne, Stanford U.  
Dennis Discher, U. of Penn.  
Gerald Dorn, Washington U. in St. Louis  
Jennifer A. Doudna, U. of California, Berkeley  
Bruce Dunn, U. of California, Los Angeles  
William Dunphy, Caltech  
Christopher Dye, U. of Oxford  
Todd Ehlers, U. of Tübingen  
Jennifer Eliseeff, Johns Hopkins U.  
Tim Elston, U. of North Carolina  
Andrea Encalada, U. San Francisco de Quito  
Nader Engheta, U. of Penn.  
Karen Ersche, U. of Cambridge  
Barry Everitt, U. of Cambridge  
Vanessa Ezenwa, U. of Georgia  
Michael Feuer, The George Washington U.  
Toren Finkel, U. of Pittsburgh Med. Ctr.  
Gwenn Flowers, Simon Fraser U.  
Peter Fratzl, Max Planck Inst. Potsdam  
Elaine Fuchs, Rockefeller U.  
Eileen Furlong, EMBL  
Jay Gallagher, U. of Wisconsin  
Daniel Geschwind, U. of California, Los Angeles  
Karl-Heinz Glassmeier, TU Braunschweig  
Ramon Gonzalez, U. of South Florida  
Elizabeth Grove, U. of Chicago  
Nicolas Gruber, ETH Zürich  
Hua Guo, U. of New Mexico  
Kip Guy, U. of Kentucky College of Pharmacy  
Taekjip Ha, Johns Hopkins U.  
Christian Haass, Ludwig Maximilians U.  
Sharon Hammes-Schiffer, Yale U.  
Wolf-Dietrich Hardt, ETH Zürich  
Louise Harra, U. College London  
Jian He, Clemson U.  
Carl-Philipp Heisenberg, IST Austria  
Ykä Helariutta, U. of Cambridge  
Janet G. Hering, Eawag  
Hans Hilgenkamp, U. of Twente  
Kai-Uwe Hinrichs, U. of Bremen  
Lora Hooper, UT Southwestern Med. Ctr.  
Fred Hughson, Princeton U.  
Randall Hulet, Rice U.  
Auke Ijspeert, EPFL  
Akiko Iwasaki, Yale U.  
Stephen Jackson, USGS and U. of Arizona  
Kai Johnson, EPFL  
Peter Jonas, IST Austria  
Matt Kaerberlein, U. of Washington  
William Kaelin Jr., Dana-Farber Cancer Inst.  
Daniel Kammen, U. of California, Berkeley  
V. Narry Kim, Seoul Nat. U.  
Robert Kingston, Harvard Med. School  
Nancy Knowlton, Smithsonian Institution  
Etienne Koelchin, École Normale Supérieure  
Alex L. Kolodkin, Johns Hopkins U.  
Julija Krupic, U. of Cambridge  
Thomas Langer, Max Planck Inst. Cologne  
Mitchell A. Lazar, U. of Penn.  
Ottoline Leyser, U. of Cambridge  
Wendell Lim, U. of California, San Francisco  
Jianguo Liu, Michigan State U.  
Luis Liz-Marzán, CIC biomaGUNE  
Jonathan Losos, Washington U. in St. Louis  
Ke Lu, Chinese Acad. of Sciences  
Christian Lüscher, U. of Geneva  
Jean Lynch-Stieglitz, Georgia Inst. of Tech.  
Fabienne Mermel, QIMR Berghofer  
Anne Magurran, U. of St. Andrews  
Oscar Marín, King's College London  
Charles Marshall, U. of California, Berkeley  
Christopher Marx, U. of Idaho  
Geraldine Masson, CNRS  
C. Robertson McClung, Dartmouth College  
Rodrigo Medellín, U. Nacional Autónoma de México  
Graham Medley, London School of Hygiene & Tropical Med.  
Jane Memmott, U. of Bristol  
Baotia Mi, U. of California, Berkeley  
Edward Mitchell, U. of California, Berkeley  
Tom Misteli, NCI, NIH  
Yasushi Miyashita, U. of Tokyo  
Alison Motesinger-Reif, NIEHS, NIH (\$) **Daniel Nettie, Newcastle U.**  
**Daniel Neumark, U. of California, Berkeley**  
**Beatriz Noheida, U. of Groningen**  
**Helga Nowotny, Vienna Science, Research & Tech. Fund**  
**Rachel O'Reilly, U. of Birmingham**  
**Harry Orr, U. of Minnesota**  
**Pilar Ossorio, U. of Wisconsin**  
**Andrew Oswald, U. of Warwick**  
**Isabella Pagano, Istituto Nazionale di Astrofisica**  
**Margaret Palmer, U. of Maryland**  
**Elizabeth Levy Paluck, Princeton U.**  
**Jane Parker, Max Planck Inst. Cologne**  
**Giovanni Parmigiani, Dana-Farber Cancer Inst. (\$) Samuel Pfaff, Salk Inst. for Biological Studies**  
**Julie Pfeiffer, UT Southwestern Med. Ctr.**  
**Matthieu Piel, Institut Curie**  
**Kathrin Plath, U. of California, Los Angeles**  
**Martin Plenio, Ulm U.**  
**Katherine Pollard, U. of California, San Francisco**  
**Elvira Polczanska, Alfred-Wegener-Inst.**  
**Julia Pongratz, Ludwig Maximilians U.**  
**Philipp Poulin, CNRS**  
**Jonathan Pritchard, Stanford U.**  
**Félix A. Rey, Institut Pasteur**  
**Trevor Robbins, U. of Cambridge**  
**Joeri Rogelj, Imperial College London**  
**Amey Rosenzweig, Northwestern U.**  
**Mike Ryan, U. of Texas at Austin**  
**Minori Saitou, Kyoto U.**  
**Shimon Sakaguchi, Osaka U.**  
**Miquel Salmeron, Lawrence Berkeley Nat. Lab**  
**Nitin Samarth, Penn. State U.**  
**Jürgen Sandkühler, Med. U. of Vienna**  
**Alexander Schier, Harvard U.**  
**Wolfram Schlenker, Columbia U.**  
**Susannah Scott, U. of California, Santa Barbara**  
**Rebecca Sear, London School of Hygiene & Tropical Med.**  
**Vladimir Shaleev, Purdue U.**  
**Jie Shan, Cornell U.**  
**Beth Shapiro, U. of California, Santa Cruz**  
**Jay Shendure, U. of Washington**  
**Steve Sherwood, U. of New South Wales**  
**Brian Shiochet, U. of California, San Francisco**  
**Robert Siliciano, Johns Hopkins U. School of Med.**  
**Lucia Sivilio, U. College London**  
**Alison Smith, John Innes Centre**  
**Richard Smith, U. of North Carolina (\$) Mark Smyth, QIMR Berghofer**  
**Pam Soltis, U. of Florida**  
**John Speakman, U. of Aberdeen**  
**Tara Spire-Jones, U. of Edinburgh**  
**Allan C. Spradling, Carnegie Institution for Science**  
**V. S. Subrahmanian, Dartmouth College**  
**Ira Tabas, Columbia U.**  
**Sarah Teichmann, Wellcome Sanger Inst.**  
**Rocio Titaniuk, Princeton U.**  
**Shubha Tole, Tata Inst. of Fundamental Research**  
**Wim van der Putten, Netherlands Inst. of Ecology**  
**Reinhold Veugeler, KU Leuven**  
**Bert Vogelstein, Johns Hopkins U.**  
**Kathleen Vohs, U. of Minnesota**  
**David Wallace, Weizmann Inst. of Science**  
**Jane-Ling Wang, U. of California, Davis (\$) David Waxman, Fudan U.**  
**Jonathan Weissman, U. of California, San Francisco**  
**Chris Wickle, U. of Missouri (\$) Terrie Williams, U. of California, Santa Cruz**  
**Ian A. Wilson, Scripps Research (\$) Yu Xie, Princeton U.**  
**Jan Zaanen, Leiden U.**  
**Kenneth Zaret, U. of Penn. School of Med.**  
**Jonathan Zehr, U. of California, Santa Cruz**  
**Xiaowei Zhuang, Harvard U.**  
**Maria Zuber, MIT**





**AAAS.ORG/COMMUNITY**



AAAS' Member Community is a one-stop destination for scientists and STEM enthusiasts alike. It's "Where Science Gets Social": a community where facts matter, ideas are big and there's always a reason to come hang out, share, discuss and explore.

**Member  
COMMUNITY**  
AAAS

AMERICAN ASSOCIATION FOR THE ADVANCEMENT OF SCIENCE



# READY FOR A TRULY LIFE-CHANGING MOMENT? APPLY NOW.

The *Science* & SciLifeLab Prize for Young Scientists is an annual prize awarded to early-career scientists. The prize is presented in four categories: Cell and Molecular Biology; Genomics, Proteomics, and Systems Biology Approaches; Ecology and Environment; and Molecular Medicine.

As a winner, you will have your essay published by *Science*, win up to USD 30,000 and be invited to Sweden where you will receive your award, present your research and meet with leading scientists in your field.

**Get ready for a life-changing moment in your scientific career  
– apply now, deadline is July 15!**

**SCIENCEPRIZE.SCILIFELAB.SE**



2019 winners (from left): Longzhi Tan, Zibo Chen, Barbara Klump and Humsa Venkatesh.

# Surviving the trauma of COVID-19

**A**s a psychological scientist who investigates how individuals and communities respond to collective traumas, I study human resilience in a range of situations—from earthquakes and hurricanes to mass violence and war. Shortly after the 11 September 2001 terrorist attacks against the United States, I sat in the White House Office of Homeland Security discussing community resilience. Although the threat to society seemed real and continuing, national leaders were anxious to get people back on airplanes and into high-rise office buildings. In retrospect, the nation proved to be quite resilient: The threat of terrorism was never eliminated, but industries and urban centers continued to thrive. Decades later, the United States and world face another threat, equally amorphous and extremely deadly. In months, severe acute respiratory syndrome coronavirus 2 (SARS-CoV-2), the virus that causes coronavirus disease 2019 (COVID-19), has infected over 10 million people, killed over 125,000 Americans, and led to more than 500,000 deaths worldwide. A vaccine for COVID-19 is perhaps a year away. What does psychological science tell us about how individuals are responding—and will respond—as the pandemic waxes and wanes? What will the postpandemic “normal” look like? Will our society prove to be resilient?

COVID-19 is a physical illness that scientists are trying to understand from many angles. But the pandemic and its associated stressors also are likely to have serious mental health consequences. It is quite normal to experience distress as a result of chronic stress of this magnitude. Losses that are real (of loved ones, without the opportunity for a ritual funeral) or symbolic (graduation celebrations) abound. There may be grief for many, and unresolved grief for some. Isolation may lead to depression for many and suicidal ideation for some. But there will be no “one size fits all” response to this crisis.

Decades of psychological science on collective traumas indicate that individuals’ responses are likely to be based on several factors. These include their prepandemic circumstances and resources—prior exposures to adversity, physical and mental health vulnerabilities, and economic and social supports. One must also consider exposures encountered during the pandemic: Did a family member get sick or worse? Did the person lose a job or health insurance? Was the individual an essential worker whose actions ensured others’ well-being?

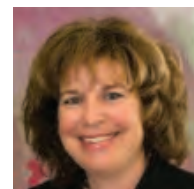
How much time was spent immersed in traditional or social media, repeatedly being exposed to hours of bad news? One must also consider community-level stressors. Did the individual live in a “hot spot”? Did shops and restaurants close, never to reopen? Was there unambiguous guidance from a governor that was backed by the best science? Emotional and behavioral responses to this ongoing crisis will be multidetermined but not random, and psychological science has isolated risk factors that can guide social service organizations and health care providers to identify the most psychologically vulnerable among us.

As the death toll due to COVID-19 crossed 125,000 in the United States, behavioral restrictions have been relaxed nationwide. Current public health guidance recommends self-protective behaviors, including frequent hand washing, social distancing, and wearing face coverings. Yet media reports show people congregating with no physical distancing at parties, beaches, and street protests. Research suggests that exposure to conflicting information from government authorities, media sources, and social networks plays a role in understanding whether or not individuals follow science-based recommendations to minimize risk and maximize public health. When Ebola virus cases appeared in the United States in 2014, the public proved to

understand risk information that is clearly and directly communicated by trusted authorities. Moreover, this trust must be maintained by honesty and competence. And just as the public returned to airplanes and high rises after 9/11, and just as people now go through x-ray machines without protest before they board a plane, most people will follow the rules.

Successfully managing COVID-19 and its aftermath will require that behavioral scientists provide a roadmap for public officials to ensure the public’s cooperation, trust in, and implementation of what is learned from biomedical science. Responsible health-protective behaviors must be encouraged with messaging that conveys clearly and consistently the costs and benefits of actions that can ensure the physical and mental health of oneself and one’s community. Although the timing of containment of COVID-19 remains unknown, most people will get to the other side of the pandemic recognizing strengths and coping skills that they did not realize they had.

—Roxane Cohen Silver



**Roxane Cohen Silver** is a professor of psychological science, public health, and medicine at the University of California, Irvine, CA, USA, and the president of the Federation of Associations in Behavioral and Brain Sciences, Washington, DC, USA. [rsilver@uci.edu](mailto:rsilver@uci.edu)

“What will the postpandemic ‘normal’ look like?”



# NEWS



A staff member at a luxury hotel in Surabaya, Indonesia, sprays a bed with disinfectant on 29 June. Some tourism-dependent countries are hoping travelers will return despite the pandemic.

## IN BRIEF

Edited by Jeffrey Brainard

### DISPATCHES FROM THE PANDEMIC

## Democrats probe grant's halt

**OVERSIGHT** | Two committees of the U.S. House of Representatives are investigating why the National Institutes of Health (NIH) in April took the unusual step of canceling a top-ranked research project on the emergence of bat coronaviruses that can infect humans. The Democratic chairs of the full committees on science and on commerce, and their respective investigative subcommittees, last week requested records and testimony from Health and Human Services Secretary Alex Azar. The grant holder was the nonprofit EcoHealth Alliance, whose collaboration with the Wuhan Institute of Virology drew fire from President Donald Trump after conservatives alleged without evidence that the pandemic virus had escaped from that laboratory. On 23 June, Anthony Fauci, director of NIH's National Institute of Allergy and Infectious Diseases, told House lawmakers that NIH canceled the grant because "we were told to." He also told *Politico* that the order came from the White House. On 24 June, NIH's Freedom

of Information Act office denied *Science's* request for documents concerning the grant cancellation on the grounds that the records "involve pending investigations."

## CDC clarifies COVID-19 risk factors

**EPIDEMIOLOGY** | Drawing on the latest evidence, the U.S. Centers for Disease Control and Prevention (CDC) on 25 June revised its guidance on how factors such as age and underlying medical conditions influence who is most at risk for getting severely ill with COVID-19. The agency now says the risk of being hospitalized, entering the intensive care unit, being put on a ventilator, or dying from COVID-19 increases throughout life; its statement in March had listed people 65 and older as at greater risk. CDC also lowered the degree of obesity that puts people at risk of severe disease, from a body mass index of 40 to 30 (equivalent to 87 kilograms in a person who is 1.7 meters tall). Obesity and type 2 diabetes are associated with "strong and consistent evidence of elevated risk"

whereas evidence that hypertension and pregnancy (p. 15) worsen COVID-19 is mixed, the agency said.

## Antiviral treatment fails test

**CLINICAL RESEARCH** | U.K. researchers announced on 29 June that they had found no benefit in treating hospitalized COVID-19 patients with lopinavir/ritonavir (Kaletra), an antiviral drug combination used to treat HIV infections. Scientists had viewed the cheap, widely available drugs as a promising therapy for the novel coronavirus after earlier, small trials had suggested some benefit. But a comparison of 1596 patients who received it in the United Kingdom's large Recovery trial and 3376 patients treated with usual care showed no significant difference in death rate after 28 days, the research team said in a press release. The trial immediately dropped that arm of the study.

**SCIENCEMAG.ORG/TAGS/CORONAVIRUS**

Read additional *Science* coverage of the pandemic.

# Ebola outbreak in eastern Congo declared over

**T**he world's second largest Ebola outbreak has ended. On 25 June, 42 days after the last infected patient finished treatment, health officials in the Democratic Republic of the Congo (DRC) said the eastern provinces of Ituri, North Kivu, and South Kivu were officially free of the disease. Since 2018, the outbreak has infected at least 3470 people and killed 2287 in the unstable conflict zone near the border with

Uganda. During the campaign to control the outbreak, health care workers identified more than 250,000 contacts of infected people and vaccinated more than 303,000 people. The DRC's fight against Ebola continues elsewhere, in Equateur province in the country's northwest, where at least 28 cases and 13 deaths have been reported as of 27 June. The largest Ebola outbreak occurred in West Africa from 2014 to 2016.

## Bayer funds glyphosate review

**HERBICIDES** | As part of a giant legal settlement, Bayer proposed last week to fund an independent scientific review of whether glyphosate, an herbicide ingredient it continues to make, causes cancer. In the deal, which a U.S. federal judge must still approve, Bayer could pay more than \$9 billion to nearly 100,000 plaintiffs who alleged the compound caused them to develop non-Hodgkin lymphoma. Any future payments to people who develop the disease could depend on the outcome of the review, for which the manufacturer and plaintiffs' attorneys would pick scientists. (In 2015, a World Health Organization research center flagged the chemical as a "probable carcinogen" but didn't evaluate the risk. U.S. and EU regulators say the weedkiller is not carcinogenic when used properly.) Also last week, Bayer agreed to pay up to \$400 million to settle claims that a different herbicide ingredient, dicamba, damaged nontarget crops by drifting from fields. Dicamba is being used more widely as weeds become resistant to Roundup, Bayer's glyphosate-based herbicide.

## Two boys die in gene therapy trial

**CLINICAL RESEARCH** | Two boys have died since April after receiving high doses of experimental gene therapy for a rare muscle disease called X-linked myotubular myopathy. The patients developed liver problems that led to sepsis—a life-threatening inflammation in response to an infection—according to a 23 June letter to families of other patients from the trial's sponsor, Audentes Therapeutics. The boys who died had existing liver disease and were older and heavier than other patients, which may have increased their risk; several younger boys tolerated lower doses. The company has stopped the 24-person clinical trial and postponed plans to seek regulatory approval. Since a 1999 death in a different

clinical trial slowed gene therapy research, the field has rebounded, and the Food and Drug Administration has approved two gene therapies for rare diseases. But recently, animal studies have suggested high doses of gene therapy can cause dangerous liver toxicity.

## Pig flu virus draws scrutiny

**INFECTIOUS DISEASES** | As the world battles the COVID-19 pandemic, an influenza virus strain widely circulating among pigs in China has the potential to spark another, researchers say. A study published this week in the *Proceedings of the National Academy of Sciences* analyzed more than 30,000 nasal swabs taken from pigs in 10 Chinese provinces over 7 years; it found that a flu strain dubbed G4 has become predominant. It uniquely blends three influenza virus lineages, including an avianlike one to which humans have no immunity and a variant of the H1N1 strain that jumped to humans and caused a pandemic in 2009. Although two cases of G4 in humans have been documented, there is no evidence of transmission between people. But because influenza virus excels at mutating into new forms, researchers are calling for stepped up surveillance of pigs and the development of a vaccine against G4 for both humans and animals.

## EPA gives up on adviser ban

**POLICY** | The U.S. Environmental Protection Agency (EPA) said last week it will not fight a judge's decision preventing the agency from barring its grantees from serving on its advisory committees. Former EPA Administrator Scott Pruitt adopted the policy in 2017, saying grantees had a conflict of interest, although industry-funded scientists were not excluded from the panels. Current EPA chief Andrew Wheeler retains broad discretion to name members.

## IN OTHER NEWS

# 25%

Share of subjects in clinical trials funded by the U.S. National Cancer Institute in 2019 who are members of racial and ethnic minority groups, up from 14% in 1999. Black enrollment (11%) is now close to the percentage of the U.S. population (13%) that is Black. Hispanic people made up 10% of enrollment but 18% of the population.

**ARRAY DELAYED** Construction in South Africa of the Square Kilometre Array, the world's largest radio telescope, has been deferred to 2021 after a 16% cut to the nation's science budget. The COVID-19 pandemic has decreased South Africa's revenues, and leaders are diverting spending to health and social programs.

**STEM CELL VOTE** Supporters of a proposed California bond measure that would provide \$5.5 billion more for stem cell research have submitted enough voter signatures to place it on the November ballot. It would fund the California Institute for Regenerative Medicine, which received \$3 billion through a 2004 ballot initiative.

**ENGINEER HONORED** NASA named its headquarters in Washington, D.C., after Mary Jackson, who became the agency's first Black female engineer in 1958. The 2016 fictionalized film *Hidden Figures*, based on a nonfiction book of the same name, recounted work by Jackson and colleagues to calculate trajectories for human space flights.





Even before a coronavirus vaccine becomes available, some activists are ready to attack it; this woman attended a “Reopen Virginia” protest in Richmond in April.

## COVID-19

# Officials gird for a war on vaccine misinformation

Fears of a rushed COVID-19 vaccine and rise of social media demand new messaging strategy

By **Warren Cornwall**

**W**ithin days of the first confirmed novel coronavirus case in the United States on 20 January, antivaccine activists were already hinting on Twitter that the virus was a scam—part of a plot to profit from an eventual vaccine.

Nearly half a year later, scientists around the world are rushing to create a COVID-19 vaccine. An approved product is still months, if not years, away and public health agencies have not yet mounted campaigns to promote it. But health communication experts say they need to start to lay the groundwork for acceptance now, because the flood of misinformation from antivaccine activists has surged.

Such activists have “kicked into overdrive,” says Neil Johnson, a physicist at George Washington University who studies the dynamics of antivaccine groups on social networks (*Science*, 15 May, p. 699). He estimates that in recent months, 10% of the Facebook pages run by people asking questions about vaccines have already switched to antivaccine views.

Recent polls have found as few as 50% of people in the United States are committed to receiving a vaccine, with another quarter wavering. Some of the communities most at risk from the virus are also the most leery: Among

Black people, who account for nearly one-quarter of U.S. COVID-19 deaths, 40% said they wouldn’t get a vaccine in a mid-May poll by the Associated Press and the University of Chicago (see graphic, below). In France, 26% said they wouldn’t get a coronavirus vaccine.

The Centers for Disease Control and Prevention (CDC) is now working on a plan to boost “vaccine confidence” as part of the federal effort to develop a vaccine, Director Robert Redfield told a Senate committee this week. Advocates urge campaigns that include personal messages and storytelling. “We better use every minute we

have between now and when that vaccine or vaccines are ready, because it’s real fragile ground right now,” says Heidi Larson, an anthropologist and head of the Vaccine Confidence Project at the London School of Hygiene & Tropical Medicine (LSHTM).

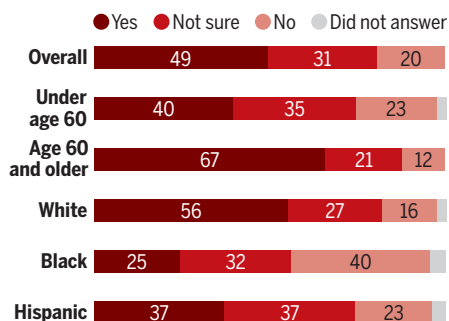
Even before the pandemic, public health agencies around the world were struggling to counter increasingly sophisticated efforts to turn people against vaccines. With vaccination rates against measles and other infectious diseases falling in some locations, the World Health Organization (WHO) in 2019 listed “vaccine hesitancy” as one of 10 major global health threats.

Any coronavirus vaccine will face additional hurdles, especially the lack of a long-term safety record, Johnson says. The frenetic pace of vaccine development may play into that concern. Even advocates have worried that the rush for a vaccine raises the risk it could be ineffective or have harmful side effects. Consider the very name for the U.S. vaccine initiative, Operation Warp Speed, says Bruce Gellin, president of the nonprofit Sabin Vaccine Institute. “What is a worse name for something that’s supposed to give you trust in a product that you want everybody to take?”

Del Bigtree, a U.S.-based vaccine critic, claims scientists are pursuing one of “the most dangerous vaccines ever attempted,” for a virus that poses little risk to most peo-

## Do you plan to get a coronavirus vaccine when one is available?

For some in the United States, the answer is no, according to a survey of 1056 people in mid-May.



ple. He says he spreads his message through an online talk show, Twitter, and presentations, and that “we have seen incredible growth” since the pandemic started.

In addition to safety concerns, activists have embraced a plethora of other antivaccine messages. In May, a documentary-style video, “Plandemic,” purporting that COVID-19 related deaths were exaggerated and a vaccine could kill millions, got more than 7 million views on YouTube before it was removed because of its unsubstantiated claims. U.S. activists in late April hosted an online “Freedom Health Summit” featuring antivaccine leaders and railing against “medical tyranny” during shutdowns. Other outlandish claims include that vitamin C can cure COVID-19 and that the disease is a conspiracy involving philanthropist Bill Gates. Statements by French doctors that coronavirus vaccines might be tested in Africa led to fears of Africans being exploited in trials.

Social media posts that create the impression of a real debate over vaccine safety can tap into psychological habits that make people think doing nothing is safer than taking action, says Damon Centola, a sociologist at the University of Pennsylvania. He fears such concerns could spread more easily among people already suspicious of medical authority, including minority communities. For example, many Black people are keenly aware of the history of medical experiments such as the infamous federal Tuskegee Study, which failed to treat Black men with syphilis. “That, to me, is the major issue of the day that I’m very worried about,” Centola says.

Accuracy and authority are at a disadvantage in a media environment that favors speed, emotion, and memorable stories, says Peter Sheridan Dodds, a complex systems scientist at the University of Vermont who studies how ideas move through social media. Antivaccine activists have used those factors to attract followers, Dodds says. “In the end, it’s story wars.”

Vaccine promoters say they need to start now to counter all this, because epidemiologists estimate that to break the pandemic, 70% of the population may need to develop immunity, either by getting a vaccine or becoming infected. Health communication experts suggest taking some pages from the antivaccine playbook. When more than 40 experts from around the world gathered online for a strategy session organized by experts with the City University of New York and LSHTM, a top recommendation was to develop faster, more creative ways to communicate with the public that “speak more directly to the emotions.”

Traditional messages promoting vaccination—authoritative and fact-filled—just don’t cut it with people worried about vaccine safety, says Larson, who helped organize the 20 May meeting. “We don’t have enough flavors” of messages, adds Larson, whose book about vaccine rumors is about to be released. “I’ve had people say to me, ‘All these social media platforms can send us to WHO or CDC. ... We’ve been there, but it doesn’t have the answers to the questions we have.’”

Some current initiatives have pioneered a more story-based approach. The National HPV Vaccination Roundtable, which promotes vaccination against the human papillomavirus, a leading cause of cervical cancer, uses YouTube videos of women who survived cervical cancer. “We need to get better at storytelling,” says Noel Brewer, a behavioral scientist at the University of North Carolina, Chapel Hill, and chair of the HPV roundtable. “We need to carry positive stories and also negative stories about the harms of not vaccinating.” The downsides of refusing a coronavirus vaccine might include not visiting grandparents and continuing to traverse the produce aisle as if it were a minefield.

In West Africa, officials are deploying the same tools that spread rumors about vaccines to counter them, says Thabani Maphosa, who oversees operations in 73 countries for Gavi, the Vaccine Alliance, which supplies and promotes vaccines around the world. In Liberia, for example, officials are using Facebook’s WhatsApp messaging app to survey people and to address the rumors behind a drop in routine vaccinations. “We need to use this as a teachable moment,” Maphosa says.

In the United States, the nonprofit Public Good Projects plans to recruit volunteers to swarm outbreaks of vaccine misinformation online and eventually develop memes and videos, says CEO Joe Smyser.

But the most effective tools may lie outside the digital realm. Real-world nudges and infrastructure, such as phone call reminders to come in for a shot, may be more powerful than any social media campaign, Brewer says. Social media doesn’t have “as much of an effect as you would imagine from the noise it’s generating,” he adds.

Public health agencies should consider taking vaccinations out of medical settings and into places where people work or shop, adds Monica Schoch-Spana, a medical anthropologist at Johns Hopkins University. That also means talking to leaders in various communities to understand their views. Such outreach could prove particularly important with minority communities. “You really do have to meet people where they are both figuratively and literally,” she says. ■

Science’s  
COVID-19  
coverage  
is supported  
by the  
Pulitzer Center.

## COVID-19

# The line starts to form for a coronavirus vaccine

U.S. and others debate who should get priority if vaccine doses are scarce

By Jon Cohen

**W**hen and if the world has a COVID-19 vaccine, who should get it first? That question came into sharp relief last week. A committee that makes vaccine use recommendations to the U.S. Centers for Disease Control and Prevention (CDC) wrestled with the issue in a virtual meeting, and new data suggested how fraught any prioritization is likely to be: Pregnant women—normally the last to receive a new vaccine, given the possibility of harm to a fetus—may have an increased risk of severe illness from COVID-19, suggesting they should be high on the list.

Bruce Gellin, former director of the U.S. government’s National Vaccine Program who now helps lead the nonprofit Sabin Vaccine Institute, says the prioritization issue comes down to a tricky balancing act between what’s best for society and individual interests. “These are tough decisions, because everybody can make a case for why somebody should be ahead of somebody else in line,” he says. “Nobody’s going to debate health care workers and first responders—people who are putting themselves at risk for others and keeping things moving. After that is when it gets complicated.”

The new coronavirus’ disproportionate toll on the elderly could put them at the front of the line—except they often have the weakest response to vaccines. Conversely, groups such as prisoners, meat packers, soldiers, and grocery store workers are often young and healthy—yet their profession or environment dramatically increases risks of getting infected. And then there is the thorny question of whether to favor specific ethnic groups hard-hit by the virus.

Even if the optimists are right and a COVID-19 vaccine is approved for widespread use as early as this fall, it is likely





COVID-19 appears to present higher risks to pregnant women, which may make vaccinating them a priority.

to be in short supply at first. CDC and the World Health Organization (WHO) are racing to plan for that possibility. Ahead of last week's meeting, a subgroup of CDC's Advisory Committee on Immunization Practices (ACIP) borrowed from a plan made for scarce pandemic influenza vaccines and developed a rough, five-tier scheme for the United States. The top tier includes 12 million people referred to as "critical health care and other workers," with the first doses going to a subset of these people who are the "highest risk medical, national security, and other essential workers," CDC's Sarah Mbaeyi explained.

Tiers two and three consist of 110 million people who also work in health care and other essential jobs, or are in these groups: those who are 65 and older, live in long-term care facilities, or have medical conditions known to increase the risk of developing severe COVID-19. The remaining "general population" of 206 million people makes up the final two tiers.

WHO on 18 June laid out its own rough "strategic allocation." It would give priority to nearly 2 billion people, lumping together "healthcare system workers," adults older than 65 or as young as 30 if they are at higher COVID-19 risk because they have comorbidities such as cardiovascular dis-

ease, cancer, diabetes, obesity, or chronic respiratory disease.

But those schemes have somewhat vague group descriptions that leave many questions unanswered, and in a 25 June meeting the ACIP subgroup turned to the full committee for guidance. COVID-19 has had a disproportionate impact on Black, Latino, and Native American communities. "Should race or ethnicity be a criterion?" Mbaeyi asked. José Romero, a pediatric infectious disease specialist at Arkansas Children's Hospital Research Institute who chairs ACIP, thought these populations should get priority. "If we fail to address this issue ... whatever comes out of our group will be looked at very suspiciously and with a lot of reservation."

Members of the full ACIP added questions of their own. Who, exactly, is a "high-risk" medical worker, given that nurses and physicians in COVID-19 units have the best protective gear, and others in the same hospitals may have bureaucratic jobs and don't interact with patients? Should the poor be given preference because they have less access to health care, live in more crowded conditions, and suffer more if they become sick and must take time off work? What about people who live in homeless shelters? How about teachers who are indoors with large groups of students?

Pregnant women present particularly vexing issues. The new data, reported in CDC's *Morbidity and Mortality Weekly Report*, compared more than 90,000 women with confirmed cases of COVID-19 who were between 15 and 44. The study has several important limitations, but in an age-adjusted analysis, the 8200 women who were pregnant were 1.5 times more likely to be admitted to an intensive care unit and 1.7 times more likely to require mechanical ventilation. "That is fairly compelling evidence" pregnant women should be prioritized for a vaccine, though there's still greater risks among those who are older than 60, says Denise Jamieson, an obstetrician/gynecologist at Emory University who is not an ACIP member.

Sonja Rasmussen, a pediatrician at the University of Florida who has collaborated with Jamieson on studies of different infections during pregnancy, says it may turn out that having COVID-19 harms not only mothers, but their fetuses. "We're trying to make really tough life-and-death decisions, and I don't think we can go too far making recommendations right now because we're still collecting data," Rasmussen says.

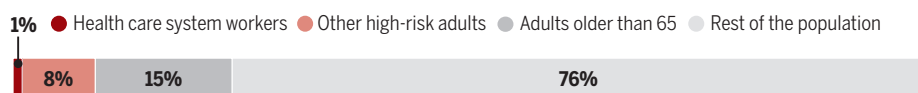
Ezekiel Emanuel, a bioethicist at the University of Pennsylvania, says there's even room for debate about the assumption that the elderly should receive the vaccine early. Emanuel, who stresses that he is not recommending "sacrificing" older people for the young, suggests it may nonetheless make more sense to prioritize vaccinating younger people because they typically develop stronger immune responses than the elderly do. "You try to get to herd immunity with people who are going to react well," he says. The less virus in circulation, the less risk to the elderly.

Tom Frieden, who headed CDC in 2009 during an influenza pandemic when a vaccine was in short supply, recalls the debates that erupted within the agency and the outside pressures it experienced. He foresees intense lobbying as a COVID-19 vaccine nears reality. "There may be groups that from a societal or health standpoint may not appropriately be in tier one but are quite insistent on it," says Frieden, who now heads the Resolve to Save Lives initiative, which combats epidemics.

Frieden says he was impressed by the ACIP discussions but stresses that even when it comes time to make the recommendations—ACIP will meet again on this issue in August and WHO plans to finalize allocation plans by the end of that month—the data will remain imperfect. "If you waited until you had perfect data about this issue, you would never act," he says. "It's not premature to plan for this." ■

## First in line

The three highest priority groups in the World Health Organization's draft plan for allocating a COVID-19 vaccine include only about one-quarter of the global population. But those 1.85 billion people could require about 4.2 billion vaccine doses (two per person plus 15% wastage).



## PLANETARY SCIENCE

# Rock seen inside Venus's orbit could solve puzzle

Mineral in first object so close to the Sun may be a clue to missing “mantle” asteroids

By **Nola Redd**

**E**arlier this year, astronomers discovered an oddball asteroid inside the orbit of Venus—the first member of a predicted flock near the Sun. No bigger than a small mountain, the asteroid has now gained another distinction: It appears to be rich in the mineral olivine, which makes up much of Earth's deep rock. Some astronomers think that is a clue to a larger set of asteroids, never properly accounted for, that was forged early in the formation of the Solar System.

“It's improbable that we look at this new population and an olivine-dominated object is the first type we see,” says Francesca DeMeo, an asteroid hunter at the Massachusetts Institute of Technology who was not part of the discovery team. “That's what makes this a cool result.”

Most of the nearly 1 million known asteroids lie in a belt beyond Mars, shepherded by Jupiter's gravity. Just 23,000 Atira asteroids—named after a Native American goddess—have been found within Earth's orbit, because interactions with the inner planets upset their orbits and eventually send them crashing into a planet or the Sun. But astronomers have long suspected the existence of an even smaller population of short-lived objects within the orbit of Venus, informally called Vatiras.

They're hard to spot. Like Venus, these objects would appear low on the horizon at dawn and dusk, barely visible against the glare of the Sun. Yet on 4 January, astronomers using a small survey telescope at the Palomar Observatory in California found one: 2020 AV2, a 1.5-kilometer-wide asteroid in a 151-day orbit around the Sun.

To find out what 2020 AV2 is made of, Marcel Popescu, a researcher at the Astronomical Institute of the Romanian Academy, and his colleagues used telescopes on the Canary Islands to prise apart the asteroid's reflected light, revealing absorption lines that are clues to chemical composition. They identified the fingerprint of olivine, a major mineral in the mantle of Earth and other planets, Popescu and his colleagues reported on 18 June in the *Monthly Notices of the Royal Astronomical Society*. “We're not able to say definitely that it is an olivine-dominated asteroid, but olivine is abundant at its surface,” Popescu says.

Separate studies of the object's trajectory

by Carlos and Raul de la Fuente Marcos, brothers who are researchers at the City University of Madrid and were also co-authors on the discovery paper, revealed that 2020 AV2 likely originated in the main asteroid belt. Gravitational interactions with Jupiter would have flung it, and potentially some neighbors, toward Earth. There, a gravitational dance with the terrestrial planets probably nudged its orbit inside Venus over millions of years. That path, along with its small size, suggests to Popescu a way to solve a decades-old “missing mantle” puzzle for asteroids.

The same separation into core, mantle, and crust that took place in rocky planets

One idea is that astronomers just can't see small enough. The olivine-rich asteroids are more easily pulverized than their harder iron cousins, suggesting most of the missing mantle sits in small pieces—a “battered-to-bits” model first proposed in the 1990s. 2020 AV2 could be a far-flung representative of a hidden population of even smaller, olivine-rich objects in the main belt that are hard to see because they're farther from Earth, Popescu says. “As soon as we are able to observe smaller objects, it is expected that we will find these objects,” he says.

Other researchers are skeptical. In her 2019 study, DeMeo searched for olivine-rich



The first Vatira, 2020 AV2, may point to asteroids resembling Earth's mantle.

soon after they formed is also thought to have occurred in small planetary embryos 4.56 billion years ago. Heat from the decay of short-lived radioactive aluminum-26 caused iron and nickel-rich rocks in these embryos to sink into their cores while olivine-rich rocks rose into a mantle and the lightest minerals formed a thin crust. Subsequent collisions shattered these embryos into asteroids.

Yet although plenty of metal-rich asteroids have been identified, the olivine-rich mantle asteroids are few and far between. “When you fragment differentiated bodies, you should get a lot of mantle out,” says Marco Delbo of the Côte d’Azur Observatory in Nice, France. “But we don't see many of these asteroids in the main belt.” In 2019, DeMeo reported finding 21 new olivine-rich asteroids in the main belt, bringing the total to 36. But that's still not enough to account for all the missing mantle material.

objects nearly as small as 2020 AV2 and found only a handful—not enough to hint at a hidden smaller population. Moreover, she says, the Vatiras are likely to hail from the inner part of the asteroid belt, where olivine-rich bodies are slightly more common. That makes 2020 AV2's composition a little less surprising, she says. The discovery “definitely adds to our body of knowledge,” she says. “I just don't think it clinches any final conclusions.”

Meanwhile, Popescu wants to observe the asteroid again and look for signs of another mineral, pyroxene, which would firm up its identity as a “mantle” asteroid. And he hopes ongoing surveys will spot more close-in asteroids. “It's a very interesting object, a peculiar one—the first of its kind,” Popescu says. “I want to see if there will be others.” ■

Nola Redd is a journalist in Atlanta.





## BIOMEDICINE

# A colorful chemotherapy agent could be made less toxic

Safer forms of doxorubicin, which kill tumor cells without damaging DNA, could spare hearts of cancer patients

By **Jocelyn Kaiser**

**C**an the red devil be defanged? Doxorubicin, an old chemotherapy drug that carries this unusual moniker because of its distinctive hue and fearsome toxicity, remains a key treatment for many cancer patients. But a new study reports the drug can be tweaked to reduce its most punishing side effect, cardiac damage, without blunting its ability to curb tumors.

The work, from an academic team in the Netherlands, upends conventional thinking about doxorubicin and related drugs, suggesting they do not need to directly damage DNA to kill cancer cells. “This idea was floating around in the literature for many years, but [until now] it has not been proven experimentally,” says Sherif El-Khamisy, who studies DNA repair at the University of Sheffield. “It’s a great study.”

The team now plans to test two potentially safer versions of doxorubicin’s drug class in people. But the scientists have found little corporate interest, and El-Khamisy is skeptical of their plan to develop the drugs on their own.

Doxorubicin belongs to a class of compounds known as anthracyclines, which

were originally extracted from *Streptomyces* bacteria. They have antibiotic properties but also proved to be some of the most potent chemotherapies ever found; anthracyclines are used to treat 1 million cancer patients each year, particularly those with leukemia and breast cancer.

But because anthracyclines can cause heart damage, physicians often avoid giving them to elderly patients. Many childhood cancers are treated with high doses of the drugs, but cardiac problems sometimes haunt survivors later in life, along with a risk of new tumors, which doctors have attributed to DNA damage from the drugs (*Science*, 15 March 2019, p. 1166).

Researchers have tried to reduce the heart risks by, for example, packaging the drugs in fat so they will home in on tumors, with limited success. But chemist Jacques Neeffes and his team at Leiden University and collaborators tried a different approach based on a surprising finding about how the drugs fight cancer, which they and a separate U.S. group reported in 2013. The textbook explanation is that the drugs kill rapidly dividing cells, such as those in a tumor, by blocking an enzyme they need to untangle and repair DNA as they replicate. But the researchers found doxorubicin also

Doxorubicin, known as the red devil for its color and toxicity, is widely used for adult and childhood cancers.

kills cancer cells by dislodging histones, the spherical proteins that DNA coils around like a spool to form a structure known as chromatin. This chromatin damage apparently interferes with the transcription of genes into proteins and other cell processes, Neeffes says.

In the new work, the Leiden team tested two anthracycline variants that remove histones without breaking DNA: an approved cancer drug called aclarubicin, and a tweaked version of doxorubicin they call diMe-Doxo. The compounds worked as well as the original drug, if not better, at killing cultured cancer cells and were nearly as effective at slowing tumor growth in mice. Yet mice prone to developing tumors that were dosed with aclarubicin did not show signs of heart damage, suggesting people treated with the drugs might be spared these effects. These mice were also much less likely to develop tumors later, the Leiden team reported online 17 June in the *Proceedings of the National Academy of Sciences*.

“I’m very excited about their findings,” says Katerina Gurova of the Roswell Park Comprehensive Cancer Center in Buffalo, New York, who is developing a cancer drug that also works by damaging chromatin. “We’re learning more about how to make these widely used drugs less toxic.”

Aclarubicin was once used in Europe for leukemia but was removed from the market in the 1990s because of manufacturing issues. Scientists at the U.S. National Cancer Institute came up with diMe-Doxo in the 1980s, but didn’t develop it further. Neither drug now has patent protection, which means companies aren’t interested, Neeffes says. So his team has raised money from public and private sources to produce diMe-Doxo and aclarubicin at the quality standards required for patients so they can run clinical trials as an academic effort.

Both drugs deserve study, he says—acalarubicin seems to work best on blood cancers whereas diMe-Doxo appears more effective for solid tumors. The group has a large grant from the Dutch Cancer Society to start a clinical trial next year of aclarubicin in relapsed leukemia patients. “We are doing what usually pharma is doing,” Neeffes says.

That will be “challenging,” El-Khamisy says. Drug companies are the experts at the steps, like studying how a compound is metabolized and demonstrating safety, that are needed to win approval for a medicine, he notes. Without a corporate partner, he fears, the study “may be yet another paper that is a good idea, but not really translatable.” ■

# Greenland rock cores to trace ice's past melting

U.S. drilling campaign could also date controversial Hiawatha impact crater

By Paul Voosen

**G**lobal warming is accelerating the melting of Greenland's ice sheet, which locks up enough water to raise sea levels by 7 meters. In 2021, U.S. researchers will go to the frozen expanse to pinpoint the last time it disappeared. The 5-year, \$7 million campaign, awarded last month by the National Science Foundation, will mark the first large U.S. ice drilling program in Greenland in more than 25 years. Unlike past projects, the target is not the climate records held in the ice, but the rocks below, which contain radioactive clocks that show when they were last exposed to air. "The whole bedrock is an archive," says Joerg Schaefer, a geochemist at Columbia University and co-leader of the project, called GreenDrill. "It's just a question of getting these freaking samples under the ice."

Greenland already accounts for 25% of global sea level rise, and that share is growing. Scientists have recently identified the island's north as a hot spot for melting during the next century. The drilling project could not only validate those near-term fears, but also inform climate models that struggle to predict the long-term fate of the ice.

As a bonus, the effort could shed light on the timing of the asteroid or comet impact that gouged the Hiawatha crater, a 31-kilometer scar hidden under the ice, sometime within the past 3 million years. Some scientists think the event was recent and the trigger for a bout of global cooling 13,000 years ago known as the "Younger Dryas." But so far, no firm dates have been recovered from crater material to support that controversial claim (*Science*, 16 November 2018, p. 738). Although GreenDrill researchers will not drill into the crater itself, one of its four sites is just 20 kilometers to the west. Rocks there could show when the ice last melted away—perhaps in the sudden heat of the impact. And any impact ejecta recovered in the rock could be sifted for minerals, such as zircons, that offer precise dates.

The larger goal of the project, however, is mapping the ebb and flow of the ice sheet over the past million years. The last major U.S. effort, the Greenland Ice Sheet Project 2 (GISP2), cored 2 kilometers of ice on its way to hitting bedrock in 1993. GreenDrill

will not go nearly as deep, but will make up for it in volume. Each of the four sites will have three holes in a transect running toward the shore: one through 300 meters of ice, one through 100 meters, and one on exposed rock near the ice's edge. It will be a major operation, says Henriette Linge, a geologist at the University of Bergen. "It's very promising that they'll get information otherwise beyond our reach."

The history of the ice is written in the rocks it covers. Cosmic rays create trace amounts of radioactive isotopes when they strike exposed rock and soil; ice blocks

## Drilling into the past

In 2021, a \$7 million U.S. campaign will begin to drill four sites in northern Greenland. Bedrock cores could reveal when ice disappeared in the past million years.



these rays, and so the resulting radioactive decay provides a clock for when the ground last saw light. In 2016, Schaefer used rocks from GISP2 to show that the ice covering the site melted sometime in the past million years, counter to prevailing beliefs that the sheet had been stable for several million years. Last year, preliminary work on dirt from another core in northwest Greenland, Camp Century, seemed to support that finding (*Science*, 1 November 2019, p. 556).

There are two prime suspects for when the ice sheet could have last collapsed: warm periods some 420,000 and 140,000 years ago. Both saw temperatures like today's, due to natural wobbles in the planet's tilt and orbit, but it's unclear whether the warmth lasted long enough to melt the entire ice sheet. Knowing whether the past warmings were enough to erase the ice is crucial to gauging the sea-level threat from Greenland today, says Paul Bierman, a geochemist at the University of Vermont who is not involved in the drilling campaign. "This project is one of the most important pieces of science we can do on Greenland."

GreenDrill will target rock rich in minerals that contain five isotopic tracers, including chlorine-36, which has a brisk, 300,000-year half-life. The clock's sharp time resolution should help researchers discern whether the ice disappeared during either of the warm periods, and how long it took to melt. Although the four sites cannot say for certain what happened elsewhere on the ice sheet, patterns of exposure between the 12 cores, integrated in a next-generation ice sheet model, will be able to constrain the ice loss.

The fate of Greenland's ice sheet amid modern warming is a drama that will play out over many centuries. But GreenDrill could also help in understanding shorter term ice loss in northern Greenland, which scientists now fear is more sensitive to melt than its south. The amplification of climate change in the Arctic means the high-latitude region is warming faster and shedding more ice than anywhere else in Greenland. Another reason for its vulnerability: As sea ice disappears, the north's low-lying inland glaciers could lose a protective buttress.

Using a fast clock based on carbon-14 isotopes found in the rocks, researchers could discover whether some of the northern GreenDrill sites were briefly exposed 8000 years ago, when regional temperatures were 3°C warmer than now, says Jason Briner, a geologist at the University at Buffalo and project co-leader. Evidence suggests the southern ice sheet was stable during the warm episode; finding that the ice in the north retreated, Briner says, would cement its place as a worrisome new climate hot spot. ■





# IMPROBABLE OASIS

Pools in the Mexican desert are a hot spot of microbial diversity—and a window into early life

By **Rodrigo Pérez Ortega**; Photography by **David Jaramillo**

**V**aleria Souza Saldívar never planned to devote her life to a remote and ancient oasis more than 1000 kilometers north of her laboratory in Mexico City. But a call in early 1999 changed that.

“It’s one of the best cold calls I’ve ever made,” says James Elser, a limnologist at the University of Montana. He had picked up the phone to invite Souza Saldívar to join a NASA-funded astrobiology project in Cuatro Ciénegas—a butterfly-shaped basin with colorful pools, or *pozas*, in the middle of Mexico’s Chihuahuan Desert.

Neither Souza Saldívar, a microbial ecologist at the National Autonomous University of Mexico, University City, nor her ecologist husband and research partner Luis Eguiarte Fruns, also at UNAM, had ever visited Cuatro Ciénegas.

That first trip convinced them to completely change their research plans. “Looking at those mountains and the water, I fell in love,” Souza Saldívar says.

The landscape—more than 300 turquoise-blue *pozas* scattered across 800 square kilometers, among marshes and majestic mountains—wasn’t the only draw. The wa-

ters, whose chemistry resembled that of Earth’s ancient seas, teemed with microbes; unusual bacterial mats and formations called stromatolites carpeted the shallows. When Souza Saldívar first cultured the organisms from the *pozas*, “The amount of microbes was enormous, as was the diversity of colors and colony sizes,” she recalls.

For her, this remote microbial hot spot was an irresistible mystery.

Since then, work by Souza Saldívar, Eguiarte Fruns, and a widening circle of collaborators in Mexico and the United States has shown that Cuatro Ciénegas—which means “four marshes” in Spanish—is one of the most biodiverse places on the planet. “There’s nowhere that has so much ancient diversity of microorganisms,” says Michael Travisano, an evolutionary ecologist at the University of Minnesota, Twin Cities, who has col-







Hundreds of spring-fed pools dapple Mexico's Chihuahuan Desert at Cuatro Ciénegas, seen from the air (opposite, bottom). Their azure water, rich in minerals but low in the nutrients and phosphorus most life requires, is a haven for ancient microbes.

Carranza, born in a village at the basin's margin, became a leader of the Mexican Revolution and president of Mexico from 1917 to 1920. Nowadays, the village is called Cuatro Ciénegas de Carranza after him.

But in the 1960s, Cuatro Ciénegas started to become famous for its biodiversity, as biologists began to describe new species of snails, fish, turtles, and plants found in the pools and marshes—and often nowhere else.

Wendell “Minck” Minckley, a renowned ichthyologist at Arizona State University (ASU), Tempe, was first lured to Cuatro Ciénegas after learning that the world's only aquatic box turtle (*Terrapene coahuila*) lived there. Over the years, Minckley made frequent trips to the *pozas*, describing their snails and fish (*Herichthys minckleyi*, a cichlid, bears his name) while making connections with the local people.

Minckley also noticed peculiar, rocky structures in the pools. They were stromatolites, biological structures normally found as fossils dating back as much as 3.5 billion years. Colonies of photosynthesizing bacteria, which boosted early Earth's oxygen, created the layered formations by depositing carbonates and trapping sediment in ancient, shallow seas. But these stromatolites were alive. Also found in other extreme environments such as Australia's warm, salty Shark Bay, living stromatolites “are sort of a window into early Earth,” Elser says. The *pozas* also nurture bacterial mats, a soft form of stromatolites normally found deep in the ocean.

As early as the 1970s, Minckley realized the pools and their diversity were under threat: Local farmers were carving canals to tap their water. Thanks in part to his lobbying, the Mexican government in 1994 designated an 85,000-hectare protected area. But the drainage continued. “Minckley knew that Cuatro Ciénegas was going to die,” Souza Saldívar says. He thought NASA might be its salvation.

In 1998, NASA established its Astrobiology Institute, a network of researchers studying life in extreme environments that might resemble conditions on other planets. Minckley saw an ideal astrobiology study site in the waters of the *pozas*, with their seemingly inhospitable chemistry and living stromatolites. But he was no expert on extreme environments, so he enlisted Elser, who specializes in how water chemistry affects ecosystems and also works at ASU. After they submitted a 1998 proposal to fund

laborated with the Mexican researchers since 2001. Among the most recent additions to that menagerie are hundreds of species of archaea, the ancient microbes that may have given rise to eukaryotes—organisms with complex, nucleated cells.

The diversity includes strains with unusual adaptations, such as the ability to build their lipid membranes with sulfur instead of the usual phosphorus, which is scarce in the waters of the *pozas*. It includes potential sources of new compounds for medicine and agriculture. And it poses a question that has occupied Souza Saldívar and Eguiarte Fruns for the past 20 years: How did this Noah's Ark of ancient microbes arise? “It's a dream for every biologist to know the origin of diversification,” Souza Saldívar says.

But her dream might be short-lived. Since the 1970s, farmers have intensively drained water from the *pozas* and rivers to irrigate

nearby fields of alfalfa, grown for cattle fodder, gradually drying the improbable oasis. Souza Saldívar has galvanized a conservation effort that has slowed the drainage; in the coming weeks, a canal that removes 100 million cubic meters of Cuatro Ciénegas's water annually is scheduled to close. In the meantime, the researchers have been trying to describe as much as they can, as fast as they can, before their beloved *pozas* dry up and the precious microscopic life that has survived undisturbed for millions of years dies off.

**CUATRO CIÉNEGAS SERVED** as a stopping point for hunter-gatherers for thousands of years. To date, 50 archaeological sites with cave paintings—some dating to 2275 B.C.E.—have been found in mountain caves around the basin. Much later, the region made a mark on history when Venustiano





Valeria Souza Saldívar and Luis Eguiarte Fruns (top) have spent 20 years studying biodiversity at Cuatro Ciénegas, where they have found thousands of new species in living structures like a bacterial mat (bottom).

the project, however, NASA said they should add experts on microbiology and evolution—and those experts had to be Mexican to help secure permits to obtain samples. Based on colleagues' suggestions, Elser called Souza Saldívar and Eguiarte Fruns, newly minted professors at UNAM. They joined, and NASA approved the 3-year project.

With two children in tow, the couple met Minckley and Elser at Cuatro Ciénegas. Next to the turquoise-blue waters of La Becerra *poza*, Minckley told them he believed the ecosystem was a glimpse of deep time. "Do you see these miniature snails in my hand?" Souza Saldívar recalls him saying. "I just scooped them from the springhead, but their direct ancestors were eating sulfur bacteria in hydrothermal vents 220 million years ago in the bottom of the ancient Pacific."

Based on the water chemistry—low in phosphorus, iron, and nitrogen—and the presence of living stromatolites, Minckley believed Cuatro Ciénegas re-created the marine conditions found worldwide millions of years ago. He challenged the two researchers to explore its mysteries—and to protect its *pozas*. "Only you, as Mexicans, can save them from the extinction caused by humans," Souza Saldívar recalls him saying.

Minckley died 2 years later, in 2001.

**TO INVENTORY THE FULL DIVERSITY** of microbes at Cuatro Ciénegas and trace their relationships, Souza Saldívar needed to study their DNA. To do so, scientists normally take microbial samples from a site and grow them in a lab. But many bacteria and archaea are difficult to culture, and only a few groups at the time had successfully analyzed DNA isolated directly from the environment. High magnesium levels in the water and "slime" from the microbes made isolating DNA from the *pozas* especially difficult.

But Souza Saldívar and her students Ana Escalante and Laura Espinosa Asuar made a start. In 2006, they reported in the *Proceedings of the National Academy of Sciences* that they had found 38 distinct groups of microbes—four times as many as in a typical salt marsh—corresponding to 10 major lineages of bacteria and one of archaea. Half the bacterial groups were most closely related to marine microbes. Almost 10% of the groups resembled ones that live on hydrothermal vents—fissures deep in the ocean where microbes thrive despite extreme heat and mineral concentrations.

As Minckley had suspected, Cuatro Ciénegas had somehow preserved ancient marine life forms deep in the desert, more than 500 kilometers from the Gulf of Mexico, at a site where the last seas retreated some 20 million years ago.

PHOTOS: DAVID JARAMILLO





Stromatolites, reeflike colonies of carbonate-secreting cyanobacteria, abounded in Precambrian seas—and thrive at Cuatro Ciénegas.

“The deep time aspect [of Cuatro Ciénegas] is very surprising,” Travisano says. It is a true “lost world,” preserved by the hostile water chemistry, he and the Mexican team argued in a 2018 paper in *eLife*. Millions of years ago, they proposed, ancient marine ancestors found their way to the place, adapted to the extreme environment, and didn’t change much.

The *pozas* themselves are not particularly ancient. The springs that nurture them are fed by deep aquifers in Sierra San Marcos y Pinos, filled with water accumulated during the last ice ages, Eguarte Fruns says. Now, the water seeps to the surface because of an active fault beneath the basin. It rises through ancient marine sediments, picking up its unusual chemistry along the way. Somehow, the ancient microbes persisted and diversified in a succession of springs that must have appeared and vanished throughout geologic time. As in an ancient clock, Souza Saldivar says, all the original mechanisms are still working together to sustain unusual life.

To Frederick Cohan, a microbial ecologist at Wesleyan University who is not part of the Cuatro Ciénegas project, the fact that many of the microbes are related to marine species and not species found inland is compel-

ling. “I think it’s saying those organisms are anciently there.”

**WHEN THE RESEARCHERS** looked at the stromatolites, they found even more diversity. Samples from one site, Pozas Azules II, yielded more than 58,000 distinct microbial sequences, predominantly from bacteria—

not a direct count of species, but an indicator of biodiversity. In the Río Mezquites, a stream that flows through the northern part of the basin and recharges several pools, they identified 30,000 sequences, mostly from cyanobacteria. More than 1000 sequences from Pozas Azules II appeared to be from archaea, the researchers reported

in *Environmental Microbiology* in 2009. The stromatolites also teemed with bacteria-infecting viruses—strains that were unique to each pool and resembled marine viruses.

Studying the microbes hasn’t been easy. “There are thousands and thousands of new bacteria that we can’t grow in culture,” Souza Saldivar says. They could, however, identify some startling adaptations to the extreme conditions. In one bacterium found only in El Churince, a system of lagoons and *pozas* on the western part of the basin, researchers sequenced the smallest genome ever found in its genus, *Bacillus*. The work, led by Gabriela Olmedo Álvarez, a genetic engineer at Center for Research and Advanced Studies of the National Polytechnic Institute, Irapuato, also showed that the microbe—*B. coahuilensis*—could synthesize membrane sulfolipids. This meant that, like some plants and cyanobacteria, it could

## Water world

In the Cuatro Ciénegas Basin, ringed with mountains and desert, an aquifer feeds hundreds of pools and marshes. But canals tapping water for agriculture threaten the wetlands and the biodiversity they host.







Endemic fishes and turtles first drew scientists to Cuatro Ciénegas, where they stumbled on its less visible microbial riches.

use sulfur from the environment—instead of phosphorus—to form its cell membranes.

“It likely ‘stole’ these genes from a cyanobacterium,” Olmedo Álvarez says, enabling it to cope with scarce phosphorus, a condition thought to have prevailed in Earth’s earliest oceans. The microbe’s small genome may also have helped it thrive, as it required less phosphorus to build its DNA. Olmedo Álvarez thinks the organism may offer a glimpse of the stratagems used by early microbes to adapt to their new environment.

“We’re just starting to understand the depth of diversity,” says Olmedo Álvarez, who found that *B. coahuilensis* is itself starting to split into strains with variations in phosphorus metabolism.

The low phosphorus conditions found in Cuatro Ciénegas not only promoted local adaptations, but also accelerated microbial diversification, Souza Saldívar and Elser argued in a perspective published in 2008 in *Nature Reviews Microbiology*. Bacteria normally share bits of DNA with their neighbors in a process called horizontal gene transfer, which blurs the divisions between strains. But in Cuatro Ciénegas, the microbes—hungry for phosphorus—essentially consume free DNA rather than incorporating it into their genomes. “They will eat the DNA to get the phosphorus,” Elser says.

Besides offering insights into evolution, Cuatro Ciénegas’s microbial diversity may hold practical payoffs. “Cuatro Ciénegas is one of the richest

places on the planet for genetic resources,” Souza Saldívar says. For example, most modern antibiotics are derived from actinobacteria, which are abundant in the *pozas*. Susana De la Torre Zavala, a biotechnologist at the Autonomous University of Nuevo León (UANL), Mederos, is searching for potential antibiotics in a library of 350 actinobacteria from the basin. Her team has also found that an extract from a microalga living in the pools shows anticancer activity.

Agriculture, too, could benefit, Olmedo Álvarez says. By 2050, the reservoirs of

phosphorus that help sustain global harvests could become scarce, and the microbes’ ability to concentrate the element from different sources could hold solutions. “We’re understanding Cuatro Ciénegas, but we’re also understanding basic principles of ecological interactions that have an application in medicine and agriculture,” she says.

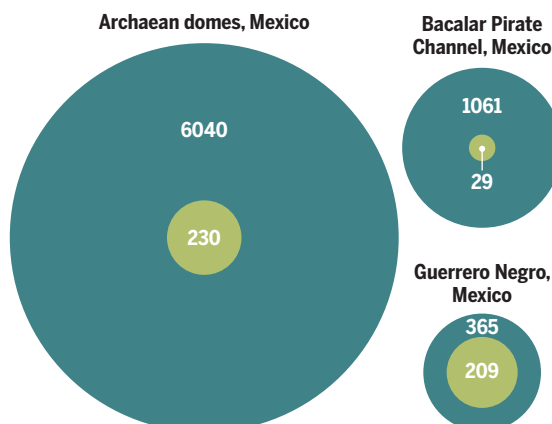
**AS THE SCIENTIFIC STORY** of Cuatro Ciénegas unfolded, its fate has hung in the balance, with Souza Saldívar fighting a long series of battles over its water with local farmers and landowners, dairy companies, and politicians. Her weapons have been her rising scientific profile and a tireless outreach to the public, especially young people.

Souza Saldívar has drawn fire—during a 2013 microbiology congress, police had to protect her from protesting locals—but she has won a series of victories. In 2007, the daughter of the CEO of LALA, a giant dairy consortium with roots in the state of Coahuila, told her father she wouldn’t speak to him because “he was killing Cuatro Ciénegas,” Souza Saldívar says. The executive promptly scheduled a meeting with the scientist. “You need to change your cows’ diet,” Souza Saldívar says she told him, refusing to accept a courtesy yogurt he offered. “I’ll accept your yogurt when you do so.” He promised not only to stop buying the region’s alfalfa, but also to

## Lost arks

Shallow, mineral-rich pools and lagoons, with conditions like those in ancient oceans, are hot spots of microbial diversity. Floating mats at Cuatro Ciénegas teem with the primordial microbes known as archaea, leading researchers to call them “archaeal domes.”

● Archaeal species ● Bacterial species



invest in environmental education projects for local children.

Two years later, she won an unusual ally, the powerful Mexican billionaire Carlos Slim. His foundation collaborated with the World Wildlife Fund (WWF) to buy the land surrounding El Churince in the western basin, and to provide researchers with a 5-year, 18 million Mexican peso (\$1.4 million) grant to study Souza Saldívar's favorite *poza*. This allowed them to set up the infrastructure to perform long-term experiments. But it did not save the water.

In 2010, Mexico's National Water Commission (CONAGUA) set out to replace the open, leaky canals, which lose 75% of the drained water, with less wasteful enclosed conduits. But the project was abandoned midway—most likely because of corruption—and the old canals were never closed. As Cuatro Ciénegas continued to dry up, the researchers raced to study El Churince, finding 5167 distinct species of bacteria and archaea in the last remaining pool. A close inspection of the genomes of *Bacillus* bacteria from one single square kilometer increased the known diversity of the group by more than 20%. By comparing DNA sequences, the team traced the *Bacillus* diversity to two ancient ancestors, one dating back 680 million years, the other 160 million years. Those dates coincide with the breakup of the supercontinents Rodinia and Pangaea, respectively, and the team thinks the oceans that formed during those convulsions carried the ancestral microbes to what is now the Cuatro Ciénegas Basin, where they have persisted ever since.

Cohan says that's plausible. *Bacillus* from elsewhere fail to thrive in Cuatro Ciénegas, most likely because they are outcompeted by the local microbes and can't adapt to the extreme conditions. And the *Bacillus* species from Cuatro Ciénegas are not found anywhere else in the world. "It's just bizarre," Cohan says, but it makes the *pozas* so much more valuable and worth saving. "It's kind of a paleontological microbial park."

In 2016, El Churince dried up just after the funding from the WWF–Carlos Slim Foundation ended. The researchers felt devastated. Souza Saldívar says it was painful to see turtle shells lying on the now-barren soil. "It's really sad," Olmedo Álvarez says. "It's gone."

**ON THE EASTERN SIDE** of the basin, things are looking brighter. In 2000, the conservation nongovernmental organization Pronatura Noreste acquired the Pozas Azules ranch: 2721 hectares hosting about 100 *pozas*. Pronatura eventually gained rights to the water as well, enabling it to close canals draining the *pozas* in the

ranch. Farmers are now encouraged to adopt water-sparing drip irrigation, and some are growing nopal—an edible cactus popular in Mexican cuisine—which requires much less water than alfalfa.

The researchers have focused their recent studies on Pozas Azules. In 2019, after an unusual spring rain, the team noticed alien-looking structures in the shallow waters of a site near Pozas Azules II: white microbial mats buoyed by gas. The gas appeared to be largely methane, and a genetic analysis showed the mats were teeming with archaea—230 distinct species, they report in a preprint. That makes the spot "the most diverse place of archaea

ing them about sustainable agriculture. In 2011, with funding from the LALA Foundation and the WWF–Carlos Slim Foundation, the scientists set up a college-level molecular biology lab at the school, which is now ranked among the best rural high schools in Mexico.

Héctor Arocha Garza is one of its graduates. Inspired by the secrets of Cuatro Ciénegas, he pursued a Ph.D. in biotechnology at UANL with De la Torre Zavala, then returned to his hometown. "My heart was in Cuatro Ciénegas," he says. Now, he's leading the scientific branch of a privately funded megaproject called Cuatro Ciénegas 2040 that aims to build a science museum and



Shaped and seeded with life by ancient seas, the Cuatro Ciénegas Basin lies at the foot of the distant Sierra San Marcos. The white dunes bordering the basin are made of gypsum, a legacy of a Jurassic ocean.

that we know of," De la Torre Zavala says.

Now, the team hopes to analyze samples from the structures, which it calls "archaeoan domes," in search of the elusive Asgard archaea, organisms previously found only in the deep ocean and thought to hold clues to the evolution of simple microbes into complex eukaryotes. Although some in her team are skeptical, Souza Saldívar is convinced they will find them. "Valeria's usually right," De la Torre Zavala says.

Such prospects have added to Souza Saldívar's determination to preserve Cuatro Ciénegas, and she is enlisting young people for support. In every field trip since 2004, her team has spent time with students from the local high school, showing them how to use a microscope and take simple environmental measurements, and teach-

make Cuatro Ciénegas a scientific tourism destination, while supporting education and medical care for the village's young people.

The effort comes at a critical moment. More than 90% of the marshes are gone, and some *pozas* and lagoons are dry. But this year, CONAGUA committed to regulating water usage and closing illegal wells, and Pronatura Noreste will close the Saca Salada Canal, which drains the Río Mezquites, as soon as the COVID-19 pandemic permits.

Those developments, and stories like Arocha Garza's, give Souza Saldívar hope for the future of Cuatro Ciénegas. "It has been a very complicated, long, and difficult process," she says. But now, she wrote in a recent book, "There is a revolution occurring in this oasis: Science is the tool and kids are the drivers." ■



# INSIGHTS

## LETTERS

### NEXTGEN VOICES

## News from a postpandemic world

We asked young scientists to imagine this scenario: **You are a science writer in the year 2040 working on a news story that answers this question: What do you hope or fear will be the long-term effects of the coronavirus disease 2019 (COVID-19) pandemic?** A selection of their responses, arranged as a newspaper, is below. Follow NextGen Voices on Twitter with hashtag #NextGenSci. Read previous NextGen Voices survey results at <https://science.sciencemag.org/collection/nextgen-voices>. —Jennifer Sills

### World

Today, scientists confirm that 1000 previously endangered species have been removed from the Vulnerable list. Biodiversity renewal has been under way since the COVID-19 pandemic 20 years ago led many governments to reevaluate their priorities. Hunting practices and bushmeat consumption were constrained to limit the transmission of new pathogens through human contact with the meat and biofluids of wild animals. Deforestation

was restricted worldwide when it became clear that land-use modifications and climate change were important drivers of vector-borne diseases. COVID-19 claimed many lives, but the political and environmental changes the pandemic inspired have likely saved many more by protecting the world's biodiversity.

**Joel Henrique Ellwanger**

Department of Genetics, Universidade Federal do Rio Grande do Sul, Porto Alegre, Rio Grande do Sul, 91501-970, Brazil.  
Email: joel.ellwanger@gmail.com

### Nation

Science and technology research budgets, now classified as an arm of the national defense force, could rival traditional military spending in a few years' time. This newfound prioritization of science was shaped by the COVID-19 pandemic, which made clear that the previous conception of military force is impractical when the enemy is invisible and formidable. The unprecedented redirection of financial resources to scientific communities to help find a cure and vaccines, along with the increased demand for scientific experts, expanded technological frontiers and gave science a well-deserved space in governance.

**Mpho Diphago Stanley Lekgoathi**

The South African Nuclear Energy Corporation, Pretoria, Gauteng, South Africa.  
Email: mpho.lekgoathi@necsa.co.za

In response to the 50th wave of COVID-19, which hit New York City last month, the U.S. government has announced that the first spaceship designated for in-orbit medical treatment of COVID-19 patients will soon transport 10,000 residents from high-risk zones to Space. Scientists say that prolonged





stay in Space colonies with exposure to controlled gamma radiation from cosmic dust may help weaken the virus's strong affinity to lung tissue. "We will do all we can to protect our residents on Earth. Unlike 2019, we are prepared for this challenge," said the President in a Capitol Hill address. The Senate has voted to fund the treatment expenses for everyone on the flight.

#### Kartik Nemani

Layered Materials and Structures Lab, Department of Mechanical and Energy Engineering, Purdue School of Engineering and Technology, Indiana University–Purdue University Indianapolis, Indianapolis, IN 46202, USA. Email: snemani@purdue.edu

## Business

Workers at major corporations staged a walk-out today, the 20th anniversary of the COVID-19 pandemic, to protest what some have deemed invasive monitoring. Many fears subsided when the first SARS-CoV-2 vaccine was broadly distributed in 2023, but subsequent zoonotic viruses emerged faster than society could prepare for them. With the world economy precariously weak, a cautious arrangement was reached: Workers

could return to their jobs if they submitted to routine infection checks. At first, these were relatively innocuous temperature probes and cough tracking. However, with the 2029 advent of low-cost RNA wastewater screening by smart toilets and ubiquitous wall-mounted infrared heat sensors, infected employees could be pinpointed before displaying acute symptoms. Later, an eCommerce/fitness-tracking consortium released artificial intelligence algorithms that combined smartwatch health metrics and recent online search history. Corporate Wellness Boards used the results to justify mandatory quarantines. Employees cried foul. The debate rages on in our courts and on the Giganet about whether the public good is served by exposing the "viral status" of the few.

#### Michael A. Tarselli

Society for Laboratory Automation and Screening, Oak Brook, IL 60523, USA. Email: mtarselli@slas.org

## Science and Health

Earlier this month, 21 individuals were quarantined in Kampala, Uganda, after a man was diagnosed with Marburg

hemorrhagic fever by the local laboratory of the International Center for Disease Prevention (ICDP). The patient, who has now fully recovered, may have been infected at the veterinary clinic where he worked in close contact with possible animal carriers. "This is a virus that spreads easily through bodily fluids and historically has been transmitted to caregivers," said Dr. Icuaf, director of the ICDP. Once again, the localized presence of centers with efficient testing capabilities made it possible to identify patient zero and contain the outbreak at its inception. As a result, "no deaths occurred, and everyone who might have been exposed has been quarantined while we monitor their health," added Dr. Icuaf. The ICDP was instituted in 2021 as a global response to the COVID-19 pandemic, which marked a revolution in public awareness of science-based policy. The cost of crisis prevention is now routinely compared with the predicted price of managing such a crisis after it has occurred.

#### Ahmed Al Harraq

Cain Department of Chemical Engineering, Louisiana State University, Baton Rouge, LA 70803, USA. Email: aahme22@lsu.edu



One of the world's leading universities is launching a large-scale screen of potential antiviral and antibacterial drugs on human volunteers. The substances show promising results in vitro but have not been tested on animals. To compensate for the risk of side effects, all volunteers will receive generous payment. "Drugs showing promising effects on mice could be ineffective on humans, making drug development expensive and slow," explained the leading scientist of the drug screen. Human rights experts warned against granting permission to conduct the study. "Offering payment for causing physical harm targets the economically vulnerable and violates basic human rights," they argued. However, doctors and politicians praise the idea, referring to the COVID-19 epidemic. "Developing a new drug through the traditional process can take years. Testing multiple potential candidates on coronavirus-infected people saved thousands of lives before basic research had a chance to catch up. Next time, we want to be prepared," explained the health minister.

#### Anna Uzonyi

Department of Molecular Genetics, Weizmann Institute of Science, Rehovot, 7610001, Israel. Email: anna.uzonyi@weizmann.ac.il

Results published today from a 20-year experiment show that a "lottery" grant funding scheme is superior to traditional peer-review assessment panels. For decades, researchers have debated the effectiveness and cost-efficiency of selecting grant recipients through a peer-review process, given the documented biases that hinder diversity and equitable decision-making. "It was a controversial move at the time, but the results are clear," said the lead author of the study. The funding experiment, which began in 2020 in response to the COVID-19 pandemic, was introduced to preserve the workforce employed on short-term contracts. During that year, pandemic-related budget cuts and social restrictions impeded the traditional peer-review process. "The lottery not only reduced peer-review bias but also added millions of dollars per year to the sector in hours saved by academics no longer devoting time to peer review," said the lead author. "That time was spent on doing more experiments, mentoring colleagues, or achieving a healthier work-life balance."

#### Ken Dutton-Regester

Department of Genetics and Computational Biology, QIMR Berghofer Medical Research Institute, Brisbane, QLD 4006, Australia. Twitter: @stemventurist

## Education

As the debate continues on the efficacy of educational methods, most universities now use a combination of in-person, remote, and technology-enhanced classrooms. The rapid expansion of evidence-based strategies such as machine learning and artificial intelligence, audio and video tools, three-dimensional environments, and simulations across disciplines began during the COVID-19 pandemic. The decision to move education to a computer-based environment to protect the health and safety of students and staff transformed the educational conversation. In the increasingly technology-enhanced world, discussions about how to teach a science class online, how to facilitate lab experiences, and how to conduct experiments with new constraints swept the research community. A nuanced understanding emerged about true online pedagogy versus synchronous, remote meetings. Two decades later, we see the results of this transformation.

#### Rachel Yoho

Department of Environmental and Global Health, University of Florida, Gainesville, FL 32603, USA. Twitter: @rachel\_yoho

## Sports

A stunning 200,000 people attended the grand opening ceremony of the 2040 Olympics yesterday in New Delhi, India. It has been 20 years since such a public event could take place safely. Only with the recent release of clothing and shoes made of technologically advanced materials that instantly kill viruses could the social distancing that began with the COVID-19 pandemic be relaxed. For added peace of mind, all attendees at the ceremony consented to the skin implantation of Viroclean, a new chip-based device that sounds an alarm when it detects viruses in the air.

#### Sudhakar Srivastava

Institute of Environment and Sustainable Development, Banaras Hindu University, Varanasi, Uttar Pradesh, 221005, India. Email: sudhakar.srivastava@gmail.com

## Arts and Leisure

This weekend, at the Coachella 2040 music festival, three aerosol biosurveillance sensors detected a SARS-like virus in the air. Smartphone tracing, using the opt-in U.S. Centers for Disease Control and Prevention (CDC) geospatial health app developed in the wake of the COVID-19 pandemic, identified two potential index cases. The CDC outbreak prevention team mobilized regional contact tracers to intercept and

test both individuals within an hour of first detection. One individual tested positive for a variant of the 2019 SARS-CoV-2 strain, previously thought to be eradicated, and is undergoing treatment in quarantine.

#### Michael Strong

Center for Genes, Environment, and Health, National Jewish Health and University of Colorado, Anschutz Medical Campus, Denver, CO 80206, USA. Email: strongm@njhealth.org

## Lifestyle

Last week's 15th annual Pan-global Remote Integrated Sciences Meeting (PRISM) attracted more than 100,000 attendees from more than 160 countries. Scientists, educators, students, entrepreneurs, policy-makers, and industry experts from fields spanning the physical, biological, and social sciences logged on to the online venue, enabled by virtual reality. Advanced machine learning algorithms provided recommendations for presentations relevant to each participant based on both their expertise and potential for interdisciplinary collaboration. As usual, the highlight of the meeting was the virtual poster sessions, driven by interactivity and streamlined to optimize small-group scientific conversation across fields. Many junior scientist attendees were surprised to learn that such events were nearly unheard of before PRISM grew from the increasing move toward virtual conferences during the coronavirus pandemic over 20 years ago. "My adviser told me that when she was a grad student, big conferences were all held in person," writes one anonymous Ph.D. student. "Can you imagine having a giant conference like this in some random convention center, with tens of thousands of scientists spending hundreds of dollars on fuel-inefficient flights and hotel booking, lugging around printed posters and just milling around for a week trying to find the optimal talks to attend? Insane."

#### Yifan Li

Department of Chemistry, University of California, Berkeley, Berkeley, CA 94720, USA. Twitter: @iWonderWhyly

## Food

Today, cell-based meat consumption has surpassed farm-produced meat for the first time. The transition began with the meat shortages and near collapse of the meat supply chain during the COVID-19 outbreak. With thousands of workers packed into poorly ventilated and unhygienic facilities, meat processing plants were hotspots for the SARS-CoV-2 virus. A global meat shortage emerged as production rates were slashed. Most people turned to the plant-based meat alternatives available at the time. The

meat industry's demise was sealed when cell-based meat entered the mainstream market the following year. Clean meat eliminated the negative effects of the meat industry, from pollution caused by runoff and antibiotics, to worker and animal cruelty, to the carbon footprint of livestock, which contributed 18% of greenhouse gas emissions at the time. Cell-based meat has been growing in popularity ever since, as traditional meat became ethically and environmentally unpalatable.

#### JiaJia Fu

Whittle School and Studios, Washington, DC 20008, USA. Email: jjnaturalist@gmail.com

Global seafood supply now relies entirely on aquaculture. The turning point came when researchers optimized the breeding techniques for edible crabs, enabling high-valued crab species such as mud crabs and blue crabs to be mass-produced in full aquaculture settings. The prioritization of aquaculture was made possible by the COVID-19 pandemic in 2020. A 12-month closure of fisheries during the wave of global stay-at-home orders led to the rejuvenation of overexploited species such as sardines and mackerels, which had been on the verge of extinction, and made people recognize the fragility of the supply chain. Full investment in aquaculture research began the following year.

#### Khor Waiho

Institute of Tropical Aquaculture and Fisheries, Universiti Malaysia Terengganu, Kuala Nerus, Terengganu, 21030, Malaysia. Email: waiho@umt.edu.my

## Environment

Next week, the United Nations will meet to assess whether the goals of the 2040 Agenda for Sustainable Development have been achieved. Unfortunately, reasons for optimism are scarce. Overexploitation of natural resources, CO<sub>2</sub> emissions, and plastic waste continue to soar. The wealthiest sector of the population consumes 80% of the resources, and the poorest people increasingly suffer from extreme weather events, famines, and freshwater scarcity. We were already heading in this direction early in the century, when the short-term vision of corporations and policy-makers prioritized economic benefits over human and environmental health. The COVID-19 pandemic exacerbated the negative trends. Since 2020, an array of wasteful practices increased, including the proliferation of single-use products and travel in private vehicles to avoid physical contact. After reviewing the past decade, the UN countries will discuss commitments to decrease inequality and pollution by 2050.

#### Isabel Marín Beltrán

Laboratory of Environmental Technologies, Centro de Ciências do Mar do Algarve, Universidade do Algarve, Campus de Gambelas, Faro, 8005-139, Portugal. Email: imbeltran@ualg.pt

For the first time, global average air temperature is more than 2°C higher than the 20th-century global average. Scientists suggest that decisions made in response to the COVID-19 pandemic led to today's disastrous climate consequences. After the

Paris Climate Agreement in 2016, scientists were hopeful. National governments were implementing increasingly ambitious measures to meet their commitments. But the economic fallout of the pandemic led growing economies such as India to relax environmental clearance guidelines for industries and infrastructure projects and cut funding allocated to environmental reforms. First-world countries such as the United States and China, instead of shifting toward renewable energy, boosted investment in fossil fuels, which in turn increased greenhouse gas emissions. Even after multiple warnings from the Intergovernmental Panel on Climate Change, G20 nations neglected to follow the advice of scientists.

#### Akash Mukherjee

Department of Physics, Indian Institute of Science Education and Research, Pune, Pune, Maharashtra, 411008, India. Twitter: @aghor\_AM

## Travel

A government report released yesterday warns of a potential spike in counterfeit immunity passports entering the market this coronavirus season. According to Jane London, the U.K. health minister, "There is a substantial increase in the number of illegal immunigrants crossing provincial and municipal borders. The public should be aware that just scanning someone's immunity passport is not enough anymore." This report comes just 6 months after the U.S. Centers for Disease Control and Prevention first released notice that the "NextGen Immunity Passport" brand had been hacked, allowing scammers and tech-savvy citizens to falsify the immunity data they carry with them by law. Asked how businesses and town-guards were detecting falsified immunity passports at checkpoints, minister of national movement John Petersfield told journalists, "This is a police matter. Any further information about detection at this time will only help counterfeiters." Widespread counterfeiting, as well as last year's false-negative scandal, has generated substantial public distrust in the use of the immunity passport system in movement legislation, now 19 years old. "We learned our lesson about free movement back in 2020," said one government official who wished to remain anonymous, "but the immunity passport system is cracking, and we don't see a fix yet."

#### Tyler D. P. Brunet

Department of History and Philosophy of Science, University of Cambridge, Cambridge, Cambridgeshire, CB2 3RH, UK. Email: tdpb2@cam.ac.uk



ILLUSTRATION: ZOE VAN DIJK



## PERSPECTIVES

## MICROBIOLOGY

# Tracing cell trajectories in a biofilm

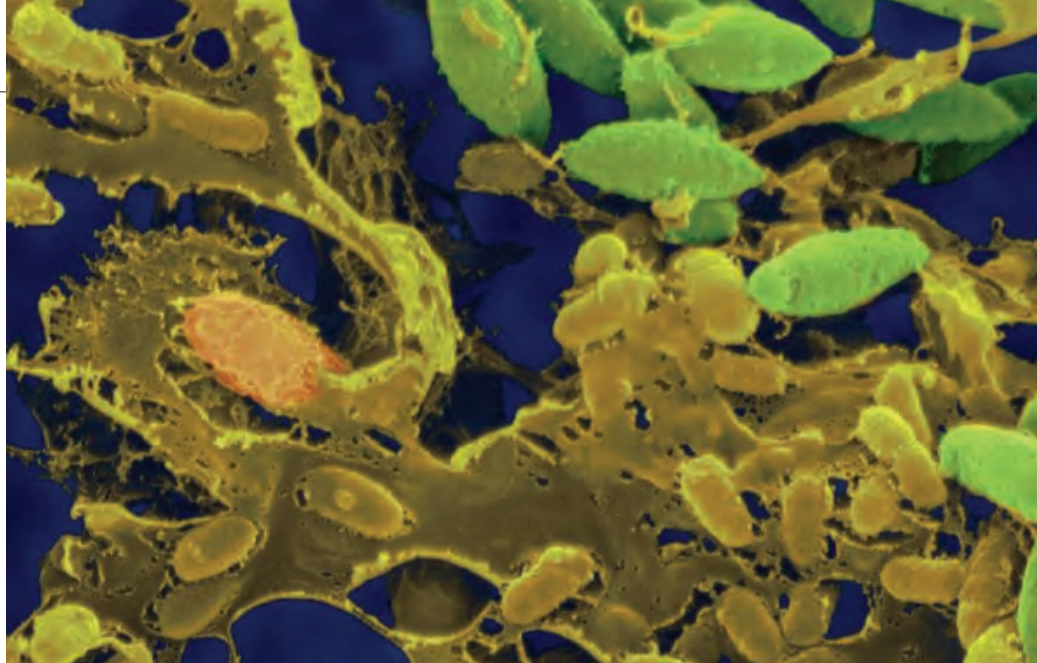
Single bacterial cells are programmed to form multicellular structures

By **Alma Dal Co** and **Michael P. Brenner**

**B**orn in 1881 on a farm in Pennsylvania, Alice C. Evans dedicated her life to studying bacteria in dairy products. Early in her career, Alice became convinced that most bacteria display multicellular behavior as part of their life cycles. At the time, the morphological changes observed in bacterial life cycles created confusion among scientists. In 1928, as the first female president of the American Society for Microbiology, Alice wrote to the scientific community: “When one-celled organisms grow in masses,...individual cells influence and protect one another.” She continued, “Bacteriologists need not feel chagrined...to admit that...forms they have considered as different genera are but stages in the life cycle of one species” (1). Nearly 100 years later, on page 71 of this issue, Qin *et al.* (2) make a substantial leap forward in deciphering cell dynamics in biofilms—groups of microorganisms that adhere to a surface, and each other, by excreting matrix components.

In the interim period, microbiologists have learned that many bacteria organize in groups. This allows bacterial cells to achieve collectively what individuals in isolation cannot, thus conferring a selective advantage on the individuals. Multicellular behaviors help cells to migrate (3), resist antibiotic treatments (4), and protect themselves from predators (5). In recent years, microbiologists have begun to unravel the mechanisms behind these multicellular behaviors, by studying single-cell gene expression, growth rate regulation, and cell-to-cell interactions (6–9), as well as by developing tools to investigate the morphology and growth of entire bacterial biofilms (10, 11).

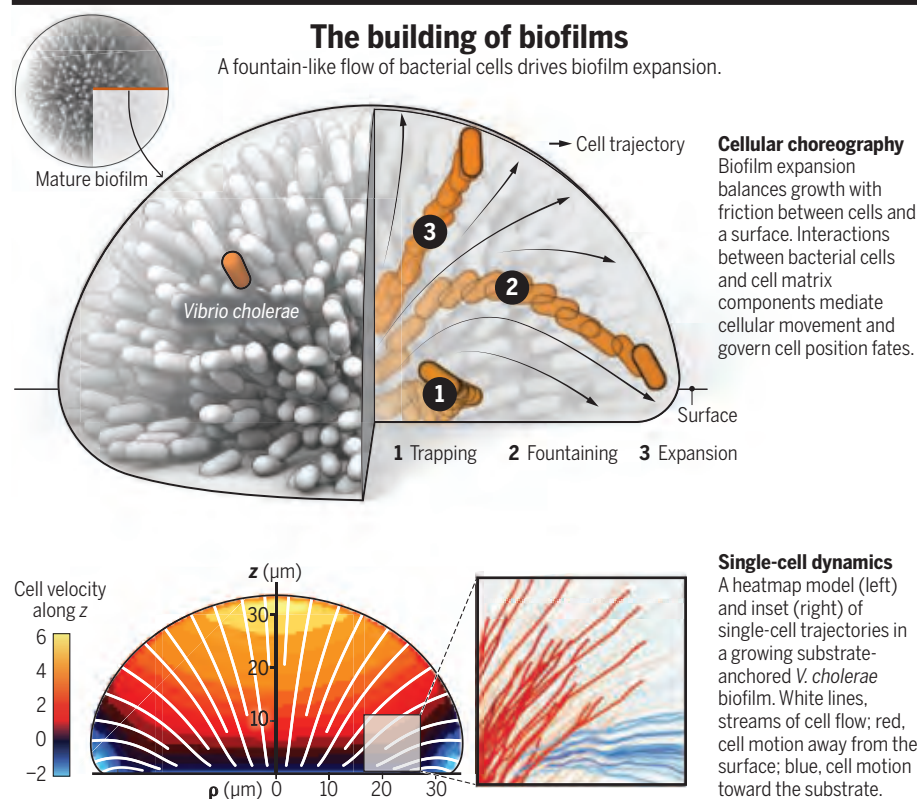
School of Engineering and Applied Sciences, Harvard University, Cambridge, MA 02139, USA. Email: adalco@seas.harvard.edu; brenner@seas.harvard.edu



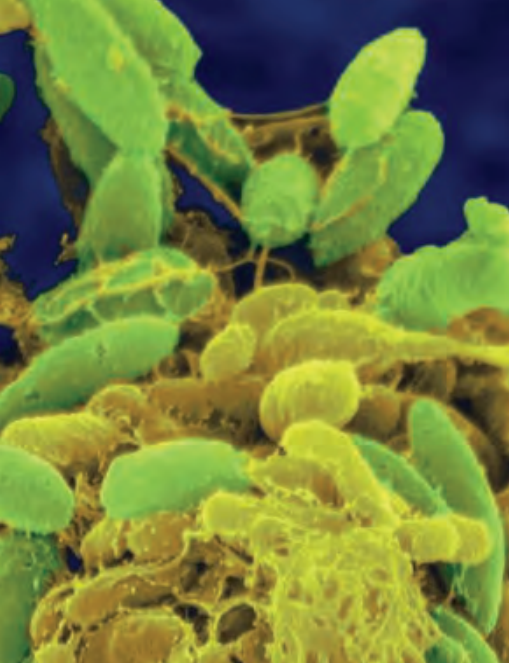
A multicellular aggregate starts with a single founder cell that grows into a mature biofilm. Despite substantial progress, scientists still lack a detailed understanding of how bacterial cells are programmed to build multicellular structures. Each cell makes individual decisions—whether to divide, move, excrete chemicals, exert forces, or express extracellular matrix components—in response to its local environment. In turn, the local environment is determined by the collective decisions of all of its cells, played out as a mosaic over time in a three-dimensional (3D)

space. A primary challenge to unraveling the mystery of how cells are programmed to produce a mature functional biofilm is that researchers lack the experimental tools needed to study how the dynamics of individual cells drive biofilm formation and structure.

In their elegant study, Qin *et al.* developed dual-view light-sheet microscopy to reconstruct single-cell trajectories in 3D *Vibrio cholerae* biofilms initiated by a single founder cell. This method fluorescently labeled cellular puncta, giving isotropic single-cell resolution in the biofilm with much less



CREDITS: (PHOTO) DENNIS KUNKEL MICROSCOPY/SCIENCE SOURCE; (GRAPHIC) V. ALTOUNIAN/SCIENCE



A scanning electron micrograph reveals a multiorganism biofilm formed on an implantable medical device. Life-threatening biofilm-associated infections resist antibiotic treatment and interfere with medical device function.

can arise from processes operating at the single-cell level. The mechanisms uncovered with a gram-negative bacterial species likely will be generalizable across other bacterial types. For example, the qualitative transitions in biofilm expansion observed in this study have analogs in other bacterial biofilms. With the gram-positive bacterium *Bacillus subtilis*, a qualitative change in colony expansion is triggered by a cellular bistable switch in which cells expressing flagella produce extracellular matrices (12, 13). Osmolarity associated with matrix production drives colony expansion (14).

More broadly, this study demonstrates the great potential for advances in imaging technology and computer vision to help unravel how collective behavior arises from the activity of individual cells and their interactions. However, there is much more going on inside a biofilm that cannot yet be seen. More complete information would allow researchers to not only reconstruct the motion of cells but also uncover their phenotypic states. Previous work on *B. subtilis* with fluorescent labeling of genetic components shows detailed spatial arrangement of various cell types, with cells carrying out different biological functions in distinct parts of the biofilm (3, 15).

One can only hypothesize about the diversity of cellular types and functions inside the beautiful fountain revealed in the present study. A deeper understanding of bacterial multicellular behavior will increase our ability to treat bacterial infections, control natural bacterial communities, and engineer synthetic ones for specific purposes. ■

#### REFERENCES AND NOTES

1. A.C. Evans, *J. Bacteriol.* **17**, 63 (1929).
2. B. Qin *et al.*, *Science* **369**, 71 (2020).
3. J. van Gestel *et al.*, *PLOS Biol.* **13**, e1002141 (2015).
4. C.W. Hall, T.-F. Mah, *FEMS Microbiol. Rev.* **41**, 276 (2017).
5. P.K. Raghupathi *et al.*, *Front. Microbiol.* **8**, 2649 (2018).
6. A. Dal Co, S. van Vliet, M. Ackermann, *Philos. Trans. R. Soc. London Ser. B* **374**, 20190080 (2019).
7. A. Dal Co *et al.*, *Nat. Ecol. Evol.* **4**, 366 (2020).
8. S. van Vliet *et al.*, *Cell Syst.* **6**, 496 (2018).
9. A. Dragoš *et al.*, *Curr. Biol.* **28**, 1903 (2018).
10. K. Drescher *et al.*, *Proc. Natl. Acad. Sci. U.S.A.* **113**, E2066 (2016).
11. R. Hartmann *et al.*, *Nat. Phys.* **15**, 251 (2019).
12. H. Vlamakis *et al.*, *Chemtracts* **20**, 427 (2007).
13. D.B. Kearns *et al.*, *Mol. Microbiol.* **55**, 739 (2005).
14. A. Seminar *et al.*, *Proc. Natl. Acad. Sci. U.S.A.* **109**, 1116 (2012).
15. H. Vlamakis *et al.*, *Nat. Rev. Microbiol.* **11**, 157 (2013).

#### ACKNOWLEDGMENTS

A.D.C. and M.P.B. are supported by the National Science Foundation (DMS-1715477), Materials Research Science and Engineering Center (DMR-1420570), the Office of Naval Research (N00014-17-1-3029), and the Simons Foundation.

photobleaching than that seen with previous methods. This advance allowed the authors to carry out simultaneous imaging of 10,000 *V. cholerae* cells for the 16 hours it takes for the biofilm to develop, with 3-min intervals between subsequent images. This frequent imaging made it possible to track the trajectories of micrometer-sized cells, giving an unprecedented view into the behaviors of individual cells as the biofilm developed (see the figure).

The measurements revealed a qualitative transition in an individual cell's behavior, in which Brownian motion changes to ballistic motion as the biofilm develops. This transition corresponds to a new phase of collective growth, when the biofilm as a whole begins its vertical expansion away from the substrate. In this phase, cells displayed two types of trajectories. Some of the cells expanded ballistically outward, whereas others became trapped at the substrate. Overall, these trajectories gave rise to a collective fountain-like flow, which transported some cells to the biofilm front, while bypassing the cells trapped at the substrate. This fountain-like flow allowed for fast lateral expansion of the biofilm.

Cell tracking allowed Qin *et al.* to precisely quantify the dynamics of various cells, while also assessing how these dynamics differ for mutant cells that overproduce matrix components. To interpret the results, the authors built a mathematical model for the mechanics of biofilm expansion, balancing growth with substrate friction. By modeling different surface frictions and comparing the predicted cell motion with the observed cell motion, Qin *et al.* were able to explain the observed behavior as long as friction between the cells and surface was a dominant effect.

This study of *V. cholerae* offers an exciting insight into how collective behavior

#### MOLECULAR BIOLOGY

## Shutting down RNA-targeting CRISPR

The discovery of an anti-CRISPR reveals viral escape from CRISPR immunity

By Rodolphe Barrangou<sup>1</sup> and Erik J. Sontheimer<sup>2</sup>

Explorations of the evolutionary arms race between bacteria and bacteriophages (viruses that infect bacteria) have unearthed a variety of defense mechanisms that include CRISPR-Cas (CRISPR-associated nuclease) adaptive immune systems (1). Understanding the mechanisms of CRISPR-mediated immunity, involving DNA-encoded, RNA-guided, sequence-specific targeting of invasive nucleic acids (2, 3), has spawned powerful genome engineering platforms based on diverse Cas effectors. Subsequent studies have also revealed anti-CRISPR proteins (4) that have proven valuable as control switches for Cas molecular machines. CRISPR-Cas immune systems encompass diverse families including DNA-targeting effectors such as Cascade-Cas3, Cas9, and Cas12 as well as the recently characterized RNA-targeting Cas13 ribonuclease (RNase) (5). The evolving immune arsenal in bacteria has been matched by diverse anti-CRISPRs that enable viruses to escape Cas nuclease targeting. On page 54 of this issue, Meeske *et al.* (6) report an anti-CRISPR mechanism that inhibits Cas13a RNase activity, with potential utility as a CRISPR effector control switch.

The Cas13 RNase is the signature protein for type VI CRISPR-Cas systems (5), which use their CRISPR RNA (crRNA) guides to target viral RNA sequences and trigger both the specific degradation of target phage RNA and the nonspecific destruction of host transcripts (7), leading to host dormancy and prevention of virus proliferation (8). Meeske *et al.* identified and

<sup>1</sup>Department of Food, Bioprocessing and Nutrition Sciences, North Carolina State University, Raleigh, NC, USA. <sup>2</sup>RNA Therapeutics Institute, University of Massachusetts Medical School, Worcester, MA, USA. Email: rbarran@ncsu.edu; erik.sontheimer@umassmed.edu



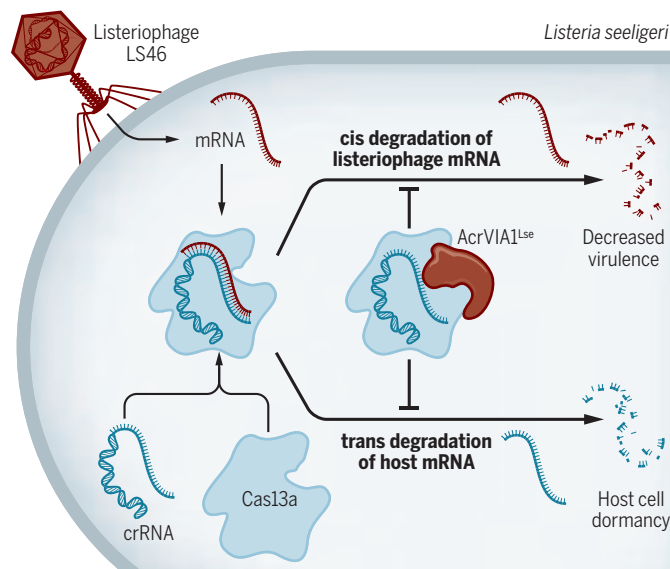
characterized a type VI anti-CRISPR protein, AcrVIA1<sup>Lse</sup>, encoded by the genome of the  $\phi$ LS46 listeriphage (see the figure). This anti-CRISPR binds to *Listeria seeligeri* Cas13a (LsCas13a) and prevents target RNA access and conformational activation of the RNase. AcrVIA1<sup>Lse</sup> comprises 232 amino acids, which is notably larger than the typically hypervariable, <150-amino acid anti-CRISPRs previously characterized. The additional residues augment the RNase domain with a DNA-binding motif that contributes to anti-CRISPR transcriptional regulation. This AcrVIA1<sup>Lse</sup> protein was able to completely thwart CRISPR-Cas13 immunity against otherwise susceptible listeriphage.

Meeske *et al.* investigated the interplay between AcrVIA1<sup>Lse</sup> and the Cas13a:crRNA complex and showed dose-dependent inhibition of RNase activity through formation of an AcrVIA1<sup>Lse</sup>:Cas13a:crRNA complex that prevents target RNA binding. Critically, both cis phage-targeting and trans host dormancy-inducing activities are abolished by AcrVIA1<sup>Lse</sup>, enhancing not only the capacity of the listeriphage to replicate but also the ability of the host *L. seeligeri* to continue metabolically. This interaction was dissected structurally, and the authors used cryo-electron microscopy to establish that LsCas13a adopts a bilobed architecture encompassing a recognition domain and an RNase domain, directed by a 51-nucleotide crRNA with the target-complementary portion configured to pair with viral RNA. AcrVIA1<sup>Lse</sup> interacts with both LsCas13a and the crRNA to prevent target RNA binding and RNase activation. Future studies will undoubtedly define AcrVIA1<sup>Lse</sup> inhibitory specificity across Cas13 homologs, as well as the impact of type VI anti-CRISPR viral resistance on bacterial biology and host-virus dynamics.

Several studies have deciphered how anti-CRISPRs can inhibit Cas effectors by blocking target nucleic acid loading and preventing Cas nuclease activity (4), but the primary focus had been on DNA-targeting Cascade-Cas3, Cas9, and Cas12. These studies revealed that physiological anti-CRISPR activity often only partially inhibits CRISPR-Cas, providing limited immune escape (9, 10). This appears to reflect a race between anti-CRISPR expression in

## Inhibiting CRISPR-associated ribonuclease activity

Listeriphage LS46 encodes the anti-CRISPR protein AcrVIA1<sup>Lse</sup>. The host, *Listeria seeligeri*, encodes a type VI CRISPR-Cas13a (CRISPR-associated 13a) immune system. Cas13a is a ribonuclease that, through complementarity between CRISPR RNA (crRNA) and target sequences in listeriphage messenger RNA (mRNA), cleaves and thus inactivates phage mRNA in cis and host mRNA in trans. AcrVIA1<sup>Lse</sup> can bind and inhibit the Cas13a:crRNA complex.



phages and host immune defense by the CRISPR effector complexes. Viral infections can fail because anti-CRISPR expression does not reach inhibitory thresholds in time to overcome CRISPR immunity, but repeated failed infections can yield gradually increasing anti-CRISPR amounts that immunosuppress the host and allow later infections to succeed. In the case of type VI CRISPR immunity, however, the DNA ge-

**“...opening new avenues for the use of CRISPR to control and shape the transcriptomes of organisms and viruses.”**

nome of the invasive phage is not specifically cleaved; instead, viral and host transcripts are the targets for Cas13-mediated degradation, and virus propagation is suppressed primarily by the induction of bacterial host cell dormancy (8). This fundamental distinction reduces the time pressure on anti-CRISPR-mediated inhibition of Cas13 because the phage genome is not specifically cleared and dormancy can often be reversed.

A single dose of AcrVIA1<sup>Lse</sup> could completely abrogate LsCas13 activity, even in unfavorable conditions such as very low viral multiplicity of infection, targeting

by multiple crRNAs, or immunity activation by early phage transcripts. Thus, mechanistically establishing how these different types of CRISPR systems function is a critical step toward understanding and repurposing these molecular machines and ultimately manipulating, engineering, and controlling Cas13-based tools.

Besides the continued rise of DNA-targeting CRISPR effectors such as Cas9 and Cas12 for genome editing, several recent studies have illustrated how valuable RNA-targeting Cas13 effectors can be, including for detection of RNA viruses such as severe acute respiratory syndrome coronavirus 2 (SARS-CoV-2), which causes coronavirus disease 2019 (COVID-19) (11). There is also much potential for Cas13 as an RNA-targeting and RNA-editing platform (for example, to correct disease-causing mutations in cellular RNAs) (12, 13), but this depends on

whether its activity can be controlled. The study of Meeske *et al.* provides a means to reduce or eliminate Cas13 activity, opening new avenues for the use of CRISPR to control and shape the transcriptomes of organisms and viruses. Indeed, type VI anti-CRISPRs can readily control Cas13a RNA targeting and dCas13a RNA editing in human cells (14). However, more studies are needed to harness this tool and establish how broadly exploitable such Cas13-based technologies (and their off switches) could be. ■

## REFERENCES AND NOTES

1. R. Barrangou *et al.*, *Science* **315**, 1709 (2007).
2. S. J. Brouns *et al.*, *Science* **321**, 960 (2008).
3. L. A. Marraffini, E. J. Sontheimer, *Science* **322**, 1843 (2008).
4. A. R. Davidson *et al.*, *Annu. Rev. Biochem.* **10**, 1146/annurev-biochem-011420-111224 (2020).
5. K. S. Makarova *et al.*, *Nat. Rev. Microbiol.* **18**, 67 (2020).
6. A. J. Meeske *et al.*, *Science* **369**, 54 (2020).
7. O. O. Abudayyeh *et al.*, *Science* **353**, aaf5573 (2016).
8. A. J. Meeske *et al.*, *Nature* **570**, 241 (2019).
9. A. L. Borges *et al.*, *Cell* **174**, 917 (2018).
10. M. Landsberger *et al.*, *Cell* **174**, 908 (2018).
11. C. M. Ackerman *et al.*, *Nature* **582**, 277 (2020).
12. O. O. Abudayyeh *et al.*, *Nature* **550**, 280 (2017).
13. D. B. T. Cox *et al.*, *Science* **358**, 1019 (2017).
14. P. Lin *et al.*, *Mol. Cell* **78**, 850 (2020).

## ACKNOWLEDGMENTS

R.B. and E.J.S. are co-founders and advisers of Intellia Therapeutics, a company involved in the development of CRISPR-based therapies.

10.1126/science.abc8243

# The secret life of histones

## Histone H3 leads a double life as a copper reductase

By Johannes Rudolph and Karolin Luger

**H**istone proteins are the ubiquitous organizers of all eukaryotic genomes (1). Two each of the histones H2A, H2B, H3, and H4 form a disk-shaped assembly around which 147 base pairs (bp) of DNA are tightly coiled. Hundreds of thousands of these connected nucleosomes wrap up further to form chromosomes. The substantial sequence conservation between eukaryotic histones and the presence of simple histones in archaea (the presumed ancestors of all eukaryotes) suggest an ancient evolutionary origin of this type of genome organization (2). Certainly, there was no reason to believe that histones had any other function, let alone enzymatic activity. On page 59 of this issue, Attar *et al.* (3) describe the unexpected discovery that histone H3 has copper reductase activity in yeast (and likely in all) cells, suggesting that histones may have evolved to adapt to oxygenated life rather than for DNA compaction.

Copper is an essential element for all living organisms because it is a cofactor for many enzymatic reactions. Copper is a required component of the energy-generating enzyme cytochrome c oxidase and the detoxifying enzyme superoxide dismutase (which renders superoxide radicals that causes many types of cell damage harmless), thus allowing for safe respiration in oxygen-utilizing organisms. As an enzymatic cofactor, copper cycles through its two readily accessible oxidation states, Cu<sup>+</sup> (cuprous) and Cu<sup>2+</sup> (cupric). However, copper mostly occurs in nature as Cu<sup>2+</sup>, which is toxic because it can readily oxidize essential thiols or ascorbic acid (vitamin C) and thus obliterate their functions. Thus, the adaptation of life from an anaerobic to an oxygenated environment (which happened in the same time frame as eukaryogenesis) required a mechanism for maintaining Cu<sup>+</sup> inside cells.

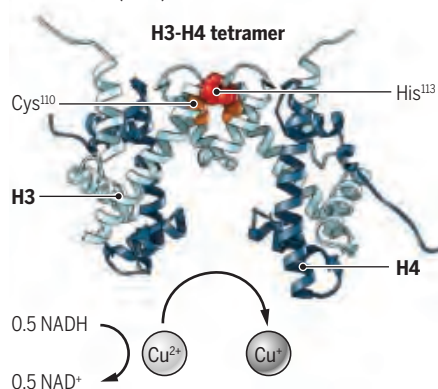
Typical Cu binding sites in proteins bind one to four ions in oxidation states ranging from Cu<sup>+</sup> to Cu<sup>3+</sup>, coordinated most often by histidine and cysteine residues as well as water (4). Thus, the conserved occurrence of two Cys-His pairs in the histone H3-H3 four-helix bundle structure that occurs in all eukaryotic organisms except for baker's yeast,

*Saccharomyces cerevisiae*, piqued the interest of Attar *et al.*, especially given the previous proposal that these Cys-His pairs could bind metal ions (5). The Cys-His pairs are part of the dimerization interface that holds together the H3-H4 tetramer (comprising two H3 and H4 dimers), which organizes the central ~80 bp of nucleosomal DNA.

Attar *et al.* demonstrate in vitro that purified frog (*Xenopus laevis*) histone H3-H4 tetramer presents a likely Cu<sup>2+</sup> binding site using the specific configuration of Cys<sup>110</sup> and His<sup>113</sup> at the H3-H3 interface (see the figure). These results are consistent with previous observations that histones can bind divalent

### Copper reductase

Two histone H3 and two histone H4 molecules form a tetramer before being assembled into a nucleosome. Cys<sup>110</sup> and His<sup>113</sup> at the histone H3-H3 interface bind Cu<sup>2+</sup>, which is reduced to Cu<sup>+</sup>, involving the reductant cofactor nicotinamide adenine dinucleotide (NAD).



metal ions, proposed to store Zn<sup>2+</sup> (zinc), detoxify Hg<sup>2+</sup> (mercury), or regulate nucleosome architecture (6, 7). Additionally, this site binds heavy atoms that were used for the original phasing of the crystal structure (8). Multiple reductant molecules can be used by purified H3-H4 tetramers to convert Cu<sup>2+</sup> to Cu<sup>+</sup>, including obligate two-electron donors. This observation raises interesting mechanistic questions worthy of further investigation, because one-electron reductions of Cu<sup>2+</sup> to Cu<sup>+</sup> are typically mediated by cofactors that can perform both one- and two-electron chemistry, such as flavins or quinones.

To test the relevance of this activity in cells, Attar *et al.* turned to the yeast *S. cerevisiae*. Although only His<sup>113</sup> (and not Cys<sup>110</sup>)

is conserved in *S. cerevisiae* (this seems to be a peculiarity of yeast), the H3-H4 tetramer also bound copper, albeit more weakly than in the purified tetramer from *X. laevis*. This offered the possibility not only to destroy the presumed activity by mutating His<sup>113</sup> but also to “improve” it by reintroducing the missing Cys<sup>110</sup>, and to monitor the effects. Mutation of His<sup>113</sup> of histone H3 in *S. cerevisiae* leads to slower growth and lower concentrations of intracellular Cu<sup>+</sup>, without affecting overall copper concentrations. Mutation of His<sup>113</sup> affected the two most prominent roles for copper: Usage of oxygen for energy metabolism (respiration) and protection from oxygen-mediated damage by superoxide dismutase. Introduction of the missing Cys<sup>110</sup> in the *S. cerevisiae* histone H3 increased intracellular amounts of Cu<sup>+</sup> and resilience to limiting copper concentrations.

Histones are rarely found in free form in the cell and, when not bound to DNA, are chaperoned by “storage proteins” (9). It is unknown if the copper reductase activity can be replicated in these contexts. The results obtained with live yeast cells suggest that this is the case, but technical limitations prevented the detection of copper reductase activity in the presence of DNA. Because copper reductase activity can only occur in the active site formed by the H3-H3 four helix bundle, a histone “chaperone” protein would have to bind an H3-H4 tetramer while still allowing enzymatic activity. Nevertheless, the findings of Attar *et al.* are potentially paradigm-shifting. Their discovery is of particular interest with respect to the evolution of histones and their adoption as packaging material for DNA. Histone-like proteins, often without the regulatory tails of eukaryotic histones, are found in many archaeal prokaryotes that typically have small genomes that do not require DNA compaction (10, 11). Perhaps the original role of histone proteins was to protect against oxygen toxicity, in response to the increase in oxygen concentrations that allowed for the evolution of eukaryotes and multicellular organisms. Further in vitro and in vivo characterization of the role of histones as copper reductases from archaeal organisms may provide valuable insight on this proposed role. ■

### REFERENCES AND NOTES

1. K. Luger *et al.*, *Nature* **389**, 251 (1997).
2. S. Henikoff, *Curr. Biol.* **27**, R1118 (2017).
3. N. Attar *et al.*, *Science* **369**, 59 (2020).
4. K. A. Koch *et al.*, *Chem. Biol.* **4**, 549 (1997).
5. R. A. Saavedra, *Science* **234**, 1589 (1986).
6. M. Adamczyk *et al.*, *FEBS Lett.* **581**, 1409 (2007).
7. W. Bal, J. Lukasz *et al.*, *Chem. Res. Toxicol.* **8**, 683 (1995).
8. T. J. Richmond *et al.*, *Nature* **311**, 532 (1984).
9. Z. A. Gurard-Levin *et al.*, *Annu. Rev. Biochem.* **83**, 487 (2014).
10. F. Mattioli *et al.*, *Science* **357**, 609 (2017).
11. P. B. Talbert *et al.*, *Nat. Rev. Genet.* **20**, 283 (2019).

Department of Biochemistry, University of Colorado at Boulder, Boulder, CO, USA. Email: johannes.rudolph@colorado.edu; karolin.luger@colorado.edu



## ORGANIC CHEMISTRY

## Stronger bonds bring bigger challenges

A polyoxometalate photocatalyst enables selective bond activation of light alkanes

By Gabriela Oksdath-Mansilla

For organic chemists, synthesizing complex molecules in a few steps without waste and with minimal energy has been a long-standing challenge. In many cases, synthetic methodology now enables the design of straightforward syntheses of molecules with different degrees of structural complexity and even their large-scale production. The starting materials are often derived ultimately from hydrocarbons in petroleum after extensive processing. Is it possible to start with hydrocarbons directly? On page 92 of this issue, Laudadio *et al.* (1) use gas-phase hydrocarbons to form more complex chemical entities by irradiating them with light. This approach was efficiently achieved not in static batch chemistry but under flow conditions through capillary tubing. This challenge was met by their design of a continuous-flow platform for the regioselective activation of gaseous hydrocarbons under mild conditions applied to carbon-carbon bond formation.

Although methane is readily available as the principal component of natural gas, its application in organic synthesis is limited by its chemical inertness. Numerous efforts have been made to activate methane and other light alkanes, for conversion into value-added products and to facilitate their storage and transportation (2). In this sense, and considering that the carbon-hydrogen (C-H) bond reactivity in alkanes is similar, the challenge is to perform such transformation under milder conditions and with high regioselective control.

Catalysis plays a key role in alkane functionalization, and reported methodologies include the use of radical intermediates, carbene or nitrene insertion, or metal-mediated C-H activation (3). The appropriate tuning of the structure and reactivity with a sterically bulky transition-metal-based homogeneous catalyst (4), or the presence of directing groups (5), has allowed access to C-H functionalization in a regio- and stereoselective way (6). Photocatalysis is an especially useful approach for C-H activa-

tion, as it can generate highly reactive species under controlled conditions to obtain products with excellent selectivity, as well as use light as a clean source of energy (7).

One of the main advances in this field is the photoinduced generation of radicals through a hydrogen-atom transfer (HAT) process (8). Recently, Hu *et al.* reported progress toward C-H activation of light alkanes. By photoexciting a coordination complex of cerium (IV) salts and alcohol, they performed an indirect HAT by generating an electrophilic alkoxy radical intermediate. With this synthetic strategy, they successfully performed amination, alkylation, and arylation of methane, along with other light hydrocarbons (9).

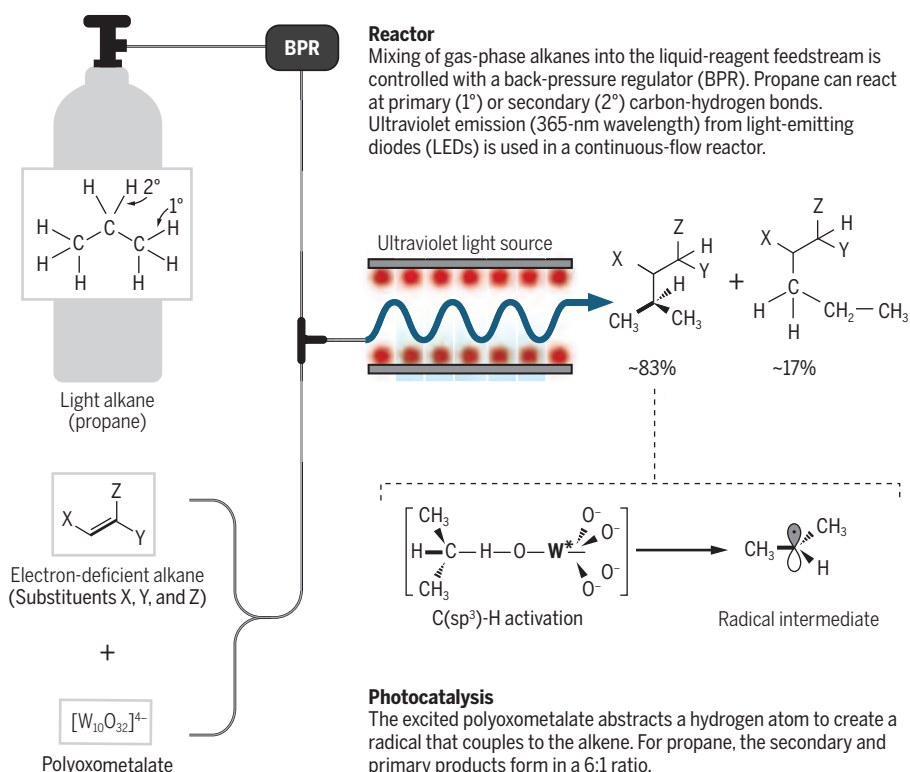
To avoid the addition of a co-catalyst, Laudadio *et al.* performed a direct HAT using suitable photocatalyst to improve C-H functionalization from methane, ethane, propane, and isobutene. Synthetic design

was critical, as different pieces of the reaction pathway were put in the correct order with the aim of forming radical intermediates that further add to a variety of electron-deficient alkene acceptors (see the figure for the case of propane). The success of their approach depended to a large extent on the use of the excited-state decatungstate anionic ( $[W_{10}O_{32}]^{4-}$ ) catalyst that directly activated the C-H bonds through single-step HAT. This polyoxometalate has highly electrophilic oxygen centers with a radical character that makes the homolytic cleavage of the C-H bond very efficient.

In addition, this photocatalyst is a bulky molecule, exhibiting steric effects that enable exceptional site selectivity to the HAT process (10). Laudadio *et al.* observed high selectivity in the C-H cleavage between secondary versus primary hydrogen (~6:1) of propane and between tertiary versus secondary hydrogen (~11.5:1) of isobutane.

## Directing direct alkane activation

Laudadio *et al.* show that normally unreactive light alkanes can be selectively activated for coupling reactions in a photocatalyzed direct hydrogen-atom transfer (HAT) process.



Thus, this method shows a substantial improvement in site selectivity over other state-of-the-art photocatalytic processes. The nucleophilic character of the formed alkyl radical also enabled its efficient addition to electron-deficient alkenes in good to excellent isolated yields.

Continuous-flow technology has been shown to provide better control over batch photochemical synthesis (11). In Laudadio *et al.*'s work, C–H functionalization of light alkanes has been particularly improved under continuous-flow conditions for many reasons. One is that it enables the handling of the gas-phase alkane reagents. Avoiding the excess of gas, it limits unwanted secondary reactions that lead to hydrogen abstraction and byproduct formation. In addition, high pressure can be used to achieve liquefaction of the gases under working conditions, which increases the efficiency of C–H activation. In this case, a back-pressure regulator was needed to perform the photochemical reaction. Further, light alkanes are combustible gases, and the use of flow technology allows work in operationally safe conditions and opens up the possibility of scaling up the process (12).

The direct C–H photoactivation achieved by Laudadio *et al.* provides a simple methodology for selective functionalization of hydrocarbons and suggests new opportunities, such as developing a suitable photocatalyst to carry out enantioselective C–H activation. In many cases, synthetic chemists have much of the reaction chemistry in hand, and will mainly have to fit the puzzle pieces together in way that enables efficient synthesis. ■

#### REFERENCES AND NOTES

1. G. Laudadio *et al.*, *Science* **368**, 92 (2020).
2. A. J. L. Pombeiro, Ed., *Alkane Functionalization* (Wiley, 2019).
3. X. Tang, X. Jia, Z. Huang, *Chem. Sci.* **9**, 288 (2018).
4. A. K. Cook, S. D. Schimler, A. J. Matzger, M. S. Sanford, *Science* **351**, 1421 (2016).
5. G. Xia *et al.*, *Nat. Chem.* **11**, 571 (2019).
6. T. G. Saint-Denis, R. Y. Zhu, G. Chen, Q. F. Wu, J.-Q. Yu, *Science* **359**, eaao4798 (2018).
7. D. Ravelli, S. Protti, M. Fagnoni, *Chem. Rev.* **116**, 9850 (2016).
8. L. Capaldo, D. Ravelli, *Eur. J. Org. Chem.* **2017**, 2056 (2017).
9. A. Hu, J. J. Guo, H. Pan, Z. Zuo, *Science* **361**, 668 (2018).
10. D. Ravelli, M. Fagnoni, T. Fukuyama, T. Nishikawa, I. Ryu, *ACS Catal.* **8**, 701 (2018).
11. F. Politano, G. Oksdath-Mansilla, *Org. Process Res. Dev.* **22**, 1045 (2018).
12. N. Kockmann, P. Thenée, C. Fleischer-Trebes, G. Laudadio, T. Noël, *React. Chem. Eng.* **2**, 258 (2017).

#### ACKNOWLEDGMENTS

I thank F. R. Bisogno and F. Politano for fruitful discussions. The National Research Council of Argentina (CONICET) INFIQC-CONICET, and Universidad Nacional de Córdoba (UNC) are kindly acknowledged for their support.

#### ECOLOGY

# When do fish succumb to heat?

## Greater sensitivity in fish reproductive stages reveals vulnerability to climate change

By Jennifer Sunday

**P**hysiological responses to temperature can provide a window into climate change vulnerability of species. How warm will it get relative to a species' ability to tolerate heat? One complication in answering this question is that an organism's temperature tolerance can change throughout its life span, and organisms in early life stages may be more sensitive to cold and heat extremes than adults (the stage commonly measured) (1, 2). On page 65 of this issue, Dahlke *et al.* (3) report comparisons of the thermal tolerance limits of almost 700 freshwater and marine fish species at four life stages. Their findings confirm that embryos, and the reproductive adults who produce them, tolerate narrower temperature extremes than larvae and non-spawning adults, with thermal breadths (the difference between upper and lower thermal tolerance) that are narrower by an average of 20°C. As a result of this difference, projected climate vulnerabilities of fishes are greater than previously thought.

Dahlke *et al.* constrained each fish species' geographic range to the locations in which spawners and embryos could survive, and then asked how much hotter it can get before that life stage is squeezed out. They did this by calculating the difference between the upper thermal limit of the most sensitive life stage and the mean maximum environmental temperature in that part of its range. The authors found that by the year 2100, in an emissions scenario consistent with current political commitments, 40% of the fish species examined could not exist in the current geographic range of their most sensitive life stage. This projection can be reduced to ~10% if ambitious action is taken to reduce emissions. Still, these values are notably greater than the number of species projected to be out of range when the authors used only adult thermal tolerance (fewer than 5% of species). Indeed, most previous studies have

analyzed thermal limits of only larvae and adults (4–6). Hence, sensitivities may have been underestimated.

Why are embryos and reproductive adults less tolerant to extreme temperatures? These findings align with predictions under the oxygen-limited thermal tolerance hypothesis, which postulates that the tolerance of aquatic ectotherms to temperature extremes is driven by an outpacing of oxygen demand relative to supply at extreme cold and hot temperatures (1, 2). It simply gets too cold or hot to breathe. During development from egg to adult, fish increase their aerobic capacity through the development of a cardiorespiratory system that improves the supply of oxygen to tissues, and adult thermal tolerance increases. During reproduction, adult fish increase their biomass and oxygen demand, without a simultaneous increase in oxygen supply. As a result, say Dahlke *et al.*, the adult's thermal

tolerance decreases. Their finding that embryos and spawning adults have both reduced heat and cold tolerance lends strong support to the oxygen-limited thermal tolerance hypothesis.

What does this mean for fish? The greater sensitivity of eggs and reproductive adults means that marine and freshwater fish are liv-

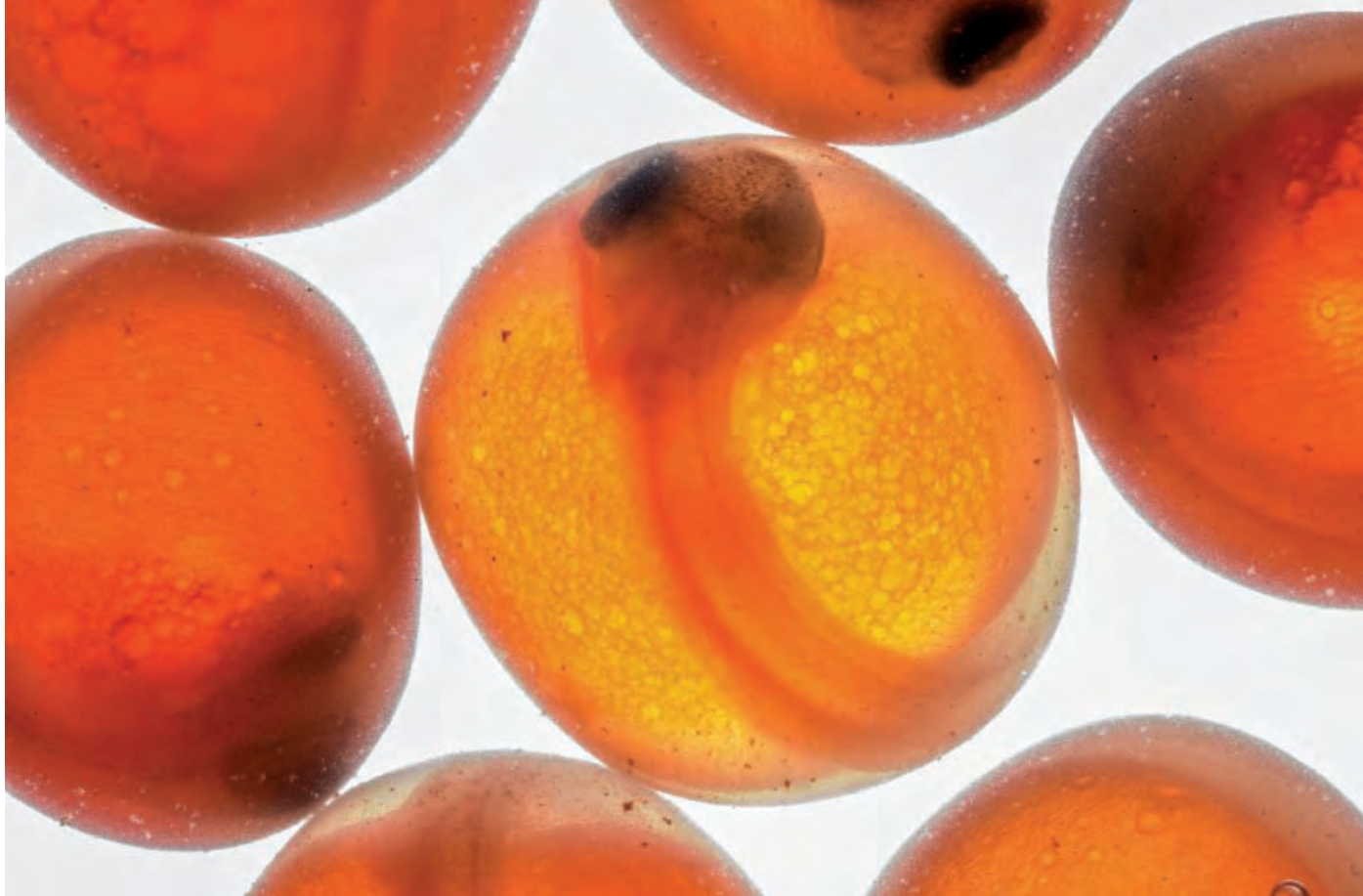
**“...marine and freshwater fish are living much closer to their thermal limits than previously thought.”**

ing much closer to their thermal limits than previously thought. Climate change is expected to provide strong selective pressure for spawning ranges of fish to move if they can, and if not, declines will be greater than predicted. However, it must be pointed out that fish populations are dynamic and have compensatory mechanisms that may disguise the survival response of any one life stage. For example, the predominance of negative density-dependent processes that regulate larval and adult survival (e.g., competition) means that populations of adults may not be altered even if many embryos fail, as long as some survive (7). In other words, per capita survival of larvae and adults can increase when there are fewer of them, compensating the adult population. Such compensatory dynamics mean that signs of dangerous spawning habitat loss in adult fish populations may not be detected until there are severe declines. The fish species assessed by Dahlke

Department of Biology, McGill University, Montreal, Quebec H3A 1B1, Canada. Email: jennifer.sunday@mcgill.ca

10.1126/science.abc6168





Fish embryos, such as these coho salmon eggs, and reproductive adults tolerate narrower temperature extremes compared to other life stages by an average of 20°C.

*et al.* cover a broad range of fish life histories, across which the immediate impacts of declining spawning habitats can be expected to vary. Stage-structured life history models will be a key asset to contextualize these important new findings.

Dahlke *et al.* also tested the hypothesis that metabolic responsiveness to temperature is greater in fish species and life stages that have narrower thermal tolerance ranges. Ectotherms have a characteristic exponential increase in their metabolic rate with temperature (8). The parameter that defines the shape of this relationship—the activation energy—is thought to reflect universal kinetic barriers that limit the rate of reactions, which in turn constrain higher-level rates such as oxygen consumption, growth rate, and development rate (8). By estimating this parameter, Dahlke *et al.* found that organisms with narrower thermal tolerance breadth (stenotherms) have higher activation energies than those with broad thermal tolerance (eurytherms). These results suggest that activation energies do not strictly conform to statistical thermodynamics [with a central tendency of ~0.60 to 0.70 eV (9)] but can be modified through selection and trade-offs.

Understanding variation in activation energy as a function of thermal breadth may provide opportunities to predict higher-level ecological responses to climate warming. For example, relative activation energies of

individual species can be used to predict temperature-related changes in trophic interactions and ecosystem stability (10). Predictions of relative biomass changes with temperature may now plausibly be applied to systems where, for example, eurytherms interact with stenotherms, or where the adults of one species feed on the eggs of another. Variation in activation energies can also be directly entered into dynamic size-based food web models that predict temperature effects on fish productivity (11).

One key opportunity for future work is to improve coverage of comparable thermal tolerance data across life stages. Dahlke *et al.* built their dataset by compiling all of the thermal tolerance data that are publicly available, and then used phylogenetic imputation to fill in the unknown values according to a phylogeny and best-fitting model of evolution. Although this has a precedent in the analyses of fish thermal limits (5), it is important to realize that when interpreting the results, many of the values shown by Dahlke *et al.* were not observed in their study. Similarly, some metrics of thermal tolerance differed systematically among life stages, because the more comparable thermal limit metrics were not available. Given the ramifications of these results, it will be critical to build a dataset in which thermal tolerance limits of embryos and spawning adults are estimated using the same meth-

ods as for larvae and nonspawning adults.

Fish are an increasingly important source of protein for human consumption as the global population grows (12), and the finding of greater sensitivity in eggs and reproductive adults on the order of 20°C is major cause for concern. The minute thermal safety margins of spawning fish and embryos in the tropics suggest that there are limited fish species on Earth that can tolerate warmer or less oxygenated habitats. Intensified efforts to stabilize global warming are warranted more than ever. ■

#### REFERENCES AND NOTES

1. H.-O. Pörtner, R. Knust, *Science* **315**, 95 (2007).
2. H.-O. Pörtner, *J. Exp. Biol.* **213**, 881 (2010).
3. F. T. Dahlke, S. Wohlrab, M. Butzin, H.-O. Pörtner, *Science* **369**, 65 (2020).
4. M. L. Pinsky, A. M. Eikeset, D. J. McCauley, J. L. Payne, J. M. Sunday, *Nature* **569**, 108 (2019).
5. L. Comte, J. D. Olden, *Proc. R. Soc. B* **285**, 20172214 (2018).
6. C. H. Trisos, C. Merow, A. L. Pigot, *Nature* **580**, 496 (2020).
7. H. K. Kindsvater, M. Mangel, J. D. Reynolds, N. K. Dulvy, *Ecol. Evol.* **6**, 2125 (2016).
8. J. H. Brown, J. F. Gillooly, A. P. Allen, V. M. Savage, G. B. West, *Ecology* **85**, 1771 (2004).
9. J. F. Gillooly, J. H. Brown, G. B. West, V. M. Savage, E. L. Charnov, *Science* **293**, 2248 (2001).
10. B. Gilbert *et al.*, *Ecol. Lett.* **17**, 902 (2014).
11. J. L. Blanchard *et al.*, *Philos. Trans. R. Soc. B* **367**, 2979 (2012).
12. Food and Agriculture Organization of the United Nations, *The State of World Fisheries and Aquaculture 2016* (2016).

10.1126/science.abd1272

## IMMUNOLOGY

# Rewilding immunology

Integrating comparative immunology can improve human, animal, and ecosystem health

By **Andrew S. Flies<sup>1</sup>** and **Wild Comparative Immunology Consortium<sup>2</sup>**

**T**he common origin of all species provides a wealth of history recorded in DNA and a lens for understanding human biology. Immunology research has traditionally used rodents as the model of choice. However, translational success has not met its full potential. Broadening immunology research to integrate comparative approaches across species and environments can amplify the potential of immunology to improve the lives of humans and other animals. Additionally, it can lead to discoveries that are not possible in a restricted set of model organisms and environments. For example, the contemporary vaccine era arose from observing human-animal interactions in a real-world environment (cowpox infection protected milkmaids from smallpox). Most emerging infectious diseases (EIDs) originate in domestic and wild animals (1), and the coronavirus disease 2019 (COVID-19) pandemic is a stark reminder of the need to think more holistically about the health of humans and animals.

The architecture of the immune system is an intricate network that has evolved over millions of years. Although no model organism can replicate all aspects of health and disease in another species, comparison of DNA and protein sequences across the tree of life is a straightforward and cost-effective means to select the most appropriate animal models for the question at hand (see the figure). For example, the current era of cancer immunotherapy was ushered in by the success of therapies that targeted the immune checkpoint protein cytotoxic T lymphocyte-associated protein 4 (CTLA4). Of the 134 mammals and 76 birds with CTLA4 orthologs listed in the National Center for Biotechnology Information Gene database, the key ligand binding motif (Met-Tyr-Pro-Pro-Tyr) in CTLA4 is identical in all 76 bird species and 131 of 134 mammals. Pigs (*Sus scrofa*) are common large-animal models for human pathologies and xenografts (implantation of tissue from another species), but they are one of

the three species that have a divergent ligand-binding motif in CTLA4 (2). Accounting for differences in key immunoregulatory genes among experimental species can be easily integrated into the experimental design stage of the research process.

The lack of reagents, such as monoclonal antibodies, for most species has historically been a barrier to integrating new species into the biomedical research cycle. However, the increasing number of fully sequenced genomes allows rapid comparison of gene networks across more than 200 species. De novo transcriptome assemblies can provide transcript sequences and expression patterns of species for which full genome sequence databases are unavailable, so that recombinant proteins can be quickly produced for protein-

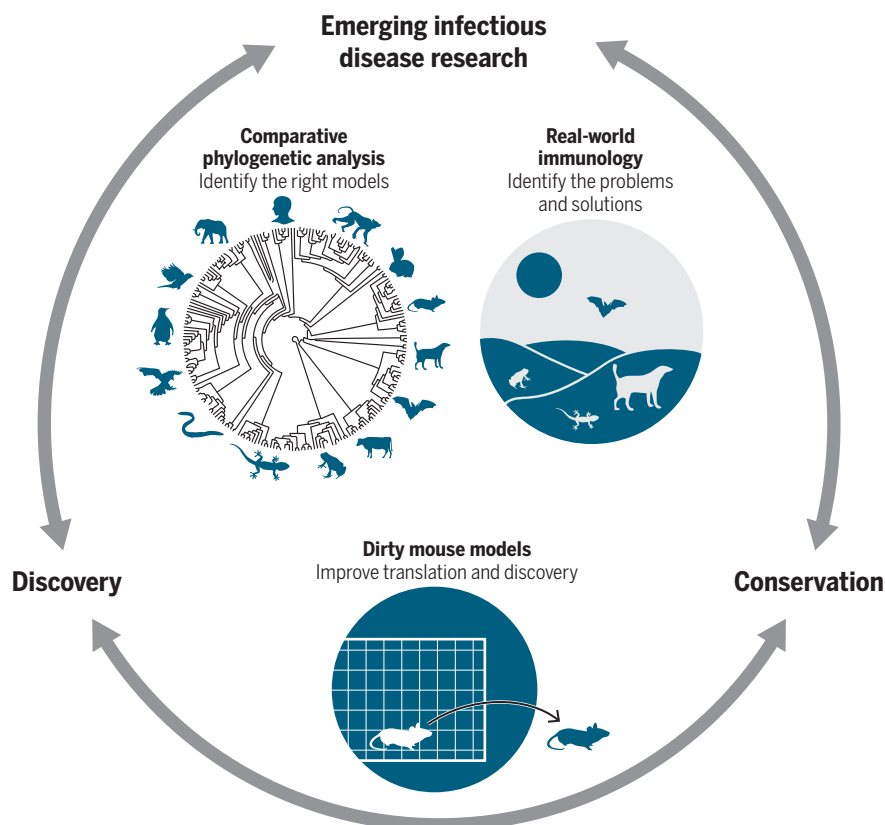
based immunology in species of interest (3).

Funding constraints that limit development of specific reagents for every species can be overcome through a systematic effort to develop and characterize antibodies, nanobodies, or aptamers that bind to conserved protein motifs across taxonomic orders. This can reduce the number of reagents that need to be developed and enhance research efficiency by reducing the need for individual laboratories to sift out cross-reactive reagents for their species of interest. For example, antibodies that bind the conserved regions of proteins (such as CTLA4 ligand-binding motif) could potentially be used for immunophenotyping and functional assays in most vertebrate species. Standardized reagent panels that can be used for serological assays of immunoglobulins [such as immunoglobulin A (IgA), IgE, IgG, and IgM] and can identify key cell types (such as resident memory T cells) will allow meaningful comparison across species and larger taxonomic groups.

The reagent development process itself has been simplified by the astute but serendipitous discovery of heavy chain-only antibodies in camels (*Camelus dromedarius*) (4). This

## Real-world immunology feedback cycle

Expanding the breadth of immunology to include more species and environments could benefit biomedical research. Phylogenetic analysis identifies appropriate model species. Successful laboratory mouse experiments replicated in “dirty” mice or natural disease models can stimulate a dynamic feedback cycle that improves preparedness for emerging infectious diseases, conservation efforts, and discovery of compounds that are not present in a restricted set of model species.



<sup>1</sup>Menzies Institute for Medical Research, College of Health and Medicine, University of Tasmania, Hobart, TAS 7000, Australia. <sup>2</sup>[www.wacimmuno.com](http://www.wacimmuno.com); Consortium authors and affiliations are listed in the supplementary materials. Email: [andy.flies@utas.edu.au](mailto:andy.flies@utas.edu.au)



new class of single-domain antibodies, also called nanobodies, streamlined the antibody-engineering process by allowing the production of high-affinity single-domain proteins. This allowed the creation of easy-to-use nanobody libraries that can be probed for binding to target proteins. For example, a nanobody library derived from a llama (*Lama glama*) that was immunized with the severe acute respiratory syndrome coronavirus (SARS-CoV, which causes SARS) spike protein that mediates target-cell entry has yielded a nanobody that binds to a conserved receptor-binding domain of the spike protein of SARS-CoV and SARS-CoV-2 (which causes COVID-19) (5). Furthermore, this nanobody has shown promising therapeutic potential after simple engineering to convert it to a bivalent human IgG Fc-fusion protein that has two linked nanobodies that bind the spike protein.

In addition to integrating new species, integrating natural environments into animal studies can enhance understanding of the complex interplay between the host immune system, microbiota, and environment. For example, cohousing inbred laboratory mice with “dirty” mice from a pet shop resulted in mice with immunophenotypes that more closely resemble adult humans (6). Moving laboratory mice into outdoor enclosures revealed that immunological differences among laboratory mouse (*Mus musculus*) genotypes and phenotypes quickly disappeared in this more natural setting (7). Like the “dirty” mouse models, wild animals ranging from mice to spotted hyenas (*Crocuta crocuta*) generally exhibit a more mature, antigen-experienced immunophenotype than that of captive animals (8, 9), providing a more realistic view of the development and regulation of the vertebrate immune system. Although environmental variation increases experimental noise, advances in analytical techniques, statistics, and computational power are capable of sifting through this variation (10). Treatment outcomes that can be replicated in natural or wild settings have a higher probability of translating into real-world medical breakthroughs. Using this environmental filter in the early stages of biomedical research could increase efficiency by eliminating ineffective treatments before they progress to large-animal models and clinical trials.

The concept that humans, nonhuman animals, and environments are linked biologically, culturally, and economically has recently become more formally recognized as “One Health.” For example, dogs and cats share homes, infections, and aspects of their

microbiotas with their owners and thus can provide a “common garden” to tease apart genetic and environmental factors that regulate immune function. This can be accomplished without the need for expensive laboratory studies by integrating local veterinary clinics into research studies and asking pet owners for consent to collect minimally invasive tissue samples from their pets. Documenting the progression and resolution of immune responses to pathogens such as *Salmonella*, noroviruses, and SARS-CoV-2 in pet owners and their pets in parallel could reveal evolutionary patterns and insight into cross-species pathogen transmission (11).

Proactive investment in comparative immunology can provide the historical baselines, tissue archives, and tools for more efficient responses to disease outbreaks. For example, an equine influenza outbreak in August 2007 in Australia incurred nearly \$800 million in direct and indirect costs before eradication by June 2008 (12). Comparative immunology studies in horses and vaccine testing against influenza years before the outbreak facilitated a swift and effective emergency response.

The variety of distinct mechanisms that wildlife species have evolved to deal with infectious diseases are a virtually untapped resource.

For example, bats (*Chiroptera*) are a taxonomic order of interest because of their reservoir capacity for viral zoonotic diseases, such as SARS, Ebola, Hendra, Nipah, and rabies. Bats have distinct genomic features and expression patterns of genes associated with antiviral immune responses, including interferon cytokines and natural killer cell receptors. Despite the potential for comparative immunology studies to provide mechanistic insight into how some bats control or tolerate viruses, bat immunology studies remain limited. New pathways and compounds can be discovered in species even more distantly related to humans. For example, a ribonuclease discovered in northern leopard frogs (*Rana pipiens*) (13) has demonstrated in vivo therapeutic effects against mesothelioma in humans and in vitro antiviral activity against SARS-CoV and is currently in human trials for treating adenoviral conjunctivitis.

Integrating new species and real-world environments into the broader immunology research paradigm will benefit not only human health but will also provide much needed resources for veterinary medicine and conservation efforts. The unprecedented loss of biodiversity in the past century was due to many factors but has been amplified by wildlife diseases. For example, chytridiomycosis,

a fungal pathogen that has spread across the globe (14), is responsible for the decline of more than 500 amphibian species and the extinction of more than 90. Understanding amphibian immunology can contribute to conservation efforts to halt the spread of the pathogen and develop prophylactic and therapeutic disease management options (15).

Evolution has been solving life-and-death problems for billions of years, and discovery of these creative solutions is only possible if research focus is expanded. A logical starting point for the expansion is to rigorously assess how current model species and environments reflect the true biology of human and animal diseases; when existing models are not adequate, new species and environments should be used. The future direction of this field should focus on real-world immunology scenarios that can maintain or accelerate the current progress of biomedical research without negatively affecting conservation efforts and generating new ethical concerns. The time is right for veterinarians, wildlife biologists, and disease ecologists to identify the key immunological questions and barriers in their research and then seek out people from other disciplines with the expertise and technical skills to overcome those barriers. However, the full potential of this emerging field cannot be achieved without support from the wider research community and funding agencies. Critical to this effort will be the willingness of immunologists to apply their scientific curiosity to the tree of life to help stimulate a dynamic interdisciplinary feedback cycle with impact for human health, EIDs, conservation, and translational research. ■

## REFERENCES AND NOTES

1. K. E. Jones *et al.*, *Nature* **451**, 990 (2008).
2. A. N. Vaughan *et al.*, *J. Immunol.* **165**, 3175 (2000).
3. A. S. Flies *et al.*, *Sci. Adv.* **6**, eaba5031 (2020).
4. C. Hamers-Casterman *et al.*, *Nature* **363**, 446 (1993).
5. D. Wrapp *et al.*; VIB-CMB COVID-19 Response Team, *Cell* **181**, 1004 (2020).
6. L. K. Beura *et al.*, *Nature* **532**, 512 (2016).
7. J. M. Leung *et al.*, *PLoS Biol.* **16**, e2004108 (2018).
8. S. Abolins *et al.*, *Nat. Commun.* **8**, 14811 (2017).
9. A. S. Flies *et al.*, *PLOS ONE* **10**, e0137679 (2015).
10. N. M. Fountain-Jones *et al.*, *Biol. Rev. Camb. Philos. Soc.* **93**, 950 (2018).
11. J. Shi *et al.*, *Science* **368**, 1016 (2020).
12. J. D. Watson *et al.*, *Rev. Sci. Tech.* **30**, 87 (2011).
13. Z. Darzynkiewicz *et al.*, *Cell Prolif.* **21**, 169 (1988).
14. B. C. Scheele *et al.*, *Science* **363**, 1459 (2019).
15. L. F. Grogan *et al.*, *Front. Immunol.* **9**, 2536 (2018).

## ACKNOWLEDGMENTS

The 2019 Wild and Comparative Immunology workshop ([www.wacimmuno.com](http://www.wacimmuno.com)) was supported by the Menzies Institute for Medical Research at the University of Tasmania, the Australian Research Council Centre of Excellence for Advanced Molecular Imaging, the Department of Biochemistry and Molecular Biology at Monash University, and Millennium Bioscience. We thank E. Flies for comments and edits on the manuscript and all participants in the 2019 Wild and Comparative workshop.

## SUPPLEMENTARY MATERIALS

[science.sciencemag.org/content/369/6499/37/suppl/DC1](https://science.sciencemag.org/content/369/6499/37/suppl/DC1)

10.1126/science.abb8664



## SCIENCE AND SOCIETY

# Improve alignment of research policy and societal values

The EU promotes Responsible Research and Innovation in principle, but implementation leaves much to be desired

By **Peter Novitzky,<sup>1</sup> Michael J. Bernstein,<sup>2</sup> Vincent Blok,<sup>1</sup> Robert Braun,<sup>3</sup> Tung Tung Chan,<sup>4</sup> Wout Lamers,<sup>4</sup> Anne Loeber,<sup>5</sup> Ingeborg Meijer,<sup>4</sup> Ralf Lindner,<sup>6</sup> Erich Griessler<sup>3</sup>**

**H**istorically, scientific and engineering expertise has been key in shaping research and innovation (R&I) policies, with benefits presumed to accrue to society more broadly over time (1). But there is persistent and growing concern about whether and how ethical and societal values are integrated into R&I policies and governance, as we confront public disbelief in science and political suspicion toward evidence-based policy-making (2). Erosion of such a social contract with science limits the ability of democratic societies to deal with challenges presented by new, disruptive technologies, such as synthetic biology, nanotechnology, genetic engineering, automation and robotics, and artificial intelligence. Many policy efforts have emerged in response to such concerns, one prominent example being Europe's Eighth Framework Programme, Horizon 2020 (H2020), whose focus on "Responsible Research and Innovation" (RRI) provides a case study for the translation of such nor-

mative perspectives into concrete policy action and implementation. Our analysis of this H2020 RRI approach suggests a lack of consistent integration of elements such as ethics, open access, open innovation, and public engagement. On the basis of our evaluation, we suggest possible pathways for strengthening efforts to deliver R&I policies that deepen mutually beneficial science and society relationships.

Alignment of R&I objectives with societal benefits, which transcend exclusive economic value, is a globally relevant concern (3). Aspiration of stronger science and society interrelationships have been visible in U.S. research management efforts, as well as in Canada and Europe. In H2020, to which the European Commission (EC) allocated nearly €80 billion for the 2014–2020 funding period, the EC enumerated RRI as a priority across all of H2020 activities (a "cross-cutting issue") to deepen science and society relationships and be responsive to societal challenges. To date, €1.88 billion have been invested across 200 different R&I areas (e.g., quantum computing, graphene nanotechnology, human brain research, artificial intelligence) in more than 1100 projects related to various dimensions of RRI (see the figure). Inclusion of RRI in

Horizon 2020 aims to integrate research policy and societal concerns, including about gender in science, and about disruptive technologies such as robotics.

H2020 reflected the commitment of the European Union (EU) to the precautionary principle with regard to R&I policy, and the deepening commitment of the EC to mainstream concerns related to science and society integration (4, 5).

RRI principles and practices have been designed to enhance inclusive and democratic modes of conducting R&I to reflect current forms and aspirations of society (4). Formal adoption and exploitation of RRI in H2020 coalesced around six thematic domains of responsibility ("keys"): public engagement, gender equality, science education and science literacy, open access, ethics, and governance (6). As a relatively young concept, these six keys cover only a part of RRI as it is discussed in the academic literature. Their integration in the European R&I ecosystem was advanced by various political- and policy-level ambitions (3–5). The forthcoming Ninth Framework Programme, Horizon Europe (2021–2027), includes further mention of RRI, as well as additional efforts to increase responsiveness of science to society through elements of the so-called "three O's agenda" (i.e., open innovation, open science, openness to the world) (7).

<sup>1</sup>Wageningen University and Research, Wageningen, Netherlands. <sup>2</sup>Arizona State University, Tempe, AZ, USA.

<sup>3</sup>Institute for Advanced Studies, Vienna, Austria. <sup>4</sup>Centre for Science and Technology Studies, Leiden University, Leiden, Netherlands. <sup>5</sup>University of Amsterdam, Amsterdam, Netherlands. <sup>6</sup>Fraunhofer Institute for Systems and Innovation Research, Karlsruhe, Germany. Email: pnovitzky@gmail.com; vincent.blok@wur.nl



Despite this fairly extensive history of EC investment in mainstreaming activities, a recent survey of more than 3100 European researcher recipients of H2020 funding showed that a vast majority of respondents were not familiar with the concept of RRI (8). Although these findings by no means suggest that researchers are irresponsible, they raise questions about the success of the EC approach to embedding normative targets for responsibility into R&I. The need for systematic evaluation is clear (9). Our study contributes to a legacy of research on the efficacy of framework programmes in light of various EC ambitions (10).

## METHODS AND FINDINGS

To answer our question about policy integration and implementation of RRI in H2020, we conducted a mixed method investigation in three stages: (i) desktop research, (ii) interviews, and (iii) case research [see supplementary materials (SM) S10 for details]. First, we collected and reviewed relevant documentation of the four H2020 Programme Sections (Excellent Science, Industrial Leadership, Societal Challenges, Diversity of Approaches) and 19 respective subthemes available on the websites of the EC. This included reviews of documents at the following levels: policy, scoping, work package, calls, projects, proposal templates, and evaluations. Review of documents extended to all three periods of H2020 (2014–2015, 2016–2017, and 2018–2020) and employed the six EC RRI keys as indicators.

Second, we conducted interviews with representatives ( $n = 257$ ) of seven stakeholder groups within the 19 subthemes of H2020. Third, using natural language processing algorithms, we obtained and analyzed texts describing project objectives of all the H2020 projects (ongoing and finished,  $n = 13,644$ ) available on the CORDIS Portal, which provides information on EU-funded R&I activities. We examined how proposal language and RRI policies translate into project activities across H2020 using text-mining approaches. We carried out keyword frequency analysis by applying a selection of 10 to 12 keywords (SM S8) associated with each of the six RRI keys. This resulted in an “RRI score” for each of six keys for each H2020 project (SM S13). This subsequent case research covered all three H2020 periods (i.e., 2014–2015, 2016–2017, and 2018–2020).

At each of these stages we produced reports for each corresponding subtheme (SM S11). The resulting body of 19 reports was then systematically reviewed for levels of policy integration. The policy-integration levels were qualitatively assessed with the EC’s own indicator assessment (6).

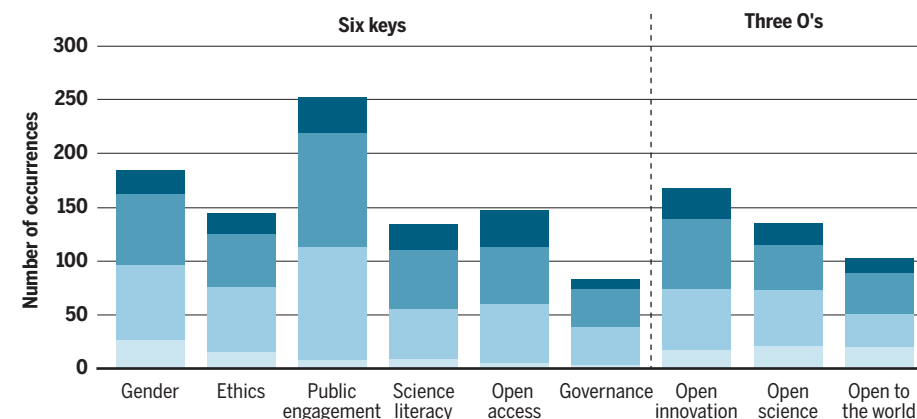
## How well is Responsible Research and Innovation represented in Horizon 2020?

Limited high-quality reference to Responsible Research and Innovation (RRI) suggests that it has largely been referred to without proper understanding, or as an empty signifier. Data combine all four Horizon 2020 (H2020) program sections and reflect the amount and quality of representation of six RRI keys and three “O’s,” across three levels: samples of internal H2020 program documents, H2020 stakeholder interviews, and H2020 project objectives. Comparison across keys within a given level is straightforward; all values are drawn from the same underlying materials. Comparison across levels within a given key should focus on relative proportions of the four colors within a given level, not on absolute values; analyses drew upon different types and amounts of underlying materials in each level. See supplementary materials for details.

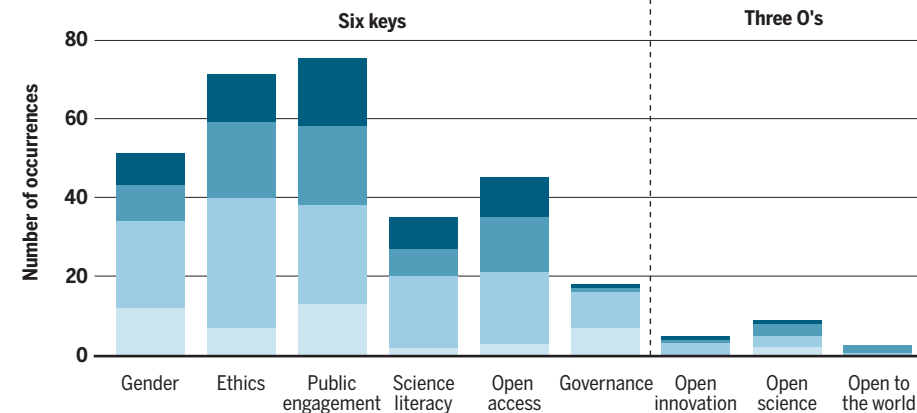
### Quality of representation

● High ● Some ● Limited ● Superficial

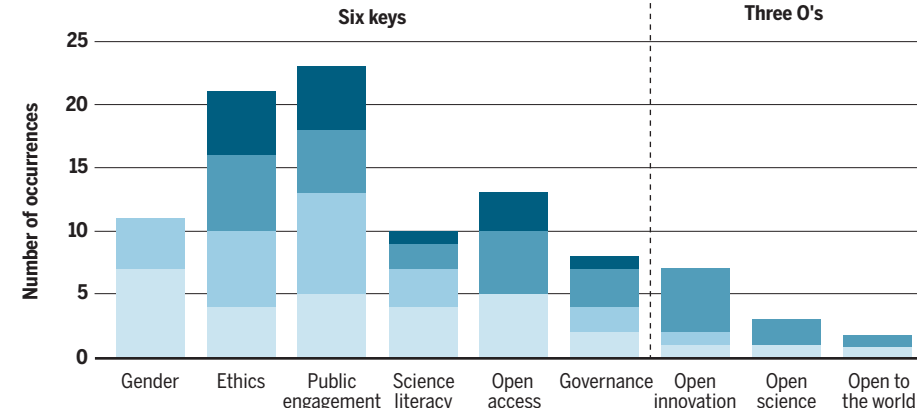
#### Internal H2020 documents



#### H2020 stakeholder interviews



#### H2020 project objectives



This assessment demonstrates which elements of the RRI framework were initially defined by the policy-makers (desktop level), which RRI attributes the stakeholders were most aware of (interview level), and which RRI elements were manifested in project proposals (case level) (SM S12; see the figure). RRI as a concept has been present in most of the four Programme Sections of H2020, and particular RRI policy elements emerge as prominent in certain subthemes, especially those addressing societal challenges or explicitly promoting the uptake of RRI. But RRI overall has largely been referred to either without proper understanding of its definition, or as empty signifier, suggesting lack of compliance with the EC's interpretation of the RRI concept (see the figure; SM S9). Integration of the three O's agenda, contemplated as a successor to the RRI framework, lagged behind that of the six RRI keys; a finding consistent with introduction of the agenda in the later stages of H2020.

## DISCUSSION

Our results suggest that the integration of the RRI framework into H2020 has fallen short of stated EC ambitions. Our data show substantial discrepancies between the inclusion of RRI concepts within official subtheme documents (e.g., on policy and work programme levels), and awareness of RRI by interviewees working on projects funded by such subthemes (see the figure). Absence of RRI keys across the majority of programme subtheme evaluation criteria is a telling example.

Such evidence suggests that (i) the RRI framework is still an evolving concept, the development of which hinders its proper understanding by those who are supposed to use it; (ii) such individuals have only superficial understanding of the notion for its effective exploitation; and (iii) although the RRI framework is present on the declarative, strategic policy level (scoping and subtheme general description), it wanes in funding calls (policy operationalization) and is largely absent in evaluation criteria used in proposal assessment. Collectively, these points further suggest that applicants have little in the way of consistently aligned incentives to regard RRI as relevant in proposal design and submission.

Although (i) and (ii) are primarily a matter of a lack of adequate information, awareness and training, (iii) points to limitations of European science policy efforts related to the pursuit of RRI. Such translation failures are typically caused by interplay of different logics of negotiation at the different levels (17), a linear model of innovation appealing to scientific excellence in R&I (12), actors' resis-

tance to change, path dependencies, cognitive boundaries, and competing policy agendas (13). As the issues covered by RRI are normatively claimed to be of high relevance by political decision-makers, as evidenced in several EC documents, we conclude that the problem is one of policy integration strategy and implementation (14). The lack of clarity in conceptualizing RRI for research policy and governance, the limited understanding among key stakeholders, and the concept's conflation with other—often conflicting—policy goals (e.g., scientific excellence, economic value, technological readiness) hinder the emergence of a specific RRI-oriented policy frame (15). Such conflicting policy goals are palpable at the core of European research funding (e.g., supporting either mission-oriented innovation or curiosity-driven basic research in key funding instruments) and highlight the structural tensions between the normative ideals and potential instrumentalization (3).

There are some limitations of this study that must be taken into account when interpreting results. First, the measurements were cross-sectional and though representative, are not exhaustive. Generalizability of findings could be increased if the study were to extend in a longitudinal fashion and possibly to better elaborate causal relationships among factors. Second, although we employed mixed methods in our investigation, the number of interviews and case studies could be further increased to provide additional qualitative information about the dynamics of RRI at the project level. Third, as the framework programme remains ongoing, our analysis was not able to evaluate the entire H2020 corpus. Although the results indicate evidence of patchy RRI implementation, highlighting the need for more consistent support to help align EC science policy and societal values, the progress made is nontrivial, given the history of science (1).

A clear discrepancy exists between the expressed strong normative position on RRI and its integration in concrete policies and practices. Fully integrating RRI as a strong normative position into research funding and governance is a necessary but not sufficient first step to creating a working policy system that drives RRI integration. Longer-lived investments are needed for building a shared understanding and awareness of the relevance of responsibility in R&I among key stakeholders. Integrating responsibility into research funding further requires RRI to shift from a “cross-cutting issue” to a “strategic concern” that receives consistent and sustained embedding in call texts and project selection criteria. This will require “policy entrepreneurs” who can stimulate interactions across subthemes to foster alignment of RRI integration and

translation. In addition, a range of integration policies are required at the system level and within subthemes, in which the issue of RRI is adopted as a goal. This is pertinent as, in case of such integration failures, it is often the normative position that is called into question instead of the implementation strategy, or actual integration pathway. The EC would benefit from enhancing previous efforts to integrate RRI and so affirm its role as a leader of ethically acceptable and societally responsible R&I on the world stage. Otherwise Europe needlessly undercuts its ability to direct research toward tackling societal challenges in ways compatible with its values. ■

## REFERENCES AND NOTES

1. M. Polanyi, J. Ziman, S. Fuller, *Minerva* **38**, 1 (2000).
2. N. Mejlgaard et al., *Science* **361**, 761 (2018).
3. R. von Schomberg, in *International Handbook on Responsible Innovation: A Global Resource*, R. von Schomberg, J. Hankins, Eds. (Edward Elgar, 2019), pp. 12–32.
4. R. Owen, P. Macnaghten, J. Stilgoe, *Sci. Public Policy* **39**, 751 (2012).
5. R. Owen, M. Pansera, in *Handbook on Science and Public Policy*, D. Simon, S. Kuhlmann, J. Stamm, W. Canzler, Eds. (Edward Elgar, 2019), pp. 26–48.
6. DGRI, “Indicators for promoting and monitoring responsible research and innovation: Report from the expert group on policy indicators for responsible research and innovation” (Report, European Commission, 2015); [http://ec.europa.eu/research/swafs/pdf/pub\\_rri/rri\\_indicators\\_final\\_version.pdf](http://ec.europa.eu/research/swafs/pdf/pub_rri/rri_indicators_final_version.pdf).
7. DGRI, Open innovation, open science, open to the world: A vision for Europe” (Directorate-General for Research and Innovation, European Union, 2016); <https://publications.europa.eu/en/publication-detail/-/publication/3213b335-1cbc-11e6-ba9a-01aa75ed71a1>.
8. S. Bührer et al., “Monitoring the evolution and benefits of responsible research and innovation: Report on the researchers’ survey – Study” [Report KI-1-18-886-EN-N, Directorate-General for Research; Innovation (European Commission), 2018].
9. A. Rip, *J. Responsib. Innov.* **3**, 290 (2016).
10. H. Rodríguez, E. Fisher, D. Schuurbijs, *Res. Policy* **42**, 1126 (2013).
11. M. Howlett, J. Vince, P. Del Río, *Politics Gov.* **5**, 69 (2017).
12. K. Rommetveit, R. Strand, R. Fjelland, S. Funtowicz, “What can history teach us about the prospects of a European research area? Joint Research Centre scientific and policy reports” (Report JRC84065, European Commission, 2013).
13. H. Colebatch, *Public Policy Admin* **33**, 365 (2017).
14. B. G. Peters et al., *Designing for Policy Effectiveness: Defining and Understanding a Concept* (Cambridge Univ. Press, 2018).
15. R. Owen, E.-M. Forsberg, C. Shelley-Egan, “RRI-practice policy recommendations and roadmaps: Responsible research and innovation in practice” (Report, RRI-Practice Project, 2019); [www.rri-practice.eu/wp-content/uploads/2019/06/RRI-Practice\\_Policy\\_recommendations.pdf](http://www.rri-practice.eu/wp-content/uploads/2019/06/RRI-Practice_Policy_recommendations.pdf).

## ACKNOWLEDGMENTS

This project received funding from the EU's Horizon 2020 research and innovation programme under grant agreement no. 741402. We acknowledge all the consortium members who contributed to the data collection and writing of the reports (SM S11), which this study is based on. We express our gratitude to H. Tobi and N. Mejlgaard, as well as to the reviewers, for their helpful and constructive comments.

## SUPPLEMENTARY MATERIALS

[science.sciencemag.org/content/369/6499/39/suppl/DC1](https://science.sciencemag.org/content/369/6499/39/suppl/DC1)

10.1126/science.abb3415





Data-driven design of school lunch lines can help students make healthier choices.

## PSYCHOLOGY

# Better homes and safer spaces

Evidence-based indoor design is more important than ever

By **Barbara Brown**

**T**he coronavirus disease 2019 (COVID-19) pandemic has transformed our homes into schools, workplaces, recreational centers, and experimental kitchens, rendering us increasingly aware of the opportunities and constraints built into their design. In her new book, *The Great Indoors*, science journalist Emily Anthes helps us channel this awareness into an appreciation of how design alters our feelings and behaviors within built environments.

Although research on the benefits of nature is booming, the reality is that North Americans and Europeans spend about 90% of their time indoors. Worldwide, the indoor environment is expected to double in square footage by 2060.

Anthes takes readers on a tour of the behavioral implications of indoor design, highlighting apartments created for neurodiverse individuals, dome homes, and electronically monitored housing. She also explores hospitals, prisons, and public spaces designed to encourage physical activity. Along the way, she interviews environmental psychologists, design professionals, and advocates of the thoughtful deployment of evidence-based design.

Google Trends has documented a recent spike in searches related to antibacterial cleansers, suggesting that many of us have come to think of the microbial world as our enemy. Yet Anthes argues that “a healthy home is one that’s full of uninvited guests.” In her “absolutely spotless” showerhead, for example, she discovers mycobacteria, which resist destruction by hot water and chlorine. Some strains of mycobacteria, she learns, can bolster human immune systems, while others cause tuberculosis.

Science has yet to disentangle the benefits and dangers posed by the microbes in our homes, but indoor ecologists are regularly discovering new strains and have even determined that different microbial signatures are left by men’s and women’s bodies. Anthes invites readers to consider the potential benefits of fostering a greater understanding of these indoor ecosystems and points to a future wherein we consciously cultivate healthy ones.

Many advances in health, such as reducing New York City’s levels of cholera, typhoid, and tuberculosis in the 1800s, were the result of better physical design and infrastructure maintenance, not pharmaceutical breakthroughs. Anthes’s prescient reminder of this fact allows readers to think about how design can enhance environmental health. One can imagine, for example, a future in which con-

tact-free buildings and services are the norm.

Because we adapt to indoor environments, we tend to overlook the possibilities that better design could provide. Private hospital rooms, for example, harbor 50% fewer pathogens than shared rooms. Meanwhile, we know that the heart rates of young people on the autism spectrum become elevated when these individuals are exposed to typical restaurant noise. Prioritizing ambient sound mitigation in such settings could help support more humane design.

Research findings often run counter to traditional design strategies and can reveal unexpected connections between design and behavior. One study Anthes cites, for example, found that face-to-face interactions declined by 72% when companies switched from cubicles to open floor plans. Another study found that by placing the operating room bed on a diagonal instead of in the traditional centered position, the anesthesiologist gains important protected workspace that minimizes disruptions and enhances patient safety.

*The Great Indoors* contains no slogs about how inclusionary zoning codes support affordable housing design. Instead, readers learn, for example, how dirt, water, and barbed wire are ingredients for easily constructed dome homes that have provided emergency housing for refugees and could better serve people in poverty.

But not all design changes bring about their desired effects. Anthes recounts how a school in rural Buckingham County, Virginia, redesigned in 2012 to encourage healthy eating and physical activity had mixed success. Hiding the calorie-laden chocolate milk behind the counter increased the consumption of white milk, and placing activity-friendly equipment in the halls reduced students’ sedentary time. But situating the outdoor playground a long walk away from the school building lessened the time available for engagement in vigorous outdoor activity, a failure that inspired more research.

A self-described fan of the indoors, Anthes encourages readers to reconsider the places where they spend most of their time and to ask themselves whether those places serve their needs. At a point when we are spending even more time than usual indoors, all of humanity could likely benefit from confronting such questions. ■



**The Great Indoors**  
Emily Anthes  
Scientific American/  
Farrar, Straus and Giroux,  
2020. 304 pp.

The reviewer is at the Department of Family and Consumer Studies, University of Utah, Salt Lake City, UT 84112, USA.  
Email: barbara.brown@fcs.utah.edu

## PHYSICS

# Physics meets America's defense agenda

War transformed 20th-century physics in sometimes subtle ways

By **Melanie Frappier**

**W**hile historically naïve, Thomas Kuhn's 1962 treatise *The Structure of Scientific Revolutions* succeeded in revealing that science is not as rational and objective as many imagined it to be, opening the doors to a new kind of history of science, one that pays attention to the complex interactions between science's conceptual frameworks and its social contexts. Yet, to this day, most history books written for the wider public favor a narrower understanding of science. David Kaiser's work is a welcomed exception.

In *Quantum Legacies: Dispatches from an Uncertain World*, Kaiser, who teaches both particle cosmology and history of science at the Massachusetts Institute of Technology, gives a witty and insightful overview of the development of modern physics. Through a series of previously published but carefully reedited essays, he explores how America's defense agenda has shaped physics research and education, from the ever-increasing size of research teams to the way we talk about quantum phenomena.

Initially, only taciturn physicists such as

Paul Dirac preferred to focus on the mathematical formalism of quantum physics rather than engaging in public debates on its philosophical implications as Albert Einstein and Erwin Schrödinger often did. Why then are so many physicists now favoring Dirac's "shut up and calculate" approach? Kaiser seems unconvinced by the oft-repeated claim that most physicists were satisfied by Niels Bohr's answers to Einstein's and Schrödinger's worries and simply turned their attention to more practical problems. The change of focus, he argues, was brought about by the complex ways in which war transformed physics.

Historians usually underline the role that new military technology, from computers to atomic bombs, played in the Allies' victory in World War II. But according to Kaiser, the most important contribution that physics departments made to the war effort was the training of soldiers. As he reminds us, this was a "physicists' war" first and foremost, because soldiers needed a basic grasp of physics to operate everyday military technology.

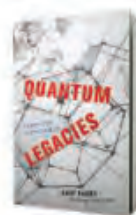
Across the country, classroom discussions of the interpretation of quantum mechanics were replaced by lectures on the fundamen-

tals of radio transmission and artillery. Far from being temporary, these drastic changes became entrenched during the Cold War as Americans feared—albeit incorrectly—that the USSR would match and perhaps surpass their scientific and military outputs. Fear of a nuclear conflict, Kaiser explains, made nuclear physicists key to national security during this period. Generous governmental funding in research and education led to soaring enrollments in physics departments.

As Kaiser demonstrates through an examination of mid-20th-century textbooks, increasingly large classes encouraged professors to continue their move away from philosophical musings in favor of more practical (and undoubtedly easier-to-grade) calculations. Gone were the days when textbooks discussed the reality of the energy levels of hydrogen atoms; now the aim was to calculate them.

The Cold War led to a golden age during which physics saw the development of the standard model and the discovery of new particles, from neutrinos to the Higgs boson. To his credit, Kaiser never suggests that military funding is key to rapid scientific development. Not only does he remind us that the reactionary counterculture of the 1960s and 1970s played a crucial role in fundamental research [as he also does in (1)], he convincingly argues that the waning of nuclear research funding caused by the détente unwittingly led to the creation of particle cosmology.

Peppered with interesting anecdotes from Kaiser's own career, *Quantum Legacies* offers a series of perceptive essays on why and how America has trained physicists in the past century. The one "legacy" the book fails to address is the flagrant absence of female and minority researchers in particle cosmology. Despite this want, *Quantum Legacies* remains an engrossing read that will give specialists and nonspecialists alike a deeper understanding of how phenomena as diverse as geopolitics and eastern mysticism have shaped physics in the past century. ■



**Quantum Legacies:**  
**Dispatches from**  
**an Uncertain World**

David Kaiser  
University of Chicago  
Press, 2020. 360 pp.

The reviewer is at the History of Science and Technology Program, University of King's College, Halifax, NS B3H 2A1, Canada. Email: melanie.frappier@ukings.ca



Doubts about quantum mechanics plagued Paul Ehrenfest (left) and Albert Einstein (right, with Ehrenfest's son).

## REFERENCES AND NOTES

1. W. P. McCray, D. Kaiser, *Science* **365**, 550 (2019).

10.1126/science.abb2973




CALL FOR PAPERS

[spj.sciencemag.org/bmef](http://spj.sciencemag.org/bmef)



# BME Frontiers

 OPEN ACCESS

*Biomedical Engineering (BME) Frontiers* is a **Science Partner Journal** distributed by the **American Association for the Advancement of Science (AAAS)** in collaboration with the **Suzhou Institute of Biomedical Engineering and Technology, Chinese Academy of Sciences (SIBET CAS)**. *BME Frontiers* aims to serve as an effective platform for the multidisciplinary community of biomedical engineering. The journal will publish breakthrough research in the fields of pathogenic mechanisms as well as disease prevention, diagnosis, treatment, and assessment.

The Science Partner Journals (SPJ) program was established by the American Association for the Advancement of Science (AAAS), the nonprofit publisher of the *Science* family of journals. The SPJ program features high-quality, online-only, open access publications produced in collaboration with international research institutions, foundations, funders and societies. Through these collaborations, AAAS expands its efforts to communicate science broadly and for the benefit of all people by providing top-tier international research organizations with the technology, visibility and publishing expertise that AAAS is uniquely positioned to **offer as the world's largest general science membership society**.

**Submit your research to *Biomedical Engineering Frontiers* today!**

Learn more at: [spj.sciencemag.org/bmef](http://spj.sciencemag.org/bmef)

# RESEARCH

## Fountain-like flow disperses bacteria in biofilms

Qin et al., p. 71



## IN SCIENCE JOURNALS

Edited by  
Michael Funk

A colored scanning microscope image of *Plasmodium berghei*, which is a useful model for malaria vaccine studies, infecting a mouse red blood cell

### MALARIA

## Defending the liver

**T**he liver is an important site of replication for *Plasmodium* parasites, and therefore a key goal in vaccination against malaria is to induce robust antiparasitic immunity in the liver. Using *Plasmodium berghei* as a model to study malaria in mice, Holz et al. developed a glycolipid-peptide conjugate vaccine that induced robust T cell responses in the liver and was able to protect mice challenged with *P. berghei*. Inclusion of the glycolipid adjuvant  $\alpha$ -galactosylceramide, which activates natural killer T cells, was vital to promoting antiparasitic immunity in the liver. The authors propose that agonists that activate natural killer T cells could be useful in priming immune responses in the liver in the context of malaria and other hepatotropic diseases. —AB *Sci. Immunol.* 5, eaaz8035 (2020).

### CLIMATE RESPONSES

## Some cope better than others

Increasingly, research is revealing how organisms may, or may not, adapt to a changing climate. Understanding the limitations placed by a species's physiology can help to determine whether it has an immediate potential to deal with rapid change. Many studies have looked at physiological tolerance to climate change in fishes, with results indicating a range of responses. Dahlke et al. conducted a meta-analysis to explore how life stage may influence a species's ability to tolerate temperature

change (see the Perspective by Sunday). They found that embryos and breeding adult fishes are much more susceptible to temperature change than those in other life stages and that this factor must therefore be considered in evaluations of susceptibility. —SNV

*Science*, this issue p. 65;  
see also p. 35

### CORONAVIRUS

## Vaccine candidate tested in monkeys

Global spread of severe acute respiratory syndrome coronavirus 2 (SARS-CoV-2)

has led to an urgent race to develop a vaccine. Gao et al. report preclinical results of an early vaccine candidate called PiCoVacc, which protected rhesus macaque monkeys against SARS-CoV-2 infection when analyzed in short-term studies. The researchers obtained multiple SARS-CoV-2 strains from 11 hospitalized patients across the world and then chemically inactivated the harmful properties of the virus. Animals were immunized with one of two vaccine doses and then inoculated with SARS-CoV-2. Those that received the lowest dose showed signs of controlling the infection, and those receiving the highest dose appeared more

protected and did not have detectable viral loads in the pharynx or lungs at 7 days after infection. The next steps will be testing for safety and efficacy in humans. —PNK

*Science*, this issue p. 77

### DIELECTRICS

## Defect-enhanced energy storage

Dielectric capacitors are vital components of electronics and power systems. The thin-film materials of which capacitors are composed are usually optimized by changing the material composition. However, Kim et al. found that postprocessing



an already effective thin-film dielectric by high-energy ion bombardment further improved the material because of the introduction of specific types of defects that ultimately improved the energy storage performance. The results suggest that postprocessing may be important for developing the next generation of capacitors. —BG

*Science*, this issue p. 81

## SOLAR CELLS

### Stable perovskites with ionic salts

Ionic liquids have been shown to stabilize organic-inorganic perovskite solar cells with metal oxide carrier-transport layers, but they are incompatible with more readily processible organic analogs. Lin *et al.* found that an ionic solid, a piperidinium salt, enhanced the efficiency of positive-intrinsic-negative layered perovskite solar cells with organic electron and hole extraction layers. Aggressive aging testing showed that this additive retarded segregation into impurity phases and pinhole formation in the perovskite layer. —PDS

*Science*, this issue p. 96

## HIV

### Sourcing HIV-1 infection

HIV-1 has a multitude of strain variants, but sexual transmission of HIV-1 is assumed to result from productive infection by only one virus particle. Knowing the genetics of the virus strains that are transmitted could be crucial for developing successful vaccine strategies. Using epidemiological and genetic data from 112 pairs of sexual partners, Villabona-Arenas *et al.* found that individuals with acute infections are more likely to transmit multiple founder virus strains. In a phylodynamic approach that integrated phylogenetic analysis of sequence data with simulation of a transmission chain, the authors

showed that multiple variant transmission is doubled during the first 3 months of infection irrespective of whether transmission was heterosexual or by men who have sex with men. —CA

*Science*, this issue p. 103

## ORGANIC CHEMISTRY

### Using hydrocarbons as reagents

Adding small alkyl groups to complex molecules usually relies on alkyl halide reagents. Laudadio *et al.* now report a convenient method to add ethane and propane directly across conjugated olefins with no prefunctionalization or by-products (see the Perspective by Oksdath-Mansilla). The C–H bond scission in this hydroalkylation is accomplished by a decatungstate photocatalyst that also acts as a hydrogen atom transfer agent to complete the process. The reaction, optimized under flow conditions, works with methane as well, albeit with lower efficiency. —JSY

*Science*, this issue p. 92;  
see also p. 34

## PAIN

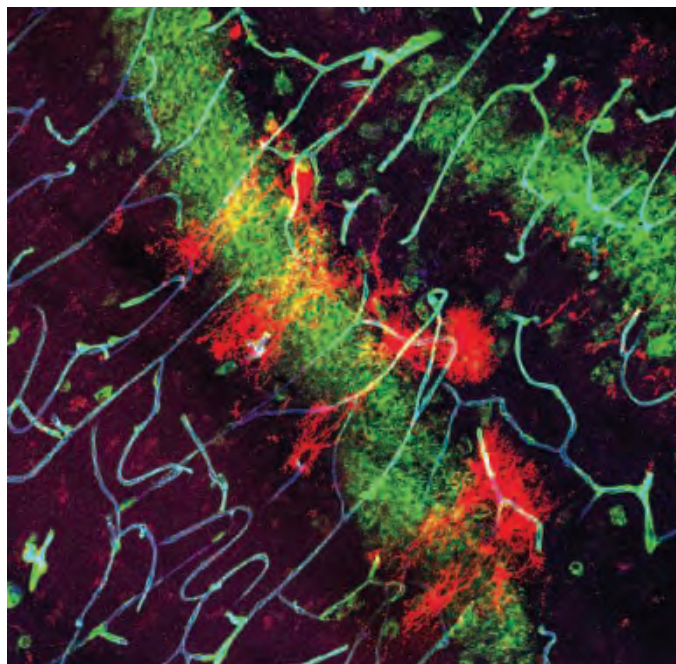
### Inflammatory pain revisits development

An increase in *N*-methyl-D-aspartate (NMDA) glutamate receptors (NMDARs) containing the GluN2B subunit in sensory neuronal synapses is associated with enhanced nociception and pain. In rodents, Zhang *et al.* found that GluN2B content in sensory neurons was progressively restricted during early development and maintained at low abundance by the E3 ubiquitin ligase Cbl-b during adulthood. Peripheral inflammation impaired the interaction of Cbl-b with GluN2B, and the increase in GluN2B abundance enhanced NMDAR activity and neuronal sensitivity to touch. —LKF

*Sci. Signal.* **13**, eaaw1519 (2020).

## IN OTHER JOURNALS

Edited by **Caroline Ash**  
and **Jesse Smith**



Section through the mouse hippocampus showing cellular processes of neural stem cells (red) associating with endothelial cells of blood vessels (blue)

## NEURODEVELOPMENT

### Bloodborne privilege for stem cells

Even in adults, neurons in the brain can regenerate. Progenitor neural stem cells (NSCs) in adult rodents are found in the subventricular zone of the lateral ventricles and the hippocampus. Radial-glia-like NSCs in the hippocampus, as their name suggests, have a tree-like structure. They send thin terminal processes from the subgranular zone into an area called the inner molecular layer. When activated by exercise, for example, NSCs transform into new neurons, but this requires bloodborne components. Licht *et al.* show that NSC processes form direct membrane-to-membrane contact with endothelial cells in specialized areas where the basement membrane is interrupted by zones of vesicular activity. In this way, NSCs circumvent the blood-brain barrier to access molecules that normally cannot penetrate the brain. —PJH

*eLife* **9**, e52134 (2020).

## CELL BIOLOGY

### Oscillator for centriole formation

Cells are not just bags of enzymes—their functions are orchestrated by organelles. Centrioles, for example, function in cell division and organization of the mitotic spindle and duplicate in coordination with the cell cycle. Centriole formation seems to be

governed by an oscillator that controls the localization and activity of Polo-like kinase 4, the master regulator of centriole biogenesis. Working with the results of experiments in fruit fly embryos, Aydogan *et al.* used a mathematical model to show that this oscillator controls centriole biogenesis independently of the cell cycle oscillator. This model also explains homeostasis of

centriole size. Other organelles may also use such oscillators to time the initiation and duration of growth, and it is possible that circadian and cell cycle oscillators entrain the local organelle-controlling oscillators. —LBR

*Cell* **181**, 1566 (2020).

## HUMAN GENETICS

### Populations of ancient France

Ancient DNA has identified changes in human population genetic structure across Europe for the past 10,000 years or so. However, the area that constitutes modern-day France is a bit of a blank. Brunel *et al.* examined mitochondria, Y chromosomes, and nuclear loci from 243 individuals and low-coverage genomes from 58 people spanning ~7000 years from sites within modern-day France. From this survey, they identified Mesolithic similarities to Iberian hunter-gatherer populations that retained genes from two Late Pleistocene lineages. During the Neolithic, and then again in the Bronze age, transitions in genetic ancestry were observed

during cultural and technological transitions. Fewer changes were observed during the transition from the Bronze Age into the Iron Age; these individuals had a genetic composition similar to that of the modern-day French. This study reveals successive migrations, major cultural changes, and admixture events, the traces of which are still found in current European populations, as well as evidence of an Upper Paleolithic admixture from the Iberian Peninsula. —LMZ

*Proc. Natl. Acad. Sci. U.S.A.* **117**, 12791 (2020).

## ANTIBIOTIC RESISTANCE

### Gut busters in a slurry

Antibiotic-resistant pathogens exist within species-rich communities of other microorganisms. Interactions between pathogens and commensal organisms are anticipated to influence resistance. The microbiota could act competitively to suppress pathogens but also allow nutrient sharing or horizontal transfer of resistance genes. To work out what might happen in a near-natural community, Baumgartner *et al.* developed

a gut microcosm setup using donated anaerobic human microbiota, an introduced tagged *Escherichia coli*, and the  $\beta$ -lactam antibiotic ampicillin. In this system, antibiotic resistance only evolved in the *E. coli* strain when the resident commensals were knocked back, even when resistance genes and plasmids were present among the commensals. —CA

*PLOS Biol.* **18**, e3000465 (2020).

## ORGANIC CHEMISTRY

### Ironing out crowded dihydroxylations

It is essential in drug synthesis to select between mirror image products, and asymmetric dihydroxylation of carbon-carbon double bonds is a means of doing so. The chief drawback of this reaction is that it requires the use of rare and toxic osmium. The alternative use of safer, more abundant metals has tended to limit the substrate scope to simple olefins. Wei *et al.* now report through ligand optimization a highly selective and efficient iron catalyst for the dihydroxylation of trisubstituted

olefins. The reaction operates at room temperature with hydrogen peroxide as oxidant. —JSY

*Angew. Chem. Int. Ed.* **10.1002/anie.202002866** (2020).

## NANOMATERIALS

### Graphene templating of hexagonal BeO

Liquid droplets encapsulated by two graphene sheets can experience high pressure (up to 1 GPa) and can act as vessels for crystallization of two-dimensional materials. Wang *et al.* studied the crystallization of beryllium oxide (BeO) in such a cell with high-resolution transmission electron microscopy and electron energy loss spectroscopy. Instead of forming the bulk wurtzite structure, it crystallized into an  $sp^2$ -coordinated hexagonal structure that was typically 20 to 30 layers thick. This thickness makes the material metastable relative to wurtzite, and the authors argue that the non-interacting graphene surface kinetically templates the hexagonal phase. —PDS

*Angew. Chem. Int. Ed.* **10.1002/anie.202007244** (2020).

Saturn's icy moon Dione may have a subsurface liquid water ocean.

## ICY MOONS

### Does Dione have a liquid water ocean?

Several icy moons orbiting the giant planets have oceans of liquid water beneath their solid ice surfaces. It has been suggested that Dione, the fourth largest moon of Saturn, could have a similar subsurface ocean. Zannoni *et al.* analyzed radio-tracking data taken when the Cassini spacecraft (named after the astronomer who discovered Dione in 1684) flew past the moon on three occasions

between 2011 and 2015. They reconstructed Dione's gravity field, combined it with measurements of topography, and then matched the geophysical properties with models of the interior structure. Their analysis supports the interpretation that Dione has a small, deep, subsurface liquid ocean, but they caution that the models are not fully constrained. —KTS

*Icarus* **345**, 113713 (2020).



## REVIEW SUMMARY

## MICROBIOLOGY

## Sharing vitamins: Cobamides unveil microbial interactions

Olga M. Sokolovskaya\*, Amanda N. Shelton\*, Michiko E. Taga†

**BACKGROUND:** Nearly every plant, animal, and environment on earth is host to a diverse community of microorganisms that influence each other and their environment. Microorganisms within communities interact on a molecular level by competing for resources or sharing valuable nutrients (such as cobamides, which we highlight in this Review). Such molecular interactions influence the physiology of individual microorganisms as well as the overall function of communities. Therefore, studying how microbes interact with each other is essential for understanding, and potentially interfering with, microbial processes that influence human and environmental health.

Cobamides are structurally diverse, cobalt-containing cofactors, the most familiar of which

is vitamin B<sub>12</sub> (also known as cobalamin). Since the initial discovery of vitamin B<sub>12</sub> as the treatment for the disease pernicious anemia in 1948, microbiologists have identified more than a dozen cobamides—B<sub>12</sub> and analogs—that are produced exclusively by bacteria and archaea. Although vitamin B<sub>12</sub> is most widely appreciated for its role in human health, B<sub>12</sub> and other cobamides also play important roles in the context of microbial communities. Microbes use cobamides as catalysts for chemical reactions involved in amino acid synthesis, carbon metabolism, and many other functions. Importantly, microorganisms in all domains of life need cobamides, but most depend on surrounding species to produce this nutrient, which results in a network of cobamide-

dependent interactions. A nuance of these interactions, derived from the structural diversity of cobamides, is that organisms are selective toward particular cobamides, and different species have distinct cobamide preferences. As

## ON OUR WEBSITE

Read the full article at <https://dx.doi.org/10.1126/science.aba0165>

a result, cobamides mediate specific associations among microorganisms and can have substantially different effects on the growth and metabolism of different species.

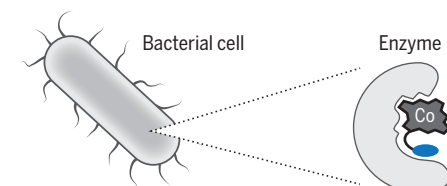
Therefore, cobamide sharing can serve as a model for the complexity of microbial interactions and provide a useful system to study the mechanisms that influence community composition and function.

**ADVANCES:** Our current understanding of the roles of cobamides in microbial communities is the result of multilayered approaches to studying cobamide biology. Historically, the differential effects of cobamides have been investigated using laboratory cultures of single species and the biochemical characterization of cobamide-dependent enzymes. However, it is only with comparative genomic analyses of thousands of microbial species that researchers have begun to fully recognize the prevalence of cobamide sharing among microorganisms. Several newly described cocultures of two to three microbial species bridge molecular analysis and community-wide studies, and these cocultures provide experimental systems for probing the mechanisms and dynamics of cobamide sharing. Integrating discoveries across these different scales of analysis is a valuable strategy for understanding the functions of important molecules in microbial communities.

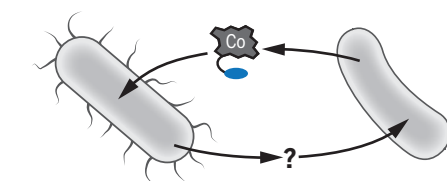
**OUTLOOK:** The structural diversity, functional specificity, and widespread use of cobamides by microorganisms have led researchers to speculate that cobamides could be used as tools to manipulate microbial community composition and function to improve environmental or human health. Performing cobamide-based manipulations in a controlled manner requires a greater understanding of how specific cobamides affect particular members of a community or might disrupt existing microbial interactions. Further integrating molecular approaches with community-wide studies will pave the way for understanding complex microbial communities in increasing mechanistic detail and may enable potential applications of cobamides in human health, agriculture, and industrial production. ■

## Scales of analysis

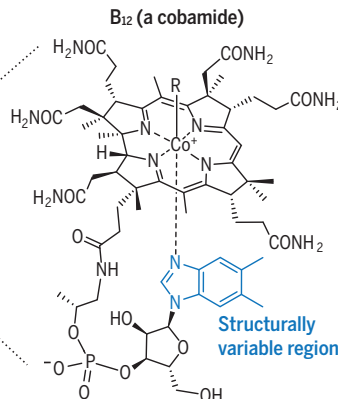
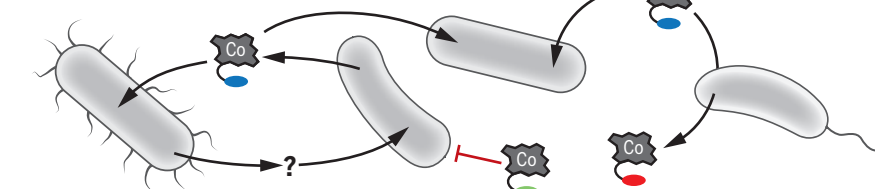
## Isolates and biochemistry



## Cocultures



## Communities



**Cobamides as models for studying microbial interactions.** Cobamides are a class of enzyme cofactors that are used for a wide variety of metabolic functions. They contain a catalytic upper ligand (R) and a structurally variable region (shown in blue, red, or green) that influences organisms' metabolism and growth. Studies of cobamide biology on multiple scales—from enzymes to microbial communities—have revealed that cobamides constitute an effective model system for studying the complexity of microbial interactions.

Department of Plant & Microbial Biology, University of California, Berkeley, Berkeley, CA, USA.

\*These authors contributed equally to this work.

†Corresponding author. Email: [taga@berkeley.edu](mailto:taga@berkeley.edu)

Cite this article as O. M. Sokolovskaya et al., *Science* 369, eaba0165 (2020). DOI: 10.1126/science.aba0165

## RESEARCH ARTICLE SUMMARY

## CANCER

# Feasibility of blood testing combined with PET-CT to screen for cancer and guide intervention

Anne Marie Lennon\*, Adam H. Buchanan\*, Isaac Kinde\*, Andrew Warren\*, Ashley Honushefsky\*, Ariella T. Cohain, David H. Ledbetter, Fred Sanfilippo, Kathleen Sheridan, Dillenia Rosica, Christian S. Adonizio, Hee Jung Hwang, Kamel Lahouel, Joshua D. Cohen, Christopher Douville, Aalpen A. Patel, Leonardo N. Hagmann, David D. Rolston, Nirav Malani, Shibin Zhou, Chetan Bettegowda, David L. Diehl, Bobbi Urban, Christopher D. Still, Lisa Kann, Julie I. Woods, Zachary M. Salvati, Joseph Vadakara, Rosemary Leeming, Prianka Bhattacharya, Carroll Walter, Alex Parker, Christoph Lengauer, Alison Klein, Cristian Tomasetti, Elliot K. Fishman, Ralph H. Hruban, Kenneth W. Kinzler†, Bert Vogelstein†, Nickolas Papadopoulos†

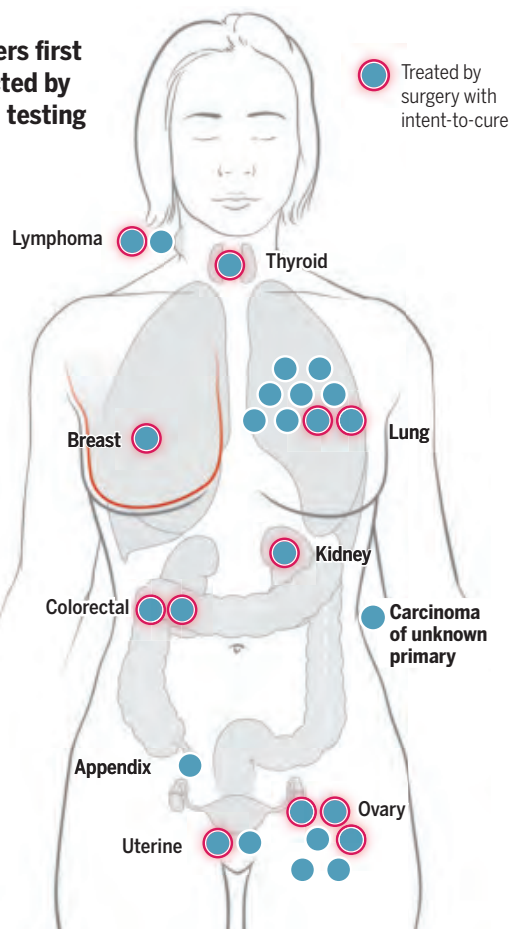
**INTRODUCTION:** The goal of earlier cancer detection is to identify the disease at a stage when it can be effectively treated, thereby offering the patient a better chance of long-term survival. Adherence to screening modalities known to decrease cancer mortality such as colonoscopy, mammography, low-dose computed tomography, and Pap smears varies widely. Moreover, the majority of cancer types are diagnosed only when symptoms occur. Multicancer blood tests offer the exciting possibility of detecting many cancer types at a relatively early stage and in a minimally invasive manner.

**RATIONALE:** Evaluation of the feasibility and safety of multicancer blood testing requires prospective interventional studies. We designed such a study to answer four critical questions: (i) Can a multicancer blood test detect cancers not previously detected by other means? (ii) Can a positive test result lead to surgical intervention with curative intent? (iii) Can testing be incorporated into routine clinical care and not discourage patients from undergoing recommended screening tests such as mammography? (iv) Can testing be performed safely, without incurring a large number of unnecessary, invasive follow-up tests?

**RESULTS:** We evaluated a blood test that detects DNA mutations and protein biomarkers of cancer in a prospective, interventional study of 10,006 women who were 65 to 75 years old and who had no prior history of cancer. Positive blood tests were followed by diagnostic positron emission tomography-computed tomography (PET-CT), which served to indepen-

dently confirm and precisely localize the site and extent of disease if present. The study design incorporated several features to maximize the safety of testing to the participants.

## Cancers first detected by blood testing



**Overview of cancers detected by blood testing.** Twenty-six cancers (blue dots) in 10 organs were first detected by blood testing. The blue dots with the red halo represent 12 of the 26 cancers that were surgically treated with intent to cure. Nine of these 12 were detected by the combination of the blood test and PET-CT, with the remaining three identified by the blood test combined with another imaging modality.

Of the 10,006 enrollees, 9911 (99.1%) could be assessed with respect to the four questions posed above. (i) Detection: Of 96 cancers incident during the study period, 26 were first detected by blood testing and 24 additional cancers by conventional screening. Fifteen of the 26 patients in whom cancer was first detected by blood testing underwent PET-CT imaging, and 11 patients developed signs or symptoms of cancer after the blood test that led to imaging procedures other than PET-CT. The specificity and positive predictive value (PPV) of blood testing alone were 98.9% and 19.4%, respectively, and combined with PET-CT, the specificity and PPV increased to 99.6% and 28.3%. The blood test first

detected 14 of 45 cancers (31%) in seven organs for which no standard-of-care screening test is available. (ii) Intervention: Of the 26 cancers first detected by blood testing, 17 (65%) had localized or regional disease. Of the 15 participants with positive blood tests as well as positive PET-CT scans, 9 (60%) underwent surgery with curative intent. (iii) Incorporation into clinical care: Blood testing could be combined with conventional screening, leading to detection of more than half of the total incident cancers observed during the study period. Blood testing did not deter participants from undergoing mammography, and surveys revealed that 99% of participants would join a similar, subsequent study if offered. (iv) Safety: 99% of participants did not require any follow-up of blood testing results, and only 0.22% underwent an unnecessary invasive diagnostic procedure as a result of a false-positive blood test.

**CONCLUSION:** A minimally invasive blood test in combination with PET-CT can safely detect and precisely localize several types of cancers in individuals not previously known to have cancer, in some cases enabling treatment with intent to cure. Further studies will be required to assess the clinical utility, risk-benefit ratio, and cost-effectiveness of such testing. ■

The list of author affiliations is available in the full article online.

\*These authors contributed equally to this work.

†Corresponding author. Email: npapado1@jhmi.edu (N.P.); vogelbe@jhmi.edu (B.V.); kinzke@jhmi.edu (K.W.K.)

Cite this article as A. M. Lennon *et al.*, *Science* 369, eabb9601 (2020). DOI: 10.1126/science.abb9601



## RESEARCH ARTICLES

## CORONAVIRUS

## SARS-CoV-2 productively infects human gut enterocytes

Mart M. Lamers<sup>1\*</sup>, Joep Beumer<sup>2\*</sup>, Jelte van der Vaart<sup>2\*</sup>, Kèvin Knoops<sup>3</sup>, Jens Puschhof<sup>2</sup>, Tim I. Breugem<sup>1</sup>, Raimond B. G. Ravelli<sup>3</sup>, J. Paul van Schayck<sup>3</sup>, Anna Z. Mykityn<sup>1</sup>, Hans Q. Duimel<sup>3</sup>, Elly van Donselaar<sup>3</sup>, Samra Riesebosch<sup>1</sup>, Helma J. H. Kuijpers<sup>3</sup>, Debby Schipper<sup>1</sup>, Willine J. van de Wetering<sup>3</sup>, Miranda de Graaf<sup>1</sup>, Marion Koopmans<sup>1</sup>, Edwin Cuppen<sup>4,5</sup>, Peter J. Peters<sup>3</sup>, Bart L. Haagmans<sup>1†</sup>, Hans Clevers<sup>2†‡</sup>

Severe acute respiratory syndrome coronavirus 2 (SARS-CoV-2) can cause coronavirus disease 2019 (COVID-19), an influenza-like disease that is primarily thought to infect the lungs with transmission through the respiratory route. However, clinical evidence suggests that the intestine may present another viral target organ. Indeed, the SARS-CoV-2 receptor angiotensin-converting enzyme 2 (ACE2) is highly expressed on differentiated enterocytes. In human small intestinal organoids (hSIOs), enterocytes were readily infected by SARS-CoV and SARS-CoV-2, as demonstrated by confocal and electron microscopy. Enterocytes produced infectious viral particles, whereas messenger RNA expression analysis of hSIOs revealed induction of a generic viral response program. Therefore, the intestinal epithelium supports SARS-CoV-2 replication, and hSIOs serve as an experimental model for coronavirus infection and biology.

Severe acute respiratory syndrome (SARS), caused by the coronavirus SARS-CoV, emerged in 2003 (1). In late 2019, a novel transmissible coronavirus, SARS-coronavirus 2 (SARS-CoV-2), was noted to cause an influenza-like disease ranging from mild respiratory symptoms to severe lung injury, multiorgan failure, and death (2–4). SARS-CoV and SARS-CoV-2 belong to the *Sarbecovirus* subgenus of the genus *Betacoronavirus* in the family Coronaviridae (5–7). The SARS-CoV receptor is angiotensin-converting enzyme 2 (ACE2) (8, 9). The spike proteins of both viruses bind to ACE2, whereas soluble ACE2 blocks infection by SARS-CoV and SARS-CoV-2 (10–13). Transmission of SARS-CoV-2 is thought to occur through respiratory droplets and fomites. The virus can be detected in upper respiratory tract samples, implicating the nasopharynx as a site of replication. In human lung, ACE2 is expressed mainly in alveolar epithelial type II cells and ciliated cells (14–16). However, the highest expression of ACE2 in the human body occurs in the brush border of intestinal enterocytes (14, 17). Even though respiratory symptoms dominate the clinical presentation of

COVID-19, gastrointestinal symptoms are observed in a subset of patients (18, 19). Moreover, viral RNA can be found in rectal swabs even after nasopharyngeal testing has turned negative, implying gastrointestinal infection and a fecal–oral transmission route (20–22).

## SARS-CoV-2 infects airway and gut organoids

Organoids are three-dimensional (3D) structures that can be grown from adult stem cells and recapitulate key aspects of the organ from which those cells derive. Because SARS-CoV and SARS-CoV-2 target the lung, we added virus to organoid-derived human airway epithelium cultured in 2D and observed that SARS-

CoV and SARS-CoV-2 readily infected differentiated airway cultures. (Fig. 1A). Immunostaining reveal that the viruses targeted ciliated cells but not goblet cells (Fig. 1, B and C).

Human small intestinal organoids (hSIOs) are established from primary gut epithelial stem cells, can be expanded indefinitely in 3D culture, and contain all proliferative and differentiated cell types of the in vivo epithelium (23). hSIOs have also allowed the first in vitro culturing of norovirus (24). We exposed ileal hSIOs grown under four different culture conditions (EXP, DIF, DIF-BMP, and EEC) to SARS-CoV and SARS-CoV-2 at a multiplicity of infection of 1. hSIOs grown in Wnt high-expansion (EXP) medium overwhelmingly consisted of stem cells and enterocyte progenitors. Organoids grown in differentiation (DIF) medium contained enterocytes, goblet cells, and low numbers of enteroendocrine cells (EECs). The addition of BMP2/4 to DIF medium (DIF-BMP medium) led to further maturation (25). In the final condition (EEC), we induced the expression of NeuroG3 from a stably transfected vector with doxycycline to raise EEC numbers (fig. S3D). Samples were harvested at multiple time points after infection and processed for the analyses shown in Figs. 2 to 5. Both SARS-CoV and SARS-CoV-2 productively infected hSIOs, as assessed by quantitative reverse transcription polymerase chain reaction (qRT-PCR) for viral sequences and by live virus titrations on VeroE6 cells (see Fig. 2 for lysed organoids and fig. S1 for organoid supernatant). Infectious virus particles and viral RNA increased for both viruses in all conditions. Because EXP medium supported virus replication (Fig. 2, A and E), enterocyte progenitors appeared to be a primary viral target. Differentiated organoids (grown in DIF and DIF-BMP medium) produced slightly (nonstatistically significant) lower levels of

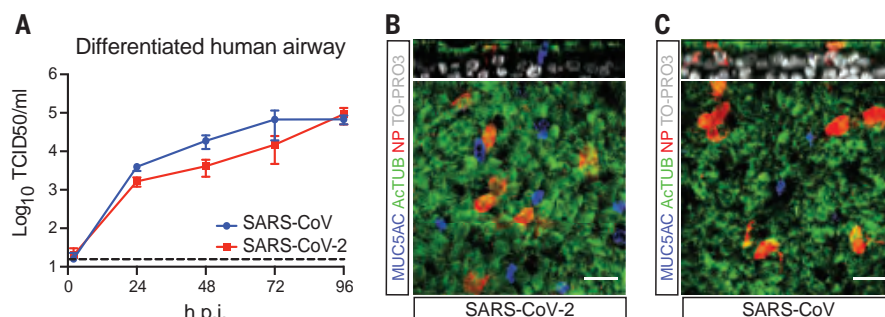


**Fig. 1. SARS-CoV and SARS-CoV-2 infect 2D human airway cultures.** (A) Live virus titers can be observed by virus titrations on VeroE6 cells of apical washes at 2, 24, 48, 72, and 96 h after infection with SARS-CoV (blue) and SARS-CoV-2 (red). The dotted line indicates the lower limit of detection. Error bars indicate SEM.  $N = 4$ . \* $P < 0.05$ , \*\* $P < 0.01$ , \*\*\* $P < 0.001$ . (B and C) Immunofluorescent staining of SARS-CoV-2-infected (B) and SARS-CoV-infected (C) differentiated airway cultures. Nucleoprotein (NP) stains viral nucleocapsid (red), which colocalized with the ciliated cell marker ActTUB (green). Goblet cells are identified by MUC5AC (blue). Nuclei are stained with TO-PRO3 (white). Scale bars, 20  $\mu$ m. Top panels are side views and bottom panels are top views.

<sup>1</sup>Viroscience Department, Erasmus Medical Center, Rotterdam, Netherlands. <sup>2</sup>Oncode Institute, Hubrecht Institute, Royal Netherlands Academy of Arts and Sciences and University Medical Center, Utrecht, Netherlands. <sup>3</sup>The Maastricht Multimodal Molecular Imaging Institute, Maastricht University, Maastricht, Netherlands. <sup>4</sup>Center for Molecular Medicine and Oncode Institute, University Medical Centre Utrecht, Utrecht, Netherlands. <sup>5</sup>Hartwig Medical Foundation, Amsterdam, Netherlands.

\*These authors contributed equally to this work.

†These authors contributed equally to this work.

‡Corresponding author. Email: h.clevers@hubrecht.eu (H.C.); b.haagmans@erasmusmc.nl (B.L.H.)

infectious virus (Fig. 2 and fig. S1). In organoids induced to generate EECs, virus yields were similar to those in EXP medium (Fig. 2, D and H). In differentiated hSIOs, SARS-CoV-2 titers remained stable at 60 hours after infection, whereas SARS-CoV titers dropped by 1 to 2 log (Fig. 2, B, C, F, and G). The latter decline was not observed in infected hSIOs grown in EXP medium. Culture supernatants across culture conditions contained lower levels of infectious virus compared with lysed hSIOs, implying that virus was primarily secreted apically (fig. S1, A to D). Despite this, viral RNA was detected readily in culture supernatants, correlating with the infectious virus levels within hSIOs (Fig. 2, E to H, and fig. S1, E to H).

ACE2 mRNA expression differed greatly between the four conditions. EXP-hSIOs expressed

300-fold less ACE2 mRNA compared with DIF-hSIOs when analyzed in bulk (fig. S2). BMP treatment induced 6.5-fold up-regulation of ACE2 mRNA compared with DIF treatment alone. Because this did not yield infection rate differences, the DIF-BMP condition was not analyzed further.

### SARS-CoV-2 infects enterocyte lineage cells

To determine the target cell type, we then performed confocal analysis on hSIOs cultured in EXP, DIF, or EEC conditions. We stained for viral double-stranded RNA (dsRNA), viral nucleocapsid protein, KI67 to visualize proliferative cells, actin (using phalloidin) to visualize enterocyte brush borders, and DNA (DAPI) and cleaved caspase 3 to visualize apoptotic cells. Generally, comparable rates of viral in-

fections were observed in the organoids growing in all three conditions. We typically noted staining for viral components (white) in rare, single cells at 24 hours. At 60 hours, the number of infected cells had substantially increased (Fig. 3A). Infected cells invariably displayed proliferative enterocyte progenitor phenotypes (EXP; Fig. 3B, top) or ApoA1<sup>+</sup> enterocyte phenotypes (DIF; Fig. 3B, bottom). SARS-CoV also readily infected enterocyte lineage cells (fig. S3, A and B), as was shown previously (26, 27). Some infected enterocyte progenitors were in mitosis (fig. S3C). Whereas EEC organoids produced appreciable titers, we never observed infection of chromogranin-A<sup>+</sup> EECs (fig. S3, D and E). We also did not observe infection of goblet cells across culture conditions. At 60 hours, apoptosis became prominent in both

**Fig. 2. SARS-CoV and SARS-CoV-2 replicate in hSIOs.** (A to D) Live virus titers can be observed by virus titrations on VeroE6 cells of lysed organoids at 2, 24, 48, and 60 h after infection with SARS-CoV (blue) and SARS-CoV-2 (red). Different medium compositions show similar results. (E to H) qRT-PCR analysis targeting the E gene of similar time points and medium compositions as (A) to (D). The dotted line indicates the lower limit of detection. Error bars indicate SEM.  $N = 3$ . \* $P < 0.05$ , \*\* $P < 0.01$ , \*\*\* $P < 0.001$ .

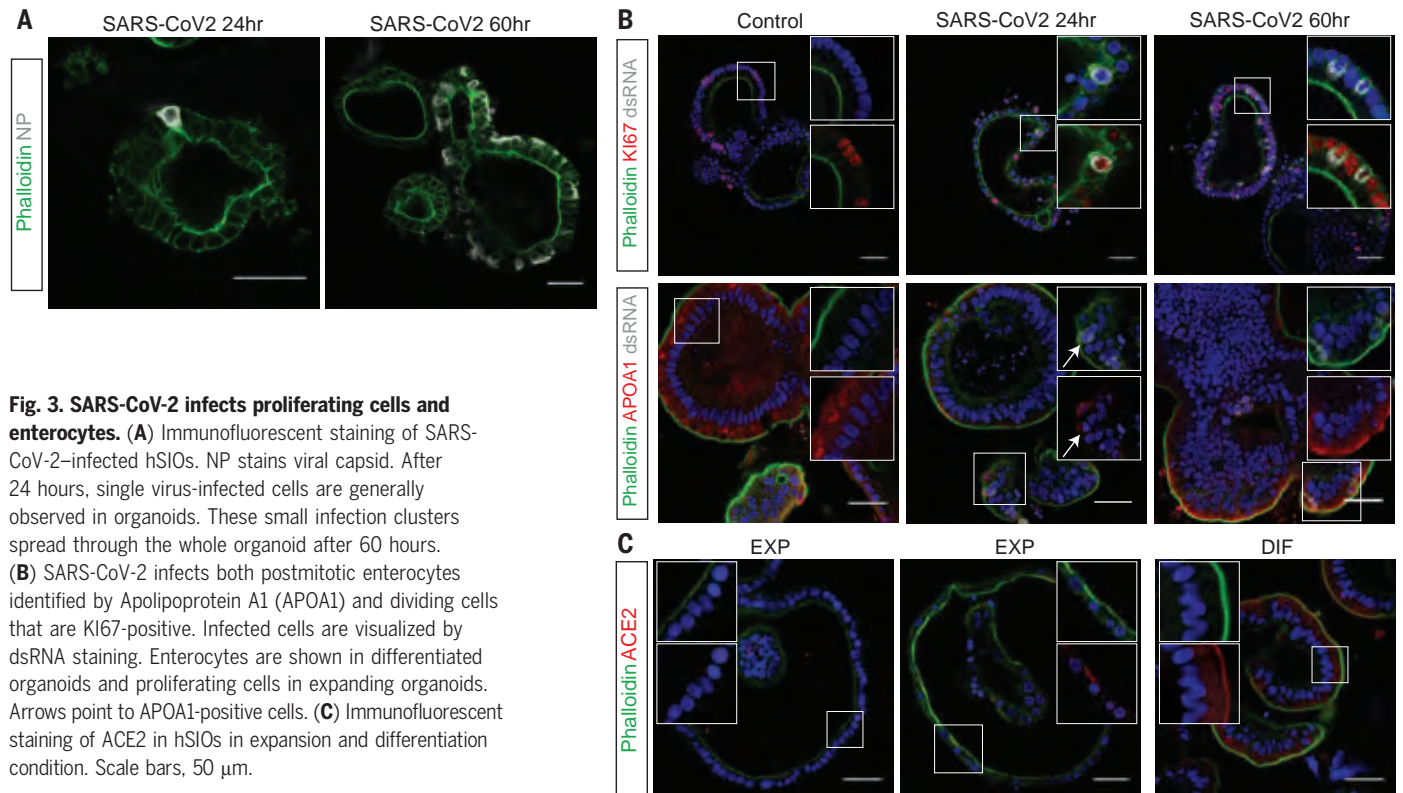
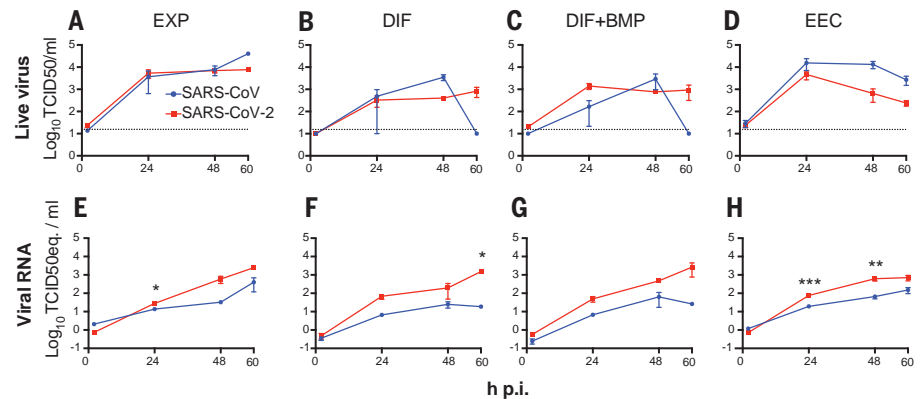
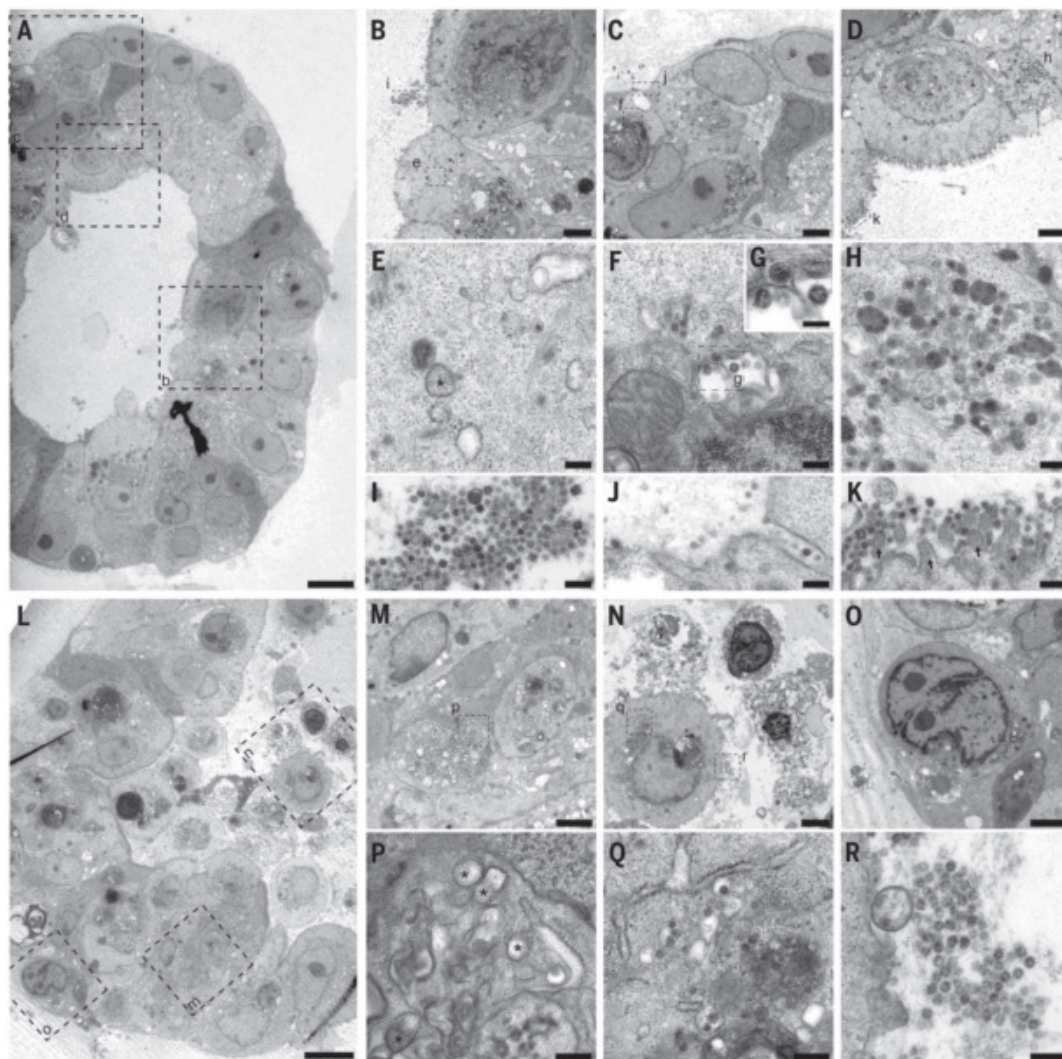


**Fig. 3. SARS-CoV-2 infects proliferating cells and enterocytes.** (A) Immunofluorescent staining of SARS-CoV-2-infected hSIOs. NP stains viral capsid. After 24 hours, single virus-infected cells are generally observed in organoids. These small infection clusters spread through the whole organoid after 60 hours. (B) SARS-CoV-2 infects both postmitotic enterocytes identified by Apolipoprotein A1 (APOA1) and dividing cells that are KI67-positive. Infected cells are visualized by dsRNA staining. Enterocytes are shown in differentiated organoids and proliferating cells in expanding organoids. Arrows point to APOA1-positive cells. (C) Immunofluorescent staining of ACE2 in hSIOs in expansion and differentiation condition. Scale bars, 50  $\mu$ m.



**Fig. 4. Transmission electron microscopy analysis of SARS-CoV-2-infected intestinal organoids.** (A to H) Overview of an intact organoid (A) showing the onset of virus infection [(B) to (D)] at different stages of the viral lifecycle, i.e., early double membrane vesicles (DMVs) [(E), asterisk], initial viral production in the Golgi apparatus [(F) and (G)], and complete occupation of virus particles inside the endomembrane system (H). (I to K) Extracellular viruses are observed in the lumen of the organoid (I) and are found at the basal side (J) and the apical side (K) alongside the microvilli (arrows). Scale bars, 10  $\mu$ m (A), 2.5  $\mu$ m [(B) to (D)], 250 nm [(E), (F), and (H) to (K)] and 100 nm (G). (L to Q) Overview of an organoid (L) showing severely infected cells [(M) and (O)], disintegrated cells (O), and stressed cells as evident from the atypical nucleoli (P). Intact cells reveal DMV areas of viral replication [(P), asterisks] and infected Golgi apparatus (Q). (R) Extracellular clusters of viruses. Scale bars, 10  $\mu$ m (L), 2.5  $\mu$ m [(M) to (P)], and 250 nm [(P) to (R)].



SARS-CoV- and SARS-CoV-2-infected enterocytes (fig. S5). ACE2 protein was readily revealed as a bright and ubiquitous brush border marker in hSIOs in DIF medium (Fig. 3C). In hSIOs in EXP medium, ACE2 staining was much lower, yet still apical, in occasional cells in a subset of organoids that displayed a more mature morphology (Fig. 3C). In immature (cystic) organoids within the same cultures, the ACE2 signal was below the detection threshold. The percentages of infected organoids under EXP and DIF conditions are given in fig. S4. Figure S5 shows images and quantification of apoptotic cells upon infection.

#### Ultrastructural analysis of the viral life cycle in enterocytes

Unsupervised transmission electron microscopy (28) was performed on selected highly infected samples. Figure 4 shows two hSIOs selected from 42 hSIOs imaged at 60 hours after SARS-CoV-2 infection. These differ in the state of infection: Whereas the cellular organization within organoid 1 was still intact

(Fig. 4A, entire organoid; B to D, intermediate magnification; E to K, high magnification), many disintegrated cells can be seen in organoid 2 (Fig. 4, bottom; L, entire organoid; M to O, intermediate magnification; P to R, high magnification). Viral particles of 80 to 20 nm occurred in the lumen of the organoid (Fig. 4I) at the basolateral (Fig. 4J) and apical side (Fig. 4K) of enterocytes. Double-membrane vesicles, which are the subcellular site of viral replication (29), are visualized in Fig. 4, E and P. The nuclei in both organoids differed from nuclei in mock-infected organoids by having a slightly rounder shape. Other differences were that the nuclear contour index (30) was  $4.0 \pm 0.5$  versus  $4.3 \pm 0.5$  for the control set, and there was more heterochromatin (Fig. 4N) and one or two dense nucleoli in the center (Fig. 4O).

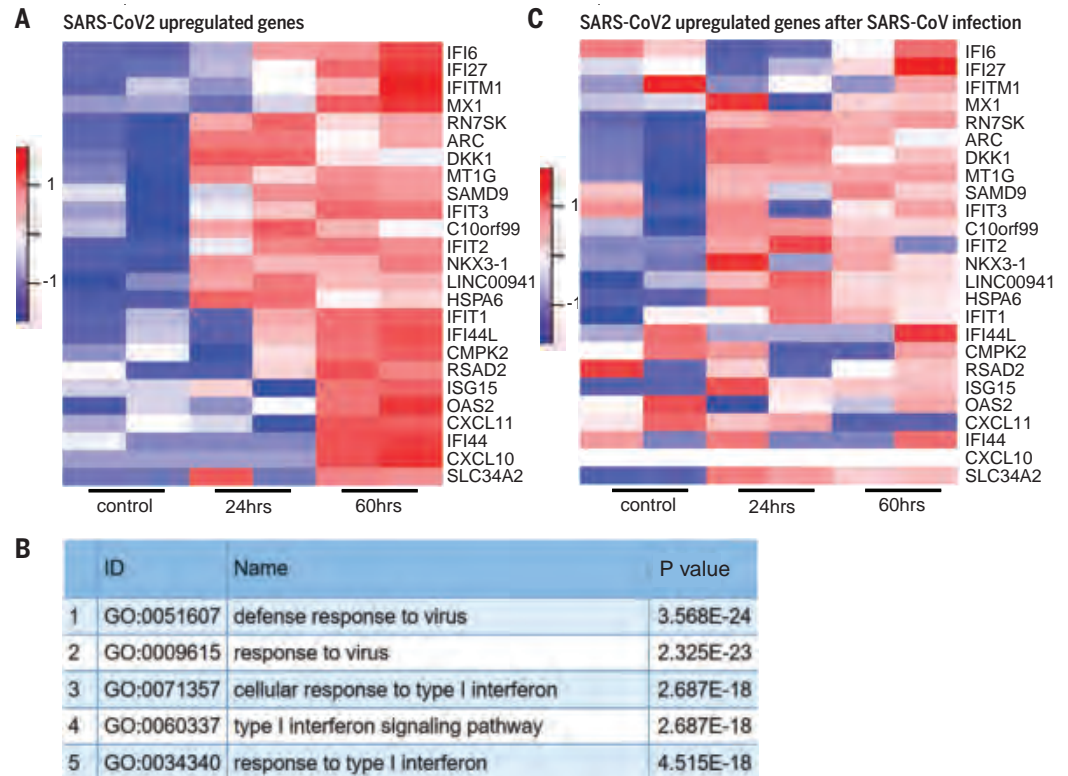
#### RNA expression changes in infected enterocytes

We then performed mRNA-sequencing analysis to determine gene expression changes induced by SARS-CoV and SARS-CoV-2-infection of

hSIOs cultured continuously in EXP medium and hSIOs cultured in DIF medium. Infection with SARS-CoV-2 elicited a broad signature of cytokines and interferon (IFN)-stimulated genes (ISGs) attributed to type I and III IFN responses (Fig. 5A and tables S1 and S2), as confirmed by gene ontology analysis (Fig. 5B). An overlapping list of genes appeared in SARS-CoV-2-infected DIF organoids (fig. S6 and table S3). mRNA-sequencing analysis confirmed differentiation of DIF organoids into multiple intestinal lineages, including ACE2 up-regulation (fig. S7). SARS-CoV also induced ISGs but to a much lower level (table S4). Figure 5C shows the regulation of SARS-CoV-2-induced genes in SARS-CoV-infected organoids. This induction was similar to infections with other viruses such as norovirus (31), rotavirus (32), and enteroviruses (33, 34). A recent study (35) described an antiviral signature induced in human cell lines after SARS-CoV-2 infection. Whereas the ISG response was broader in hSIOs, the induced gene sets were in close agreement between the two datasets (fig. S8).

**Fig. 5. Transcriptomic analysis of SARS-CoV-2-infected intestinal organoids.**

(A) Heatmaps depicting the 25 most significantly enriched genes upon SARS-CoV-2 infection in expanding intestinal organoids. (B) Colored bar represents the Z-score of log<sub>2</sub>-transformed values. Shown is the gene ontology term enrichment analysis for biological processes of the 50 most significantly up-regulated genes upon SARS-CoV-2 infection in intestinal organoids. (C) Heatmaps depicting the genes from (A) in SARS-CoV-infected expanding organoids. Colored bar represents the Z-score of log<sub>2</sub>-transformed values.



One obvious similarity was the low expression of type I and III IFNs: We only noticed a small induction of the type III IFN IFNL1 in SARS-CoV-2-infected organoids. In SARS-CoV-infected organoids, we did not observe any type I or type III IFN induction. We confirmed these findings by enzyme-linked immunosorbent assay (ELISA) on the culture supernatant and qRT-PCR on extracted RNA of the hSIOs, which in addition to IFNL1, picked up low levels of type I IFN IFNB1 in SARS-CoV-2- but not in SARS-CoV-infected organoids (fig. S9). The specific induction of IP-10/CXCL10 and ISG15 by SARS-CoV-2 was also confirmed by ELISA and qRT-PCR, respectively (fig. S10). As in a previous study (35), a few cytokine genes were induced by both viruses, albeit to modest levels. For a comparison with (35), see fig. S11. Altogether, these data indicate that SARS-CoV-2 induces a stronger IFN response than SARS-CoV in hSIOs.

Finally, the infection was repeated in a second experiment in the same ileal hSIO line and analyzed after 72 hours. Analysis involved viral titration (fig. S12), confocal imaging (fig. S13), and mRNA sequencing (fig. S14). This experiment essentially confirmed the observations presented above. A limited, qualitative experiment applying confocal analysis demonstrated the infectability of two other lines available in the laboratory (one ileal and one duodenal) from independent donors (fig. S13). This study shows that SARS-CoV and SARS-CoV-2 infect enterocyte lineage cells in an

hSIO model. We observed similar infection rates of enterocyte precursors and enterocytes, whereas ACE2 expression increased ~1000-fold upon differentiation at the mRNA level (fig. S2). This suggests that low levels of ACE2 may be sufficient for viral entry.

SARS-CoV-2 is the third highly pathogenic coronavirus (after SARS-CoV and MERS-CoV) to jump to humans within <20 years, suggesting that new zoonotic coronavirus spillovers are likely to occur in the future. Despite this, limited information is available on coronavirus pathogenesis and transmission, in part because of the lack of in vitro cell models that accurately model host tissues. Very recently, it was shown that human induced pluripotent stem cells differentiated toward a kidney fate supported replication of SARS-CoV-2 (13). Our data suggest that human organoids represent faithful experimental models with which to study the biology of coronaviruses.

#### REFERENCES AND NOTES

- C. Drosten et al., *N. Engl. J. Med.* **348**, 1967–1976 (2003).
- W. J. Guan et al., *N. Engl. J. Med.* **382**, 1708–1720 (2020).
- S. Jiang, L. Du, Z. Shi, *Emerg. Microbes Infect.* **9**, 275–277 (2020).
- N. Zhu et al., *N. Engl. J. Med.* **382**, 727–733 (2020).
- K. G. Andersen, A. Rambaut, W. I. Lipkin, E. C. Holmes, R. F. Garry, *Nat. Med.* **26**, 450–452 (2020).
- R. Lu et al., *Lancet* **395**, 565–574 (2020).
- A. E. Gorbalenya et al., *Nat. Microbiol.* **5**, 536–544 (2020).
- Y. Imai et al., *Nature* **436**, 112–116 (2005).
- K. Kuba et al., *Nat. Med.* **11**, 875–879 (2005).
- A. C. Walls et al., *Cell* **181**, 281–292.e6 (2020).
- Y. Wan, J. Shang, R. Graham, R. S. Baric, F. Li, *J. Virol.* **94**, e00127–20 (2020).

- D. Wrapp et al., *Science* **367**, 1260–1263 (2020).
- V. Monteil et al., *Cell* **10.1016/j.cell.2020.04.004** (2020).
- F. Qi, S. Qian, S. Zhang, Z. Zhang, *Biochem. Biophys. Res. Commun.* **526**, 135–140 (2020).
- Y. Zhao, Z. Zhao, Y. Wang, Y. Zhou, Y. Ma, W. Zuo, Single-cell RNA expression profiling of ACE2, the receptor of SARS-CoV-2. *bioRxiv* 2020.01.26.919985 [Preprint]. 9 April 2020. <https://doi.org/10.1101/2020.01.26.919985>.
- H. P. Jia et al., *J. Virol.* **79**, 14614–14621 (2005).
- The Human Protein Atlas, ACE2 protein expression summary (2020); <https://www.proteinatlas.org/ENSG00000130234-ACE2>.
- J. Gu, B. Han, J. Wang, *Gastroenterology* **158**, 1518–1519 (2020).
- G. Cholaneril et al., *Gastroenterology* **10.1053/j.gastro.2020.04.008** (2020).
- W. Wang et al., *JAMA* (2020). [10.1001/jama.2020.3786](https://doi.org/10.1001/jama.2020.3786).
- M. L. Holshue et al., *N. Engl. J. Med.* **382**, 929–936 (2020).
- F. Xiao et al., *Gastroenterology* **S0016-5085(20)30282-1** (2020). [10.1053/j.gastro.2020.02.055](https://doi.org/10.1053/j.gastro.2020.02.055).
- T. Sato et al., *Gastroenterology* **141**, 1762–1772 (2011).
- K. Ettayebi et al., *Science* **353**, 1387–1393 (2016).
- J. Beumer et al., *Nat. Cell Biol.* **20**, 909–916 (2018).
- W. K. Leung et al., *Gastroenterology* **125**, 1011–1017 (2003).
- W. S. Chan et al., *Mod. Pathol.* **18**, 1432–1439 (2005).
- F. G. A. Faas et al., *J. Cell Biol.* **198**, 457–469 (2012).
- K. Knoops et al., *PLOS Biol.* **6**, e226 (2008).
- N. S. McNutt, W. R. Crain, *Cancer* **47**, 698–709 (1981).
- M. Hosmillo et al., *mBio* **11**, e00215–20 (2020).
- K. Saxena et al., *Proc. Natl. Acad. Sci. U.S.A.* **114**, E570–E579 (2017).
- C. G. Drummond et al., *Proc. Natl. Acad. Sci. U.S.A.* **114**, 1672–1677 (2017).
- C. Good, A. I. Wells, C. B. Coyne, *Sci. Adv.* **5**, eaau4255 (2019).
- D. Blanco-Melo et al., *Cell* **10.1016/j.cell.2020.04.026** (2020).

#### ACKNOWLEDGMENTS

We thank E. Eenjes and R. Rottier for providing human lung material, A. de Graaff and the Hubrecht Imaging Centre (HIC) for microscopy assistance, Single Cell Discoveries for RNA library preparation, and the Utrecht Sequencing Facility (subsidized by the University Medical Center Utrecht, Hubrecht Institute, Utrecht University and NWO project 184.034.019). **Funding:** This work was supported by ERC Advanced Grant 67013 and by Lung Foundation



Netherlands to H.C. and by NWO Grant 022.005.032. K.K., J.Q.D., P.J.P., and R.B.G.R. received funding from the Dutch Technology Foundation STW (UPON 14207) and from European Union's Horizon 2020 Programme (grant no. 766970 Q-SORT). **Author contributions:** M.L., J.B., and J.V. performed experiments and designed the study. K.K. and J.Q.D. prepared samples. K.K. and R.B.G.R. performed imaging. K.K., J.P.v.S., P.J.P., and R.B.G.R. interpreted results. T.B., A.M., S.R., D.S., and M.G. measured virus titers. J.P. analyzed RNA-sequencing data. E.C. performed sequencing. M.K., B.H., and H.C. supervised the project. **Competing interests:** H.C. is an inventor on patents held by the Royal Netherlands Academy of Arts and Sciences that cover organoid technology (PCT/NL2008/050543, WO2009/022907; PCT/NL2010/000017, WO2010/090513; PCT/IB2011/002167, WO2012/014076; PCT/IB2012/052950, WO2012/168930; PCT/EP2015/060815, WO2015/173425; PCT/EP2015/077990,

WO2016/083613; PCT/EP2015/077988, WO2016/083612; PCT/EP2017/054797, WO2017/149025; PCT/EP2017/065101, WO2017/220586; PCT/EP2018/086716, and GB1819224.5). H.C.'s full disclosure is given at <https://www.uu.nl/staff/JCClevers/>. **Data and materials availability:** Organoid lines may be requested directly from the nonprofit HUB (<https://huborganoids.nl/>), which does not directly benefit from this research. RNA-sequencing data can be accessed through GEO GSE149312. Data were deposited to the Image Data Resource (<https://idr.openmicroscopy.org>) under accession number idr0083. This work is licensed under a Creative Commons Attribution 4.0 International (CC BY 4.0) license, which permits unrestricted use, distribution, and reproduction in any medium, provided the original work is properly cited. To view a copy of this license, visit <https://creativecommons.org/licenses/by/4.0/>. This license does not apply to figures/photos/artwork or other content included in the article that is credited to a third

party; obtain authorization from the rights holder before using such material.

#### SUPPLEMENTARY MATERIALS

[science.sciencemag.org/content/369/6499/50/suppl/DC1](https://science.sciencemag.org/content/369/6499/50/suppl/DC1)  
Materials and Methods  
Figs. S1 to S14  
Tables S1 to S4  
References (36–44)  
MDAR Reproducibility Checklist

9 April 2020; accepted 29 April 2020

Published online 1 May 2020

10.1126/science.abc1669

## CRISPR BIOLOGY

# A phage-encoded anti-CRISPR enables complete evasion of type VI-A CRISPR-Cas immunity

Alexander J. Meeske<sup>1\*</sup>, Ning Jia<sup>2\*</sup>, Alice K. Cassel<sup>1</sup>, Albina Kozlova<sup>1</sup>, Jingqiu Liao<sup>3,4</sup>, Martin Wiedmann<sup>3,4</sup>, Dinshaw J. Patel<sup>2†</sup>, Luciano A. Marraffini<sup>1,5†</sup>

The CRISPR RNA (crRNA)-guided nuclease Cas13 recognizes complementary viral transcripts to trigger the degradation of both host and viral RNA during the type VI CRISPR-Cas antiviral response. However, how viruses can counteract this immunity is not known. We describe a listeriophage ( $\phi$ LS46) encoding an anti-CRISPR protein (AcrVIA1) that inactivates the type VI-A CRISPR system of *Listeria seeligeri*. Using genetics, biochemistry, and structural biology, we found that AcrVIA1 interacts with the guide-exposed face of Cas13a, preventing access to the target RNA and the conformational changes required for nuclease activation. Unlike inhibitors of DNA-cleaving Cas nucleases, which cause limited immunosuppression and require multiple infections to bypass CRISPR defenses, a single dose of AcrVIA1 delivered by an individual virion completely dismantles type VI-A CRISPR-mediated immunity.

**C**RISPR-Cas systems are prokaryotic adaptive immune systems that protect their hosts from invasion by viruses (1) and plasmids (2). CRISPR loci contain short DNA repeats separated by spacer sequences of foreign origin (3–5). To achieve immunity, the locus is transcribed and processed into small CRISPR RNAs (crRNAs), which associate with RNA-guided Cas nucleases (6) to locate and cleave complementary nucleic acid sequences (protospacers) (7). CRISPR systems are categorized into six types (I to VI) that differ in their *cas* gene content and mechanism of immunity (8). Although most types neutralize invaders through destruction of their DNA, Cas13, the RNA-guided nuclease of type VI systems, unleashes nonspecific RNA degradation (*trans*-RNase activity) upon recognition of a phage target transcript (9–11). The cleavage of host transcripts leads to a growth arrest that

prevents further propagation of the phage, allowing the uninfected cells in the population to survive and proliferate (12). Because the phage genome is not directly affected by Cas13, it continues to produce target transcripts, leading to a persistent activation of the nuclease and to growth arrest (12).

## Identification of the Cas13a inhibitor AcrVIA1

Presumably in response to the pressure imposed by CRISPR-Cas immunity, phages evolved anti-CRISPR (Acr) proteins, small proteins (usually <150 amino acids) that are produced during infection and inactivate Cas nucleases (12). Acrs also exhibit exceptional diversity of sequences and mechanisms and, with few exceptions, specifically inhibit one CRISPR subtype (12–17). Recently, inhibitors of Cas13a were independently reported (18); however, how they allow phages to overcome the type VI-A CRISPR-Cas response is not known. To investigate the molecular mechanisms used by Acr-carrying phages to inhibit Cas13 during infection of a natural host, we first obtained temperate phages from a collection of 62 environmental isolates of *Listeria* spp., an organism that commonly harbors type VI-A CRISPR-Cas systems. We induced prophages with mitomycin C and isolated phages that infected a

mutant of *Listeria seeligeri* SLCC3954 (19) lacking its two restriction-modification (RM) systems and the type VI-A CRISPR array (*L. seeligeri*  $\Delta$ RM  $\Delta$ spc; fig. S1A). We isolated 15 phages (fig. S1B), which we used to infect wild-type (WT) *L. seeligeri*, and obtained 10 lysogens carrying different prophages in their genomes (fig. S1C). We then tested each lysogen for its ability to disable Cas13a-mediated immunity against plasmid conjugation (fig. S1D). Only the  $\phi$ LS46 lysogen exhibited a high efficiency of plasmid transfer (Fig. 1A and fig. S1D), suggesting the possibility that this prophage harbors a Cas13a inhibitor.

Sequencing of the  $\phi$ LS46 genome revealed an organization similar to a previously characterized temperate phage of *L. seeligeri*,  $\phi$ RR4 (11), which harbors an anti-CRISPR region containing six genes, two of them with homology to the Cas9 inhibitors AcrIIA1 and AcrIIA2 (fig. S1E). In  $\phi$ LS46, however, this region contains four genes, none of which displayed strong homology to known inhibitors (Fig. 1B and fig. S1E). To investigate whether this region contains a type VI Acr, we cloned the operon with its native promoter into a plasmid (*pgp1-4*), introduced it into WT *L. seeligeri*, and tested for Cas13a-mediated immunity against plasmid conjugation. Indeed, the presence of *pgp1-4* allowed plasmid conjugation even in the presence of Cas13a targeting, and cloning each individual gene allowed us to identify *gp2* as the gene responsible for this anti-CRISPR phenotype (Fig. 1C). Accordingly, we renamed *gp2* “type VI-A anti-CRISPR 1,” or AcrVIA1 (AcrVIA1<sup>Lse</sup> to distinguish from other genes). AcrVIA1 is a protein of 232 amino acids, considerably larger than most previously discovered Acrs. Gp1, AcrVIA1, and Gp4 exhibit no detectable homology to proteins of known function, but we noted that Gp3 contains a helix-turn-helix (HTH) domain with limited similarity to AcrIIA6 from *Streptococcus* phage DT1, suggesting that it may be an inhibitor of type II-A CRISPR-Cas systems. Many listeriophages harbor the HTH-containing AcrIIA1, which serves dual roles as an Acr and as a transcription autorepressor of the *acr* cassette during late lytic infection (20). To test whether Gp3 plays a similar role in

<sup>1</sup>Laboratory of Bacteriology, The Rockefeller University, New York, NY 10065, USA. <sup>2</sup>Structural Biology Program, Memorial Sloan Kettering Cancer Center, New York, NY 10065, USA. <sup>3</sup>Department of Food Science, Cornell University, Ithaca, NY 14853, USA. <sup>4</sup>Graduate Field of Microbiology, Cornell University, Ithaca, NY 14853, USA. <sup>5</sup>Howard Hughes Medical Institute, The Rockefeller University, New York, NY 10065, USA.

\*These authors contributed equally to this work.

†Corresponding author. Email: [marraffini@rockefeller.edu](mailto:marraffini@rockefeller.edu) (L.A.M.); [pateld@mskcc.org](mailto:pateld@mskcc.org) (D.J.P.)

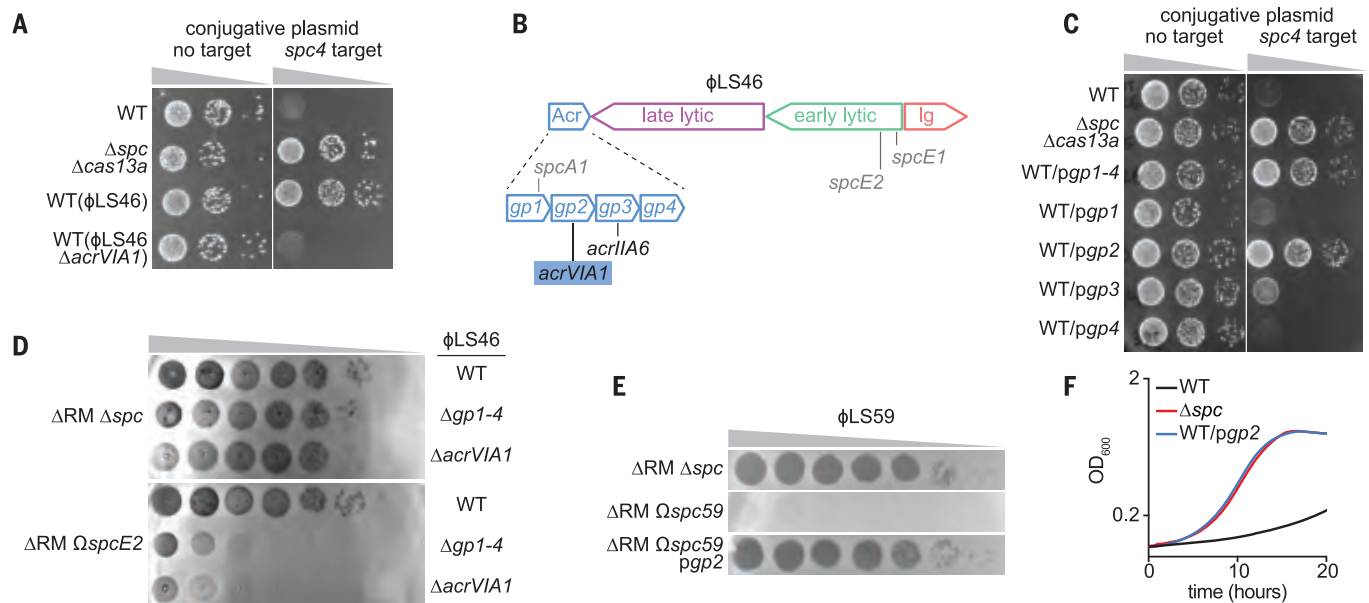


**Fig. 1. AcrVIA1 inhibits type VI-A CRISPR-Cas immunity against plasmids and phages.** (A) Transfer of a conjugative plasmid with or without the *spc4* target of the *L. seeligeri* type VI-A CRISPR-Cas system into different strains: WT,  $\Delta spc \Delta cas13a$ , or WT harboring the  $\phi LS46$  or  $\phi LS46 \Delta acrVIA1$  prophages. (B) Schematic of the  $\phi LS46$  genome showing the four main transcription units (*acr*, lysogeny, and early- and late-lytic genes). *gp2* was renamed *acrVIA1*. The locations of the targets of spacers used in this study are shown in gray. (C) Same

as (A) but using strains carrying plasmids to express different *acr* genes from  $\phi LS46$ . (D) Detection of phage propagation after spotting 10-fold dilutions of WT,  $\Delta gp1-4$ , or  $\Delta acrVIA1$  phage  $\phi LS46$  on lawns of *L. seeligeri*  $\Delta RM \Delta spc$  or  $\Delta RM \Omega spcE2$ . (E) Same as (D) but spotting  $\phi LS59$  into lawns of *L. seeligeri*  $\Delta RM \Delta spc$ ,  $\Delta RM \Omega spc59$ , or  $\Delta RM \Omega spc59/pgp2$ . (F) Growth of WT,  $\Delta spc$ , and WT/*pgp2* *L. seeligeri* strains expressing an *spc4* target RNA under the control of an anhydrotetracycline-inducible promoter after the addition of the inducer.

$\phi LS46$ , we fused the *acrVIA1* promoter to a *lacZ* reporter and measured  $\beta$ -galactosidase activity in the presence and absence of *pgp3* (fig. S2). We observed an ~10-fold reduction in transcription from the *acr* promoter in the presence of *Gp3*, a result that confirmed its role as a regulator of *AcrVIA1* expression.

Next, we investigated whether *AcrVIA1* was necessary for inhibition of *Cas13a* during  $\phi LS46$  infection. We created a derivative of the  $\Delta RM \Delta spc$  strain in which we ectopically integrated different spacer sequences, with their transcription controlled by the native CRISPR promoter (strain  $\Delta RM \Omega spcX$ ; fig. S1A). First, we inserted spacers targeting transcripts of either a conjugative plasmid or phage  $\phi LS59$ , the genome of which lacks *acr* genes, and confirmed that they could provide efficient immunity in this experimental system (fig. S3, A and B). We then cloned 10 spacers targeting different transcript regions of  $\phi LS46$  (fig. S3C), none of which conferred immunity (fig. S3D). Finally, we isolated phage mutants in the *Acr* region of  $\phi LS46$  and tested the same spacers for immunity against them. Although none of the spacers protected against WT  $\phi LS46$ , both the  $\Delta gp1-4$  and  $\Delta acrVIA1$  mutants exhibited one to six orders of magnitude higher sensitivity to *Cas13a* interference compared with a non-targeting control (Fig. 1D and fig. S3D). We expressed *AcrVIA1* using the *pgp2* plasmid and found that it inhibited targeting of the *Cas13a*-susceptible phage  $\phi LS59$  (Fig. 1E). Finally,

the inhibition of antiplasmid immunity observed in the WT( $\phi LS46$ ) lysogen was abolished when we performed the conjugation assay using the WT( $\phi LS46 \Delta acrVIA1$ ) lysogen (Fig. 1A). To explore the effect of *AcrVIA1* on the *Cas13a*-induced host cell dormancy that is fundamental for type VI-A immunity, we induced the expression of *spc4* target RNA, which was previously shown to cause a severe growth defect as a result of nonspecific host transcript degradation (11). Expression of the inhibitor using the *pgp2* plasmid, however, reverted this growth defect (Fig. 1F). Thus, *acrVIA1* is necessary and sufficient to inhibit *Cas13a*-induced growth arrest and thereby thwart type VI CRISPR immunity against plasmids and phages.

#### **AcrVIA1 binds *Cas13a* and inhibits *cis*- and *trans*-RNase activities**

The inhibition of *Cas13a*-induced growth arrest suggested that *AcrVIA1* could inhibit the *trans*-RNase activity of *Cas13a*. To investigate this, we purified both proteins (fig. S4, A and B) and tested their activities using in vitro RNA protospacer cleavage assays. A radiolabeled target RNA was used to investigate inhibition of *Cas13a*'s *cis*-RNase activity. Purified *L. seeligeri* *Cas13a*<sup>crRNA</sup> catalyzed rapid RNA cleavage of protospacer RNA, and this activity was gradually decreased in the presence of increasing concentrations of *AcrVIA1* (Fig. 2, A and B). Similarly, *AcrVIA1* inhibited *Cas13a*-mediated *trans*-cleavage of a labeled nontarget

RNA upon addition of unlabeled protospacer RNA (Fig. 2C). To look for an interaction between the nuclease and its inhibitor, we added C-terminal hexahistidine and 3xFLAG tags to *Cas13a* and *AcrVIA1*, respectively, and confirmed that both were functional in *L. seeligeri* (fig. S4C) and in vitro (Fig. 2, A and C). We expressed *Cas13a*-His6 either alone or in the presence of *AcrVIA1*-3xFLAG and then performed immunoprecipitation with anti-Flag antibody resin. Analysis of the input, unbound, and immunoprecipitated fractions by immunoblot using antibodies against His6, FLAG, and the *L. seeligeri* housekeeping sigma factor  $\sigma^A$  as a control showed a specific coimmunoprecipitation of *Cas13a*-His6 with *AcrVIA1*-3xFLAG (Fig. 2D). Finally, we investigated whether the interaction of *AcrVIA1* with *Cas13a* prevents binding of the *Cas13a*<sup>crRNA</sup> complex to its complementary target RNA. To test this, we performed an electrophoretic mobility shift assay (EMSA) to measure the association of labeled protospacer RNA with a nuclease-dead d*Cas13a*<sup>crRNA</sup> complex (Fig. 2E). In the presence of this complex, most of the target RNA was shifted to multiple higher-molecular-weight species: one corresponding to a crRNA-protospacer RNA duplex and higher species representing the d*Cas13a*<sup>crRNA</sup>-protospacer ternary complex. By contrast, in the presence of equimolar *AcrVIA1*, the target RNA remained mostly unbound and unassociated with d*Cas13a*<sup>crRNA</sup>. Collectively, these results indicate that *AcrVIA1*



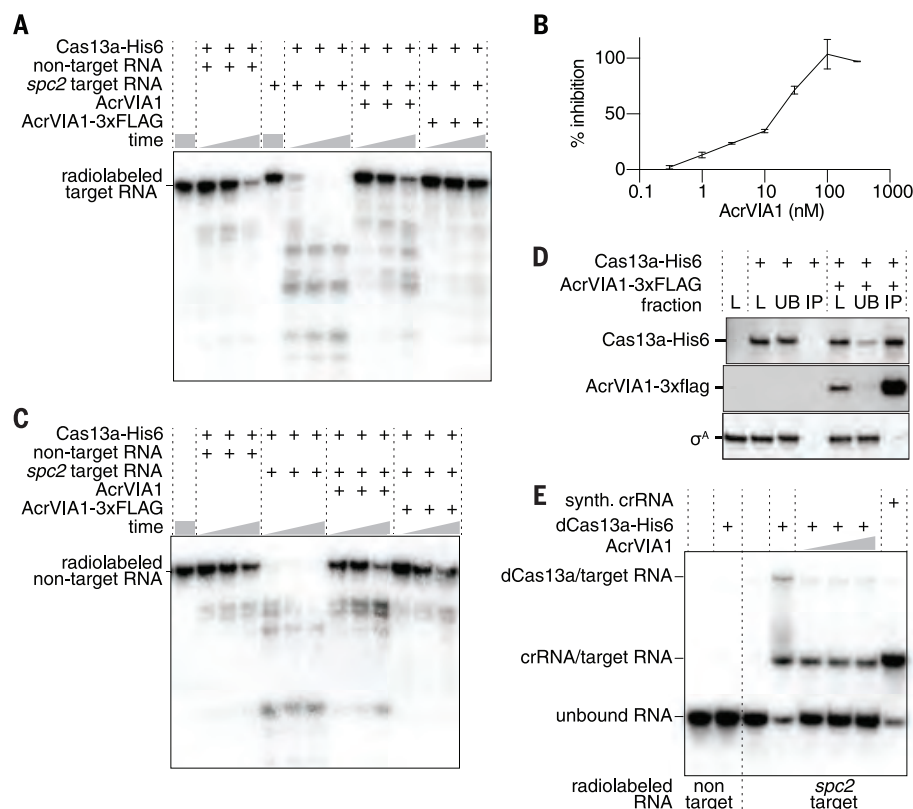


**Fig. 2. AcrVIA1 interacts with Cas13a<sup>crRNA</sup> to prevent binding of the target RNA and RNase activation.** (A) *cis*-RNA cleavage time course with purified *L. seeligeri* Cas13a-His6, AcrVIA1, and/or AcrVIA1-3xFLAG using radiolabeled nontarget or *spc2*-target RNA substrates. Reactions were analyzed after 5, 10, or 20 min of incubation. (B) Dose response of Cas13a *cis*-RNase inhibition by AcrVIA1-3xFLAG. (C) *trans*-RNA cleavage time course as in (A) but using a radiolabeled nontarget RNA substrate in the presence of unlabeled nontarget or *spc2*-target RNA. (D) Anti-FLAG immunoprecipitation using protein extracts from *L. seeligeri* cells expressing either Cas13a-His6 alone or coexpressing AcrVIA1-3xFLAG. The His6 and FLAG epitopes and the  $\sigma^A$  protein were detected by immunoblot. (E) EMSA of radiolabeled nontarget or *spc2*-target RNAs in the presence of dCas13a-His6, with 2:1, 1:1, or 1:2 equivalents of AcrVIA1-3xFLAG.

forms a complex with Cas13a<sup>crRNA</sup> that prevents binding of the complementary target RNA and therefore inhibits both its *cis*- and *trans*-RNase activities.

### Structure of the AcrVIA1-Cas13a<sup>crRNA</sup> complex

To further investigate how AcrVIA1 suppresses Cas13a<sup>crRNA</sup> activity, we isolated a stable homogeneous AcrVIA1-Cas13a<sup>crRNA</sup> complex (fig. S5) and determined its cryo-electron microscopy (cryo-EM) structure, along with that of Cas13a<sup>crRNA</sup> alone, at 3.0- and 3.2-Å resolution, respectively (fig. S6 and table S1). Cas13a<sup>crRNA</sup> adopts a bilobed architecture, consisting of recognition [REC; N-terminal domain (NTD) and Helical-1 domain] and nuclease (NUC; Helical-2 and two HEPN domains connected by a Linker element) lobes (Fig. 3, A and C), similar to previously reported structures of Cas13a from other species (21, 22). The complex contained a natural 51-nucleotide mature crRNA, which was processed and loaded in

the native host (Fig. 3B and fig. S7A). Nucleotides 8 to 12 and 13 to 19 in the crRNA spacer region adopted an approximately A-form helical conformation, with their outward direction positioned to pair with the target RNA (fig. S7B), a feature different from the crRNA alignment in *Leptotrichia buccalis* Cas13a (22). The 5' end of the repeat is located in the cleft between the Helical-1 and HEPN-2 domains (fig. S7A). Mutations in residues within this region of Cas13a (R1048A, K1049A) abrogate type VI interference against plasmid conjugation (fig. S7C), revealing their importance for crRNA maturation.

In the AcrVIA1-Cas13a<sup>crRNA</sup> complex, the inhibitor is positioned on the crRNA-exposed face of Cas13a and directly interacts with the crRNA and residues in the Helical-1, NTD, HEPN-1, and Linker domains of Cas13a (Fig. 3, D to H, and fig. S8, A to D), with a buried interface area of ~1800 Å<sup>2</sup>. There is no structural similarity between AcrVIA1 and other reported structures according to a DALI search (23), indicating

a new fold for this inhibitor. Residues in AcrVIA1 form extensive hydrophobic and hydrophilic interactions with the crRNA, which has been shown previously to undergo large conformational changes, especially at its 3' end, upon target RNA binding to activate Cas13a RNase activity (22). Notably, the 3' end of the crRNA in the AcrVIA1-Cas13a<sup>crRNA</sup> complex is stabilized by hydrogen bonds formed by N43, S40, and S93 and stacking interactions between U21 in crRNA and Y39 and V94 in AcrVIA1 (Fig. 3F), F69 stacks on A17 in the middle spacer region of crRNA (Fig. 3G), and F103 stacks on U27 in the 5' repeat region of crRNA (Fig. 3E). In addition, the acidic loop E131 to E134 in the inhibitor points toward and blocks access to the central C13 to A17 region of the crRNA (Fig. 3G). This region has been shown previously to be critical for target RNA binding and to turn on Cas13a RNase activity (9, 22).

AcrVIA1 also interacts directly with Cas13a, making several intermolecular contacts in the complex. Residues S93, Q96, and I97 in the inhibitor form hydrogen bonds with N259 and K261 in the Helical-1 domain of the nuclease (Fig. 3F), and residue F69 in AcrVIA1 stacks on R310 of the same domain (Fig. 3G). S68 in AcrVIA1 forms hydrogen bonds with R90 in the NTD domain (Fig. 3G), whereas residues I2 and Y4 in the inhibitor stack on K1097 in the HEPN-1 domain (Fig. 3H). The two C-terminal helices of AcrVIA1 form extensive interactions with the Linker domain of Cas13a, locking it in place (Fig. 3H) and thereby preventing the conformational changes reported to occur upon target RNA binding (22). Finally, we detected only minimal structural changes of Cas13a upon AcrVIA1 binding (fig. S9A). By contrast, the 3' end of crRNA underwent a large conformational rearrangement (fig. S9, B and C). Thus, AcrVIA1 prevents conformational changes in the crRNA that occur upon target RNA binding, which are required for activation of Cas13a. To investigate the importance of the observed contacts between the nuclease and its inhibitor, we mutated the relevant residues in AcrVIA1-3xFLAG and tested their importance in inhibiting Cas13a immunity against plasmid conjugation (Fig. 3I), as well as their impact on protein stability by immunoblot (Fig. 3J). Mutations in I2A or Y4A or deletion of the E131 to E134 loop affected both the stability and the function of the inhibitor. By contrast, the quintuple mutant Y39A, S40A, N43A, S93A, Q96A and the truncation mutant lacking the two AcrVIA1 C-terminal helices ( $\Delta$ N173-N232) caused nearly complete loss of function with little or no effect on protein expression, corroborating their importance for Cas13a inhibition. When tested individually, none of the five substitutions affected inhibition (fig. S7D), a result that suggests a very strong association between AcrVIA1 and Cas13a that does not rely on a single interaction. The S68A, F69A double

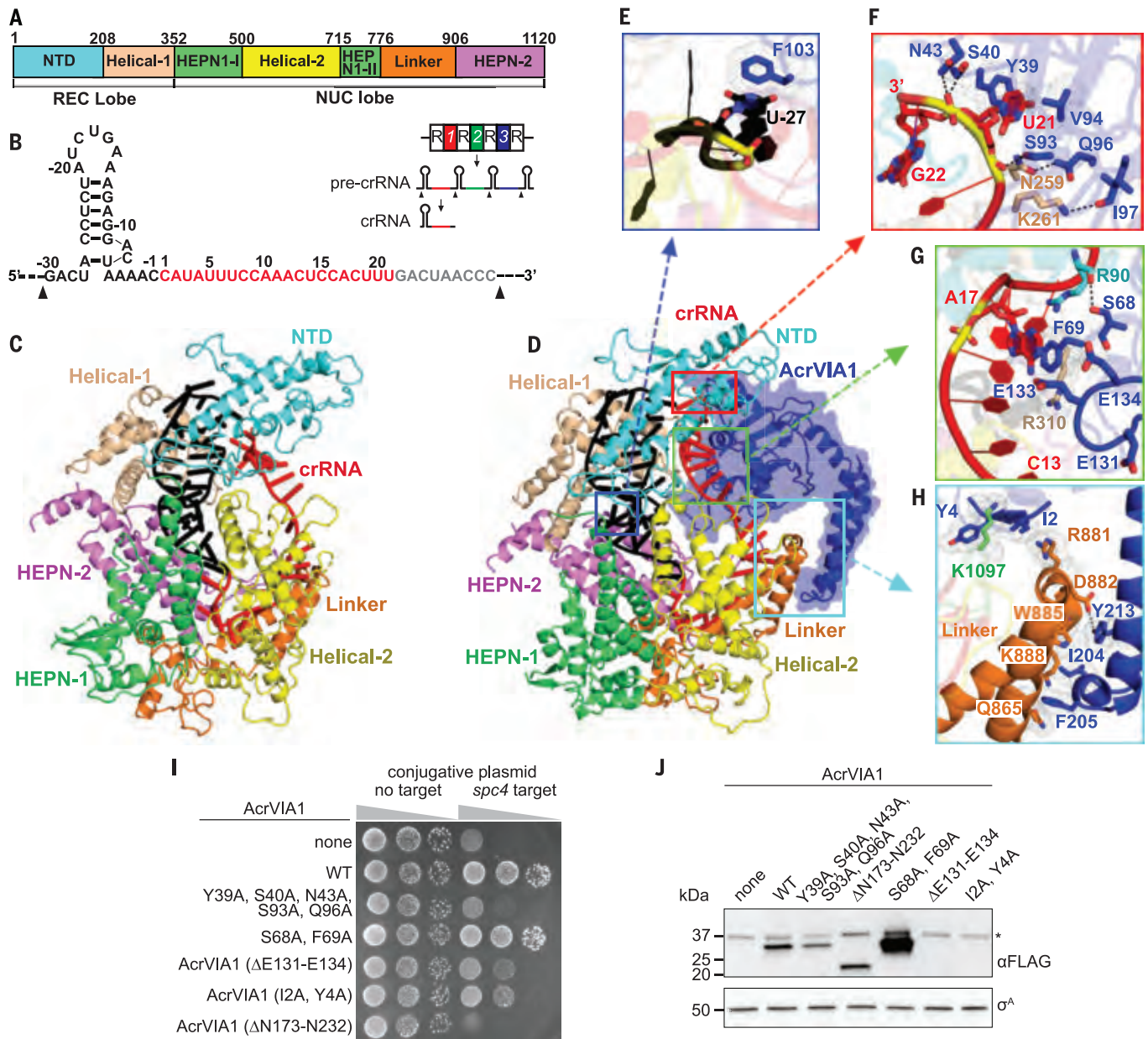


**Fig. 3. Cryo-EM structures of Cas13a<sup>crRNA</sup> and AcrVIA1-Cas13a<sup>crRNA</sup> complexes.** (A) Domain organization of *L. seeligeri* Cas13a. (B) Schematic representation of the crRNA sequence. The repeat and spacer regions within crRNA are shown in black and red, respectively. The disordered region is shown in gray. The black arrow shows the cleavage site of the pre-crRNA. Inset: crRNA maturation pathway; repeats are represented as "R" and spacers as numbers. (C) Ribbon representation of the structure of Cas13a<sup>crRNA</sup>.

(D) Ribbon and surface (AcrVIA1) representations of the AcrVIA1-Cas13a<sup>crRNA</sup> complex. (E to H) Detailed interactions between AcrVIA1 and Cas13a<sup>crRNA</sup> in the complex. (I) Transfer of conjugative plasmid with or without the *spc4* target of the *L. seeligeri* type VI CRISPR-Cas system into WT *L. seeligeri* harboring plasmid-borne WT or mutant alleles of *acrVIA1-3xflag*. (J) Anti-Flag immunoblot of AcrVIA1 mutants tested in (I) and an anti-σ<sup>A</sup> loading control. \*Cross-reacting protein.

mutant retained full function, suggesting that the interaction with Cas13a is unperturbed in this mutant. However, the mutation also led to an increase in expression levels, which could compensate for a partial loss of function.

AcrVIA1 had no effect on protospacer RNA cleavage by purified *L. buccalis* Cas13a<sup>crRNA</sup> (fig. S10A). We performed a structural comparison of *L. seeligeri* Cas13a with *L. buccalis*

Cas13a (PDB 5XWY). Superposition of *L. seeligeri* Cas13a<sup>crRNA</sup> and *L. buccalis* Cas13a<sup>crRNA</sup> revealed differences in the NTD domain (fig. S10B) and the 3' end of crRNA (fig. S10C) that generated obvious clashes between *L. buccalis* Cas13a<sup>crRNA</sup> and AcrVIA1 (fig. S10, D and E). In addition, there were no identifiable overall structural similarities with the other subtype family members Cas13b (24, 25) or Cas13d (26). Thus, our structural

analysis and biochemical tests suggest that AcrVIA1 is limited to neutralizing only the *L. seeligeri* type VI-A CRISPR-Cas immune response.

#### AcrVIA1 enables complete evasion of type VI-A CRISPR-Cas immunity

Previously described anti-CRISPRs that inhibit type I and II CRISPR systems require multiple rounds of infection to completely inhibit



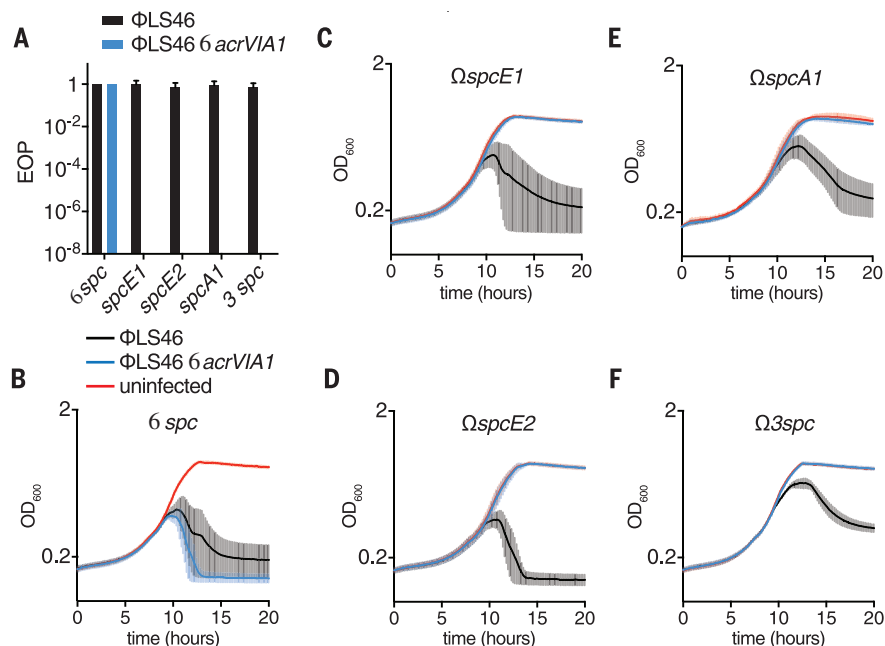


**Fig. 4. AcrVIA1 enables full phage escape from type VI-A CRISPR-Cas immunity.** (A) Efficiency of plaquing (relative to the number of plaques formed in lawns of *L. seeligeri*  $\Delta$ RM  $\Delta$ spc) of phages  $\phi$ LS46 or  $\phi$ LS46  $\Delta$ acrVIA1 in lawns of bacteria expressing *spcA1*, *spcE1*, *spcE2*, or all three (3*spc*). Error bars represent SEM from three biological replicates. (B to F) Growth of *L. seeligeri*  $\Delta$ RM  $\Delta$ spc (B),  $\Delta$ RM  $\Omega$ spcE1 (C),  $\Delta$ RM  $\Omega$ spcE2 (D),  $\Delta$ RM  $\Omega$ spcA1 (E), and  $\Delta$ RM  $\Omega$ 3spc (F), measured as optical density at 600 nm (OD<sub>600</sub>) over time after infection with  $\phi$ LS46 or  $\phi$ LS46  $\Delta$ acrVIA1 phages or no infection. The average curves of three different replicates are reported, with  $\pm$  SEM values shown.

antiphage immunity and fail in conditions of strong CRISPR defense or low viral load (27, 28). To investigate whether AcrVIA1 also displayed limited inhibition capabilities, we first tested its efficacy in conditions of weak or strong type VI-A CRISPR-Cas immunity by infecting cells harboring either one or three targeting spacers, respectively (Fig. 1B). As a control, we performed infections with the  $\phi$ LS46  $\Delta$ acrVIA1 mutant phage and measured the efficiency of plaquing (EOP) in the different host backgrounds. When compared with infection of hosts without targeting spacers, all three individual spacers as well as the triple combination provided efficient immunity against this mutant, reducing the EOP by at least eight orders of magnitude, below our limit of detection. By contrast, immunity was completely abrogated ( $\sim$ 100% EOP) during infections with WT  $\phi$ LS46 when plating on either the single-spacer or triple-spacer strains (Fig. 4A). The 100% EOP value obtained indicated that each viral particle was able to inhibit Cas13a and form a visible plaque. To test this further, we performed infection of liquid cultures of *L. seeligeri*  $\Delta$ RM at an extremely low multiplicity of infection (MOI), 0.000001, and followed their growth over time. In the absence of a targeting spacer, both WT and  $\Delta$ acrVIA1 mutant phage led to

the lysis of the bacteria in the culture (Fig. 4B). Although *L. seeligeri* strains harboring a single  $\phi$ LS46-targeting spacer were immune to the  $\Delta$ acrVIA1 mutant phage, WT  $\phi$ LS46 was able to lyse the cultures (Fig. 4, C to E; figs. S3, C and D, and S11), showing that AcrVIA1 efficiently inhibits type VI-A CRISPR immunity even in conditions of low MOI. Infection of the strain containing three targeting spacers resulted in a delay in lysis (Fig. 4F), consistent with the stronger immunity provided by the presence of multiple spacers, yet still led to inhibition of the type VI-A CRISPR immune response. To explore the mechanism of inhibition further, we performed RNA sequencing over the course of  $\phi$ LS46 infection to determine the timing and expression of each protospacer. We found that many of the spacers used in this study targeted phage transcripts that were abundantly produced within 10 min of infection (e.g., those targeted by *spcA1*, *spcE1*, and *spcE2*; fig. S12) yet were unable to provide Cas13a-mediated immunity in the presence of AcrVIA1. Thus, AcrVIA1 overcame immunity against protospacers transcribed very early (even earlier than the inhibitor itself, as in the case of target A1) during the phage lytic cycle. Altogether, these results demonstrate that AcrVIA1 can enable viral propagation in conditions that

are extremely unfavorable for the success of Cas13a inhibition (rapid targeting, low MOI, and multiple Cas13a targeting spacers) that normally would lead to the failure of type I and II Acrs (27, 28).

## Discussion

AcrVIA1 inhibits Cas13a by interacting with the crRNA-exposed face of nuclease and making specific contacts with both protein and guide RNA residues that prevent the binding of a complementary target RNA and activation of Cas13a RNase function. In heterologous hosts, AcrVIA1 could be a useful component of the Cas13 toolbox, allowing control of this nuclease during editing, knockdown, and/or visualization of RNA molecules (29, 30), as is the case for other recently found type VI-A anti-CRISPRs (18). More importantly, in its natural host, AcrVIA1 can completely neutralize type VI-A CRISPR-Cas immunity against  $\phi$ LS46 even in unfavorable conditions for inhibition, such as multiple protospacer targeting and low viral load. We believe this to be a consequence of the lack of phage DNA clearance during the type VI response (17). This would lead to a continuous transcription and translation of AcrVIA1 and progressive neutralization of Cas13a. Assuming that the collateral RNA degradation generated by activation of Cas13a in *Listeria* hosts allows a low level of AcrVIA1 transcription and translation, enough inhibitor will accumulate to inactivate all the Cas13a molecules inside the bacterial cell. This is in contrast to type I and II Acrs, the initial production of which inhibits only a fraction of Cascade-Cas3 and Cas9 molecules, respectively, and the Acr-harboring phage is destroyed by the nucleases that remain active (27, 28). Gradual inhibition of Cas13a after phage infection would require AcrVIA1 to constantly capture the Cas13a<sup>crRNA</sup> molecules that disengage from the target RNA and prevent them from finding their targets again. Alternatively, the inhibitor could displace the target RNA molecules from activated Cas13a<sup>crRNA</sup> nucleases. Such a mechanism would be especially effective when the target RNA is a transcript that is produced, and therefore activates Cas13a, before AcrVIA1 is generated. Finally, the genetic, biochemical, and structural findings of this work highlight the astounding diversity of molecular strategies at play during the host-virus evolutionary arms race.

## REFERENCES AND NOTES

1. R. Barrangou et al., *Science* **315**, 1709–1712 (2007).
2. L. A. Marraffini, E. J. Sontheimer, *Science* **322**, 1843–1845 (2008).
3. A. Bolotin, B. Quinquis, A. Sorokin, S. D. Ehrlich, *Microbiology* **151**, 2551–2561 (2005).
4. F. J. Mojica, C. Díez-Villaseñor, J. García-Martínez, E. Soria, *J. Mol. Evol.* **60**, 174–182 (2005).
5. C. Pourcel, G. Salvignol, G. Vergnaud, *Microbiology* **151**, 653–663 (2005).
6. S. J. Brouns et al., *Science* **321**, 960–964 (2008).

7. R. N. Jackson, P. B. van Erp, S. H. Sternberg, B. Wiedenheft, *Curr. Opin. Microbiol.* **37**, 110–119 (2017).
8. K. S. Makarova et al., *Nat. Rev. Microbiol.* **18**, 67–83 (2020).
9. O. O. Abudayyeh et al., *Science* **353**, aaf5573 (2016).
10. A. East-Seletsky et al., *Nature* **538**, 270–273 (2016).
11. A. J. Meeske, S. Nakandakari-Higa, L. A. Marraffini, *Nature* **570**, 241–245 (2019).
12. J. Bondy-Denomy, A. Pawluk, K. L. Maxwell, A. R. Davidson, *Nature* **493**, 429–432 (2013).
13. B. J. Rauch et al., *Cell* **168**, 150–158.e10 (2017).
14. A. Pawluk et al., *Cell* **167**, 1829–1838.e9 (2016).
15. Y. Bhoobalan-Chitty, T. B. Johansen, N. Di Cianni, X. Peng, *Cell* **179**, 448–458.e11 (2019).
16. N. D. Marino et al., *Science* **362**, 240–242 (2018).
17. K. E. Watters, C. Fellmann, H. B. Bai, S. M. Ren, J. A. Doudna, *Science* **362**, 236–239 (2018).
18. P. Lin et al., *Mol. Cell* **51**, 1097–1105 (2013).
19. J. Rocourt, A. Schrettenbrunner, H. Hof, E. P. Espaze, *Pathol. Biol. (Paris)* **35**, 1075–1080 (1987).
20. B. A. Osuna et al., *Cell Host Microbe* **19**, 3128–3138 (2015).
21. L. Liu et al., *Cell* **170**, 714–726.e10 (2017).
22. L. Liu et al., *Cell* **168**, 121–134.e12 (2017).
23. L. Holm, C. Sander, *Trends Biochem. Sci.* **20**, 478–480 (1995).
24. I. M. Slaymaker et al., *Cell Rep.* **26**, 3741–3751.e5 (2019).
25. B. Zhang et al., *Cell Res.* **28**, 1198–1201 (2018).
26. C. Zhang et al., *Cell* **175**, 212–223.e17 (2018).
27. A. L. Borges et al., *Cell* **174**, 917–925.e10 (2018).
28. M. Landsberger et al., *Cell* **174**, 908–916.e12 (2018).
29. O. O. Abudayyeh et al., *Nature* **550**, 280–284 (2017).
30. D. B. T. Cox et al., *Science* **358**, 1019–1027 (2017).

## ACKNOWLEDGMENTS

We thank all members of the Marraffini laboratory for helpful discussions, R. Calendar (UC Berkeley) for A118 and U153 listeriolysins, S. Kilcher (ETH Zürich) for plasmid pSK1, D. Rudner (Harvard Medical School) for anti- $\sigma^A$  antibody, M. J. De La Cruz for assistance in data collection on the Sloan Kettering Titan KRIOS cryo-EM, and E. Eng (New York Structural Biology Center) for assistance in cryo-EM data processing. **Funding:** This work was supported by a National Institutes of Health Director's Pioneer Award (1DP1GM128184-01 to L.A.M.), funds from the Geoffrey Beene Cancer Research Center and NIH GM129430 to D.J.P., and by a Memorial Sloan-Kettering Cancer Center Core Grant (P30CA008748). L.A.M. is an investigator of the Howard Hughes Medical Institute. A.J.M. is a Helen Hay Whitney postdoctoral fellow. **Author contributions:** A.J.M. and L.A.M. conceived the study. A.J.M. performed all the in vivo and biochemistry experiments with the help of A.K.C. and A.K. N.J. performed all the cryo-EM experiments. J.L. and M.W. isolated *L. seeligeri* strains. A.J.M., N.J., L.A.M., and D.J.P. wrote the manuscript. All authors read and approved the manuscript. **Competing interests:** L.A.M. and A.J.M. are coinventors on a patent application filed by The Rockefeller University relating to work in this study. L.A.M. is a founder of and adviser for Intellia Therapeutics and Eligo Biosciences. **Data and materials availability:** The *L. seeligeri* strains LS46 and LS59 draft genome assemblies have been deposited at GenBank (accession no. JAAIYQ000000000). Raw genome sequencing reads and RNA-sequencing reads have been deposited at the Sequence Read Archive (accession no. PRJNA607241). The atomic coordinates have been deposited in the Protein Data Bank with the codes 6VRC (Cas13a<sup>crRNA</sup>) and 6VRB (AcrVIA1-Cas13a<sup>crRNA</sup>). The cryo-EM density maps have been deposited in the Electron Microscopy Data Bank with the codes EMD-21367 (Cas13a<sup>crRNA</sup>) and EMD-21366 (AcrVIA1-Cas13a<sup>crRNA</sup>).

## SUPPLEMENTARY MATERIALS

science.sciencemag.org/content/369/6499/54/suppl/DC1  
Materials and Methods  
Figs. S1 to S12  
Tables S1 to S7  
References (31–44)  
MDAR Reproducibility Checklist

6 March 2020; accepted 15 May 2020  
Published online 28 May 2020  
10.1126/science.abb6151

## HISTONE FUNCTION

# The histone H3-H4 tetramer is a copper reductase enzyme

Narsis Attar<sup>1,2\*</sup>, Oscar A. Campos<sup>1,2\*</sup>, Maria Vogelauer<sup>1\*</sup>, Chen Cheng<sup>1</sup>, Yong Xue<sup>1</sup>, Stefan Schmollinger<sup>3†</sup>, Lukasz Salwinski<sup>1,4</sup>, Nathan V. Mallipeddi<sup>1</sup>, Brandon A. Boone<sup>1</sup>, Linda Yen<sup>5</sup>, Sichen Yang<sup>1</sup>, Shannon Zikovich<sup>1</sup>, Jade Dardine<sup>1</sup>, Michael F. Carey<sup>1,2</sup>, Sabeeha S. Merchant<sup>3†</sup>, Siavash K. Kurdistani<sup>1,2,6†</sup>

Eukaryotic histone H3-H4 tetramers contain a putative copper (Cu<sup>2+</sup>) binding site at the H3-H3' dimerization interface with unknown function. The coincident emergence of eukaryotes with global oxygenation, which challenged cellular copper utilization, raised the possibility that histones may function in cellular copper homeostasis. We report that the recombinant *Xenopus laevis* H3-H4 tetramer is an oxidoreductase enzyme that binds Cu<sup>2+</sup> and catalyzes its reduction to Cu<sup>1+</sup> in vitro. Loss- and gain-of-function mutations of the putative active site residues correspondingly altered copper binding and the enzymatic activity, as well as intracellular Cu<sup>1+</sup> abundance and copper-dependent mitochondrial respiration and Sod1 function in the yeast *Saccharomyces cerevisiae*. The histone H3-H4 tetramer, therefore, has a role other than chromatin compaction or epigenetic regulation and generates bioavailable Cu<sup>1+</sup> ions in eukaryotes.

Eukaryotic histones evolved from histone-like proteins of Archaea, single-celled organisms that lack nuclei and display genomes that are smaller than those of eukaryotes. Archaeal histones form a structure similar to the eukaryotic H3-H4 tetramer (1) but, unlike eukaryotic histones, typically lack extended N-terminal tails and posttranslational modifications. Because Archaea have no apparent capability for histone-based epigenetic regulation or requirement for genome compaction to fit within a nucleus, this prompted us to consider whether the conserved histone H3-H4 tetramer may have an additional function.

The dimerization interface of the two histone H3 proteins contains cysteine and histidine residues (Fig. 1A) in an arrangement typical of Cu<sup>2+</sup> binding sites in other proteins (2). The evolutionary conservation of residues in this region is greater than expected from their contributions to nucleosome stability (3), consistent with a potential metal binding capability (4–6).

Eukaryotes emerged about the same time as the initial accumulation of oxygen (7). This oxygenation event decreased the biological usability and increased the toxicity of transition metals such as copper (8). We hypothesize that histones may have facilitated metal utilization in oxidizing conditions.

Copper often serves as a redox cofactor for enzymes such as cytochrome c oxidase in the mitochondrial electron transport chain (ETC) and Cu, Zn-superoxide dismutases (e.g., Sod1) (9). As a redox cofactor, copper cycles between the cupric (Cu<sup>2+</sup>) and cuprous (Cu<sup>1+</sup>) states. However, it is the cuprous form that is trafficked and sensed intracellularly, suggesting a need to maintain cellular copper in the Cu<sup>1+</sup> oxidation state for proper distribution and utilization (10). Whether protein-based mechanisms have evolved to regulate intracellular Cu<sup>2+</sup> reduction is unknown. Here, we present evidence that the eukaryotic H3-H4 tetramer binds Cu<sup>2+</sup>, catalyzes Cu<sup>2+</sup> reduction, and improves the utilization of copper by nuclear, cytoplasmic, and mitochondrial proteins.

## Recombinant histone H3-H4 tetramer binds cupric ions

To determine whether copper ions interact with the residues at the H3-H3' interface (4) (Fig. 1, A and B), we assembled and purified recombinant *Xenopus laevis* wild-type (Xl WT) histone H3-H4 tetramers (11) (fig. S1, A to C). Incubation of the Xl WT tetramer with increasing amounts of Cu<sup>2+</sup> in a Tricine buffer resulted in an ultraviolet (UV) absorbance band that is characteristic of copper-cysteine interactions (12) (Fig. 1C and fig. S1D). UV absorbance plateaued at a molar ratio of ~1, suggesting a stoichiometry of one copper ion per tetramer (Fig. 1C and fig. S1D). Mutation of Cys<sup>110</sup> (C110) to alanine (H3C110A) (fig. S1, B and C) abolished

<sup>1</sup>Department of Biological Chemistry, David Geffen School of Medicine, University of California Los Angeles, Los Angeles, CA 90095, USA. <sup>2</sup>Molecular Biology Institute, University of California Los Angeles, Los Angeles, CA 90095, USA.

<sup>3</sup>Institute for Genomics and Proteomics, Department of Chemistry and Biochemistry, University of California Los Angeles, Los Angeles, CA 90095, USA. <sup>4</sup>UCLA-DOE Institute for Genomics and Proteomics, University of California Los Angeles, Los Angeles, CA 90095, USA. <sup>5</sup>Department of Molecular, Cell, and Developmental Biology, University of California Los Angeles, Los Angeles, CA 90095, USA.

<sup>6</sup>Eli and Edythe Broad Center of Regenerative Medicine and Stem Cell Research, David Geffen School of Medicine, University of California Los Angeles, Los Angeles, CA 90095, USA.

\*These authors contributed equally to this work. †Present address: QB3-Berkeley, University of California Berkeley, Berkeley, CA 94720, USA.

‡Corresponding author. Email: skurdistani@mednet.ucla.edu



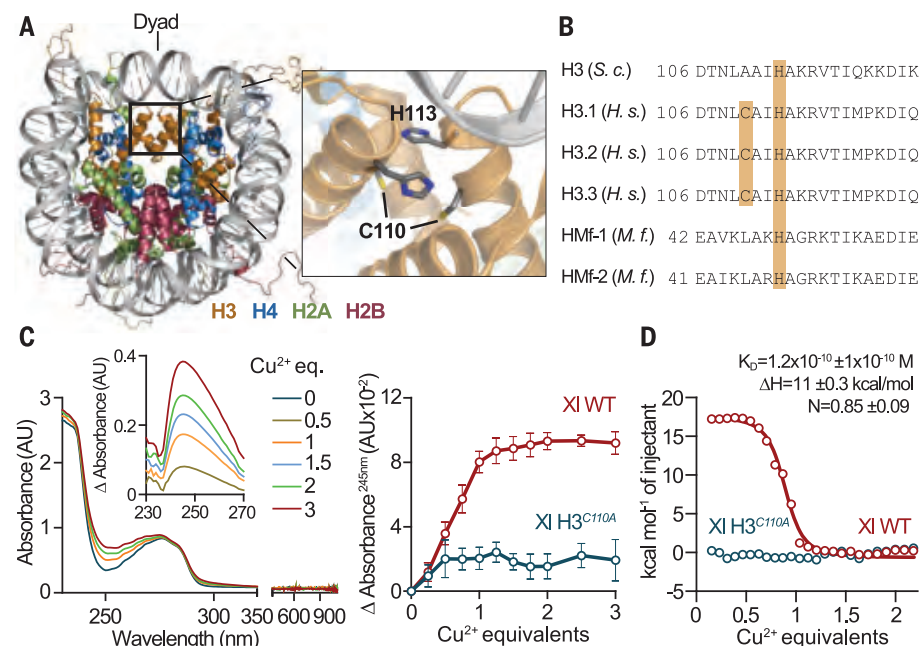


**Fig. 1. Recombinant *X. laevis* histone H3-H4 tetramer interacts with cupric ions.** (A) Left: *X. laevis* (XI) nucleosome core particle structure [Protein Data Bank (PDB) 1KX5] (38). The box delineates the H3-H3' interface. Right: Interface residues H3H113 and H3C110 are shown. (B) Alignment of the C-terminal region of *S. cerevisiae* (*S. c.*) and *Homo sapiens* (*H. s.*) histone H3 and archaeal [*Methanothermobacter ferrooxidans* (*M. f.*)] histones. (C) Left: UV-visible absorbance spectrum of the XI H3-H4 tetramer incubated with or without  $\text{Cu}^{2+}$ . Inset: Differential absorbance compared to tetramer without  $\text{Cu}^{2+}$ . Right: Buffer-corrected differential absorbance of the indicated XI tetramers. AU, absorbance units; eq., equivalents. (D) Representative ITC titration profile of the XI H3-H4 tetramer. Circles are experimental data, and the line is the fitted curve. Average dissociation constant ( $K_D$ ), enthalpy change ( $\Delta H$ ), and stoichiometry ( $N$ )  $\pm$  SD of the H3-H4 tetramer- $\text{Cu}^{2+}$  complex calculated from three experiments are shown. Single-letter abbreviations for the amino acid residues are as follows: A, Ala; C, Cys; D, Asp; E, Glu; F, Phe; G, Gly; H, His; I, Ile; K, Lys; L, Leu; M, Met; N, Asn; P, Pro; Q, Gln; R, Arg; S, Ser; T, Thr; V, Val; W, Trp; and Y, Tyr.

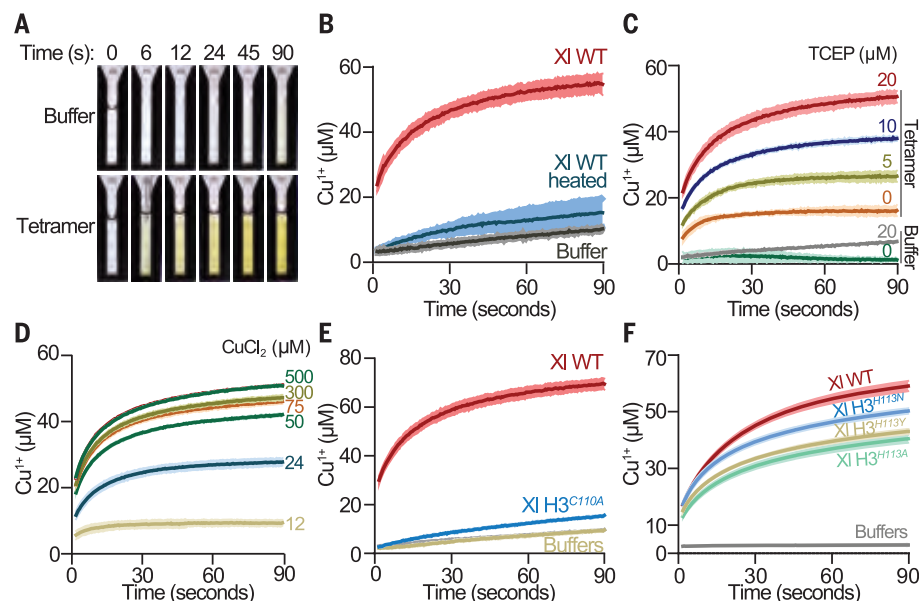


**Fig. 2. The *X. laevis* H3-H4 tetramer catalyzes reduction of cupric ions.** (A) Photographic representation of in vitro  $\text{Cu}^{2+}$  reduction assay. The yellow color is due to  $\text{NC}_2\text{-Cu}^{1+}$  complex formation. (B) Progress curves of  $\text{Cu}^{2+}$  reduction with 1  $\mu\text{M}$  of tetramer, heated tetramer, or buffer in presence of 30  $\mu\text{M}$  TCEP and 1 mM  $\text{CuCl}_2$ -10 mM Tricine. Lines and shading represent the mean  $\pm$  SD of three to five assays. (C to F) Same as (B) but with the indicated amount of (C) TCEP or (D)  $\text{CuCl}_2$ ; or with (E) 1  $\mu\text{M}$  of the indicated tetramers or (F) 5  $\mu\text{M}$  of the indicated tetramers in the presence of 100  $\mu\text{M}$  TCEP and 0.5 mM  $\text{CuCl}_2$ -ADA pH 8.

this copper-dependent absorbance change (Fig. 1C). Isothermal titration calorimetry (ITC) analysis further demonstrated high affinity of the tetramer for  $\text{Cu}^{2+}$  and an approximately equimolar stoichiometry (Fig. 1D). The WT H3-H4 complex also exhibited greater retention on a  $\text{Cu}^{2+}$  affinity column than the H3<sup>C110A</sup> counterpart (fig. S1E).

### The histone H3-H4 tetramer catalyzes cupric ion reduction

We next hypothesized that a mechanism to maintain the  $\text{Cu}^{1+}$  state intracellularly may be beneficial in oxidizing conditions. Thus, we asked whether the H3-H4 tetramer catalyzes the reduction of  $\text{Cu}^{2+}$  to  $\text{Cu}^{1+}$  in the presence of a source of electrons. We developed an assay using the chelators neocuproine (NC) or bicinehoninic acid (BCA) to detect  $\text{Cu}^{1+}$  production spectrophotometrically (Fig. 2A and fig. S2A). Assays contained reduced forms of either tris(2-carboxyethyl)phosphine (TCEP), nicotinamide adenine dinucleotide (NADH), or its phosphate form (NADPH) as electron donors. Reactions were initiated by addition of  $\text{Cu}^{2+}$  in the form of either  $\text{CuCl}_2$ -Tricine,  $\text{CuCl}_2$ -N-(2-acetamido)iminodiacetic acid (ADA), or  $\text{CuCl}_2$ -nitrilotriacetic acid (NTA) solutions (fig. S2B). Spontaneous  $\text{Cu}^{1+}$  production occurred at a slow rate, but the rate of  $\text{Cu}^{1+}$  production substantially increased in the presence of the XI WT tetramer (Fig. 2B and fig. S2, C to E). Production of  $\text{Cu}^{1+}$  eventually plateaued owing to near full consumption of the electron source (Fig. 2B). No appreciable production of  $\text{Cu}^{1+}$  occurred in the absence of TCEP, indicating that it, and not the tetramer, was the source of electrons. The tetramer enhanced  $\text{Cu}^{2+}$  reduction in anaerobic conditions as well, ruling out any role for oxygen (fig. S2F). The XI WT tetramer assembled into a complex with the C terminus of the human histone chaperone Spt2 (13) also enhanced  $\text{Cu}^{2+}$  reduction (fig. S2, G to I). Additionally, the tetramer could use natural reductants such as NADPH to increase  $\text{Cu}^{2+}$  reduction (fig. S3A). Direct measurement of NADPH confirmed its oxidation during  $\text{Cu}^{2+}$  reduction (fig. S3B). The effect of the tetramer was specific to cupric ions because there was no enhancement of ferric ion reduction.

Heating (Fig. 2B) or proteinase K digestion (fig. S3C) of the XI WT tetramer abolished  $\text{Cu}^{2+}$  reduction activity. The unassembled XI histone H3 or the yeast H2A also did not enhance  $\text{Cu}^{2+}$  reduction (fig. S3, C and D). Increasing rates of  $\text{Cu}^{1+}$  production occurred with increasing amounts of either TCEP (Fig. 2C) or  $\text{Cu}^{2+}$  (Fig. 2D), eventually approaching a maximum rate, consistent with protein-based catalysis (fig. S3, E and F).

The H3C110A mutation substantially reduced the rate of  $\text{Cu}^{2+}$  reduction (Fig. 2E), as did treatment with *N*-ethylmaleimide (NEM) (fig. S3G). Ribonuclease A (RNase A), which

contains redox-reactive cysteines (14), did not enhance  $\text{Cu}^{2+}$  reduction (fig. S3H). Similarly, dithiothreitol (DTT) directly reduced an equimolar amount of  $\text{Cu}^{2+}$  but did not substantially enhance the rate of  $\text{Cu}^{2+}$  reduction by TCEP (fig. S3H). These data underscore the importance of H3C110 to the tetramer enzyme activity.

Mutation of H3 His<sup>113</sup> (H3H113) (4, 5) to alanine (H3H113A), or to asparagine or tyrosine (H3H113N or H3H113Y), which have been found in certain cancers (15), had little effect on the rate of reduction with  $\text{Cu}^{2+}$ -Tricine as the substrate but diminished  $\text{Cu}^{2+}$  reduction with  $\text{Cu}^{2+}$ -ADA (Fig. 2F and fig. S2B) or  $\text{Cu}^{2+}$ -NTA as substrates (figs. S2B and S3I), likely because of the differing  $\text{Cu}^{2+}$  coordination ability of different buffers. Altogether, our data reveal that the H3-H4 tetramer catalyzes  $\text{Cu}^{2+}$  reduction by various electron donors and is thus a cupric reductase.

The yeast histone H3 (yH3) contains H113 but lacks the C110 residue found in most other eukaryotic H3s (Fig. 1B). Consistently, recombinant yH3-H4 tetramer did not absorb UV light in the 245-nm range when incubated with  $\text{Cu}^{2+}$ . However, a broad peak centered at 680 nm was observed at high concentrations of yeast tetramer and high ionic strength (2 M NaCl), consistent with weakly absorbing d-d transitions typical of coordinated  $\text{Cu}^{2+}$  ions (16) (Fig. 3A and fig. S4A). The H3H113A mutation (fig. S4, B and C) decreased the copper-dependent absorbance change at 680 nm (Fig. 3A). Furthermore, retention of the yH3-H4 complex on a  $\text{Cu}^{2+}$  affinity column was reduced by the H3H113A, N, or Y mutations (fig. S4, B to F), consistent with a role of H3H113 in  $\text{Cu}^{2+}$  interaction.

Mutation of H3A110 to cysteine (yH3<sup>A110C</sup> tetramer) (fig. S4, G and H) elicited a copper-dependent UV absorbance band nearly identical to that observed with the Xl WT tetramer (Fig. 3B). Furthermore, the H3H113A mutation of the yH3<sup>A110C</sup> tetramer (i.e., yH3<sup>A110CH113A</sup> tetramer) (fig. S4, G to I) diminished copper-dependent absorbance at 245 nm (Fig. 3B), indicating that H3H113 affects the cysteine- $\text{Cu}^{2+}$  interaction. The yH3<sup>A110C</sup> tetramer also displayed cupric reductase activity, which was diminished by the H3H113A mutation (Fig. 3C). In the absence of H3C110, the yeast tetramer did not display cupric reductase activity in standard salinity, likely because of deficient  $\text{Cu}^{2+}$  binding, which required 2 M NaCl (Fig. 3A). High salinity interfered with other assay components, precluding further investigation. Nonetheless, our findings suggest that the yH3-H4 tetramer can display cupric reductase activity and that H3H113 participates in this function.

#### Mutation of histone H3H113 results in loss of function in yeast

We next investigated whether mutation of the H3H113 residue in vivo would diminish

the  $\text{Cu}^{1+}$  pool. Mutation of H3H113 to alanine is lethal in *Saccharomyces cerevisiae* (17) (fig. S5A). However, introduction of either H3H113N or H3H113Y mutations in the two chromosomal copies of the histone H3 gene generated viable and somewhat slow-growing yeast strains H3<sup>H113N</sup> and H3<sup>H113Y</sup> (fig. S5B).

Yeast strains in which the H3H113N and H3H113Y mutant histones were expressed from one locus, with the other locus deleted, were severely sick compared with strains expressing both histone loci (fig. S5C). This finding identifies H3H113N and H3H113Y as loss-of-function alleles, coincident with

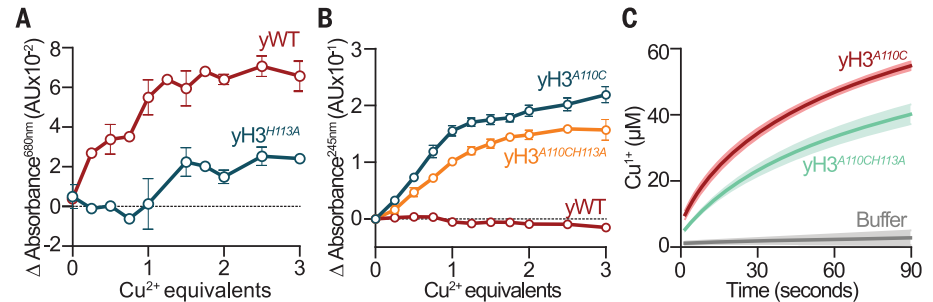


**Fig. 3. The yeast H3-H4 tetramer potentially is a copper reductase.** (A and B) Buffer-corrected differential absorbance of the indicated yeast tetramers. (C) Progress curves of  $\text{Cu}^{2+}$  reduction with 5  $\mu\text{M}$  of tetramers in the presence of 100  $\mu\text{M}$  TCEP and 0.5 mM  $\text{CuCl}_2$ -ADA pH 8.

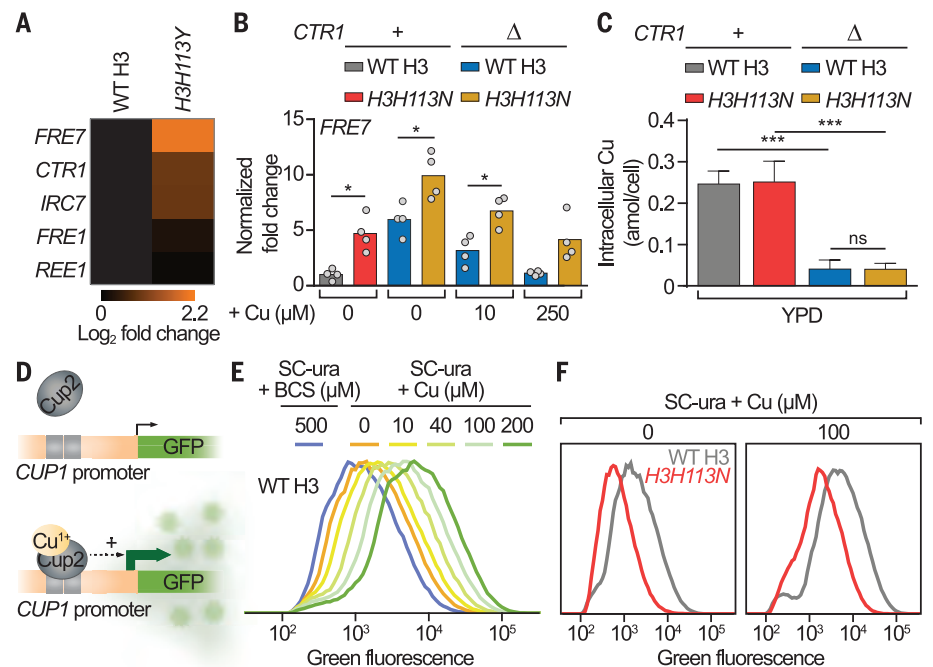


**Fig. 4. H3H113 regulates  $\text{Cu}^{1+}$ -dependent transcriptional activities of Mac1 and Cup2.** (A and B) Reverse transcription quantitative polymerase chain reaction (RT-qPCR) analyses of Mac1 target gene (39) expression relative to WT and normalized to *ACT1* expression. The (A) boxes and (B) bars show means from four independent experiments (dots) in YPD with or without  $\text{CuSO}_4$ . Baseline copper concentration in YPD is  $\sim 1 \mu\text{M}$ . (C) Intracellular copper content of exponentially growing strains. Bars are means  $\pm$  SD from three to six experiments. (D) Schematic representation of the p(CUP1)-GFP reporter system. (E and F) Average flow cytometry distributions of cells containing the p(CUP1)-GFP plasmid grown in SC lacking uracil (SC-ura) with or without BCS or  $\text{CuSO}_4$  from five or six experiments. Baseline copper concentration in SC is  $\sim 0.25 \mu\text{M}$ . \* $P \leq 0.05$ ; \*\*\* $P \leq 0.001$ ; ns, not significant.



the loss of Cu<sup>2+</sup> binding in vitro. We mostly used the *H3H113N* mutation in genetic experiments because *H3H113Y* results in a more severe growth defect, potentially confounding the interpretation of phenotypes.

H3H113 mutations alter cuprous ion availability

We next assayed the activity of the transcription factor Mac1 as a readout of nuclear Cu<sup>1+</sup> abundance because it is directly inhibited by Cu<sup>1+</sup> and does not bind Cu<sup>2+</sup> (18). Gene expression analysis revealed largely similar profiles in WT and *H3<sup>H113N</sup>* strains in rich fermentative media [synthetic complete (SC) and yeast extract peptone dextrose (YPD)] (fig. S6A). However, Mac1 target genes were up-regulated in both the *H3<sup>H113N</sup>* (fig. S6B) and *H3<sup>H113Y</sup>* strains (Fig. 4A). Deletion of *CTR1* (*ctr1Δ*), the main copper importer in yeast (19), increased Mac1 target expression (Fig. 4B and fig. S6, B and C). However, Mac1 targets displayed even greater up-regulation and incomplete repression in response to exogenous copper in *H3<sup>H113N</sup> ctr1Δ* (Fig. 4B and fig. S6C). *ctr1Δ* substantially reduced total copper concentrations, whereas the *H3H113N* mutation did not (Fig. 4C), suggesting that the H3H113 mutations decrease Cu<sup>1+</sup>

abundance without affecting total copper concentration.

We developed a reporter plasmid to assess Cu<sup>1+</sup> abundance by employing the Cup2 transcription factor, which is directly activated by Cu<sup>1+</sup> but not Cu<sup>2+</sup> (20). The plasmid harbors the green fluorescent protein (*GFP*) gene downstream of the *CUP1* promoter, which is the main target of Cup2 (21) (Fig. 4D and fig. S6D). GFP expression was proportional to the expected Cu<sup>1+</sup> abundance in both physiological and genetic assays (Fig. 4E and fig. S6, E and F) and was reduced in *H3<sup>H113N</sup>* (Fig. 4F and fig. S6G), further indicating that H3H113 is required to maintain cellular Cu<sup>1+</sup> availability.

The H3H113 residue supports copper utilization for mitochondrial respiration

We next asked whether the H3H113 mutations impair copper utilization outside the nucleus. We first tested mitochondrial respiration by assessing copper-dependent cytochrome c oxidase function. Although *H3<sup>H113N</sup>* did not display a defect in mitochondrial respiration, the *H3<sup>H113Y</sup>* strain displayed a significant loss of O<sub>2</sub> consumption (Fig. 5A and fig. S7A). This defect was exacerbated in the presence of the copper

chelator bathocuproinedisulfonic acid (BCS) and was recovered by excess exogenous copper (fig. S7, B and C).

To relate the defects in mitochondrial respiration to disruption of copper utilization, we assessed the ability of cells to increase respiratory function as they were shifted from a copper-depleted state to a copper-replete state. Copper depletion by means of *CTR1* deletion resulted in a low rate of antimycin-sensitive O<sub>2</sub> consumption (Fig. 5B and fig. S7D) and cytochrome c oxidase activity (Fig. 5C), which were gradually increased by addition of exogenous copper. However, substantially more copper was required to rescue *ctr1Δ* in the context of *H3H113N* (Fig. 5, B and C). More copper was also required to rescue respiratory growth of *ctr1Δ* in the context of *H3H113N* or *H3H113Y* (Fig. 5D and fig. S7E). *H3H113N* also diminished the copper-dependent rescue of cells lacking *MAC1*, which activates *CTR1* expression (18) (fig. S7F). Addition of iron, zinc, or manganese did not rescue the respiratory growth defects of *ctr1Δ* strains (fig. S7G).

Consistent with the hypomorphic nature of *H3H113N*, a strain with one WT H3 and one *H3H113N* gene displayed an intermediate defect compared with strains containing two *H3H113N*

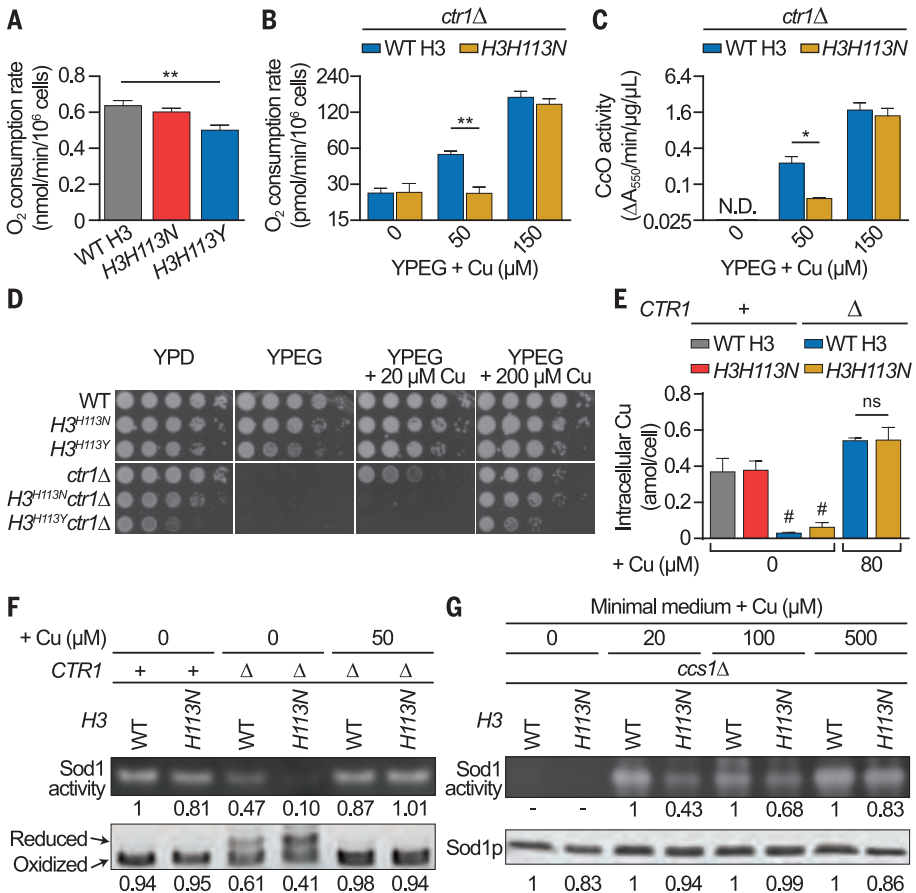


**Fig. 5. H3H113 is required for utilization of copper for mitochondrial respiration and Sod1 function.** (A and B) Oxygen consumption assays of cells incubated for (A) 18 or (B) 4 hours in liquid YPEG (yeast extract peptone ethanol glycerol) with or without CuSO<sub>4</sub>. Baseline copper concentration in YPEG is ~1 μM. Bars show means in (A) linear and (B) log<sub>2</sub> scale ± SD from three experiments. Bars in (A) are scaled to mitochondrial DNA contents. (C) Cytochrome c oxidase assays of cells incubated for 4 hours in liquid YPEG with or without CuSO<sub>4</sub>. Bars show means in log<sub>2</sub> scale ± SD from three experiments. N.D., not detectable. (D) Spot test assays in media with or without CuSO<sub>4</sub>. (E) Intracellular copper content of cells grown in YPEG with or without CuSO<sub>4</sub>. Bars show means ± SD from three to six experiments. #The *ctr1Δ* strains, which do not grow in nonfermentable media, were incubated in YPEG for 12 hours and assessed for metal content for reference. (F) Representative Sod1 activity (top) and Sod1 disulfide-bond assays (bottom) from three experiments for cells grown in SC with or without CuSO<sub>4</sub>. Relative signal intensities are indicated (bottom numbers are the ratio of oxidized to total Sod1). (G) Same as (F) but for cells grown in minimal medium with or without CuSO<sub>4</sub>. Baseline copper concentration in minimal medium is ~0.25 μM. \**P* ≤ 0.05; \*\**P* ≤ 0.01; ns, not significant.

or two WT H3 genes (fig. S8A). Similarly, deleting one of the two copies of the H3 and H4 genes (*hht1-hhf1Δ*) (fig. S8, B to D) increased the copper requirement in *ctr1Δ* for respiratory growth (fig. S8E).

Total copper and iron concentrations were similar between *H3<sup>H113N</sup>* and WT in respiratory medium (Fig. 5E and fig. S9A). Addition of excess copper increased total copper concentrations similarly in both strains (Fig. 5E), indicating that the copper utilization defect in *H3<sup>H113N</sup>ctr1Δ* was not due to changes in total copper abundance. Inefficient recovery of *ctr1Δ* in the context of *H3H113N* was not due to increased  $\text{Cu}^{1+}$  sequestration by the metallothionein Cup1, because loss of Cup1 (*cup1<sup>F8stop</sup>*) had no effect on the requirement for copper in *H3<sup>H113N</sup>ctr1Δ* (fig. S9B).

We considered whether potential disruptions in chromatin accessibility or gene regulation account for the copper utilization defects of the H3H113 mutants. The *H3H113N* mutation or deletion of Asf1, a histone chaperone that facilitates nucleosome assembly in part through interaction with H3H113 (22, 23), resulted in minimal disruption of chromatin accessibility (fig. S9C). However, *asf1Δ* did not phenocopy the H3H113 mutants in respiratory media (fig. S9D). Global gene expression patterns were similar between WT and *H3<sup>H113N</sup>* strains in respiratory media (fig. S9E), with compa-

table up-regulation of genes involved in respiratory growth and copper regulation (fig. S9, F and G).

Deletion of membrane-bound metalloredutases *FRE1* and *FRE2* (24) did not phenocopy the H3H113 mutations (fig. S10A), suggesting that the intracellular role of histone H3 on copper utilization is distinct from extracellular metal reduction. Glutathione (GSH) also participates in cellular copper metabolism (25). Decreasing GSH abundance, by deleting the *GSH1* gene, increased the amount of copper required to rescue *ctr1Δ* but to a lesser extent than *H3H113N* (fig. S10B). Combining *H3H113N* with *gsh1Δ* caused an even greater defect in copper utilization (fig. S10B), suggesting that histones have a distinct role in copper utilization.

### Histone H3 supports copper utilization for Sod1 function

We next considered whether histone H3 might also affect copper utilization by Sod1. Total Sod1 activity was ~40% less in *H3<sup>H113Y</sup>* compared with WT, which was recovered by excess exogenous copper (fig. S11, A and B). *H3H113N* also decreased Sod1 activity by ~20% (Fig. 5F). Deletion of *CTR1* reduced Sod1 activity and formation of its internal disulfide bond, which are dependent on  $\text{Cu}^{1+}$  and the copper chaperone Ccs1 (26) (Fig. 5F). Com-

binning *ctr1Δ* with *H3H113N* further decreased the internal disulfide bond and Sod1 activity, which were restored by addition of excess exogenous copper (Fig. 5F). Loss of function of Sod1 causes lysine auxotrophy in yeast (27). Correspondingly, *H3<sup>H113N</sup>ctr1Δ* exhibited a growth defect in lysine-deficient conditions (fig. S11C).

Deletion of *CCS1* substantially decreased Sod1 activity (Fig. 5G), which was restored by addition of excess copper, but the *H3H113N* mutation substantially increased the amount of copper required for recovery (Fig. 5G). Considerably more copper was also required to rescue the lysine auxotrophy of *ccs1Δ* in the context of *H3H113N* (fig. S11, D and E). Unlike the effect of *H3H113N*, deletion of *CTR1* did not increase the requirement of *ccs1Δ* for exogenous copper (fig. S11F), suggesting that histones contribute to copper utilization differently than Ctr1. Excess copper did not rescue the lysine auxotrophy of *sod1Δ* strains (fig. S11G), whereas hypoxia rescued the lysine auxotrophy of *ccs1Δ* and *sod1Δ* regardless of H3H113 (fig. S11H), indicating that H3H113 is relevant to this phenotype when Sod1 function is required.

Addition of manganese, zinc, or iron did not rescue *ccs1Δ* lysine auxotrophy (fig. S11I). The increased copper requirement of *H3<sup>H113N</sup>ccs1Δ* was not due to differences in Cup1-dependent

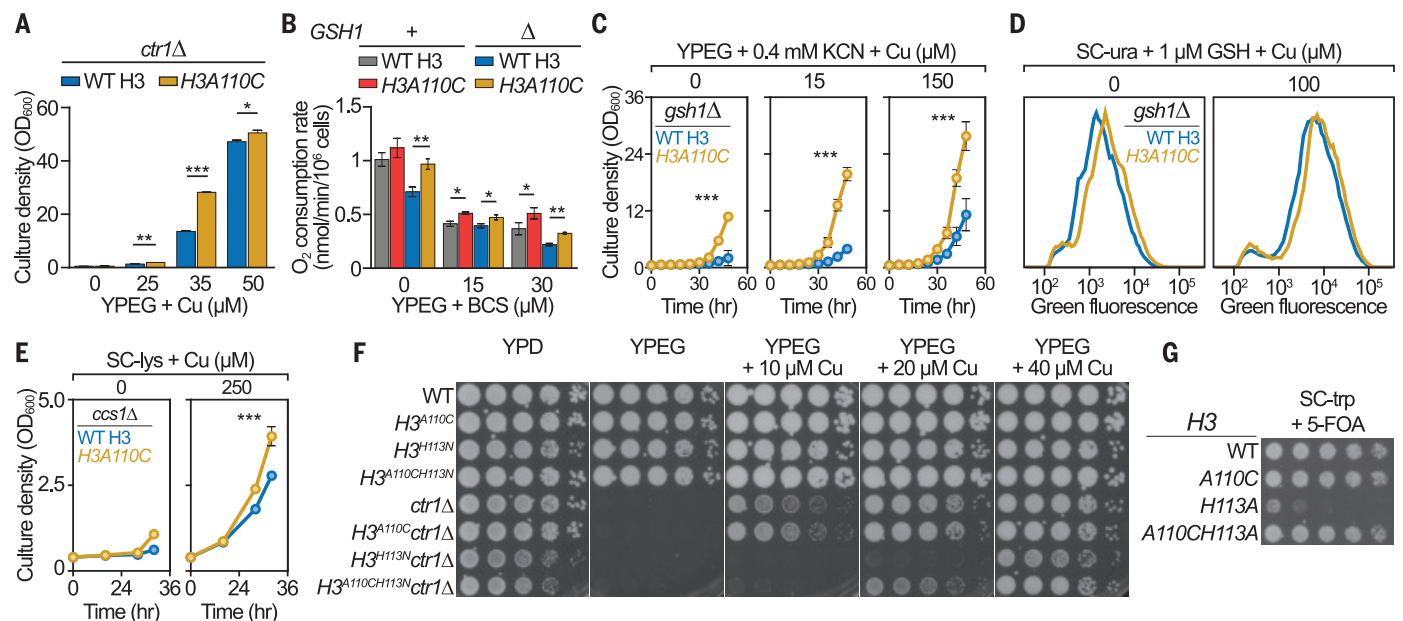


**Fig. 6. The *H3A110C* mutation enhances copper utilization in *S. cerevisiae*.**

(A) Growth after 48 hours in liquid YPEG with or without  $\text{CuSO}_4$ . Bars show mean optical density at a wavelength of 600 nm ( $\text{OD}_{600}$ )  $\pm$  SD from three experiments. (B) Oxygen consumption assays of cells grown in the indicated media for 12 hours. Bars show mean  $\pm$  SD of three experiments and are scaled to mitochondrial DNA contents. (C) Growth curves in YPEG with potassium cyanide (KCN) with or without  $\text{CuSO}_4$ . Lines show means at each time point  $\pm$  SD from three experiments. *P* value is

based on all time points. (D) Average flow cytometry distributions of cells containing the p<sup>(CUP1)</sup>-GFP plasmid grown in liquid media with or without  $\text{CuSO}_4$  from three experiments. (E) Same as (C) but for cells grown in SC lacking lysine (SC-lys) with or without  $\text{CuSO}_4$  from four experiments. (F) Spot test assays in media with or without  $\text{CuSO}_4$ . (G) Plasmid shuffle assay with strains harboring WT H3 on a URA3 plasmid and the indicated H3 gene on a TRP1 plasmid. 5-fluoroorotic acid (5-FOA) is lethal to cells that cannot lose the URA3 plasmid. \**P* < 0.05; \*\**P*  $\leq$  0.01; \*\*\**P*  $\leq$  0.001.



Cu<sup>1+</sup> sequestration (fig. S12A), intracellular copper and iron concentrations (fig. S12, B and C), or Asf1 (fig. S11E). Gene expression differences also did not account for defective copper utilization because *ccs1Δ* and *H3<sup>H113N</sup> ccs1Δ* displayed similar patterns (fig. S12, D to F). Altogether, our findings reveal that the H3H113 residue is also important for copper utilization by Sod1. The considerable impacts of H3H113 mutations on Cu<sup>1+</sup> abundance and on at least three separate copper-dependent functions support the model that the cupric reductase function of the H3-H4 tetramer regulates Cu<sup>1+</sup> availability in yeast.

### The H3A110C mutation enhances cuprous ion availability and copper utilization

The in vitro copper reductase results suggested that *H3A110C* might serve as a gain-of-function mutation to increase Cu<sup>1+</sup> and improve copper utilization in vivo. The yeast *H3<sup>A110C</sup>* strain grew similarly to WT cells (fig. S13A) but enhanced the ability of exogenous copper to restore the respiratory growth of *ctr1Δ* (Fig. 6A). We reasoned that increased provision of Cu<sup>1+</sup> might mitigate the depletion of cellular GSH. Indeed, *H3<sup>A110C</sup> gsh1Δ* grew better than *gsh1Δ* in copper-depleted respiratory conditions (fig. S13B) with a greater O<sub>2</sub> consumption rate (Fig. 6B and fig. S13C). *H3<sup>A110C</sup>* exhibited a copper-dependent growth advantage in the presence of a sublethal amount of potassium cyanide, an inhibitor of cytochrome c oxidase, independently of GSH abundance (Fig. 6C and fig. S13D). Correspondingly, the *H3<sup>A110C</sup> gsh1Δ* strain displayed greater Cup2 activity than *gsh1Δ* (Fig. 6D), indicating increased Cu<sup>1+</sup> abundance. Additionally, the *H3A110C* mutation enhanced the copper-dependent rescue of lysine auxotrophy in *ccs1Δ* (Fig. 6E). The *H3A110C* mutation even rescued the diminished Cup2 activity of *H3<sup>H113N</sup> ctr1Δ* (fig. S13E), the copper utilization defect of the *H3<sup>H113N</sup> ctr1Δ* strain (Fig. 6F), and the lethality of the *H3H113A* mutation (Fig. 6G), corroborating the opposing effects of the H3A110 and H3H113 mutations both in vivo and in vitro. These results highlight the advantage in copper utilization conferred by the *H3A110C* mutation and further support that the yeast histone H3 regulates the Cu<sup>1+</sup> pool and copper utilization.

### Discussion

Histones have been known as packaging and regulatory proteins for the eukaryotic genome. We now reveal that the histone H3-H4 tetramer is also a cupric reductase that provides usable Cu<sup>1+</sup> for the cell. The enzymatic activity suggests that the protein complex has many uncharacterized features, including a catalytic site at the H3-H3' interface, that contribute to Cu<sup>2+</sup> binding, increasing its reduction potential and promoting electron transfer (28).

The H3-H3' interface forms in vivo mostly during nucleosome assembly. Therefore, the commencement of enzymatic activity may be coupled to the protection of DNA as it wraps around the nucleosome. Such a coupling may decrease the toxicity of Cu<sup>1+</sup> by the very enzymes that produce it as a beneficial adaptation in species that require its intracellular use. However, proteins such as Spt2 (13) may stabilize the H3-H3' interface outside of the nucleosomal context, affecting regulation and timing of enzymatic activity relative to other chromatin-based events.

The mechanism of electron transfer by the tetramer is unclear but may involve direct transfer from reductants to Cu<sup>2+</sup> at the active site or through a chain of residues from a distant site (29, 30). Copper is present in the nucleus (31, 32) but is likely bound (33) and transported to and from histones through as-yet-to-be-identified chaperones, possibly including Atox1 (34). Copper disproportionately accumulates in the nucleus when its cellular efflux is compromised, such as in Wilson's disease (35, 36), suggesting that the nucleus is a major transit hub for cellular copper.

The oxidoreductase function of the H3-H4 tetramer provides a reasonable hypothesis for why the archaeal ancestor of the eukaryotes possessed histone tetramers. Such enzymatic activity, with an associated intracellular Cu<sup>1+</sup> transit system, could have helped maintain a functioning ETC in the proto-mitochondria, thereby making the presence of histones in the ancestral archaeon not incidental (37), but rather essential for eukaryogenesis.

### REFERENCES AND NOTES

1. F. Mattioli et al., *Science* **357**, 609–612 (2017).
2. A. Kaufman Katz et al., *Helv. Chim. Acta* **86**, 1320–1338 (2003).
3. S. Ramachandran, L. Vogel, B. D. Strahl, N. V. Dokholyan, *PLOS Comput. Biol.* **7**, e1001042 (2011).
4. R. A. Saavedra, *Science* **234**, 1589–1589 (1986).
5. M. Adamczyk, J. Poznański, E. Kopera, W. Bal, *FEBS Lett.* **581**, 1409–1416 (2007).
6. W. Bal, J. Lukszo, M. Jezowska-Bojczuk, K. S. Kasprzak, *Chem. Res. Toxicol.* **8**, 683–692 (1995).
7. A. D. Anbar, *Science* **322**, 1481–1483 (2008).
8. M. A. Saito, D. M. Sigman, F. M. M. Morel, *Inorg. Chim. Acta* **356**, 308–318 (2003).
9. T. Nevitt, H. Ohrvik, D. J. Thiele, *Biochim. Biophys. Acta* **1823**, 1580–1593 (2012).
10. R. A. Pufahl et al., *Science* **278**, 853–856 (1997).
11. P. N. Dyer et al., *Methods Enzymol.* **375**, 23–44 (2004).
12. E. I. Solomon, M. D. Lowery, L. B. LaCroix, D. E. Root, *Methods Enzymol.* **226**, 1–33 (1993).
13. S. Chen et al., *Genes Dev.* **29**, 1326–1340 (2015).
14. T. A. Klink, K. J. Woycechowsky, K. M. Taylor, R. T. Raines, *Eur. J. Biochem.* **267**, 566–572 (2000).
15. S. A. Forbes et al., *Nucleic Acids Res.* **43**, D805–D811 (2015).
16. J. G. Mesu et al., *Inorg. Chem.* **45**, 1960–1971 (2006).
17. H. Huang et al., *Genome Res.* **19**, 674–681 (2009).
18. J. A. Graden, D. R. Winge, *Proc. Natl. Acad. Sci. U.S.A.* **94**, 5550–5555 (1997).
19. A. Dancis, D. Haile, D. S. Yuan, R. D. Klausner, *J. Biol. Chem.* **269**, 25660–25667 (1994).

20. G. N. George, J. Byrd, D. R. Winge, *J. Biol. Chem.* **263**, 8199–8203 (1988).
21. D. J. Thiele, *Mol. Cell. Biol.* **8**, 2745–2752 (1988).
22. M. Agez et al., *Structure* **15**, 191–199 (2007).
23. M. W. Adkins, S. R. Howar, J. K. Tyler, *Mol. Cell* **14**, 657–666 (2004).
24. R. Hassett, D. J. Kosman, *J. Biol. Chem.* **270**, 128–134 (1995).
25. J. H. Freedman, M. R. Ciriolo, J. Peisach, *J. Biol. Chem.* **264**, 5598–5605 (1989).
26. Y. Furukawa, A. S. Torres, T. V. O'Halloran, *EMBO J.* **23**, 2872–2881 (2004).
27. S. J. Lin, V. C. Culotta, *Mol. Cell. Biol.* **16**, 6303–6312 (1996).
28. J. Liu et al., *Chem. Rev.* **114**, 4366–4469 (2014).
29. M. F. Lucas, D. L. Rousseau, V. Guallar, *Biochim. Biophys. Acta* **1807**, 1305–1313 (2011).
30. K. R. Williams et al., *J. Am. Chem. Soc.* **119**, 613–614 (1997).
31. R. McRae, B. Lai, C. J. Fahrni, *Metallomics* **5**, 52–61 (2013).
32. L. Yang et al., *Proc. Natl. Acad. Sci. U.S.A.* **102**, 11179–11184 (2005).
33. T. D. Rae, P. J. Schmidt, R. A. Pufahl, V. C. Culotta, T. V. O'Halloran, *Science* **284**, 805–808 (1999).
34. S. Itoh et al., *J. Biol. Chem.* **283**, 9157–9167 (2008).
35. D. Huster et al., *Am. J. Pathol.* **168**, 423–434 (2006).
36. J. L. Burkhead, M. Ralle, P. Wilmarth, L. David, S. Lutsenko, *J. Mol. Biol.* **406**, 44–58 (2011).
37. K. Sandman, J. N. Reeve, *Science* **280**, 499 (1998).
38. C. A. Davey, D. F. Sargent, K. Luger, A. W. Maeder, T. J. Richmond, *J. Mol. Biol.* **319**, 1097–1113 (2002).
39. C. Gross, M. Kelleher, V. R. Iyer, P. O. Brown, D. R. Winge, *J. Biol. Chem.* **275**, 32310–32316 (2000).

### ACKNOWLEDGMENTS

We thank H. Christofk for discussions, M. Thompson for proofreading, M. Morselli for RNA sequencing assistance, V. Culotta for the anti-SOD1 antibody and helpful guidance in Sod1 assays, M. Phillips and W. Silkworth of the UCLA-DOE Institute, and the UCLA Broad Stem Cell Center Sequencing Core. **Funding:** This work was supported by a W. M. Keck Foundation Award to S.K.K. and S.S.M. and by NIH grants CA178415 to S.K.K., GM074701 to M.F.C., GM42143 to S.S.M., and CA188592 to M.V. O.A.C. was supported by the Whitcome; O.A.C. and C.C. by UCLA Dissertation Year Fellowships; N.A. by the NCI Ruth L. Kirschstein NRSA CA186619 and NIH GM8042; L.S. by NIH GM123126; L.Y. by the NCI Ruth L. Kirschstein NRSA GM007185; S.Z. by the Amgen Scholars Program; the UCLA JCCC flow cytometry core by NIH P30 CA016042 and 5P30 A1028697; and the UCLA-DOE Institute by DE-FC02-02ER63421. **Author contributions:** N.A., O.A.C., and M.V. contributed equally to this work and are listed alphabetically. Conceptualization: N.A., O.A.C., M.V., Y.X., and S.K.K.; Methodology: N.A., O.A.C., M.V., Y.X., M.F.C., S.S.M., and S.K.K.; Investigation: N.A., O.A.C., M.V., Y.X., C.C., S.S., L.S., N.V.M., B.A.B., L.Y., S.Y., S.Z., J.D., and S.K.K.; Formal analysis: N.A., O.A.C., and M.V.; Writing – original draft: N.A., O.A.C., M.V., and S.K.K.; Writing – review & editing: N.A., O.A.C., M.V., Y.X., L.Y., S.S., M.F.C., S.S.M., and S.K.K.; Resources: N.A., O.A.C., M.V., C.C., L.Y., M.F.C., S.S.M., and S.K.K.; Visualization: N.A., O.A.C., and M.V.; Supervision: S.K.K.; Project administration: S.K.K.; Funding acquisition: M.F.C., S.S.M., and S.K.K. **Competing interests:** The authors declare no competing interests. **Data and materials availability:** All data are available in the main text or the supplementary materials. Gene expression datasets are available on the NCBI GEO database (GSE100034).

### SUPPLEMENTARY MATERIALS

science.sciencemag.org/content/369/6499/59/suppl/DC1  
Materials and Methods  
Figs. S1 to S13  
Table S1  
References (40–56)  
MDAR Reproducibility Checklist

13 January 2020; accepted 13 May 2020  
10.1126/science.aba8740

## CLIMATE RESPONSES

# Thermal bottlenecks in the life cycle define climate vulnerability of fish

Flemming T. Dahlke<sup>1\*</sup>, Sylke Wohlrab<sup>1,2</sup>, Martin Butzin<sup>1</sup>, Hans-Otto Pörtner<sup>1,3\*</sup>

Species' vulnerability to climate change depends on the most temperature-sensitive life stages, but for major animal groups such as fish, life cycle bottlenecks are often not clearly defined. We used observational, experimental, and phylogenetic data to assess stage-specific thermal tolerance metrics for 694 marine and freshwater fish species from all climate zones. Our analysis shows that spawning adults and embryos consistently have narrower tolerance ranges than larvae and nonreproductive adults and are most vulnerable to climate warming. The sequence of stage-specific thermal tolerance corresponds with the oxygen-limitation hypothesis, suggesting a mechanistic link between ontogenetic changes in cardiorespiratory (aerobic) capacity and tolerance to temperature extremes. A logarithmic inverse correlation between the temperature dependence of physiological rates (development and oxygen consumption) and thermal tolerance range is proposed to reflect a fundamental, energetic trade-off in thermal adaptation. Scenario-based climate projections considering the most critical life stages (spawners and embryos) clearly identify the temperature requirements for reproduction as a critical bottleneck in the life cycle of fish. By 2100, depending on the Shared Socioeconomic Pathway (SSP) scenario followed, the percentages of species potentially affected by water temperatures exceeding their tolerance limit for reproduction range from ~10% (SSP 1–1.9) to ~60% (SSP 5–8.5). Efforts to meet ambitious climate targets (SSP 1–1.9) could therefore benefit many fish species and people who depend on healthy fish stocks.

The identification of biological patterns and underlying principles is fundamental for understanding and predicting ecological processes (1), including climate change effects (2). A central observation in this context is that aquatic ectothermic animals such as fish have specific temperature limits and tolerance ranges, which determine their latitudinal distribution limits and sensitivity to climate change (3). Mechanistic prin-

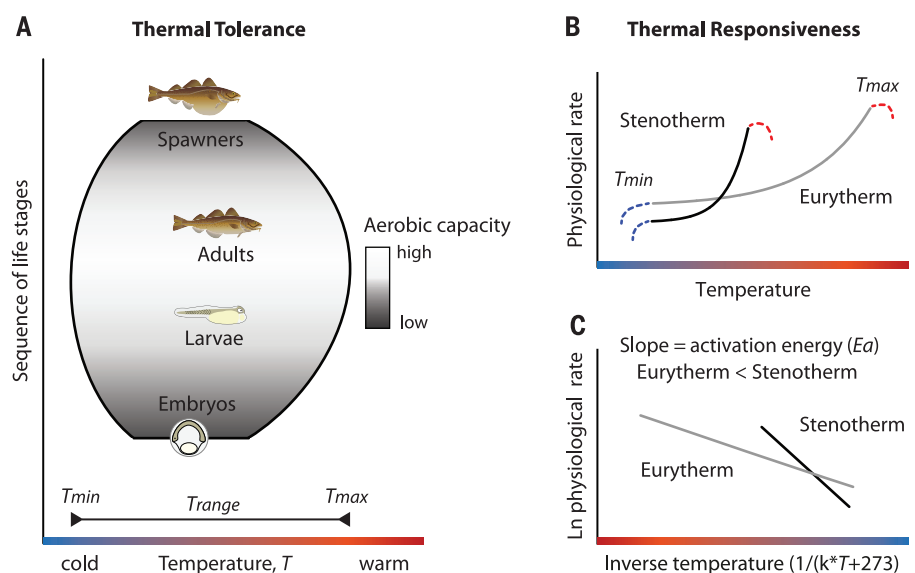
ciples potentially related to this pattern include the temperature dependence of physiological rates and thus oxygen (O<sub>2</sub>) demand (4, 5). Different cardiorespiratory capacities to sustain adequate O<sub>2</sub> supply to tissues during temperature changes are suggested to explain why tolerance ranges are narrower for some fish species than for others (6). Thermal tolerance is also expected to change during the life cycle of species according to the development of aerobic

capacities in relation to O<sub>2</sub> demand (2, 7) (Fig. 1A). Specifically, tolerance ranges are hypothesized to widen from embryo to larval and adult stages after the development of cardiorespiratory organs (7, 8). During reproduction (spawning stage), tolerance ranges may narrow again as the result of a net decrease in aerobic capacity associated with additional energy and thus O<sub>2</sub> demand for gamete production and biomass (2, 7). These principles are supported by empirical data for some well-studied species such as Atlantic cod (*Gadus morhua*) (6), but it is currently unknown whether the proposed ontogenetic shift in thermal tolerance represents a globally consistent pattern.

Thermal adaption of species and life stages to local climatic conditions probably involves energetic optimizations and trade-offs (9, 10). Available data suggest that tolerance ranges are as narrow as possible to ensure survival under local conditions while minimizing costs for maintaining homeostasis over wide temperature ranges (6). Consequently, tolerance ranges are expected to reflect the magnitude of local temperature variability (11), with wider tolerance ranges in temperate regions relative to polar and tropical regions (12). Potential trade-offs between energy efficiency and thermal tolerance may be linked to thermodynamic properties of metabolic processes (i.e., thermal responsiveness) (9, 13). Mechanistic theory predicts that “stenothermal” organisms with narrow temperature ranges display higher thermal responsiveness than more tolerant “eurythermal” organisms (13) (Fig. 1, B and C). In contrast, the concept of universal temperature dependence implies that there is no variation

**Fig. 1. Thermal tolerance differs between life stages, and thermal responsiveness is higher in stenothermal than in eurythermal organisms.**

(A) Lower and upper temperature thresholds ( $T_{\min}$  and  $T_{\max}$ ) are defined as ultimate temperature limits that relate to behavioral avoidance, impaired physiological functions, and mortality (22), thereby reflecting limits to the geographic distribution of species (3, 4). The specific temperature ranges ( $T_{\text{range}} = T_{\max} - T_{\min}$ ) of species are expected to differ between life stages according to changes in the relationship between oxygen demand and supply capacity (4). This hypothesis implies that from embryo to adult, aerobic capacity (and thus  $T_{\text{range}}$ ) increases with the development of the cardiorespiratory system, but then declines again with increasing body size. During the spawning season, aerobic capacity and  $T_{\text{range}}$  may decrease further as a result of additional energy requirements for the production of gametes and their biomass (2, 7). (B) Physiological rates (solid lines) are temperature-dependent and typically scale exponentially within  $T_{\text{range}}$  (1). Lines with different slopes suggest that stenothermal species or life stages with narrow  $T_{\text{range}}$  (black line) are more responsive (steeper slope) than eurythermal ones (gray line) (13). As a benefit, the energy demand of stenotherms may be lower than that of eurytherms (49). (C) Thermal responsiveness is quantified in Arrhenius form (log-transformed rate versus inverse absolute temperature) and is expressed as activation energy ( $E_a$ ) in electron volts (27).





in thermal responsiveness among ectothermic species [(14), but see (15, 16)].

Fish usually reproduce at certain times of the year (spawning seasons) and in certain places (spawning habitats) that provide suitable conditions for offspring survival (17, 18). Reproductive success is likely at risk under climate change when spawning habitat temperatures exceed the tolerance limit of the most sensitive life stage, forcing species to reproduce at different times and/or places (18). To date, mainly because of the scarcity of experimental data, potential life cycle bottlenecks in thermal tolerance are rarely considered in large-scale risk assessments (19–21), limiting our ability to determine whether climate mitigation targets are sufficient to sustain healthy fish stocks. Here, we address this limitation by combining experimental and observational data as well as phylogenetic data imputation (22) to generate a comprehensive set of stage-specific thermal tolerance metrics for 694 marine and freshwater fish species from all climate zones. With this dataset, we addressed the following hypotheses: (i) Upper and lower temperature limits ( $T_{\max}$ ,  $T_{\min}$ ) and temperature ranges ( $T_{\text{range}} = T_{\max} - T_{\min}$ ) differ consistently between life stages (Fig. 1A). (ii) Thermal responsiveness is higher in stenothermal organisms than in eurythermal ones (Fig. 1B). Furthermore, stage-specific tolerance limits were used to assess climatic risks under different Shared Socio-economic Pathway (SSP) scenarios of global change developed during the sixth phase of the Coupled Model Intercomparison Project (CMIP6) (23).

### Thermal tolerance depends on phylogeny, geographic origin, and ontogeny

We collated empirical thermal tolerance data of four life stages: egg stage (“embryos”), pre-metamorphosis stage (“larvae”), post-metamorphosis stage (“adults”), and reproductive stage (“spawners”). Data on embryos, larvae, and adults are experimental estimates of physiological ultimate temperature limits (22). Because experimental data for spawners are extremely scarce, in situ observations (e.g., fisheries monitoring and tagging data) of behavioral temperature limits were considered for this life stage. A direct comparison revealed no significant difference between experimental and observational  $T_{\max}$  data of spawners (two-sided paired  $t$  test,  $P = 0.189$ ,  $n = 15$  species; fig. S1 and table S1). Temperature ranges ( $T_{\text{range}}$ ) were estimated as the difference between  $T_{\max}$  and  $T_{\min}$ . Midpoint temperatures ( $T_{\text{mid}}$ ) are

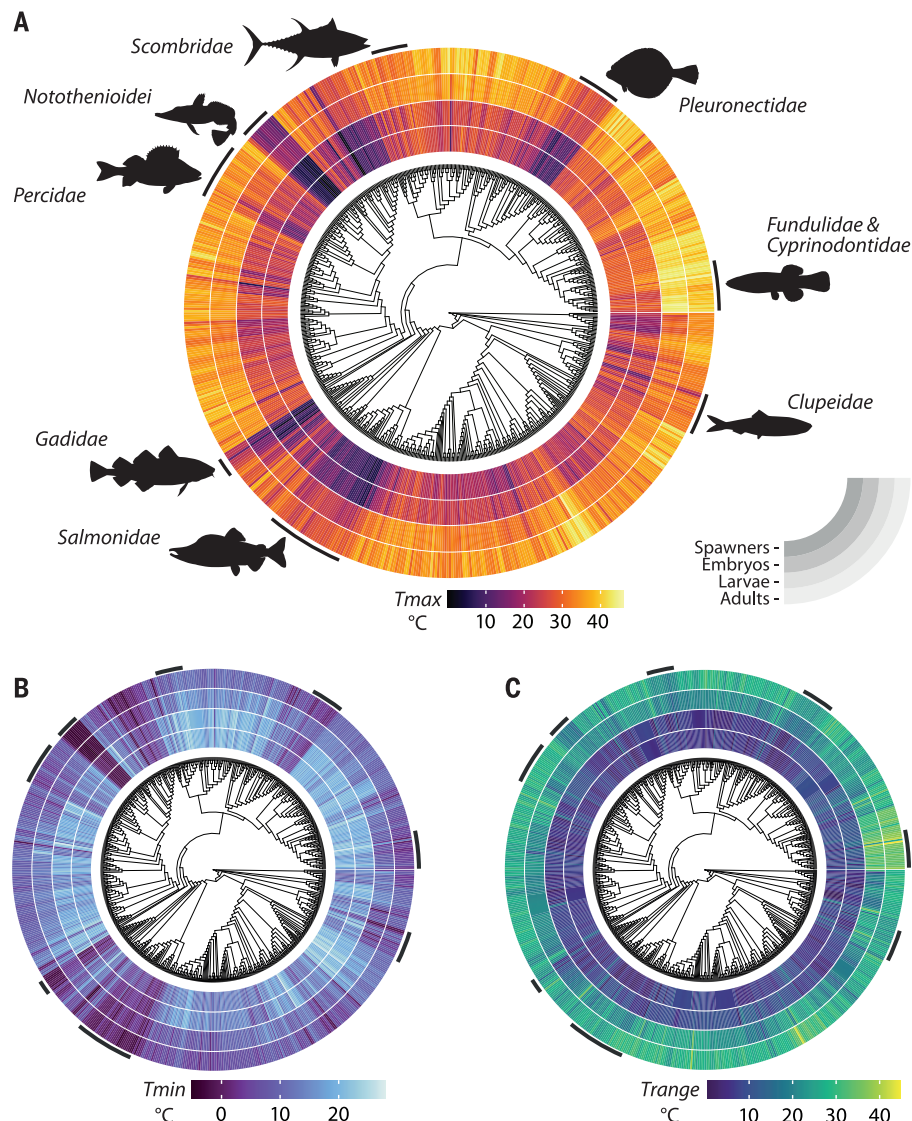


**Fig. 2. Phylogenetic and ontogenetic patterns in thermal tolerance of fish.** (A to C) Circular chronograms show upper temperature limits ( $T_{\max}$ ) (A), lower temperature limits ( $T_{\min}$ ) (B), and thermal tolerance ranges ( $T_{\text{range}}$ ) (C) of species and their life stages from inside to outside: spawners, embryos, larvae, and adults. Prominent taxonomic groups as well as particularly warm-eurythermal (Fundulidae and Cyprinodontidae) and cold-stenothermal groups (Notothenioidei) are highlighted.

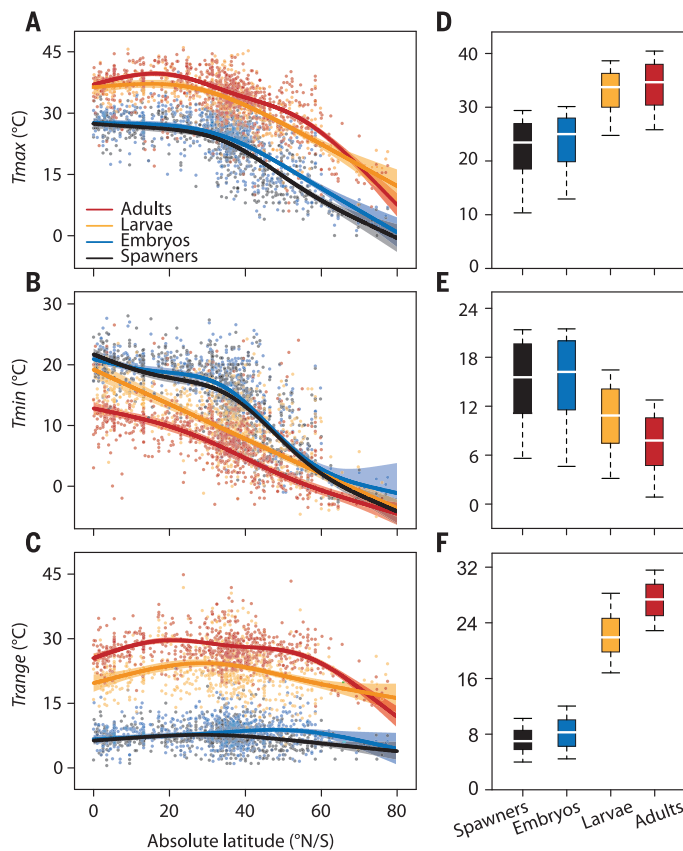
either observed temperature optima or arithmetic means of  $T_{\min}$  and  $T_{\max}$ . For 694 of 777 species, we obtained at least one empirical thermal tolerance metric ( $T_{\max}$ ,  $T_{\min}$ , or  $T_{\text{mid}}$ ) as well as time-calibrated phylogeny from the Fish Tree of Life (24). Phylogenetic imputation (22) was then used to estimate missing  $T_{\max}$  and  $T_{\min}$  values. We confirmed phylogenetic niche conservatism (i.e., similar trait values among closely related species) as a prerequisite for reliable data imputation (25) a priori, based on phylogenetic signal indices (Pagel's  $\lambda$ ,  $P < 0.001$ ; table S2). Precision of imputed data was assessed on the basis of correlation analysis and variance estimation (fig. S2 and table

S3). Ontogenetic differences in thermal tolerance were assessed using generalized additive models (GAMs), taking into account variation related to geographic origin (latitude and marine versus freshwater) as well as uncertainty related to data imputation by including the inverse of estimated variances as weights.

The completed dataset (26) reveals phylogenetic and ontogenetic patterns in thermal tolerance of fish (Fig. 2). In addition to existing evidence for niche conservatism in adult fish (20), we find that phylogenetic clustering of temperature limits ( $T_{\max}$  and  $T_{\min}$ ; Fig. 2, A and B) and tolerance ranges ( $T_{\text{range}}$ ; Fig. 2C) is consistent across life stages (table S2). In line

<sup>1</sup>Alfred Wegener Institute, Helmholtz Centre for Polar and Marine Research, 27570 Bremerhaven, Germany. <sup>2</sup>Helmholtz Institute for Functional Marine Biodiversity, 26129 Oldenburg, Germany. <sup>3</sup>University of Bremen, 28359 Bremen, Germany. \*Corresponding author. Email: flemming.dahlke@gmx.de (F.T.D.); hans.poertner@awi.de (H.-O.P.)

**Fig. 3. Ontogenetic changes in thermal tolerance are consistent across latitudes. (A to C)** Upper temperature limits ( $T_{\max}$ ) (A), lower temperature limits ( $T_{\min}$ ) (B), and thermal tolerance ranges ( $T_{\text{range}} = T_{\max} - T_{\min}$ ) (C) of spawners (black), embryos (blue), larvae (orange), and adults (red) as a function of absolute latitude. Regression fits (solid lines) with 95% CIs (colored shadings) are based on generalized additive models (GAM,  $P < 0.0001$ ;  $n = 698$  to 735 for each life stage), accounting for uncertainty related to phylogenetic data imputation (22). Only the correlation between latitude and  $T_{\text{range}}$  of embryos (C) is not significant ( $P > 0.05$ ). (D to F) Corresponding to (A)



to (C), box plots indicate differences in  $T_{\max}$ ,  $T_{\min}$ , and  $T_{\text{range}}$  between life stages. Boxes and whiskers show 25th to 75th and 10th to 90th percentiles, respectively; white lines indicate the median. When accounting for geographic variation (latitude and marine versus freshwater; table S4), life stages differ significantly in terms of  $T_{\max}$ ,  $T_{\min}$ , and  $T_{\text{range}}$  (two-sided pairwise comparisons with Tukey correction, all  $P < 0.05$ ).

with expected ontogenetic shifts in aerobic capacity (2), we find that  $T_{\text{range}}$  is narrower for spawners and embryos than for larvae and adults (GAM,  $P < 0.0001$ ; Fig. 2C and table S4). Ontogenetic differences in thermal tolerance metrics are also consistent across latitudes (Fig. 3, A to C) and aquatic realms (i.e., marine and freshwater) (fig. S3). In support of the climate variability hypothesis (11),  $T_{\text{range}}$  tends to decrease toward high and low latitudes (Fig. 3C and table S4), with the most stenothermal species found in the Antarctic Ocean (Antarctic icefishes, Notothenioidae) and the most eurythermal ones in temperate freshwater systems (killifishes, Fundulidae) (Fig. 2A). Thermal tolerance ranges of freshwater species and their life stages are on average  $\sim 1^\circ\text{C}$  wider than for marine species (GAM,  $P < 0.0001$ ; fig. S3), probably reflecting higher temperature variability in lakes and rivers than in oceans. When accounting for geographic variation in thermal tolerance metrics, mean  $T_{\text{range}}$  values [ $\pm 95\%$  confidence intervals (CIs)] increase by more than  $20^\circ\text{C}$  from spawners ( $7.2^\circ \pm 0.3^\circ\text{C}$ ) and embryos ( $8.4^\circ \pm 0.4^\circ\text{C}$ ) to larvae ( $22.3^\circ \pm 0.7^\circ\text{C}$ )

and adults ( $27.5^\circ \pm 0.4^\circ\text{C}$ ) (Fig. 3F). These results clearly identify the temperature requirements of spawners and embryos as critical bottlenecks in the life cycle of fish.

#### Thermal responsiveness is inversely correlated with thermal tolerance

Thermal responsiveness and its correlation with thermal tolerance ( $T_{\text{range}}$ ) were assessed on the basis of the temperature dependence of development rate (DR) and oxygen consumption rate ( $\text{MO}_2$ ) of embryos (DR and  $\text{MO}_2$ , 83 species), larvae ( $\text{MO}_2$ , 16 species) and adults ( $\text{MO}_2$ , 54 species) (26). Direct comparison of the temperature dependences of DR and  $\text{MO}_2$  revealed no systematic difference between them (fig. S4). Only experimental data measured under controlled, noncritical temperature conditions were used (22). Individual responses (Fig. 4A) were evaluated using the Boltzmann-Arrhenius function (27), in which the scaling of physiological rates ( $R$ ) with temperature ( $T$ ) is

$$R = R_0 \exp\left(\frac{-E_a}{kT}\right) \quad (1)$$

Thermal responsiveness is given by the value of  $-E_a$  in electron volts (eV, positivized hereafter), which is the activation energy of the rate-limiting biochemical (metabolic) process,  $R_0$  is an organism-specific coefficient, and  $k$  is Boltzmann's constant. Analyses of ontogenetic differences in  $E_a$  (linear mixed-effect model, LMM) and the correlation between  $E_a$  and  $T_{\text{range}}$  (generalized additive mixed-effect model, GAMM) accounted for phylogenetic nonindependence.

Thermal responsiveness of embryos is on average 24% higher than in larvae and adults (LMM,  $P < 0.0001$ ; Fig. 4B). Thermal responsiveness of embryos (mean  $E_a$ , 0.87 eV; 95% CI, 0.83 to 0.91 eV) also exceeds the range predicted by the universal temperature dependence concept (0.6 to 0.7 eV) (14). The correlation between  $E_a$  and  $T_{\text{range}}$  (GAMM,  $P < 0.0001$ ; Fig. 4C) supports the hypothesis that the metabolism of stenotherms is more responsive to temperature changes than that of eurytherms (4, 13). The correlation between  $E_a$  and  $T_{\text{range}}$  is also consistent within life stages (embryos and adults) and within individual species such as Atlantic cod (fig. S5). These results suggest that temperature-rate responses do not strictly conform to statistical thermodynamics (14) but instead may reflect an outcome of energetic optimizations (reduction of costs) and trade-offs related to lifestyle and ontogeny (10). Biophysical models using a generalized  $E_a$  of 0.6 to 0.7 eV (14, 28) rather than the actual responsiveness of fish species or life stages may therefore lead to imprecise projections of ecological processes. For example, a scenario that assumes  $3^\circ\text{C}$  warming and an embryonic  $E_a$  of 0.65 eV would underestimate the change in development time of Atlantic cod embryos ( $E_a = 0.92$  eV) (29) and associated probability functions (e.g., predation mortality) by  $\sim 80\%$  (fig. S6).

#### Safety margins of critical life stages define species' vulnerability to warming

The vulnerability of species to climate warming is often assessed according to the difference between the upper thermal tolerance limit ( $T_{\max}$ ) of adult life stages and the maximum habitat temperature during summer—a metric called the thermal safety margin (TSM). However, the tolerance of adults to summer heat is potentially less critical for the persistence of species than the ultimate temperature limit for reproduction, which we assessed on the basis of  $T_{\max}$  of spawners and embryos. Specifically, we compared current and future TSMs of adults (the difference between  $T_{\max}$  and the mean temperature of the warmest summer month) with the TSMs of spawners and embryos, estimated as the difference between their  $T_{\max}$  and the mean temperature of the coldest month during the species-specific spawning season [mainly spring or monsoon time (22)]. In



**Fig. 4. Thermal responsiveness is higher in stenothermal life stages.** (A) Exponential temperature responses of embryos (blue), larvae (orange), and adults (red) based on Eq. 1.

Thermal responsiveness is indicated by the slope of individual responses (thin lines). Thick lines indicate the median responsiveness of different life stages. Normalization (response values estimated at any temperature divided by their value at 15°C) was done for illustrative purposes. (B) Thermal responsiveness expressed as Arrhenius activation energy ( $E_a$  in electron volts, eV). Box plots (as in Fig. 3) with different letters indicate significant differences between life stages (two-sided pairwise comparisons with Tukey correction,  $P < 0.05$ ).

(C) Correlation between thermal responsiveness and thermal tolerance of different life stages (colored symbols). The regression fit (line with 95% CIs as shading) accounts for phylogenetic nonindependence (generalized additive mixed-effect model, GAMM).

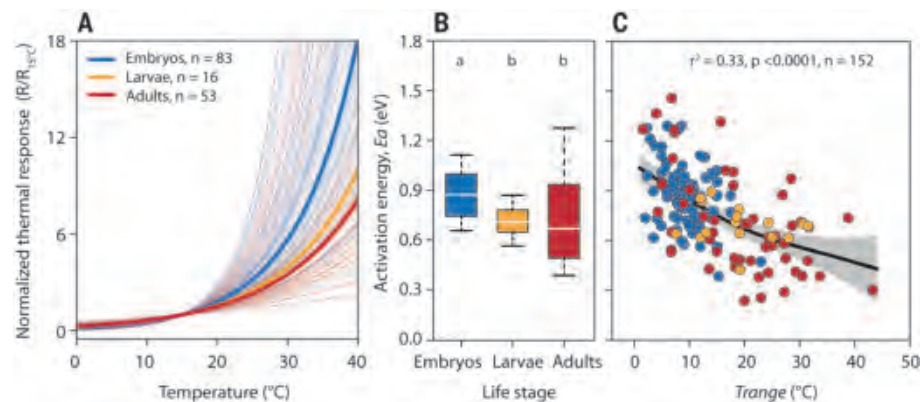
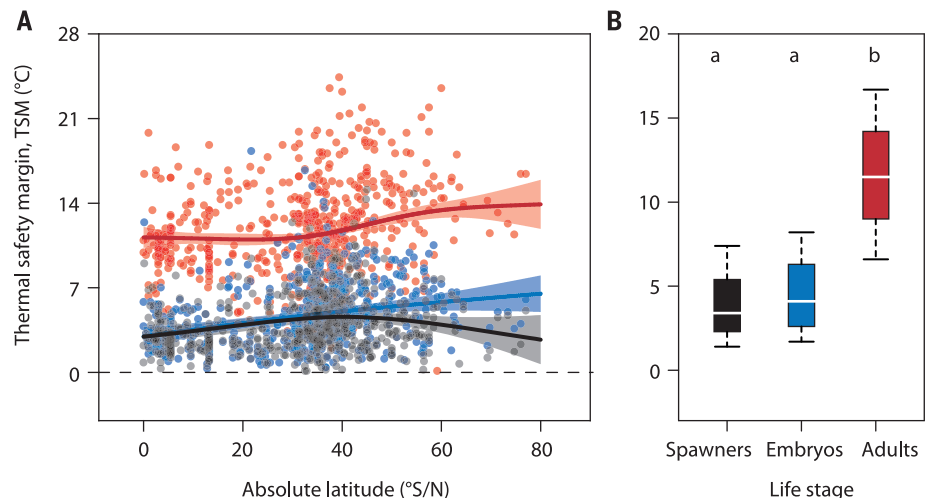


**Fig. 5. Smaller safety margins of spawners and embryos versus adults.** (A) Thermal safety margins (TSMs) of spawners (black), embryos (blue), and adults (red) based on recent habitat (water) temperatures (1981 to 2000) as a function of absolute latitude.

Regression fits (colored lines) with 95% CIs as shadings are based on generalized additive models (GAM,  $P < 0.0001$ ;  $n = 543$  for spawners, 554 for embryos, 580 for adults; 630 species in total), taking into account uncertainty related to phylogenetic data imputation (24). (B) Corresponding to (A), box plots (as in Fig. 3) with different letters indicate significant differences between TSMs of different life stages (two-sided pairwise comparisons with Tukey correction,  $P < 0.05$ ).



this way, future TSMs of spawners and embryos indicate whether climate change will affect the ability of species to reproduce at preferred times and locations. Seasonal habitat temperatures of adults, spawners, and embryos [630 species (26)] are spatial averages according to distribution records, depth preferences, spawning times and locations, and temperature data of atmospheric and ocean reanalyses (current TSMs, 1981 to 2000) and SSP climate projection scenarios (future TSMs, 20-year averages until 2100) (22). Deep-sea species (>500 m) and species with unknown spawning times were excluded. Selected SSPs include a low radiative forcing scenario consistent with 1.5°C warming by 2100 (SSP 1–1.9), a medium-forcing scenario (SSP 4–6.0), and a high-forcing scenario (SSP 5–8.5) representing a warming of about 5°C relative to preindustrial levels (23).

Current TSMs (mean  $\pm$  95% CI; Fig. 5) are significantly narrower for spawners ( $4.1^\circ \pm 0.3^\circ\text{C}$ ) and embryos ( $4.5^\circ \pm 0.4^\circ\text{C}$ ) than for adults ( $11.6^\circ \pm 0.3^\circ\text{C}$ ) (GAM,  $P < 0.0001$ ;  $n = 1677$ ) (table S5). Differences in TSMs of marine and

freshwater species are not significant (GAM,  $P = 0.0663$ ), and large variability found at all latitudes implies that regional climatology plays a less important role than microclimatic conditions in shaping stage-specific TSMs of marine and freshwater species. The narrowest TSMs of spawners and embryos (TSM between  $1^\circ$  and  $0^\circ\text{C}$ ,  $n = 37$ ; Fig. 5) indicate that some marine and freshwater species from different latitudes may already experience critically warm temperature conditions for reproduction. Although we note that the horizontal resolution of observed and simulated habitat temperatures ( $1^\circ \times 1^\circ$ ) is not always sufficient to capture specific microclimates, the cutoff threshold for considering a species at risk from future warming is set to  $\text{TSM} \leq 0.0^\circ\text{C}$ .

Projected changes in TSMs of the most sensitive life stage (67% spawners and 33% embryos) differ considerably between species and emission scenarios (Fig. 6 and figs. S7 to S9). By the end of this century, more than 60% (median of five models) of marine and freshwater species considered in this study could be con-

fronted with water temperatures exceeding tolerance limits in their current habitat ( $\text{TSM} \leq 0.0^\circ\text{C}$ ) if emissions continue to rise unabated (SSP 5–8.5; Fig. 6B). TSMs below zero indicate that reproduction at preferred seasons and locations is no longer possible, forcing species to adapt or shift their spawning activity into cooler seasons or regions to avoid extinction. Emission pathways consistent with current political commitments (SSP 4–6.0) would still threaten more than one-third of the marine and freshwater species under consideration (Fig. 6B). A positive outlook is that the percentage of species at risk could be reduced to 10 to 15% if global warming is limited to 1.5°C (SSP 1–1.9; Fig. 6B), in line with the Paris Agreement (30). For comparison, when considering adult TSMs only, the fraction of species below the cutoff threshold is below 5% under SSP 5–8.5 (Fig. 6B). Accordingly, although assessments based on adult temperature limits or proxies thereof (e.g., species distribution records) can provide important information on the geographical distribution

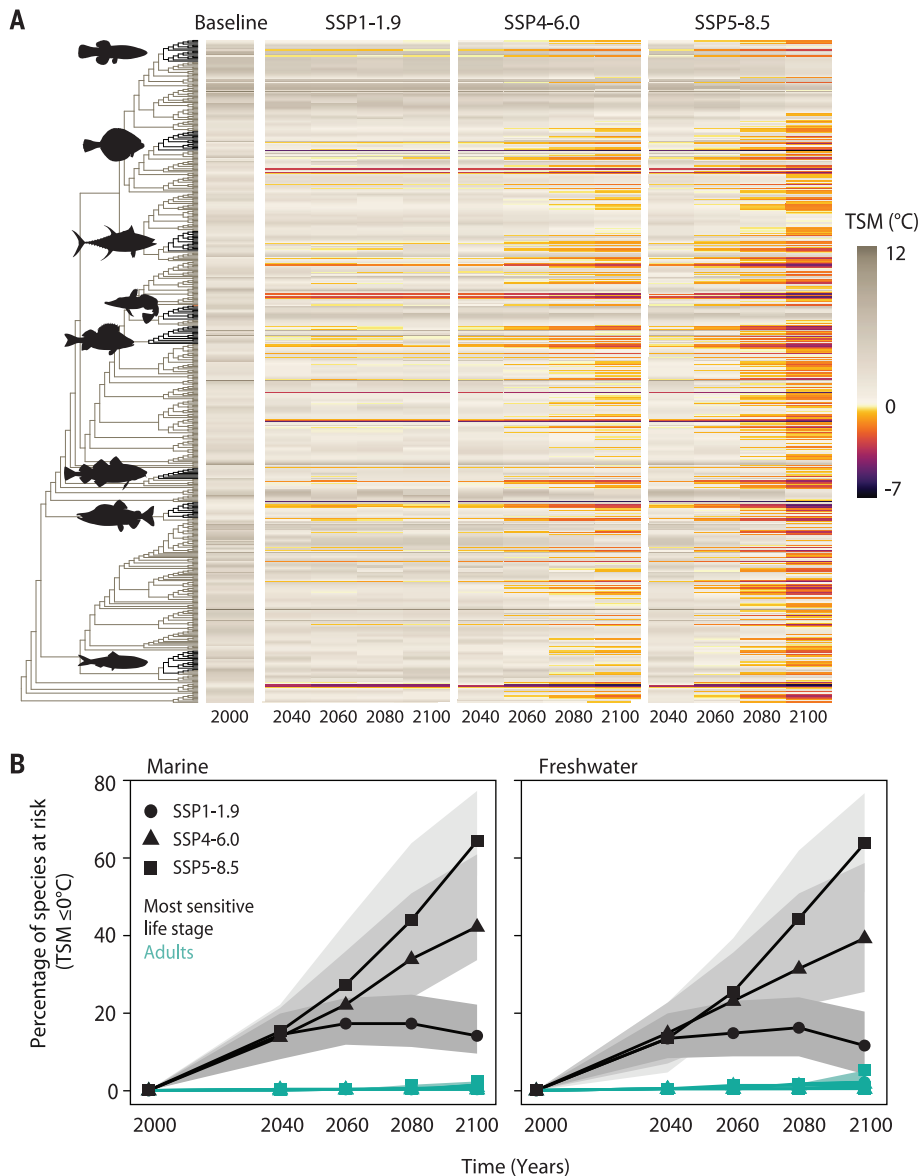


**Fig. 6. Shrinking safety margins of critical life stages put many fish species at risk in their current habitat. (A)** Cladogram for investigated fish species with tips colored according to estimated TSMs for recent conditions (1981 to 2000), and future Shared Socioeconomic Pathway (SSP) scenarios considering the TSM of the most critical life stages (~67% spawners, ~33% embryos) in their respective habitats. SSP scenarios were developed during the sixth phase of the Coupled Model Intercomparison Project (CMIP6), representing low (SSP 1–1.9), intermediate (SSP 4–6.0), and high (SSP 5–8.5) radiative forcing pathways (23). **(B)** Median percentage of marine ( $n = 367$ ) and freshwater species ( $n = 263$ ) with TSMs less than or equal to 0.0°C. Black lines consider TSMs of the most sensitive life stage; green lines indicate adult TSMs ≤ 0.0°C. Gray shadings denote the range between lower and upper percentile bounds of the climate model ensemble scenarios.

of climatic vulnerability (19–21), such analyses miss the most sensitive life stages and are likely to underestimate impact risks at the species level.

## Discussion

This study identifies spawners and embryos as the most temperature-sensitive stages in the life cycle of fish. The observed ontogenetic

shift in thermal tolerance is consistent with previous analyses of smaller datasets (17, 31) and corresponds to the concept of oxygen- and capacity-limited thermal tolerance (4), suggesting that ontogenetic changes in aerobic capacity lead to corresponding changes in upper and lower temperature limits (2). Increases in aerobic capacity from egg to adult follow the development of the cardiorespiratory system

(heart and gills), which facilitates effective  $O_2$  supply to tissues and thus improves tolerance to temperature extremes (8). In addition, the development of homeostasis functions (e.g., ion regulation) and repair mechanisms, including heat shock responses, may contribute to an increase in tolerance to extreme temperatures from egg to adult (32, 33). Immature aerobic and homeostatic capacities of fish embryos and larvae also explain their sensitivity to other environmental factors such as hypoxia, salinity stress, and  $CO_2$ -driven acidification (29, 34). When adults become sexually mature, additional metabolic loads for gamete production [often >20% of body mass (35)] are expected to cause a concomitant decrease in thermal tolerance due to warming-induced loss in aerobic capacity (2, 7). Hypoallometric growth of aerobic capacity relative to body mass may also lead to a narrowing of tolerance ranges and a shift toward lower optimal temperatures in large, nonreproducing adults, as suggested by experiments with Atlantic cod (36) and field observations in eelpout (*Zoarces viviparus*) (5). Indirect evidence of reduced aerobic capacity of spawners relative to nonreproductive adults comes from experiments indicating increased sensitivity to hypoxia at the final stage of gonadal development (37). In addition to oxygen limitation, temperature stress can directly impair gonadal development by affecting the production and release of sex hormones (38). Narrow tolerance ranges of spawners may therefore reflect a combination of thermal constraints on aerobic metabolism and endocrine processes related to gametogenesis. The pattern of stage-specific thermal tolerance demonstrated in this study may also apply to other ectothermic animals (39), although oxygen limitation as a causal principle may be more relevant for aquatic versus terrestrial organisms, owing to the much lower concentration and diffusivity of oxygen in water.

The higher thermal responsiveness of stenothermal species relative to eurythermal species and life stages implies a mechanistic link between physiological thermodynamics and organismal thermal tolerance in fish (10, 13). This prediction is based on the idea that elevated activation energies (kinetic barriers) of rate-limiting reactions in the citric acid cycle constrain metabolic flux and cost and promote resource efficiency (13). However, as relatively small temperature changes have a marked impact on metabolic and developmental rates, such an energetic optimization associated with tolerance to a restricted temperature range (i.e., stenothermality) is beneficial only when environmental temperature variability is low (Fig. 4C). Eurythermal organisms are thermally less responsive and have wider tolerance ranges, which promote an active lifestyle in habitats with daily, seasonal, and/or vertical temperature gradients and variability. For instance, low responsiveness allows relatively constant



levels of performance and thus foraging ability in summer and winter as well as across depth-related temperature gradients. The trade-off in this case may involve elevated baseline energy turnover, as seen in many eurythermal species with an active pelagic lifestyle (40). Accordingly, in contrast to the concept of universal temperature dependence (14), we argue that thermal responsiveness is adaptive and shaped to meet environmental conditions and ecological requirements (9). Building on the indirect evidence presented here (correlation between  $E_a$  and  $T_{\text{range}}$ ; Fig. 4C), further experimental work and analyses that take into account potentially relevant traits (e.g., body mass, activity, trophic level) are necessary to confirm a general relationship among energy efficiency, metabolic thermal responsiveness, and thermal tolerance range.

Narrow thermal safety margins of spawners and embryos indicate that the temperature requirements for reproduction define the climate change vulnerability of fish. For many species, the highest warming trajectory (SSP 5–8.5) represents a major threat, as water temperature may exceed their current tolerance limit for reproduction (Fig. 6). Coping with climate change would be achieved through changes in thermal tolerance [through acclimatization of individuals, or through evolutionary adaptation across generations (41)] and by shifting the timing and/or location of spawning to cooler seasons or regions [niche tracking (42, 43)]. However, adaptation over generations is probably too slow to cope with major anthropogenic change (44, 45). In addition, shifts in spawning times and locations can be problematic and in some cases impossible, depending on species' reproductive strategy and geographical distribution (18). For instance, to provide offspring with suitable feeding conditions, spawning times are usually synchronized with seasonal peaks in plankton productivity (46), especially outside the tropics (18). Moreover, spawning locations may provide essential substrates for egg deposition and hydrographic features that ensure dispersal of pelagic eggs and larvae toward suitable nursery habitats (47). This means that despite more suitable temperature conditions, alternative spawning seasons and locations may not necessarily meet the ecological requirements for successful reproduction (18). Relative to most marine species, freshwater fishes are less flexible in terms of niche tracking because of geographic barriers between habitats and anthropogenic habitat degradation (e.g., dams, hydroelectric power plants, and pollution) (20).

Note that quantitative risk assessments for individual species or populations (e.g., changes in abundance and productivity) may require not only information on sublethal temperature thresholds constraining functional scope (e.g., indicated by reduced growth performance) (5), but also more detailed data on acclimatization

and adaptation potential, spawning ecology, population structure, habitat connectivity, and microclimatic conditions than are available for most species considered in this study. Furthermore, our qualitative risk assessment is probably conservative because exposure to additional climate change factors such as deoxygenation, acidification, and temperature extremes during stochastic heat waves (30) is not considered.

## Conclusion

Phylogenetic, geographic, and ontogenetic patterns in thermal physiology revealed in this study suggest that many fish species face greater risks due to global warming than previously expected. Narrow temperature ranges for reproduction in relation to future warming scenarios underscore the urgency to investigate the adaptive potential of species and populations while taking measures to protect existing and alternative (spawning) habitats from human impacts (48). Very clearly, many fish species and people who depend on healthy fish stocks would benefit from intensified efforts to stabilize global warming at 1.5°C or even less.

## REFERENCES AND NOTES

1. A. Clarke, *Principles of Thermal Ecology: Temperature, Energy and Life* (Oxford Univ. Press, 2017).
2. H.-O. Pörtner, A. P. Farrell, *Science* **322**, 690–692 (2008).
3. J. M. Sunday, A. E. Bates, N. K. Dulvy, *Nat. Clim. Change* **2**, 686–690 (2012).
4. H.-O. Pörtner, *Comp. Biochem. Physiol. A* **132**, 739–761 (2002).
5. H.-O. Pörtner, R. Knust, *Science* **315**, 95–97 (2007).
6. H.-O. Pörtner, C. Bock, F. C. Mark, *J. Exp. Biol.* **220**, 2685–2696 (2017).
7. H.-O. Pörtner, M. A. Peck, *J. Fish Biol.* **77**, 1745–1779 (2010).
8. P. J. Rombough, in *Fish Physiology*, vol. 11 (Elsevier, 1988), pp. 59–161.
9. A. Clarke, *Trends Ecol. Evol.* **18**, 573–581 (2003).
10. H.-O. Pörtner et al., *Physiol. Biochem. Zool.* **79**, 295–313 (2006).
11. D. H. Janzen, *Am. Nat.* **101**, 233–249 (1967).
12. J. Sunday et al., *Philos. Trans. R. Soc. London Ser. B* **374**, 20190036 (2019).
13. H.-O. Pörtner, M. Lucassen, D. Storch, *Fish Physiol.* **22**, 79–154 (2005).
14. J. H. Brown, J. F. Gillooly, A. P. Allen, V. M. Savage, G. B. West, *Ecology* **85**, 1771–1789 (2004).
15. A. I. Dell, S. Pawar, V. M. Savage, *Proc. Natl. Acad. Sci. U.S.A.* **108**, 10591–10596 (2011).
16. T. P. Smith et al., *Nat. Commun.* **10**, 5124 (2019).
17. J. Brett, *Q. Rev. Biol.* **31**, 75–87 (1956).
18. L. Ciannelli, K. Bailey, E. M. Olsen, *ICES J. Mar. Sci.* **72**, 285–296 (2015).
19. M. L. Pinsky, A. M. Eikeset, D. J. McCauley, J. L. Payne, J. M. Sunday, *Nature* **569**, 108–111 (2019).
20. L. Comte, J. D. Olden, *Nat. Clim. Change* **7**, 718–722 (2017).
21. C. H. Trisos, C. Merow, A. L. Pigot, *Nature* **580**, 496–501 (2020).
22. See supplementary materials.
23. M. Gidden et al., *Geosci. Model Dev.* **12**, 1443–1475 (2019).
24. D. L. Rabosky et al., *Nature* **559**, 392–395 (2018).
25. E. W. Goolsby, J. Bruggeman, C. Ané, *Methods Ecol. Evol.* **8**, 22–27 (2017).
26. See the acknowledgments (data and materials availability).
27. R. M. Sibily, J. H. Brown, A. Kodric-Brown, *Metabolic Ecology: A Scaling Approach* (Wiley, 2012).
28. M. E. Dillon, G. Wang, R. B. Huey, *Nature* **467**, 704–706 (2010).
29. F. T. Dahlke et al., *Sci. Adv.* **4**, eaas8821 (2018).

30. O. Hoegh-Guldberg et al., *Science* **365**, eaaw6974 (2019).
31. P. J. Rombough, in *Seminar Series—Society for Experimental Biology*, vol. 61 (Cambridge Univ. Press, 1997), pp. 177–224.
32. A. Hamdoun, D. Epel, *Proc. Natl. Acad. Sci. U.S.A.* **104**, 1745–1750 (2007).
33. F. Dahlke et al., *J. Exp. Biol.* **223**, jeb212589 (2020).
34. R. Przeslawski, M. Byrne, C. Mellin, *Glob. Change Biol.* **21**, 2122–2140 (2015).
35. D. R. Barneche, D. R. Robertson, C. R. White, D. J. Marshall, *Science* **360**, 642–645 (2018).
36. B. Björnsson, A. Steinarrson, *Can. J. Fish. Aquat. Sci.* **59**, 494–502 (2002).
37. R. S. Wu, in *Fish Physiology*, vol. 27 (Elsevier, 2009), pp. 79–141.
38. N. W. Pankhurst, P. L. Munday, *Mar. Freshw. Res.* **62**, 1015–1026 (2011).
39. B. S. Walsh et al., *Trends Ecol. Evol.* **34**, 249–259 (2019).
40. B. A. Seibel, J. C. Drazen, *Philos. Trans. R. Soc. London Ser. B* **362**, 2061–2078 (2007).
41. M. J. J. Angilletta, *Thermal Adaptation: A Theoretical and Empirical Synthesis* (Oxford Univ. Press, 2009).
42. M. L. Pinsky, B. Worm, M. J. Fogarty, J. L. Sarmiento, S. A. Levin, *Science* **341**, 1239–1242 (2013).
43. A. Brugué, P. Alvarez, A. Fontán, U. Cotano, G. Chust, *Front. Mar. Sci.* **3**, 86 (2016).
44. M. Byrne, S. A. Foo, P. M. Ross, H. M. Putnam, *Glob. Change Biol.* **26**, 80–102 (2020).
45. H.-O. Pörtner et al., Ocean systems. In *Climate Change 2014: Impacts, Adaptation, and Vulnerability. Part A: Global and Sectoral Aspects. Contribution of Working Group II to the Fifth Assessment Report of the Intergovernmental Panel on Climate Change* (Cambridge Univ. Press, 2014).
46. A. B. Neuheimer, B. R. MacKenzie, M. R. Payne, *Sci. Adv.* **4**, eaar4349 (2018).
47. R. J. Wootton, C. Smith, *Reproductive Biology of Teleost Fishes* (Wiley, 2014).
48. C. M. Duarte et al., *Nature* **580**, 39–51 (2020).
49. H.-O. Pörtner et al., *Clim. Res.* **37**, 253–270 (2008).

## ACKNOWLEDGMENTS

We thank D. Storch for constructive comments on an earlier version of this manuscript. The Earth System Grid Federation is acknowledged for providing access to CMIP6 climate model output. **Funding:** Supported by the research project METAFISCH of the German Federal Ministry of Education and Research (BMBF grant FZK01LS1604A to H.-O.P. and F.T.D.) and by the Deutsche Forschungsgemeinschaft (Po 278/16-1 and -2) as part of the Research Unit Tersane (FO 2332). S.W. was funded through HIFMB based on the collaboration between the Alfred Wegener Institute, Helmholtz Centre for Polar and Marine Research, and the Carl von Ossietzky University Oldenburg, initially funded by the Ministry for Science and Culture of Lower Saxony and the Volkswagen Foundation through the Niedersächsisches Vorab grant program (grant ZN3285). **Author contributions:** H.-O.P. and F.T.D. conceived the research idea; F.T.D. collated thermal tolerance and thermal responsiveness data and coordinated all analyses and visualizations; S.W. compiled distribution data and conducted phylogenetic imputation of thermal tolerance data, including visualization; M.B. compiled and analyzed climate model data, including the calculation of habitat temperatures; and F.T.D. drafted the manuscript. All authors wrote and edited the manuscript. **Competing interests:** The authors declare that they have no competing interests. **Data and materials availability:** All data needed to evaluate the conclusions in the paper are present in the paper and/or the supplementary materials and data files. The raw data supporting the findings of this study are available from PANGAEA, a member of the ICSU World Data System, at <https://doi.org/10.1594/PANGAEA.917796>.

## SUPPLEMENTARY MATERIALS

[science.sciencemag.org/content/369/6499/65/suppl/DC1](https://science.sciencemag.org/content/369/6499/65/suppl/DC1)  
Materials and Methods  
Figs. S1 to S10  
Tables S1 to S6  
References (50–127)

4 September 2019; accepted 14 May 2020  
10.1126/science.aaz3658

## BIOFILMS

# Cell position fates and collective fountain flow in bacterial biofilms revealed by light-sheet microscopy

Boyang Qin<sup>1,2</sup>, Chenyi Fei<sup>1,3</sup>, Andrew A. Bridges<sup>1,4</sup>, Ameya A. Mashruwala<sup>1,4</sup>, Howard A. Stone<sup>2</sup>, Ned S. Wingreen<sup>1,3,5</sup>, Bonnie L. Bassler<sup>1,4\*</sup>

Bacterial biofilms represent a basic form of multicellular organization that confers survival advantages to constituent cells. The sequential stages of cell ordering during biofilm development have been studied in the pathogen and model biofilm-former *Vibrio cholerae*. It is unknown how spatial trajectories of individual cells and the collective motions of many cells drive biofilm expansion. We developed dual-view light-sheet microscopy to investigate the dynamics of biofilm development from a founder cell to a mature three-dimensional community. Tracking of individual cells revealed two distinct fates: one set of biofilm cells expanded ballistically outward, while the other became trapped at the substrate. A collective fountain-like flow transported cells to the biofilm front, bypassing members trapped at the substrate and facilitating lateral biofilm expansion. This collective flow pattern was quantitatively captured by a continuum model of biofilm growth against substrate friction. Coordinated cell movement required the matrix protein RbmA, without which cells expanded erratically. Thus, tracking cell lineages and trajectories in space and time revealed how multicellular structures form from a single founder cell.

Complex organizations of cells can emerge from simple starting points (1–3). For example, both eukaryotic embryos and prokaryotic biofilms arise from single founder cells (4–7). In both cases, development via cell division produces three-dimensional (3D) collections of cells encased in extracellular matrices. Despite a common origin, descendant cells in both systems differ in spatial positions, nutrient access, signaling gradients, and states of mechanical stress (8–14). Lineage and cell trajectory maps have been made for cells in developing embryos (4, 5, 15), yet no such maps exist for bacterial biofilms. Many fundamental activities that transcend all of biology are relevant in bacterial biofilms. Cells in biofilms communicate, undertake both individual and collective tasks, enjoy survival benefits conferred by the multicellular structure and internal organization, and display clear differences in temporal and spatial gene expression patterns (11, 12, 16–18). Thus, tracing lineages and spatial trajectories of bacterial cells in biofilms is essential to understanding biofilm development and to identifying the underlying biological and physical principles governing multicellular development. A roadblock in this undertaking is that conventional confocal microscopy is insufficient to achieve the spatial and temporal resolution required to map cell paths in densely packed biofilms containing micrometer-sized bacteria (19).

In this study, we combined dual-view light-sheet microscopy (5, 20–23) with intracellular puncta labeling technology (24, 25) to explore individual and collective cell dynamics and developmental patterns in living wild-type (WT) *Vibrio cholerae* biofilms (Fig. 1, A and B, and movies S1 and S2). We found that biofilm cells had one of two cell fates: They either became trapped by the substrate to anchor the biofilm, or they moved ballistically to expand the biofilm. We observed an emergent collective fountain-like cell flow that coordinated global biofilm expansion driving its overall morphology. RbmA, an extracellular matrix protein secreted by biofilm cells, was required for coherent cell motion.

## Dual-view light-sheet microscopy enables mapping of individual cell trajectories

To overcome limitations in temporal resolution of conventional confocal microscopy, we adapted a dual-view inverted selective plane illumination microscope (diSPIM) for the study of prokaryotic cells in biofilms (20, 21). We achieved isotropic resolution in the axial and lateral directions (Fig. 1C and fig. S1) with photobleaching an order of magnitude lower (Fig. 1D and fig. S2) than in traditional spinning disk confocal microscopy at equivalent magnification. We used diSPIM to image isolated biofilm clusters for 16 hours at a time resolution of 3 min, which allowed us to follow individual cells in time. To spatially resolve densely packed micrometer-sized bacteria and overcome the optical sectioning limitations of light-sheet microscopy, we introduced constitutively produced mNeonGreen- $\mu$ NS (mNG- $\mu$ NS) fluorescent protein (tables S1 and S2) that forms a defined cytoplasmic punctum in each cell (25). The avian reovirus protein  $\mu$ NS self-assembles to form a single particle in the bacterial cytoplasm. Once

formed, a punctum exhibited minimal intracellular displacement (fig. S3). During successive divisions, the punctum was inherited by the mother cell, and the daughter cell gradually gained a new punctum (Fig. 1E and fig. S4). Because each punctum persisted along only one branch of the lineage (Fig. 1F), the punctum trace provided a high-resolution representation of a cell's trajectory over a prolonged period. This strategy enabled sufficient spatiotemporal resolution to map individual cell trajectories and cell positions for up to  $10^4$  cells over the full course of biofilm development (movies S3 and S4).

## The Brownian-to-ballistic transition in cell motion underlies the 2D to 3D biofilm architectural transition

Time-resolved cell trajectories showed a distinct transition in cell motion during biofilm development. In the initial phase (Fig. 1, G and H, 0 to 5 hours), in which the biofilm grew predominantly in the lateral plane, cells frequently changed their directions of motion, akin to random walks. As the biofilm developed (Fig. 1, G and H, 5 to 10 hours), however, individual cells began to engage in persistent and straight trajectories, which dominate the bulk of the biofilm at the later stage (Fig. 1, G and H, 10 to 15 hours). Biofilm expansion is driven by cell division, extracellular matrix secretion, and osmotic swelling (26). This kinematic transition in cell movement was quantified by measuring the mean squared displacement (MSD) of cell trajectories versus lag time  $\tau$ , the time offset between cell location observations (Fig. 2, A and B), where the scaling exponent  $\nu$  ( $\text{MSD} \sim \tau^\nu$ ) characterizes cell motions. The MSD exponent  $\nu$  is independent of cell movement speeds and biofilm expansion rates but dependent on how strongly cell trajectories are correlated in time. At early times (1 to 6 hours),  $\nu$  was around 1.2, suggesting that cell motion is close to random and Brownian (Fig. 2C and fig. S5). At around 7 hours,  $\nu$  rapidly increased to a plateau value of 1.8, indicating a transition to nearly straight and persistent cell trajectories. The Brownian-to-ballistic transition of cell motion coincided with the transition from predominantly lateral biofilm expansion to accelerated vertical expansion (Fig. 2D), that is, a transition from two to three dimensions.

## Ballistic motion is driven by matrix production, and loss of matrix alters cell motion

The dynamical and architectural transitions of cells in *V. cholerae* biofilms require the extracellular *Vibrio* polysaccharide (Vps) (27, 28). A  $\Delta vpsL$  mutant that does not produce Vps adhered to the substrate, but after division, most daughter cells were released. Presumably, in the absence of polysaccharide matrix, Vps-associated matrix proteins that promote cell-cell adhesion are not retained (29–31). The

<sup>1</sup>Department of Molecular Biology, Princeton University, Princeton, NJ 08544, USA. <sup>2</sup>Department of Mechanical and Aerospace Engineering, Princeton University, Princeton, NJ 08544, USA. <sup>3</sup>Lewis-Sigler Institute for Integrative Genomics, Princeton University, Princeton, NJ 08544, USA. <sup>4</sup>The Howard Hughes Medical Institute, Chevy Chase, MD 20815, USA. <sup>5</sup>Princeton Center for Theoretical Science, Princeton University, Princeton, NJ 08544, USA.

\*Corresponding author. Email: bbassler@princeton.edu



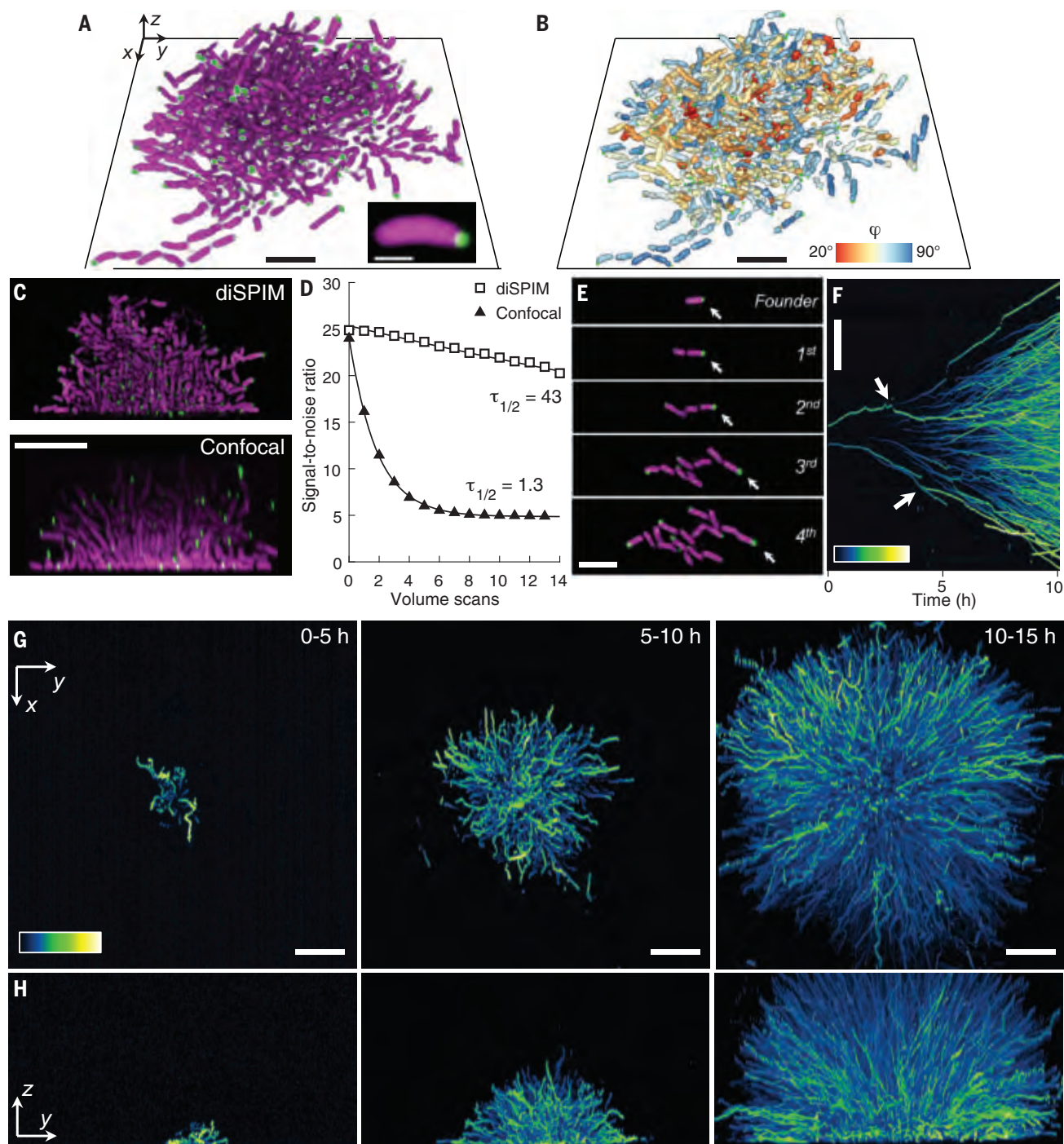


**Fig. 1. Single-cell tracking of WT *V. cholerae* biofilm cells using dual-view light-sheet microscopy and a cytoplasmic fluorescent protein marker.**

(A) 3D view of biofilm cells that constitutively produced mScarlet-I (cell contour) and an mNeonGreen- $\mu$ NS protein fusion (puncta). Scale bar, 10  $\mu$ m. (Inset) mNeonGreen- $\mu$ NS localization at the cell pole. Scale bar, 1  $\mu$ m. (B) Segmented cells and mNeonGreen- $\mu$ NS puncta (green dots). Colors denote cell orientation  $\phi$  (angle between cell long axis and the +z axis). (C) Side view of a biofilm cluster imaged using light-sheet microscopy (diSPIM) versus spinning disk confocal microscopy. Scale bar, 10  $\mu$ m. (D) Comparison of photobleaching by diSPIM and confocal microscopy measured as the fluorescence signal-to-noise ratio (SNR) of biofilm clusters undergoing repeated volume scans of identical initial SNR in

the shot-noise dominated regime (table S3). Curves represent exponential fits;  $\tau_{1/2}$  denotes number of volume scans to reduce SNR by half. (E) Four successive cell divisions showing inheritance of the mNeonGreen- $\mu$ NS puncta. Arrows indicate the punctum in the founder cell. Scale bar, 10  $\mu$ m. (F) Space-time kymograph of mNeonGreen- $\mu$ NS puncta (in the lateral coordinate  $y$  over biofilm development time) shows cell divisions (arrows) and cell lineage traces. Scale bar, 5  $\mu$ m. Color bar indicates mNeonGreen intensity (arbitrary units, a.u.). (G) Top-view projections of biofilm cell trajectories at 3-min time resolution obtained from particle tracking. Color bar indicates mNeonGreen intensity (a.u.). Scale bars, 10  $\mu$ m. (H) Side-view projections of the tracked cell trajectories in (G), with identical scale and color code.

biofilm, as a result, did not transition from the 2D to the 3D morphology. The MSD exponents at the beginning of the experiments ( $<3$  hours) were comparable among the mutants, which all underwent surface attachment and had similar division rates. We observed that substrate-bound  $\Delta vpsL$  cells exhibited suppressed cell movement; the cell MSD decreased over time (Fig. 2B) and reached a scaling exponent of  $\nu \approx 0.5$  at 16 hours (Fig. 2, B and C), implying subdiffusive cell motion and increased trapping at the surface over time. By contrast, the rugose (Rg) strain with a mutation that drives overproduction of extracellular matrix (32) progressed to ballistic-type motion and achieved a plateau MSD exponent similar to that of WT (Fig. 2C and fig. S5).

### Cell trapping occurs near the substrate and early in biofilm development

Is cell trapping a consequence of proximity to the substrate for WT cells? To quantify trapping, we defined a dimensionless trapping parameter  $\alpha$  as the fraction of a cell's displacements that does not contribute to the net (end-to-end) displacement of that cell's trajectory (33). Here,  $\alpha = 0$  implies a persistent motion in one direction (transport), while  $\alpha = 1$  implies a trajectory that meanders and eventually returns to its starting point (trapping). For WT biofilm cells, high levels of trapping  $\alpha$  occurred in the biofilm core (planar radius  $\rho \leq 18 \mu\text{m}$  and height  $z \leq 4 \mu\text{m}$ ), where cells essentially remained fixed in space (Fig. 3A). These cells were trapped at the substrate, moving only minimally over the course of biofilm development (Fig. 3A). Compared to the entire population of biofilm cells, which was dominated by cells moving with straight trajectories ( $\alpha \approx 0$ ),

the group of cells that localized near the substrate ( $z \leq 4 \mu\text{m}$ ) at any time experienced much stronger trapping (Fig. 3B). Because the biofilm morphology was initially predominantly two-dimensional, cells born early (0 to 7 hours) were more likely to remain trapped near the substrate than cells born later (12 to 16 hours) (Fig. 3C).

### Biofilm expansion is inhibited near the substrate

Given that cells near the substrate experienced trapping, we were curious whether biofilm expansion was also hindered near the substrate, that is, in the lateral plane. To probe this possibility, we divided WT cell trajectories into four position-dependent subgroups according to their trajectory polar angle  $\phi$  relative to the  $z$  axis in the spherical coordinate system (Fig. 3D and fig. S6) and compared their average radial expansion speeds  $u_r$  (Fig. 3, E and F). For cells distant from the substrate ( $0^\circ \leq \phi \leq 68^\circ$ ) (Fig. 3E), expansion speed was roughly linear with radial distance  $r$ , which implied exponential growth in biofilm volume and cell growth and division rates that were uniform along the biofilm radius. By contrast, cells near the substrate ( $68^\circ \leq \phi \leq 90^\circ$ ) (Fig. 3, E and F) had markedly lower  $u_r$ , which deviated from a linear profile. The reduced  $u_r$  of cells at the substrate were maintained throughout the three indicated biofilm development time periods (Fig. 3F) and at different radial positions (fig. S7C).

### Continuum modeling reveals that substrate friction reduces biofilm expansion near the substrate

We hypothesized that the reduced expansion speed of cells near the substrate is due to friction at the biofilm-substrate interface. To

test this hypothesis, we developed continuum models that consider uniform and isotropic biofilm growth in the presence of substrate friction. Biofilms are viscoelastic materials (34–36). In this study, we considered two extremes: treating the *V. cholerae* biofilm as a viscous fluid or as a hyperelastic solid. We found that the two models yield similar overall shape development (fig. S8), but the fluid model, which we focus on here, better describes the large deformations and time evolution that occur in a growing biofilm. The friction with the substrate, which presumably arises from binding and unbinding of biofilm extracellular polymers and proteins (37), is modeled as viscous drag (33). The expansion velocity field of the modeled biofilm is obtained by solving the internal force balance (33). Indeed, in close agreement with the experimental biofilms, the modeling results show reduced cell motion near the substrate compared to that in the bulk (Fig. 3, G and H).

### An emergent fountain-like flow drives 3D biofilm expansion

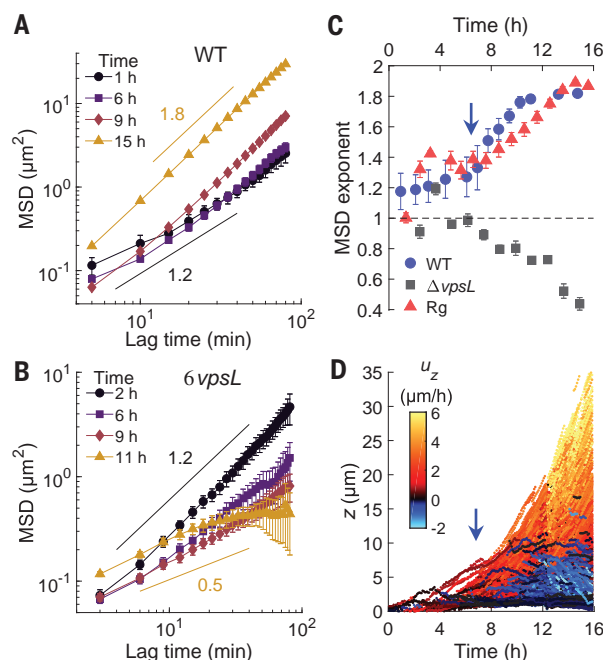
How do the dynamical motions of *V. cholerae* biofilm cells drive overall biofilm expansion? To monitor the fates of individual cells, we defined three types of cell motion based on the deviation in cell trajectories from strictly radial motion. This deviation was measured by the end-to-end change in polar angle  $\Delta\phi$  for each cell trajectory (Fig. 4A and movie S5). While 60% of the biofilm cells expanded radially with very small angular deviations ( $|\Delta\phi| < 5^\circ$ ), two subsets of cells that originated near the biofilm core demonstrated substantial deviation from radial expansion: one group moved vertically away from the substrate (Fig. 4A, red), while the other group moved upward initially and then curved back down (Fig. 4A, blue), leapfrogging cells that were trapped at the substrate (Fig. 3, A and B) to continue expanding the biofilm in the lateral direction.

To reveal the underlying collective cell motion, we ensemble-averaged the velocities of cells in local proximity to one another (33). This velocity map demonstrated a distinct fountain-like flow for the WT and Rg strains (Fig. 4, B and C, and fig. S9). We observed curved mean flow streamlines near the substrate (Fig. 4, B and C, and fig. S9), which rerouted cells near the biofilm core toward the lateral expansion front.

### Fountain-like flow facilitates lateral biofilm expansion along the substrate

How does fountain-like flow shape the 3D structure of a biofilm? Compared to the hypothetical case in which the radius of the biofilm increased with the average cell velocity at the substrate, the actual biofilm lateral expansion speed was more rapid (fig. S10). Thus, our calculations suggest that the fountain-like

**Fig. 2. Bacterial trajectory dynamics at single-cell resolution.** (A and B) Mean squared displacement (MSD) of bacterial cell trajectories versus lag time at the indicated time points for (A) WT *V. cholerae* and (B) the  $\Delta vpsL$  mutant. (C) MSD scaling exponents  $\nu$  in 90-min time windows sampled for three strains: WT, Rg, and  $\Delta vpsL$ . The blue arrow shows the diffusive ( $\nu \approx 1$ ) to ballistic ( $\nu \approx 2$ ) transition of cell trajectories at around 7 hours. (D) Vertical displacements versus time for cells in the WT biofilm in (C). The blue arrow marks the 7-hour time point highlighted in (C). Color indicates cell vertical velocity  $u_z$ .





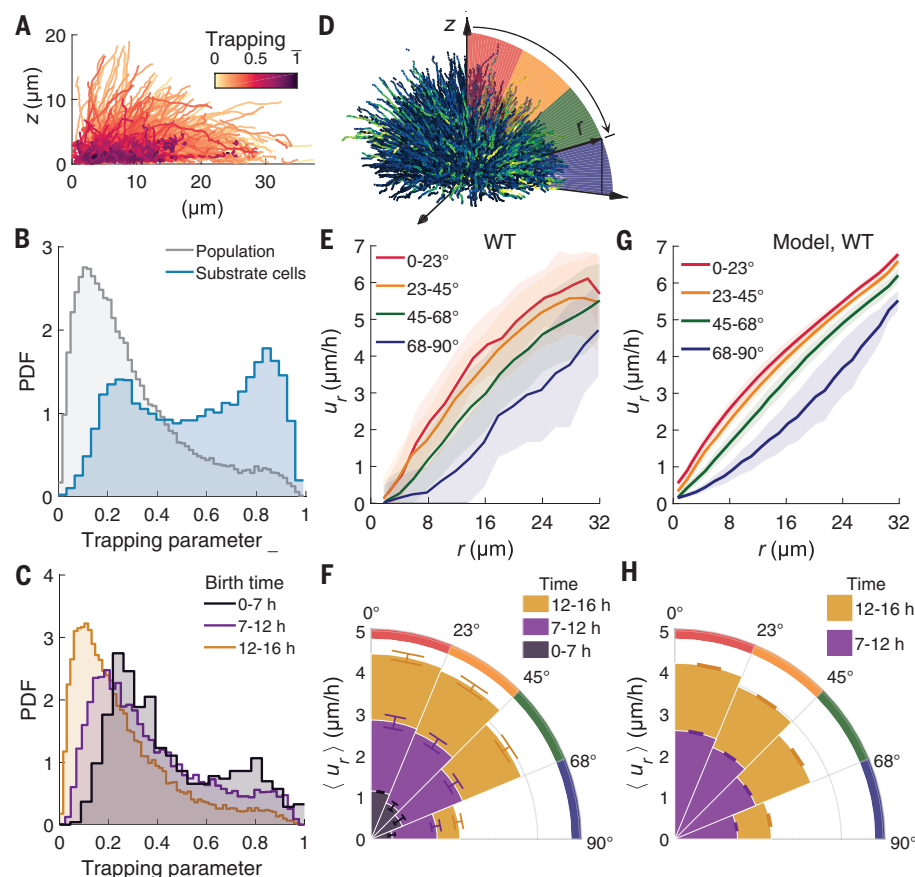


**Fig. 3. Cell trapping and reduced biofilm expansion occur near the substrate.** (A) Cell trajectories colored by trajectory trapping parameter  $\alpha$  for all cells located within  $4\ \mu\text{m}$  of the substrate at any point in their trajectories. (B) Probability distribution function (PDF) of the trajectory trapping parameter  $\alpha$  for WT cells near the substrate (blue) and the full population (gray). (C) Probability distribution function of  $\alpha$  for different age groups at birth times of 0 to 7 hours, 7 to 12 hours, and 12 to 16 hours. In (B) and (C),  $n = 3$  biofilm clusters. (D) Schematic of the spherical coordinate system. Sample trajectories are colored by mNeonGreen- $\mu\text{NS}$  puncta intensity. Cells are divided into four cohorts based on their trajectory polar angle:  $\phi = 0^\circ$  to  $23^\circ$  (red),  $\phi = 23^\circ$  to  $45^\circ$  (yellow),  $\phi = 45^\circ$  to  $68^\circ$  (green), and  $\phi = 68^\circ$  to  $90^\circ$  (blue). (E) Radial expansion velocity  $u_r$  versus radial distance  $r$  plotted for the four  $\phi$  cohorts from (D). (F) Polar plot of the average radial expansion velocity  $\langle u_r \rangle$  of the cohorts from (D), distinguished by polar angle range in (E) during the indicated time windows. Radial sectors for each color extend from  $\langle u_r \rangle = 0$  to the specified value of  $\langle u_r \rangle$ . Sectors are overlaid for clarity. Error bars denote standard errors. (G) Simulation expansion velocities corresponding to experimental results in (E). (H) Simulation average expansion velocities corresponding to the experimental results in (F). Error bars denote standard errors. The simulation initiates after 7 hours, that is, after the onset of the 2D to 3D transition in experiments.

flow pattern, which transported biofilm cells to the expansion front over preexisting cells that were trapped at the substrate, accelerated lateral biofilm expansion.

#### Collective fountain-like flows stem from growth against substrate friction

The mean flow pattern in the expanding biofilm was accurately captured by our continuum modeling. Both the model cell paths (Fig. 4D, flow path lines) and the velocity field (Fig. 4E, fig. S11, and movie S6) show clear fountain-like flow at the biofilm periphery near the substrate. Moreover, the friction parameter of the model is uniquely determined by fitting the overall biofilm shape development. A quan-

titative comparison can be made between the velocity field of the modeled biofilm and the experimental biofilm (33). The viscous fluid model captures the experimental fountain-like flow at the biofilm periphery better than the elastic solid model (fig. S11). Thus, at short times (below the cell division time scale of 30 min), cells are locally immobilized within the matrix, while at long times, the biofilm plastically deforms and flows like a liquid, akin to colloidal glasses (38, 39). The local velocity field obtained from the viscous fluid model closely agrees with the experimental cell flows (Fig. 4E, i to iii), with relative differences of  $\sim 10\%$  (figs. S12 and S13). Thus, our minimal mechanical model of growth in the presence of substrate

friction accounts for the fountain-like flow of *V. cholerae* cells during 3D biofilm development.

#### Substrate friction alters biofilm morphology

Our model predicts the influence of substrate friction on overall biofilm morphology. For negligible substrate friction (Fig. 4F, top, and fig. S8), the modeled biofilm maintains a relatively flat shape and can readily spread along the substrate. For larger substrate friction (Fig. 4F, bottom, and fig. S8), however, substrate retardation of biofilm lateral expansion is pronounced, and the modeled biofilm extends farther in the vertical  $z$  direction than in the planar  $xy$  directions. The temporal evolution of the two models is compared in movie S6. This increased height-to-radius biofilm aspect ratio with increasing friction is a universal feature of growth against friction, largely independent of the specific material properties (fig. S14). Compared to WT, the Rg strain overproduces matrix components, which presumably increases friction with the substrate. This increased friction could contribute to the increased height-to-radius aspect ratio of Rg biofilms compared to that of WT (Fig. 4, B and C).

#### Collective cell flow and trajectory coherence require the matrix component RbmA

Although matrix components facilitate cell-cell adhesion and confer biofilm structural rigidity (16, 30, 40), their roles, if any, in modulating the mobility of individual biofilm cells and in driving overall biofilm expansion are largely unknown. To investigate their functions, we imaged  $yz$  projections of biofilm development for WT and three matrix mutants,  $\Delta\text{rbmA}$ , Rg, and Rg  $\Delta\text{rbmA}$  (Fig. 5, A to D). The WT and Rg cells followed coherent paths, while  $\Delta\text{rbmA}$  cells moved randomly in space with uncorrelated trajectories (Fig. 5, A to C, and movies S7 and S8). To characterize the coherence of cell motion, we leveraged the concept of affine transformation (translation, rotation, shear, and dilation) and defined a nondimensional metric, the rearrangement strength  $\chi$  (33), which quantifies the level of nonaffine rearrangements in the cell traces (fig. S15). For WT and Rg cells, the distribution of  $\chi$  peaked at small values (Fig. 5E), with a population average close to 0.2 (Fig. 5F). By contrast, the  $\Delta\text{rbmA}$  cells displayed large rearrangement strength  $\chi$  values (Fig. 5E), with a population average near 0.5 (Fig. 5F), indicating highly irregular cell motions and nonaffine rearrangements during biofilm development. These cell motions were not due to swimming motility via flagellar rotation (fig. S16) but rather stemmed from growth via cell divisions and biofilm expansion. Thus, by binding cells together and to the matrix (29, 41, 42), RbmA appears to restrict the random motions of individual cells and suppresses premature separation of mother-daughter cells. These RbmA adhesive functions,

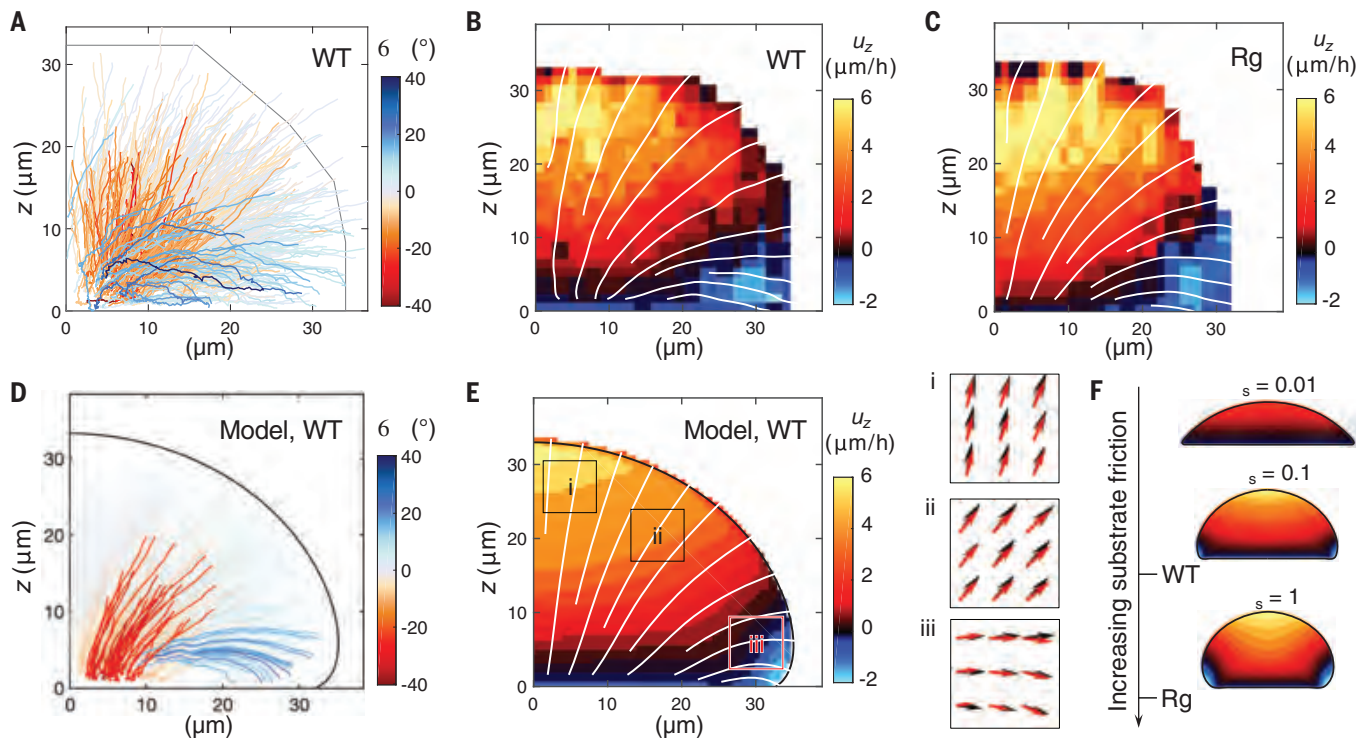


**Fig. 4. Internal fountain-like cell flow patterns underlie 3D biofilm expansion.**

(A) Cell trajectories plotted in the cylindrical coordinates with radius  $\rho$  and height  $z$ , colored by the end-to-end change in polar angle  $\Delta\phi$ . Blue indicates cell motion reorienting toward the substrate (positive  $\Delta\phi$ ), and red indicates reorienting away from the substrate (negative  $\Delta\phi$ ). The gray curve indicates the biofilm boundary. (B and C) Heatmaps of locally averaged vertical cell velocity  $u_z$  with streamlines (white) for the internal flow of cells for (B) WT *V. cholerae* and (C) the Rg biofilms with approximately 1500 puncta. (D) Modeled cell trajectories in a viscous biofilm plotted in cylindrical coordinates. Color

code as in (A). (E) Heatmap of vertical velocity  $u_z$  with flow streamlines (white) of the modeled biofilm. The dimensionless surface friction parameter  $\xi_s = 0.5$  was chosen by fitting the overall shape of the modeled biofilm to that of the experimental biofilm [black arrows, data from (E)] compared with those of the WT experimental biofilm [red arrows, data from (B)]. (F) Morphologies of modeled biofilms at the indicated substrate frictions  $\xi_s$ . WT corresponds to  $\xi_s = 0.5$  and Rg corresponds to  $\xi_s = 3.2$ . Colors indicate local vertical velocity  $u_z$ . Color code as in (E).

however, do not constrain the overall outward movement of cells, and thus the overall expansion of the biofilm. The collective fountain-like flow thus enabled biofilm expansion while maintaining cell trajectory coherence.

#### Cell motion coherence in the *rbmA* mutant can be partially rescued through elevated expression of other matrix genes

Introduction of the mutation that confers the Rg biofilm phenotype to *V. cholerae* elevated expression of genes encoding matrix components compared to the WT (Fig. 5G). In turn, global morphological changes occurred (Fig. 4, B and C) along with a reduced cell density at the biofilm core (fig. S7, D and H) and increased substrate friction (Fig. 4F and fig. S8). We wondered how increased matrix production influences the cell trajectories in biofilms. Introduction of the Rg mutation into the  $\Delta rbmA$  strain drastically elevated expression of *rbmC*, *bap1*, and *vpsL*, encoding the other matrix components (Fig. 5G). Moreover, cell trajectory coherence was increased, and rearrangement strength was decreased (Fig. 5, D and E). Specifically, the rearrangement

strength of cells possessing the Rg and  $\Delta rbmA$  mutations was intermediate between that of the  $\Delta rbmA$  single mutant and the WT (Fig. 5, E and F). Thus, some or all of the matrix components encoded by *rbmC*, *bap1*, and *vpsL* must act synergistically with RbmA to mediate the coherence of individual cell trajectories and drive collective flow in biofilms.

#### Outlook

In this study, we tracked cell lineages and trajectories in space and time throughout bacterial biofilm development to provide insight into how these ancient multicellular structures form from a single founder cell. By combining dual-view light-sheet microscopy, intracellular fluorescent puncta labeling, mutagenesis, quantitative reverse transcription polymerase chain reaction (qRT-PCR), and mathematical modeling, we established mechanistic principles underpinning cell position fates and collective cell motions during biofilm formation (fig. S17). Spatiotemporal imaging with high resolution allowed us to uncover two distinct cell behaviors in biofilms: substrate trapping and ballistic outward expansion, which together

determine each cell's final position in the mature biofilm. We suspect that a cell's ultimate position will determine its local environment and gene expression pattern and, thus, whether it remains or exits the community during subsequent biofilm dispersal. Furthermore, we identified an emergent collective fountain-like cellular flow that drives biofilm expansion. This group-transport pattern enables cells at the biofilm core to leapfrog cells trapped at the substrate, allowing biofilm expansion in the face of substrate friction. We linked the roles of extracellular matrix and mechanical forces to individual cell trajectories and dynamics during biofilm expansion. Specifically, RbmA maintains the coherence of collective cellular flow, which allows the biofilm to expand on surfaces while maintaining its structural robustness.

It remains to be investigated whether biofilm cells are capable of modulating the production of the Bap1 and RbmC matrix components responsible for biofilm-substrate interactions to produce distinct cellular flow patterns and, in turn, biofilm architectures that exhibit superior function in particular environments.



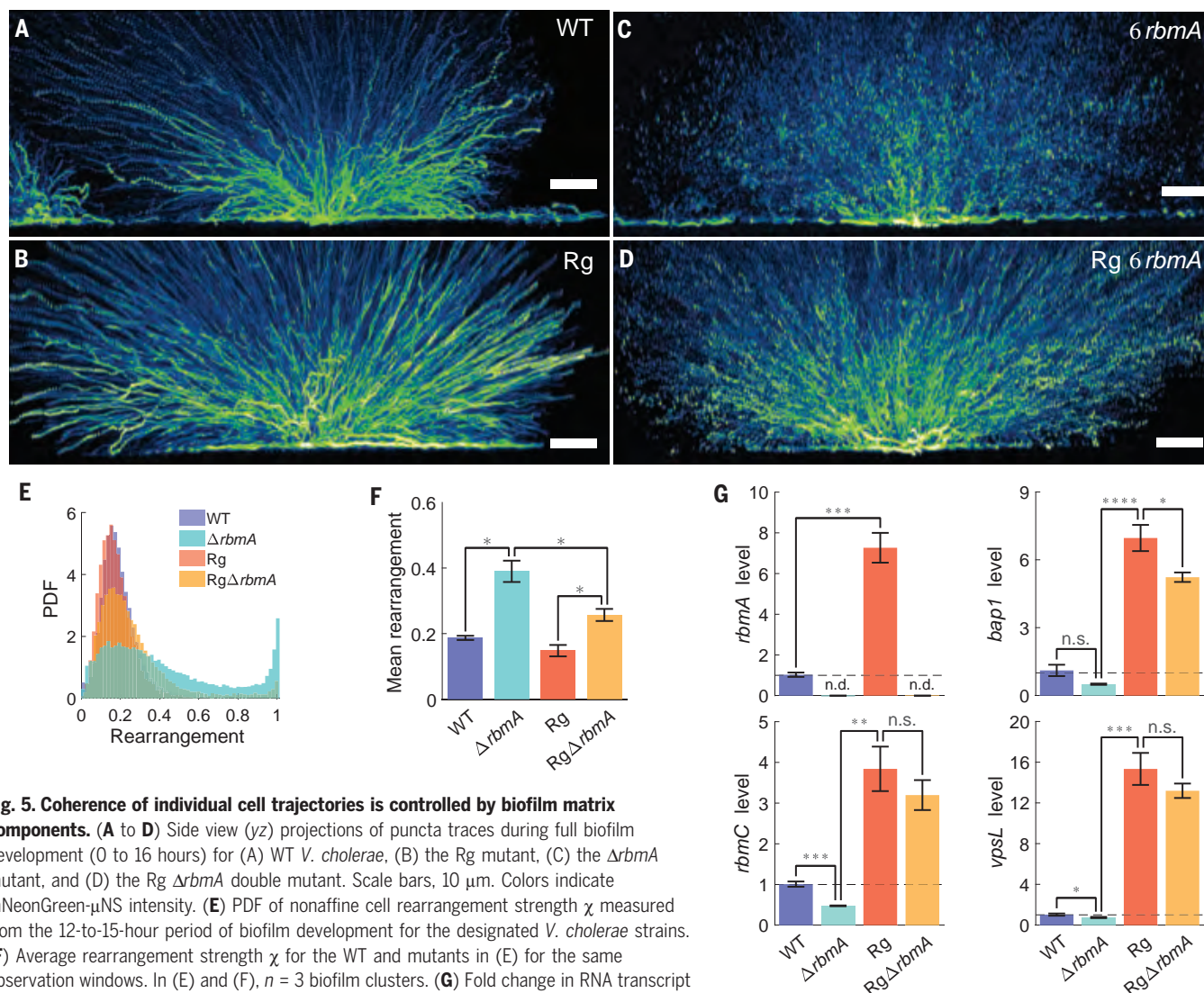


**Fig. 5. Coherence of individual cell trajectories is controlled by biofilm matrix components.**

(A to D) Side view (yz) projections of puncta traces during full biofilm development (0 to 16 hours) for (A) WT *V. cholerae*, (B) the Rg mutant, (C) the  $\Delta rbmA$  mutant, and (D) the Rg  $\Delta rbmA$  double mutant. Scale bars, 10  $\mu$ m. Colors indicate mNeonGreen- $\mu$ NS intensity. (E) PDF of nonaffine cell rearrangement strength  $\chi$  measured from the 12-to-15-hour period of biofilm development for the designated *V. cholerae* strains. (F) Average rearrangement strength  $\chi$  for the WT and mutants in (E) for the same observation windows. In (E) and (F),  $n = 3$  biofilm clusters. (G) Fold change in RNA transcript levels for *rbmA*, *bap1*, *rbmC*, and *vpsL* relative to that in the WT in the designated strains measured by qRT-PCR ( $n = 3$  biological and 2 technical replicates). DNA gyrase (*gyrA*) and the WT strain transcript levels were used for normalization. Colors as in (E). Dashed lines represent the WT level. Unpaired *t*-tests with Welch's correction were performed for statistical analyses. In (F) and (G), *P* values are denoted as \* $P < 0.05$ ; \*\* $P < 0.01$ ; \*\*\* $P < 0.001$ ; \*\*\*\* $P < 0.0001$ ; n.s.,  $P > 0.05$ ; and n.d., not detected.

Our modeling demonstrates that the magnitude of substrate friction forces, which depend on biofilm matrix components, can influence the overall biofilm morphology, in particular the height-to-radius aspect ratio. These collective cellular flow patterns and cell-matrix-substrate interaction principles may be relevant in other prokaryotic and eukaryotic systems and could underpin multicellular development and organization.

## REFERENCES AND NOTES

- M. J. F. Barresi, S. F. Gilbert, *Developmental Biology* (Oxford Univ. Press, ed. 12, 2019).
- G. O'Toole, H. B. Kaplan, R. Kolter, *Annu. Rev. Microbiol.* **54**, 49–79 (2000).
- L. Hall-Stoodley, J. W. Costerton, P. Stoodley, *Nat. Rev. Microbiol.* **2**, 95–108 (2004).
- P. J. Keller, A. D. Schmidt, J. Wittbrodt, E. H. K. Stelzer, *Science* **322**, 1065–1069 (2008).
- K. McDole et al., *Cell* **175**, 859–876.e33 (2018).
- K. Drescher et al., *Proc. Natl. Acad. Sci. U.S.A.* **113**, E2066–E2072 (2016).
- J. Yan, A. G. Sharo, H. A. Stone, N. S. Wingreen, B. L. Bassler, *Proc. Natl. Acad. Sci. U.S.A.* **113**, E5337–E5343 (2016).
- D. Ben-Zvi, B. Shilo, A. Fainsod, N. Barkai, *Nature* **453**, 1205–1211 (2008).
- B. Monier et al., *Nature* **518**, 245–248 (2015).
- V. E. Deneke et al., *Cell* **177**, 925–941.e17 (2019).
- P. S. Stewart, M. J. Franklin, *Nat. Rev. Microbiol.* **6**, 199–210 (2008).
- E. Karatan, P. Watnick, *Microbiol. Mol. Biol. Rev.* **73**, 310–347 (2009).
- S. Mukherjee, B. L. Bassler, *Nat. Rev. Microbiol.* **17**, 371–382 (2019).
- A. Persat et al., *Cell* **161**, 988–997 (2015).
- Y. Wan, K. McDole, P. J. Keller, *Annu. Rev. Cell Dev. Biol.* **35**, 655–681 (2019).
- J. K. Teschler et al., *Nat. Rev. Microbiol.* **13**, 255–268 (2015).
- C. D. Nadell, K. Drescher, K. R. Foster, *Nat. Rev. Microbiol.* **14**, 589–600 (2016).
- H. C. Flemming et al., *Nat. Rev. Microbiol.* **14**, 563–575 (2016).
- J. Pawley, Ed., *Handbook of Biological Confocal Microscopy* (Springer, ed. 3, 2006).
- Y. Wu et al., *Nat. Biotechnol.* **31**, 1032–1038 (2013).
- A. Kumar et al., *Nat. Protoc.* **9**, 2555–2573 (2014).
- B. C. Chen et al., *Science* **346**, 1257998 (2014).
- T. L. Liu et al., *Science* **360**, eaaq1392 (2018).
- T. J. Broering et al., *J. Virol.* **79**, 6194–6206 (2005).
- B. R. Parry et al., *Cell* **156**, 183–194 (2014).
- A. Seminara et al., *Proc. Natl. Acad. Sci. U.S.A.* **109**, 1116–1121 (2012).
- F. H. Yildiz, G. K. Schoolnik, *Proc. Natl. Acad. Sci. U.S.A.* **96**, 4028–4033 (1999).
- J. C. N. Fong, K. A. Syed, K. E. Klose, F. H. Yildiz, *Microbiology* **156**, 2757–2769 (2010).
- C. Absalon, K. Van Dellen, P. I. Watnick, *PLOS Pathog.* **7**, e1002210 (2011).
- V. Berk et al., *Science* **337**, 236–239 (2012).
- D. R. Smith et al., *Proc. Natl. Acad. Sci. U.S.A.* **112**, 10491–10496 (2015).
- B. Lim, S. Beyhan, J. Meir, F. H. Yildiz, *Mol. Microbiol.* **60**, 331–348 (2006).
- Materials and methods are available as supplementary materials.
- I. Klapper, C. J. Rupp, R. Cargo, B. Purvedorj, P. Stoodley, *Biotechnol. Bioeng.* **80**, 289–296 (2002).
- J. Yan et al., *Adv. Mater.* **30**, e1804153 (2018).

36. S. G. V. Charlton et al., *J. Bacteriol.* **201**, e00101-19 (2019).
37. C. Fei et al., *Proc. Natl. Acad. Sci. U.S.A.* **117**, 7622–7632 (2020).
38. P. Schall, D. A. Weitz, F. Spaepen, *Science* **318**, 1895–1899 (2007).
39. G. L. Hunter, E. R. Weeks, *Rep. Prog. Phys.* **75**, 066501 (2012).
40. H. C. Flemming, J. Wingender, *Nat. Rev. Microbiol.* **8**, 623–633 (2010).
41. J. C. N. Fong et al., *eLife* **6**, e26163 (2017).
42. J. C. N. Fong, K. Karplus, G. K. Schoolnik, F. H. Yildiz, *J. Bacteriol.* **188**, 1049–1059 (2006).
43. B. Qin et al., Code and dataset for: Cell position fates and collective fountain flow in bacterial biofilms revealed by light-sheet microscopy, Zenodo (2020); <https://doi.org/10.5281/zenodo.3828028>.

## ACKNOWLEDGMENTS

We thank G. Laevsky, M. Guo, H. Vishwasrao, and H. Shroff for assistance with light-sheet microscopy. We thank Y. Cao,

R. Alert, and S. Mao for helpful discussions on modeling. **Funding:** This work was supported by the Howard Hughes Medical Institute (B.L.B.); National Science Foundation grants MCB-1713731 (B.L.B.) and MCB-1853602 (B.L.B., H.A.S., and N.S.W.); NIH grants 1R21AI144223 (B.L.B., H.A.S., and N.S.W.), 2R37GM065859 (B.L.B.), and GM082938 (N.S.W.); the NSF through the Princeton University Materials Research Science and Engineering Center DMR-1420541 (B.L.B. and H.A.S.); and the Max Planck Society-Alexander von Humboldt Foundation (B.L.B.). A.A.B. is a Howard Hughes Medical Institute Fellow of the Damon Runyon Cancer Research Foundation (DRG-2302-17). A.A.M. is a Howard Hughes Medical Institute Fellow of the Life Sciences Research Institute. **Author contributions:** B.Q., N.S.W., and B.L.B. designed the experiments. B.Q. performed the experiments. C.F. performed modeling. A.A.B. performed strain cloning. A.A.M. performed qRT-PCR. B.Q., C.F., A.A.B., A.A.M., H.A.S., N.S.W., and B.L.B. analyzed the data. B.Q., C.F., A.A.B., A.A.M., H.A.S., N.S.W., and B.L.B. wrote the paper. **Competing interests:** The

authors declare no competing interests. **Data and materials availability:** Data and codes are available online at Zenodo (43).

## SUPPLEMENTARY MATERIALS

science.sciencemag.org/content/369/6499/71/suppl/DC1  
Materials and Methods  
Supplementary Text  
Figs. S1 to S17  
Tables S1 to S3  
References (44–77)  
MDAR Reproducibility Checklist  
Movies S1 to S8

22 March 2020; accepted 19 May 2020  
Published online 11 June 2020  
10.1126/science.abb8501

## REPORTS

## CORONAVIRUS

## Development of an inactivated vaccine candidate for SARS-CoV-2

Qiang Gao<sup>1\*</sup>, Linlin Bao<sup>2\*</sup>, Haiyan Mao<sup>3\*</sup>, Lin Wang<sup>1\*</sup>, Kangwei Xu<sup>4\*</sup>, Minnan Yang<sup>5\*</sup>, Yajing Li<sup>1</sup>, Ling Zhu<sup>5</sup>, Nan Wang<sup>5</sup>, Zhe Lv<sup>5</sup>, Hong Gao<sup>2</sup>, Xiaoqin Ge<sup>1</sup>, Biao Kan<sup>6</sup>, Yaling Hu<sup>1</sup>, Jiangning Liu<sup>2</sup>, Fang Cai<sup>1</sup>, Deyu Jiang<sup>1</sup>, Yanhui Yin<sup>1</sup>, Chengfeng Qin<sup>7</sup>, Jing Li<sup>1</sup>, Xuejie Gong<sup>1</sup>, Xiuyu Lou<sup>3</sup>, Wen Shi<sup>3</sup>, Dongdong Wu<sup>1</sup>, Hengming Zhang<sup>1</sup>, Lang Zhu<sup>1</sup>, Wei Deng<sup>2</sup>, Yurong Li<sup>1</sup>, Jinxing Lu<sup>6†</sup>, Changgui Li<sup>4†</sup>, Xiangxi Wang<sup>5†</sup>, Weidong Yin<sup>1†</sup>, Yanjun Zhang<sup>3†</sup>, Chuan Qin<sup>2†</sup>

The coronavirus disease 2019 (COVID-19) pandemic caused by severe acute respiratory syndrome coronavirus 2 (SARS-CoV-2) has resulted in an unprecedented public health crisis. Because of the novelty of the virus, there are currently no SARS-CoV-2-specific treatments or vaccines available. Therefore, rapid development of effective vaccines against SARS-CoV-2 are urgently needed. Here, we developed a pilot-scale production of PiCoVacc, a purified inactivated SARS-CoV-2 virus vaccine candidate, which induced SARS-CoV-2-specific neutralizing antibodies in mice, rats, and nonhuman primates. These antibodies neutralized 10 representative SARS-CoV-2 strains, suggesting a possible broader neutralizing ability against other strains. Three immunizations using two different doses, 3 or 6 micrograms per dose, provided partial or complete protection in macaques against SARS-CoV-2 challenge, respectively, without observable antibody-dependent enhancement of infection. These data support the clinical development and testing of PiCoVacc for use in humans.

The World Health Organization declared the outbreak of coronavirus disease 2019 (COVID-19) to be a Public Health Emergency of International Concern on 30 January 2020 and classified it as a pandemic on 11 March 2020. It is reported that ~80% of COVID-19 patients have mild to moderate symptoms, whereas ~20% develop serious manifestations such as severe pneumonia, acute respiratory distress syndrome, sepsis, and even death (1). The number of COVID-19 cases has increased at a staggering

rate globally. Severe acute respiratory syndrome coronavirus 2 (SARS-CoV-2), the causative virus of the ongoing pandemic, belongs to the genus *Betacoronavirus* (β-CoV) of the family Coronaviridae (2). SARS-CoV-2, along with the severe acute respiratory syndrome coronavirus (SARS-CoV) and the Middle Eastern respiratory syndrome-related coronavirus (MERS-CoV), constitute the three most life-threatening species of the coronaviruses that affect humans. SARS-CoV-2 harbors a linear, single-stranded, positive-sense RNA genome

encoding four structural proteins, spike (S), envelope (E), membrane (M), and nucleocapsid (N). Of these, S is a major protective antigen that elicits highly potent neutralizing antibodies (NAbs), 16 nonstructural proteins (nsp1 to nsp16), and several accessory proteins (3). No specific antiviral drugs or vaccines against the newly emerged SARS-CoV-2 are currently available. Therefore, urgency in the development of vaccines is of vital importance to curb the pandemic and to prevent new viral outbreaks.

Multiple SARS-CoV-2 vaccine types, such as DNA- and RNA-based formulations, recombinant subunits containing viral epitopes, adenovirus-based vectors, and purified inactivated virus, are under development (4–6). Purified inactivated viruses have been traditionally used for vaccine development, and such vaccines have been found to be safe and effective for the prevention of diseases caused by viruses such as influenza virus and poliovirus (7, 8). To develop preclinical in vitro neutralization and challenge models for a candidate SARS-CoV-2 vaccine, we isolated SARS-CoV-2 strains from bronchoalveolar lavage fluid samples of 11 hospitalized patients (including five patients in intensive care), of which five are from China, three from Italy, one from Switzerland, one from the United Kingdom, and one from Spain (table S1). These patients were infected with SARS-CoV-2 during the most recent outbreak. The 11 samples contained SARS-CoV-2 strains that are widely scattered on the phylogenetic tree constructed from all available sequences, representing to some extent circulating SARS-CoV-2 populations (Fig. 1A and fig. S1). We chose strain CN2 to develop a purified inactivated SARS-CoV-2 virus vaccine, PiCoVacc, and another 10 strains,

<sup>1</sup>Sinovac Biotech Ltd., Beijing, China. <sup>2</sup>Key Laboratory of Human Disease Comparative Medicine, Chinese Ministry of Health, Beijing Key Laboratory for Animal Models of Emerging and Reemerging Infectious Diseases, Institute of Laboratory Animal Science, Chinese Academy of Medical Sciences and Comparative Medicine Center, Peking Union Medical College, Beijing, China. <sup>3</sup>Department of Microbiology, Zhejiang Provincial Center for Disease Control and Prevention, Hangzhou, China. <sup>4</sup>Division of Respiratory Virus Vaccines, National Institute for Food and Drug Control, Beijing, China. <sup>5</sup>CAS Key Laboratory of Infection and Immunity, National Laboratory of Macromolecules, Institute of Biophysics, Chinese Academy of Sciences, Beijing, China. <sup>6</sup>National Institute for Communicable Disease Control and Prevention, Chinese Center for Disease Control and Prevention, Changping, Beijing, China. <sup>7</sup>Institute of Microbiology and Epidemiology, Academy of Military Medical Sciences, Beijing, China.

\*These authors contributed equally to this work.

†Corresponding author. Email: qinchuan@pumc.edu.cn (C.Q.); yjzhang@cdc.zj.cn (Y.Z.); yinwd@sinovac.com (W.Y.); xiangxi@ibp.ac.cn (X.W.); changgui@aliyun.com (C.L.); lujinxing@icdc.cn (J.L.)



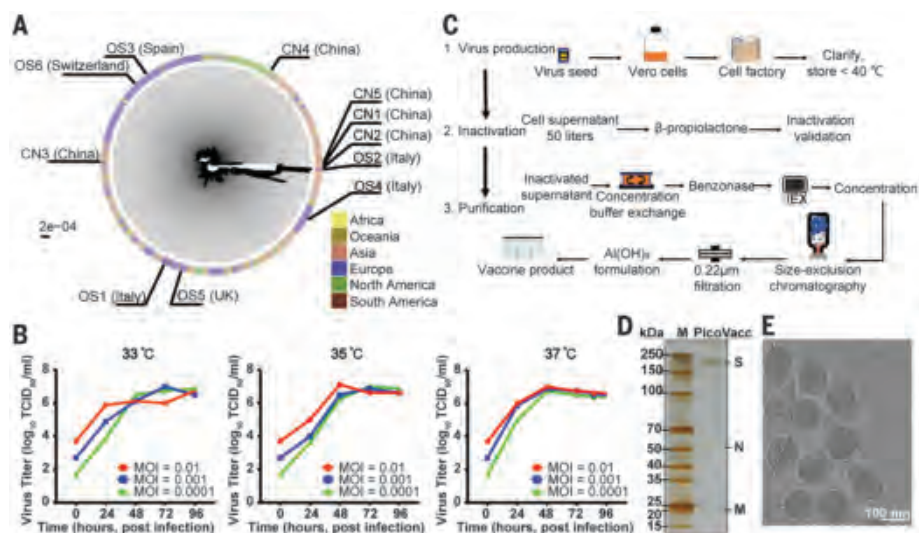


**Fig. 1. Characterization of the SARS-CoV-2 vaccine candidate PiCoVacc.** (A) SARS-CoV-2 maximum likelihood phylogenetic tree. The SARS-CoV-2 isolates used in this study are depicted with black lines and labeled. Viral strains were isolated in infected patients who traveled from the continents indicated. (B) Growth kinetics of PiCoVacc (CN2) P5 stock in Vero cells. (C) Flowchart of PiCoVacc preparation. (D) Protein composition and purity evaluation of PiCoVacc by NuPAGE 4 to 12% Bis-Tris gel. (E) Representative electron micrograph of PiCoVacc. White scale bar 100 nm.

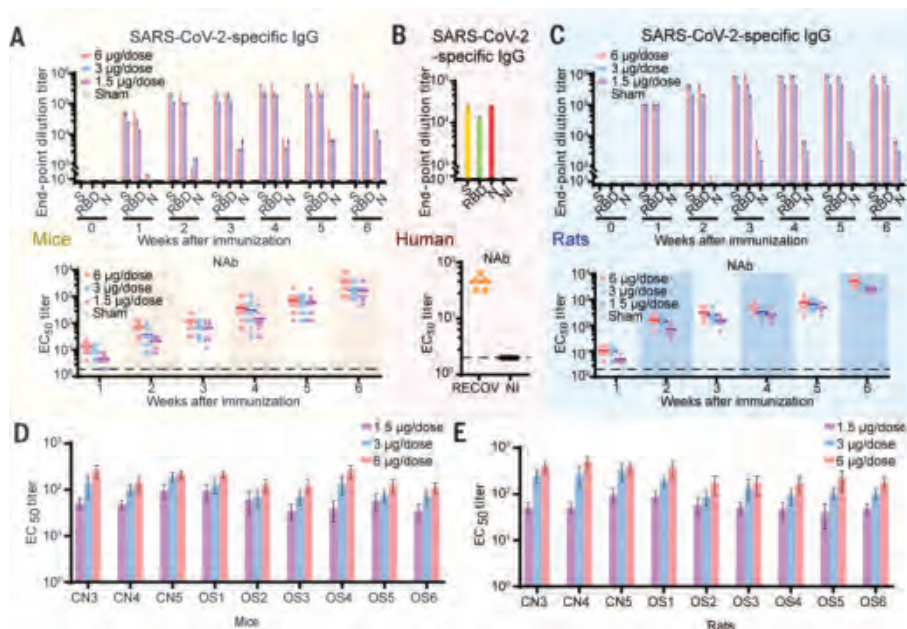


**Fig. 2. PiCoVacc immunization elicits an NAb response against 10 representative SARS-CoV-2 isolates.** BALB/c mice and Wistar rats were immunized with various doses of PiCoVacc or control (adjuvant only) ( $n = 10$ ). Sera from recovered COVID19 patients (RECOV) and noninfected (NI) individuals were used as positive and negative controls, respectively. The antibody responses were analyzed in mice (A), humans (B), and rats (C). Top: SARS-CoV-2-specific IgG responses as measured by ELISA. Bottom: NAb titer as determined by microneutralization assay. The spectrum of neutralizing activities elicited by PiCoVacc was investigated in mice (D) and rats (E). Neutralization assays against the other nine isolated SARS-CoV-2 strains were performed using mouse and rat sera collected 3 weeks after vaccination. Data points represent mean  $\pm$  SEM of individual animals and humans from five to 10 independent experiments. Error bars indicate SEM. Dotted lines indicate the limit of detection. Horizontal lines indicate the geometric mean titer of median effective concentration (EC<sub>50</sub>) for each group.

CN1, CN3 to CN5, and OS1 to OS6, as preclinical challenge strains. The CN1 and OS1 strains are closely related to 2019-nCoV-BetaCoV Wuhan/WIV04/2019 and EPI\_ISL\_412973, respectively, which have been reported to cause severe clinical symptoms, including respiratory failure requiring mechanical ventilation (9, 10).

To obtain a viral stock adapted for efficient growth in Vero cells for PiCoVacc production, the CN2 strain was first plaque purified and passaged once in Vero cells to generate the P1 stock. After this, another four passages were performed to generate the P2 to P5 stocks. Growth kinetics analysis of the P5 stock in Vero cells showed that this stock replicated efficiently and reached a peak titer of 6 to 7 log<sub>10</sub> median tissue culture infectious dose (TCID<sub>50</sub>/ml) by 3 or 4 days post-infection (dpi) at multiplicities of infection of 0.0001 to 0.01 and temperatures between 33° and 37°C (Fig. 1B). To evaluate the genetic stability of PiCoVacc, five more passages were performed to obtain the P10 stock, and its whole genome, together with those of the P1, P3, and P5 stocks, was sequenced. Compared with P1, only two amino acid substitutions, Ala→Asp at E residue 32 (E-A32D) and Thr→Ile at nsp10 residue 49 (nsp10-T49I), occurred in the P5 and P10 stocks (table S2), suggesting that the PiCoVacc CN2 strain has excellent genetic stability without the S mutations that might potentially alter the NAb epitopes. To produce pilot-scale PiCoVacc for animal studies, the virus was propagated in a 50-liter culture of Vero cells using the Cell Factory system and inactivated using β-propiolactone (Fig. 1C). The virus was purified using depth filtration and two optimized steps of chromatography, yielding a highly pure preparation of PiCoVacc (Fig. 1D). Additionally, cryo-electron microscopy analysis showed intact, oval-shaped particles with diameters of 90 to 150 nm, which were embellished with crown-like spikes, representing a prefusion state of the virus (Fig. 1E).

To assess the immunogenicity of PiCoVacc, groups of BALB/c mice ( $n = 10$ ) were injected at days 0 and 7 with various doses of PiCoVacc mixed with alum adjuvant (0, 1.5, 3, or 6 μg per dose, with 0 μg in physiological saline as the sham group). No inflammation or other adverse effects were observed. Spike-specific, receptor binding domain (RBD)-specific, and N-specific antibody responses were evaluated by enzyme-linked immunosorbent assays (ELISAs) at weeks 1 to 6 after the initial immunization (fig. S2). SARS-CoV-2 S-specific and RBD-specific immunoglobulin G (IgG) developed quickly in the sera of vaccinated mice and peaked at a titer of 819,200 (>200 μg/ml) and 409,600 (>100 μg/ml), respectively, at week 6 (Fig. 2A). RBD-specific IgG accounted for half of the S-induced antibody responses, suggesting that RBD is the dominant immunogen; this closely matches the serological profile of the blood of recovered COVID-19 patients (Fig. 2, A and B) (17).

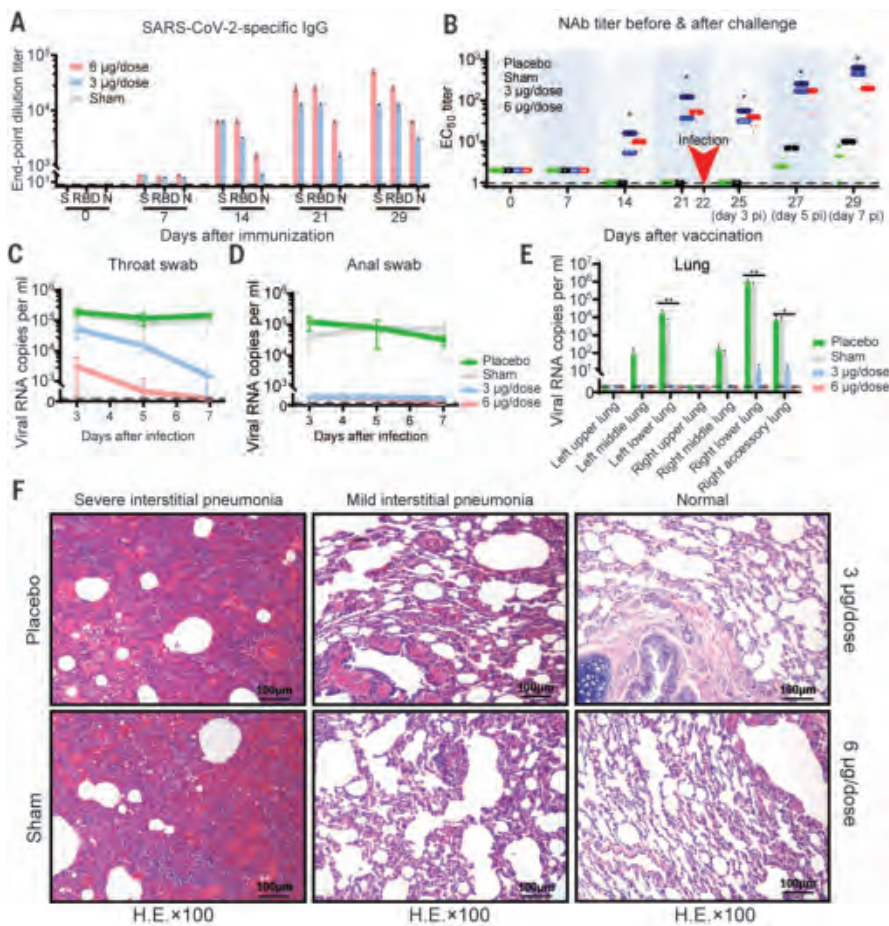


**Fig. 3. Immunogenicity and protective efficacy of PiCoVacc in nonhuman primates.** Macaques were immunized three times intramuscularly with various doses of PiCoVacc or adjuvant only (sham) or placebo ( $n = 4$ ). SARS-CoV-2-specific IgG response (**A**) and NAb titer (**B**) were measured. Data points represent mean  $\pm$  SEM of individual macaques from four independent experiments. Error bars indicate SEM. Dotted lines indicate the limit of detection. Horizontal lines indicate the geometric mean titer of EC<sub>50</sub> for each group. (**C** to **F**) The protective efficacy of PiCoVacc against SARS-CoV-2 challenge at week 3 after immunization was evaluated in macaques. Viral loads of throat (**C**) and anal (**D**) swab specimens collected from the inoculated macaques at 3, 5, and 7 dpi were monitored. Viral loads in various lobes of lung tissue from all the inoculated macaques at 7 dpi were measured (**E**). RNA was extracted and viral load was determined by quantitative reverse transcription polymerase chain reaction. All data are presented as means  $\pm$  SEM from four independent experiments. Error bars indicate SEM. Asterisks indicate significance: \* $P < 0.05$  and \*\* $P < 0.01$ . (**F**) Histopathological examinations in lungs from all the inoculated macaques at 7 dpi. Lung tissue was collected and stained with hematoxylin and eosin.

Unexpectedly, the amount of N-specific IgG induced was ~30-fold lower than that of antibodies targeting S or RBD in immunized mice (Fig. 2A). Previous studies have shown that the N-specific IgG is abundant in the sera of COVID-19 patients and serves as one of the clinical diagnostic markers (11). PiCoVacc could elicit ~10-fold higher S-specific antibody titers in mice compared with serum from the recovered COVID-19 patients (Fig. 2, A and B). Although this observation is currently not indicative of PiCoVacc's ability to produce similar results in humans, it highlights its potential to induce a strong and potent immune response. Our findings, coupled with the fact that the antibodies targeting N of SARS-CoV-2 do not provide protective immunity against the infection (12), suggest that PiCoVacc might be capable of eliciting more effective antibody responses (Fig. 2, A and B).

Next, we measured SARS-CoV-2-specific NAb over time using microneutralization (MN50) assays. Similar to S-specific IgG responses, the NAb titer against the CN1 strain emerged at week 1 (titer of 12 for the high-dose immunization), surged after the week 2 booster, and reached a titer up to 1500 for the low and medium doses and 3000 for the high dose at week 7 (Fig. 2A). By contrast, the sham group

did not develop detectable SARS-CoV-2-specific antibody responses (Fig. 2, A and B). In addition, immunogenic evaluations of PiCoVacc in Wistar rats with the same immunization strategy yielded similar results: The maximum neutralizing titers reached 2048 to 4096 at week 7 (Fig. 2C). To investigate the spectrum of neutralizing activities elicited by PiCoVacc, we conducted neutralization assays against the other nine isolated SARS-CoV-2 strains using mouse and rat serum collected 3 weeks after vaccination. Neutralizing titers against these strains demonstrated that PiCoVacc is capable of eliciting antibodies that may exhibit potent neutralization activities against the SARS-CoV-2 strains circulating worldwide (Fig. 2, D and E).

We next evaluated the immunogenicity and protective efficacy of PiCoVacc in rhesus macaques (*Macaca mulatta*), a nonhuman primate species that shows a COVID-19–like disease caused by SARS-CoV-2 infection (13). Macaques were immunized three times intramuscularly with medium doses (3 µg per dose) or high doses (6 µg per dose) of PiCoVacc at days 0, 7, and 14 ( $n = 4$ ). S-specific IgG and NAb were induced at week 2 and rose to ~12,800 and ~50, respectively, at week 3 (before virus challenge) in both vaccinated groups; their titers were

similar to those of sera from the recovered COVID-19 patients (Fig. 3, A and B). Unexpectedly, NAb titers (61) in the medium-dose group were ~20% greater than those (50) observed in the high-dose group at week 3, possibly because of individual differences in the ability of one animal in the medium-dose group in eliciting an ~10-fold higher titer compared with the other three animals (Fig. 3B). Excluding this exception, the NAb titer in the medium-dose group decreased to 34, ~40% lower than that in the high-dose group. Subsequently, we conducted a challenge study by a direct inoculation of  $10^6$  TCID<sub>50</sub> of SARS-CoV-2 CN1 into the animals' lungs intratracheally at day 22 (1 week after the third immunization) in vaccinated and control macaques to verify the protective efficacy. As expected, all control macaques [those receiving adjuvant (sham group) and those receiving physiological saline (placebo group)] showed excessive copies ( $10^4$  to  $10^6$ /ml) of viral genomic RNA in the pharynx, crissum, and lung by 3 to 7 dpi, along with severe interstitial pneumonia (Fig. 3, C to F). By contrast, all vaccinated macaques were largely protected against SARS-CoV-2 infection, with very mild and focal histopathological changes in a few lobes of lung, probably caused by a direct



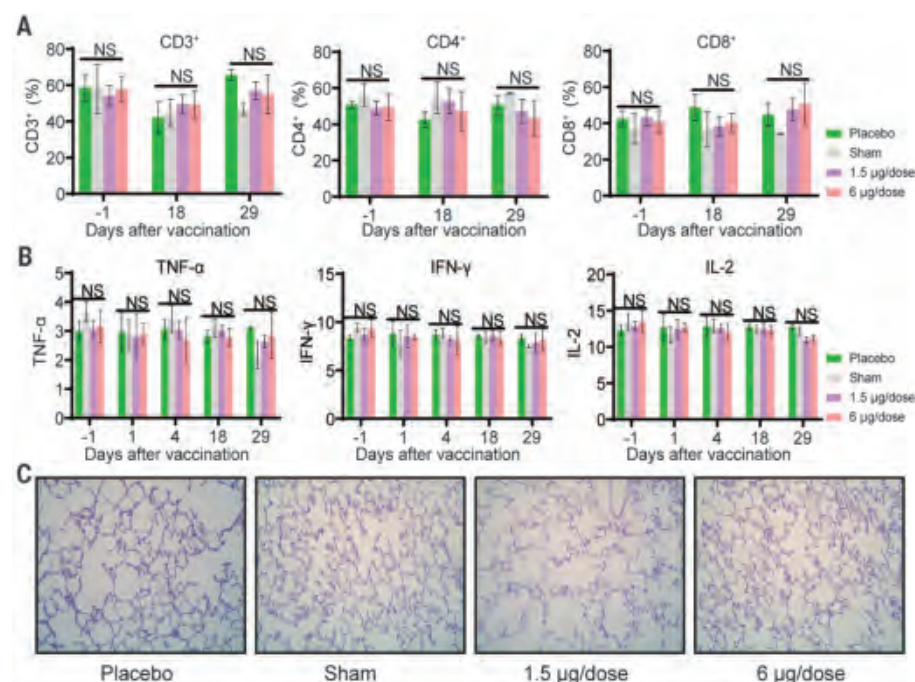


**Fig. 4. Safety evaluation of PiCoVacc in nonhuman primates.** Macaques were immunized three times at days 0, 7, and 14 intramuscularly with low-dose (1.5 µg per dose) or high-dose (6 µg per dose) PiCoVacc or adjuvant only (sham) or placebo. **(A and B)** Hematological analysis in all four groups of macaques ( $n = 4$ ). **(A)** Percentage of lymphocytes, including CD3<sup>+</sup>, CD4<sup>+</sup>, and CD8<sup>+</sup>, were monitored at days -1 (1 day before vaccination), 18 (3 days after the second vaccination), and 29 (7 days after the third vaccination). **(B)** Key cytokines containing TNF-α, IFN-γ, and IL-2 were examined at days -1, 1 (the day of the first vaccination), and 4, 18, and 29 after vaccination. Data points show mean ± SD from four independent experiments. Error bars indicate SD. **(C)** Histopathological evaluations in lungs from four groups of macaques at day 29. Lung tissue was collected and stained with hematoxylin and eosin.

inoculation of  $10^6$  TCID<sub>50</sub> of virus into the lung through the intratracheal route that needed a longer time (>1 week) to recover completely (Fig. 3F). Viral loads decreased significantly in all vaccinated macaques but increased slightly in control animals at 3 to 7 dpi (Fig. 3, C to E). All four macaques that received the high dose had no detectable viral loads in pharynx, crissum, or lung at 7 dpi. In the medium-dose group, we indeed partially detected the viral blip from pharyngeal (3/4), anal (2/4), and pulmonary (1/4) specimens at 7 dpi, whereas viral loads presented an ~95% reduction compared with the sham groups (Fig. 3, C to E). The NAb titer in vaccinated groups decreased by ~30% by 3 dpi to neutralize viruses, then rapidly increased from 5 to 7 dpi to maintain neutralization efficacy. Compared with the high-dose group (titer of ~145), the higher NAb titers observed in the medium-dose group at 7 dpi (titer of ~400 for four macaques) might have resulted from relatively low levels of viral replication, suggesting that a longer time was required for complete viral clearance. No antibody-dependent enhancement (ADE) of infection was observed for the vaccinated macaques despite the observation that a relatively low NAb titer existed

within the medium-dose group before infection, offering partial protection. The possibility of manifestation of ADE after antibody titers wane could not be ruled out in this study. Further studies involving observation of challenged animals at longer periods of time after vaccination are warranted to address this.

Previous reports on the development of SARS and MERS vaccine candidates raised concerns about pulmonary immunopathology, either directly caused by a type 2 helper T-cell (Th2) response or as a result of ADE (4, 14, 15). Although T cell responses elicited by many vaccines have been demonstrated to be crucial for acute viral clearance, protection from subsequent coronavirus infections is largely mediated by humoral immunity (16, 17). The “cytokine storm” induced by excessive T cell responses has actually been shown to accentuate the pathogenesis of COVID-19 (18, 19). Therefore, T cell responses elicited by any SARS-CoV-2 vaccine(s) would have to be well controlled to avoid immunopathology. In this context, we systematically evaluated the safety of PiCoVacc in macaques by recording a number of clinical observations and biological indices. Two groups of macaques ( $n = 10$ ) were immunized

by intramuscular injection with low (1.5 µg) or high (6 µg) doses, and another two groups of macaques ( $n = 10$ ) were immunized with adjuvant (sham) and physiological saline (placebo) three times at the 0, 7, and 14 dpi time points. Neither fever nor weight loss was observed in any macaque after immunization with PiCoVacc, and the appetite and mental state of all animals remained normal (fig. S3). Hematological and biochemical analysis, including biochemical blood test, lymphocyte subset percentage (CD3<sup>+</sup>, CD4<sup>+</sup>, and CD8<sup>+</sup>), and key cytokines [tumor necrosis factor (TNF)-α, interferon (IFN)-γ, and interleukin (IL)-2, IL-4, IL-5, and IL-6], showed no notable changes in the vaccinated groups compared with the sham and placebo groups (Fig. 4, A and B, and figs. S4 and S5). In addition, histopathological evaluations of various organs, including lung, heart, spleen, liver, kidney, and brain, from the four groups at day 29 demonstrated that PiCoVacc did not cause any notable pathology in macaques (Fig. 4C and fig. S6).

The serious COVID-19 pandemic and the precipitously increasing numbers of deaths worldwide necessitate the urgent development of a SARS-CoV-2 vaccine, and this requires a new pandemic paradigm. Safety and efficacy are essential for vaccine development at both preclinical studies and clinical trials. Although it is still too early to define the best animal model for studying SARS-CoV-2 infections, rhesus macaques, which mimic COVID-19-like symptoms after SARS-CoV-2 infection, appear to be promising candidates. We provide evidence for the safety of PiCoVacc in macaques, and did not observe infection enhancement or immunopathological exacerbation in our studies. Our data also demonstrate complete protection against SARS-CoV-2 challenge with a 6-µg dose of PiCoVacc in macaques. Collectively, these results suggest a path forward for the clinical development of SARS-CoV-2 vaccines for use in humans. Phase I, II, and III clinical trials with PiCoVacc, as well as other SARS-CoV-2 vaccine candidates, are expected to begin later this year.

## REFERENCES AND NOTES

1. Z. Wu, J. M. McGoogan, *JAMA* **323**, 1239–1242 (2020).
2. Coronaviridae Study Group of the International Committee on Taxonomy of Viruses, *Nat. Microbiol.* **5**, 536–544 (2020).
3. A. Wu et al., *Cell Host Microbe* **27**, 325–328 (2020).
4. N. Lurie, M. Saville, R. Hatchett, J. Halton, *N. Engl. J. Med.* **10.1056/NEJMp2005630** (2020).
5. K. Dhama et al., *Hum. Vaccin. Immunother.* **10.1080/21645515.2020.1735227** (2020).
6. E. Kim et al., *EBioMedicine* **102743** (2020).
7. A. D. Murdin, L. Barreto, S. Plotkin, *Vaccine* **14**, 735–746 (1996).
8. C. Vellozzi et al., *Vaccine* **27**, 2114–2120 (2009).
9. P. Stefanelli et al., *Euro. Surveill.* **25**, 2000305 (2020).
10. P. Zhou et al., *Nature* **579**, 270–273 (2020).
11. L. Liu, S. Wang, S. Zheng, A preliminary study on serological assay for severe acute respiratory syndrome coronavirus 2 (SARS-CoV-2) in 238 admitted hospital patients. *medRxiv* **2020.03.06.20031856** [Preprint]. 8 March 2020; <https://doi.org/10.1101/2020.03.06.20031856>.

12. L. E. Gralinski, V. D. Menachery, *Viruses* **12**, E135 (2020).
13. P. Yu et al., *Animal Model. Exp. Med.* **3**, 93–97 (2020).
14. C. T. Tseng et al., *PLOS ONE* **7**, e35421 (2012).
15. C. Y. Yong, H. K. Ong, S. K. Yeap, K. L. Ho, W. S. Tan, *Front. Microbiol.* **10**, 1781 (2019).
16. E. Prompetchara, C. Ketloy, T. Palaga, *Asian Pac. J. Allergy Immunol.* **38**, 1–9 (2020).
17. J. Zhao et al., *J. Virol.* **89**, 6117–6120 (2015).
18. J. M. Nicholls et al., *Lancet* **361**, 1773–1778 (2003).
19. H. Y. Zheng et al., *Cell. Mol. Immunol.* **17**, 541–543 (2020).

## ACKNOWLEDGMENTS

We thank F. Gao, Z. Rao, and J. Wang for project discussion; W. Zhai and M. Li for phylogenetic analysis; and the researchers who submitted sequences to the GISAID's EpiFlu Database on which this research is based. **Funding:** This work was supported by the National Key Research and Development Program (2020YFC0842100, 2020YFA0707500), the Strategic Priority Research Program (XDB29010000), the CAMS initiative for Innovative Medicine of China (Grant No. 2016-I2M-2-006), National Mega projects of China for Major Infectious Diseases

(2017ZX10304402), National Key Research and Development Project of China (Grant No. 2016YFD0500304), Zhejiang Province Science and Technology Major Project (2020C03124), and the Beijing science and technology plan (Z201100005420006). X.W. was supported by the Ten Thousand Talent Program and the NSFS Innovative Research Group (grant no. 81921005). **Author contributions:** L.B., H.M., L.W., K. Xu., Y.-J. L., H.G., X.G., B.K., Y.H., J.L., F.C., D.J., Y.Y., C.-F.Q., J.L., X.L., W.S., D.W., H.Z., L.Z., W.D., and Y.-R.L. performed experiments; Q.G., C.Q., Y.Z., W.Y., X.W., C.L., J.-X.L., and X.G. designed the study; all authors analyzed data; and X.W. wrote the manuscript. **Competing interests:** Q.G., L.W., Y.L., Z.L., X.G., F.C., Y.Y., and Y.L. are inventors on patent applications PCT/CN2020/086892 and PCT/CN2020/085413 submitted by Sinovac Biotech, Ltd. that covers "inactivated vaccine for SARS-CoV-2 and the preparation thereof." **Data and materials availability:** The complete genome sequences of SARS-CoV-2 used in this study have been deposited in GenBank under accession numbers MT407649, MT407650, MT407651, MT407652, MT407653, MT407654, MT407655, MT407656, MT407657, MT407658, and MT407659. This work is licensed under a Creative Commons Attribution 4.0 International (CC BY 4.0) license,

which permits unrestricted use, distribution, and reproduction in any medium, provided the original work is properly cited. To view a copy of this license, visit <https://creativecommons.org/licenses/by/4.0/>. This license does not apply to figures/photos/artwork or other content included in the article that is credited to a third party; obtain authorization from the rights holder before using such material.

## SUPPLEMENTARY MATERIALS

science.sciencemag.org/content/369/6499/77/suppl/DC1  
Materials and Methods  
Figs. S1 to S6  
Tables S1 and S2  
References (20–23)

10 April 2020; accepted 2 May 2020  
Published online 6 May 2020  
10.1126/science.abc1932

## DIELECTRICS

# Ultrahigh capacitive energy density in ion-bombarded relaxor ferroelectric films

Jieun Kim<sup>1</sup>, Sahar Saremi<sup>1</sup>, Megha Acharya<sup>1</sup>, Gabriel Velarde<sup>1</sup>, Eric Parsonnet<sup>2</sup>, Patrick Donahue<sup>1</sup>, Alexander Qualls<sup>2</sup>, David Garcia<sup>1</sup>, Lane W. Martin<sup>1,3\*</sup>

Dielectric capacitors can store and release electric energy at ultrafast rates and are extensively studied for applications in electronics and electric power systems. Among various candidates, thin films based on relaxor ferroelectrics, a special kind of ferroelectric with nanometer-sized domains, have attracted special attention because of their high energy densities and efficiencies. We show that high-energy ion bombardment improves the energy storage performance of relaxor ferroelectric thin films. Intrinsic point defects created by ion bombardment reduce leakage, delay low-field polarization saturation, enhance high-field polarizability, and improve breakdown strength. We demonstrate energy storage densities as high as ~133 joules per cubic centimeter with efficiencies exceeding 75%. Deterministic control of defects by means of postsynthesis processing methods such as ion bombardment can be used to overcome the trade-off between high polarizability and breakdown strength.

**D**ielectric materials can store charge and release it upon application and removal of an electric field. Electrostatic capacitors based on dielectrics have become key components in modern electronics and electric power systems because of their inherently fast charging and discharging rates and their high reliability (1–5). Capacitors generally have low energy densities relative to other energy storage systems such as batteries or fuel cells. The requirements for cost reduction and device miniaturization have driven rapid growth in research to develop dielectric capacitors that have high energy density, are efficient and reliable, and exhibit robust temperature stability (4).

One of the key parameters for energy storage in capacitors is the discharged-energy density  $U_d$ , defined as  $\int_{P_{\text{rem}}}^{P_{\text{max}}} E dP$ , where  $E$  is

the electric field,  $P_{\text{max}}$  is the maximum polarization, and  $P_{\text{rem}}$  is the remanent polarization (6). The other key parameter is the efficiency  $\eta = [U_d / (U_d + U_{\text{loss}})] \times 100\%$ , where  $U_{\text{loss}}$  is the energy dissipated as a result of leakage or hysteresis and corresponds to the area inside the polarization–electric field hysteresis loop. To achieve high  $U_d$  and  $\eta$ , a dielectric capacitor should have a large change in polarization ( $P_{\text{max}} - P_{\text{rem}}$ ) during discharge and a large breakdown electric field ( $E_b$ ). These two characteristics are usually inversely correlated,  $E_b = k^{-0.65}$  (where  $k$  is the dielectric constant), because of a sharper rise in local electric field in high- $k$  materials (7). The focus of several investigations has been on optimizing the energy storage performance by inducing relaxor behavior to reduce  $P_{\text{rem}}$  in ferroelectrics with large  $P_{\text{max}}$  and hysteresis (1), enhancing  $E_b$  in ferroelectrics with relaxor behavior (8), enhancing  $P_{\text{max}}$  of simple dielectrics with high  $E_b$  (9), or some combination thereof (2, 10).

Although the main idea for materials design has been to modify ferroelectrics into relaxors

to exploit their delayed polarization saturation and relatively weak hysteresis through chemical doping or heterostructure design (1, 2, 4, 6, 11, 12), little is known about how to improve the energy storage performance of relaxors themselves. To achieve this, we propose a new strategy based on ion bombardment. By creating intrinsic point defects in epitaxial films of the prototypical relaxor ferroelectric 0.68Pb(Mg<sub>1/3</sub>Nb<sub>2/3</sub>)O<sub>3</sub>-0.32PbTiO<sub>3</sub> (PMN-PT) using high-energy (3 MeV) helium ions that are made incident on PMN-PT postsynthesis (13), we can achieve simultaneous enhancement of switchable polarization ( $P_{\text{max}} - P_{\text{rem}}$ ) and  $E_b$ . We demonstrate ultrahigh energy densities ( $U_d > 130 \text{ J/cm}^3$ ) with high efficiency ( $\eta > 75\%$ ), excellent reliability ( $>10^8$  cycles), and temperature stability ( $-100^\circ$  to  $200^\circ\text{C}$ ) in such ion-bombarded PMN-PT films.

Defects are, in general, thought to be deleterious to (relaxor) ferroelectrics and are blamed for high leakage currents, aging, and other negative effects (14). Recent studies have shown that defects produced by ion bombardment with high-kinetic energy species can be used to create favorable intrinsic point defects and complexes (e.g., defect dipoles), which can improve ferroelectric/electrical properties or even create novel function (15–25). Both point defects and defect dipoles or complexes can interact with free charge, producing deep-level trap states, or with polarization (biasing, pinning domain walls, etc.) (14). As a result, they have been used to induce numerous desirable effects such as enhancing electrical resistivity (15), tuning coercive fields and imprint and manipulating relaxor character (17), enhancing Curie temperatures (21), stabilizing morphotropic phase boundaries (22), driving large reversible piezoelectric strains (23), creating colossal permittivity (24), and even producing multistate stability (20, 25).

We illustrate the effect of ion bombardment on the PMN-PT films in a schematic of the ferroelectric polarization–electric field hysteresis loops for as-grown and ion-bombarded materials in Fig. 1A. Region 1 represents the presaturation

<sup>1</sup>Department of Materials Science and Engineering, University of California, Berkeley, CA 94720, USA. <sup>2</sup>Department of Physics, University of California, Berkeley, CA 94720, USA.

<sup>3</sup>Materials Sciences Division, Lawrence Berkeley National Laboratory, Berkeley, CA 94720, USA.

\*Corresponding author. Email: [lwmartin@berkeley.edu](mailto:lwmartin@berkeley.edu)



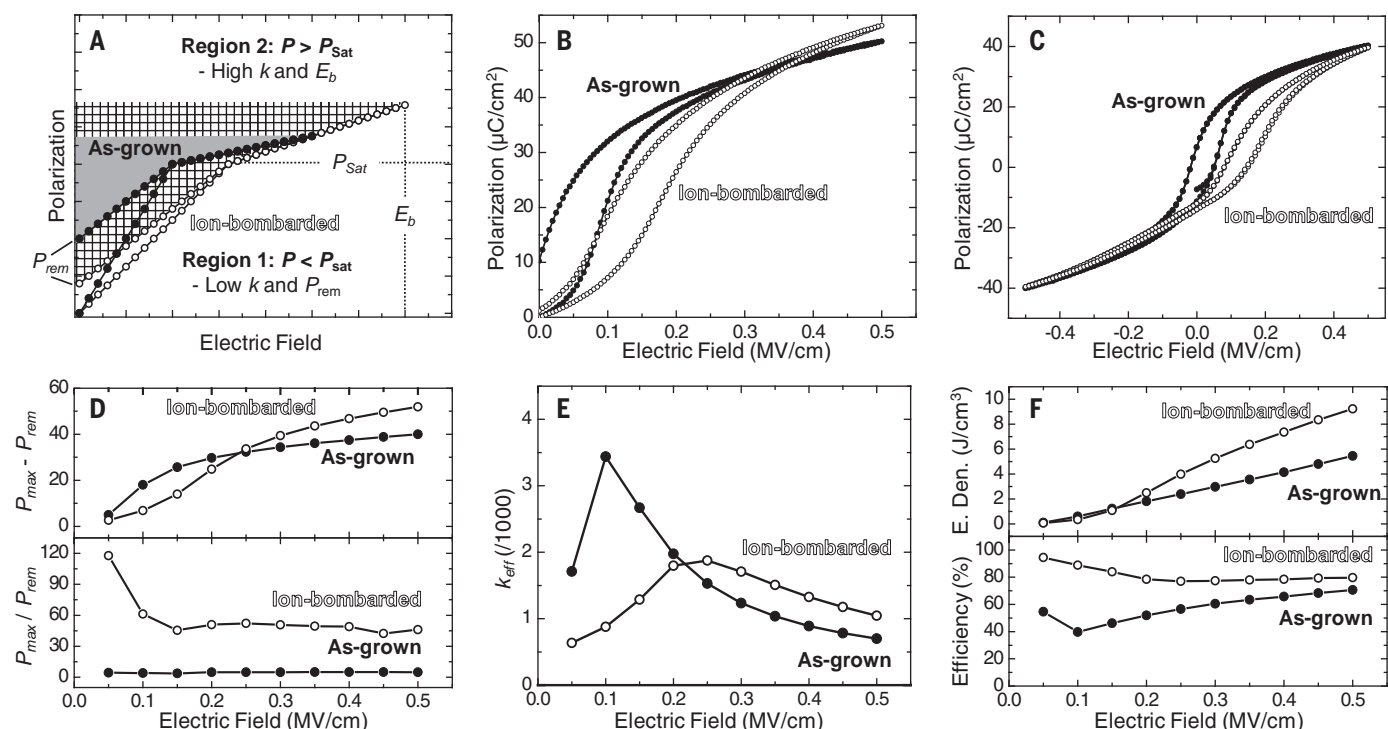


**Fig. 1. Delayed polarization saturation and low-field energy storage properties.** (A) Schematic illustrating the effect of ion bombardment on unipolar polarization–electric field hysteresis loops. Filled and cross-hatched areas in the hysteresis loops represent the energy density for as-grown and ion-bombarded films, respectively. Key features of the ion-bombarded state are indicated for each region. (B and C) Unipolar (B) and bipolar (C) hysteresis loops out to  $E = 0.5$  MV/cm measured at 10 kHz. (D to F)  $P_{\max} - P_{\text{rem}}$  and  $P_{\max}/P_{\text{rem}}$  (D),  $k_{\text{eff}}$  (E), and energy density (E. Den.) and efficiency (F) calculated from unipolar hysteresis loops.

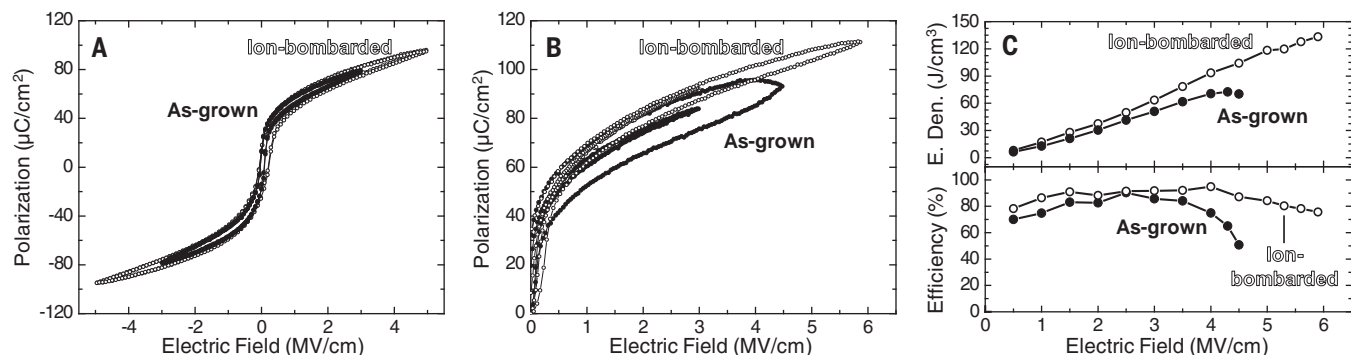


**Fig. 2. High-field energy storage properties.** (A and B) Bipolar (A) and unipolar (B) hysteresis loops at moderate and maximum  $E$  measured at 10 kHz. (C) Energy density and efficiency calculated from unipolar hysteresis loops.

regime where  $E \ll E_b$  and  $P < P_{\text{sat}}$  (saturation polarization) and is characterized by increased dielectric loss and  $P_{\text{rem}}$  with increasing  $E$ . Here,  $U_d$  and  $\eta$  are improved by lowering the effective dielectric constant  $k_{\text{eff}}$  (because the energy density during the charging cycle  $U = \frac{1}{2}k_{\text{eff}}\epsilon_0 E^2$ , where  $\epsilon_0$  is the permittivity of free space) and lowering  $P_{\text{rem}}$ . Region 2 represents the post-saturation regime where  $E \leq E_b$  and  $P > P_{\text{sat}}$  and is characterized by nonlossy enhancement of polarization with increasing  $E$ . The lack of hysteresis is attributable either to polarization elongation after complete switching of the do-

main in ferroelectrics or to the fast dynamics of polarization fluctuations in relaxors (26). In this region, higher values of  $k_{\text{eff}}$  and  $E_b$  are advantageous to maximize the energy density. We observed highly nonlinear switching behavior, early polarization saturation, and moderate  $P_{\text{rem}}$  and  $E_b$  for as-grown PMN-PT films (Fig. 1A). The early polarization saturation and relatively low  $E_b$  result in small  $U_d$  (Fig. 1A, filled area). To improve the energy storage performance, we would like to delay polarization saturation and lower  $P_{\text{rem}}$  in region 1 and to induce high polarizability ( $k_{\text{eff}}$ ) and high  $E_b$  in region 2.

We realized this by purposely increasing the concentration of intrinsic point defects (e.g., lead, titanium, and/or oxygen vacancies, etc.), which are created when helium ions knock target ions from their lattice sites (fig. S1). The increased defect concentration produces two beneficial effects: a reduction of leakage (15) and an introduction of stable imprint (i.e., a horizontal shift of the hysteresis loop) (17). The creation of charged point defects (e.g.,  $V_{\text{Pb}}''$ ,  $V_{\text{Ti}}'$ ,  $V_{\text{O}}^\bullet$ , etc.) can, in turn, give rise to the formation of neutral defect dipoles (e.g.,  $V_{\text{O}}^\bullet - V_{\text{Pb}}''$ ,  $V_{\text{O}}^\bullet - V_{\text{Mg}}''$ , etc.) or more complicated defect

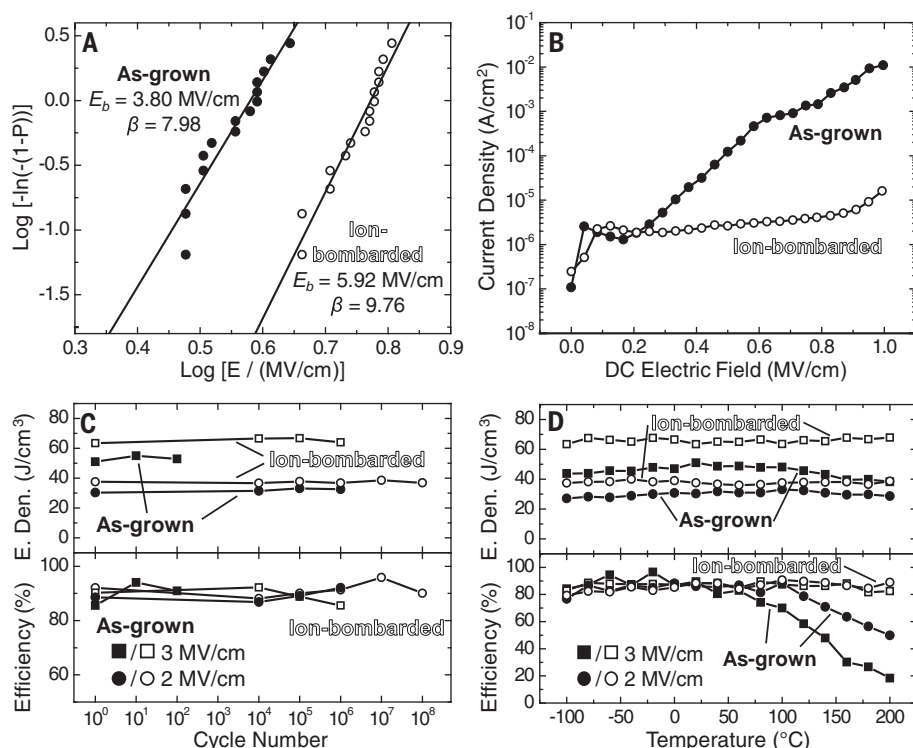


**Fig. 3. Reliability and temperature stability.** (A) Two-parameter Weibull distribution analysis of breakdown strengths. (B) Leakage current density as a function of dc electric field. (C and D) Fatigue test (C) and temperature dependence ( $-100^{\circ}$  to  $200^{\circ}\text{C}$ ) (D) of energy density and efficiency as a function of cycle number and temperature at  $E = 2$  or  $3 \text{ MV/cm}$  and measured at  $10 \text{ kHz}$ .

complexes (e.g.,  $V_{\text{O}}^{\bullet}-V_{\text{Ti}}^{\bullet}-V_{\text{O}}^{\bullet}$ , etc.) to preserve charge neutrality (27, 28). Such defect dipoles can align their elastic and electric dipole moments along the elongated direction of the lattice and/or polarization directions (23). We controlled the defect-dipole alignment to be along the out-of-plane direction by growing PMN-PT films under small in-plane compressive strain, which leads to the appearance of an imprint in the hysteresis loops (17, 21, 29). At the same time, the formation of defect dipoles or complexes leads to a reduction of the leakage current by eliminating shallow-hole trap states such as isolated  $\text{Pb}^{3+}$  and  $V_{\text{Pb}}^{\bullet}$  defects with small activation energies ( $\sim 0.26 \text{ eV}$  and  $\sim 0.56 \text{ eV}$ , respectively) and forming deep-level trap states ( $\sim 1 \text{ eV}$  from the band edge) (30, 31).

In particular, we study  $150\text{-nm PMN-PT}/25\text{-nm Ba}_{0.5}\text{Sr}_{0.5}\text{RuO}_3/\text{NdScO}_3$  (110) heterostructures produced via pulsed-laser deposition. The samples are first patterned with  $100\text{-nm-thick Ba}_{0.5}\text{Sr}_{0.5}\text{RuO}_3$  circular top electrodes with a diameter of  $25 \mu\text{m}$  (13). Smaller electrodes reduce the chance of extrinsic contributions to critical failure (e.g., pinholes) and are thus favorable for studying intrinsic properties (13). After device fabrication, half of the samples are uniformly exposed to ion bombardment (13). Although we have explored a range of ion doses, we focus on a dose of  $3.33 \times 10^{15} \text{ cm}^{-2}$ , which provides the best combination of perform-

ance. Increasing the ion-bombardment dosage would further increase film resistance (15), but it also reduces relaxor character (17), which results in increased  $U_{\text{loss}}$  (i.e., reduced  $\eta$ ) (fig. S2).

The PMN-PT heterostructures were highly crystalline, single-phase, stoichiometric, and coherently strained to the substrate ( $0.5\%$  compressive strain) (figs. S3 to S6). We measured unipolar hysteresis loops by driving the top electrode in both the as-grown and ion-bombarded PMN-PT heterostructures with small magnitudes of positive electric field (Fig. 1B). The sign of the electric field was chosen to be the same as that of the imprint (13). Enhancement of the low-field performance is important because real devices are typically operated at  $E \ll E_b$  to avoid catastrophic failure. This requires avoiding materials design that pushes for larger  $U_d$  and  $\eta$  but results in poor low-field performance. Relative to the as-grown PMN-PT, ion-bombarded PMN-PT has lower  $P_{\text{rem}}$  and higher  $P_{\text{max}}$ . Examination of bipolar hysteresis loops (Fig. 1C) reveals that these differences arise from an increase in the magnitude of the self-polarization and imprint (the hysteresis loops for the as-grown and ion-bombarded PMN-PT are centered at  $0.015 \text{ MV/cm}$  and  $0.115 \text{ MV/cm}$ , respectively). This results in a larger magnitude of negative self-polarization ( $\sim 13.2 \mu\text{C/cm}^2$ ) in the ion-bombarded PMN-PT relative to the as-grown state ( $\sim 7 \mu\text{C/cm}^2$ ),

which leads to larger  $P_{\text{max}}$  in the unipolar hysteresis loop (Fig. 1B) despite similar  $P_{\text{max}}$  under positive and negative fields ( $\sim 40 \mu\text{C/cm}^2$ ; Fig. 1C). The magnitude of  $P_{\text{max}}^+ - P_{\text{max}}^-$  ( $\sim 80 \mu\text{C/cm}^2$ ) is in good agreement with previously reported values for PMN-PT thin films of similar composition (32). Plots of  $P_{\text{max}} - P_{\text{rem}}$  and  $P_{\text{max}}/P_{\text{rem}}$  (Fig. 1D),  $k_{\text{eff}}$  (Fig. 1E),  $U_d$ , and  $\eta$  (Fig. 1F) calculated from the unipolar hysteresis loops (Fig. 1B) as a function of  $E$  reveal delayed polarization saturation below  $E \approx 0.25 \text{ MV/cm}$  at  $P_{\text{sat}}$  ( $\sim 40 \mu\text{C/cm}^2$ ) for the ion-bombarded PMN-PT. This behavior is consistent with suppressed extrinsic contributions to  $k$  (fig. S7). At  $E > 0.25 \text{ MV/cm}$ , however, ion-bombarded PMN-PT shows higher  $k_{\text{eff}}$  (Fig. 1E), which is consistent with reduced tunability in ion-bombarded heterostructures (fig. S8). The combination of delayed polarization saturation, high  $k_{\text{eff}}$  after polarization saturation, and large  $P_{\text{max}}/P_{\text{rem}}$  resulted in higher  $U_d$  and  $\eta$  in ion-bombarded PMN-PT (Fig. 1F). These trends suggest enhanced energy storage performance at higher magnitudes of  $E$ .

We proceeded to examine the high-field energy storage performance by measuring bipolar hysteresis loops at maximum  $E$  before breakdown (Fig. 2A). The ion-bombarded PMN-PT withstands substantially larger  $E$  prior to breakdown. We measured unipolar hysteresis loops at various magnitudes of maximum  $E$  (Fig. 2B). The magnitudes of maximum  $E$  that we could apply to as-grown and ion-bombarded PMN-PT were  $\sim 4.5 \text{ MV/cm}$  and  $\sim 5.9 \text{ MV/cm}$ , respectively. At the maximum  $E$ , ion-bombarded PMN-PT maintains high  $\eta$ , as can be seen from the difference in  $U_{\text{loss}}$  ( $68 \text{ J/cm}^3$  at  $4.5 \text{ MV/cm}$  and  $42.9 \text{ J/cm}^3$  at  $5.9 \text{ MV/cm}$  for the as-grown and ion-bombarded PMN-PT, respectively; Fig. 2B). We extracted  $U_d$  and  $\eta$  from the unipolar hysteresis loops (Fig. 2C). The maximum  $U_d$  for the ion-bombarded PMN-PT was  $133.3 \text{ J/cm}^3$  (with a corresponding  $\eta$  of  $75\%$ ) at  $5.9 \text{ MV/cm}$ . The  $U_d$  of ion-bombarded PMN-PT was enhanced by  $84\%$  relative to the as-grown PMN-PT while maintaining high  $\eta$ . Given that as-grown PMN-PT already exhibits  $U_d$  comparable to the highest reported value for lead-based systems (33), this combination of properties for the ion-bombarded films highlights the importance of postsynthesis processing to enhance energy storage performance.

Reliability and thermal stability are also key factors for discharge capacitors. As was seen in other performance metrics, the ion-bombarded PMN-PT also exhibited superior cyclability and temperature stability due to the enhanced breakdown strength. We obtained statistical values of  $E_b$  from testing 15 capacitors to failure, and fitted the distribution of breakdown strengths to a standard Weibull distribution (Fig. 3A). We found the characteristic  $E_b$  (and Weibull modulus  $\beta$ , which represents the dispersion in the data) to be  $3.80 \pm 0.43 \text{ MV/cm}$



( $\beta = 7.98$ ) and  $5.92 \pm 0.55$  MV/cm ( $\beta = 9.76$ ) for as-grown and ion-bombarded PMN-PT, respectively. Leakage current was also measured under dc electric field, and at  $E = 1$  MV/cm it was found to be reduced by about three orders of magnitude in the ion-bombarded heterostructures (Fig. 3B). We attribute the reduction of leakage current in ion-bombarded PMN-PT to a delay of the onset of the bulk-limited Poole-Frenkel mechanism (fig. S9) (13, 15). We also probed the fatigue behavior by completing unipolar hysteresis loops after applying a 10-kHz triangular waveform at  $E = 1, 2$ , and  $3$  MV/cm for  $10^x$  ( $x = 1, 2, 3, \dots, 8$ ) cycles (Fig. 3C). At  $E = 1$  MV/cm, both the as-grown and ion-bombarded PMN-PT maintained stable performance after  $>10^9$  cycles (fig. S10). At  $E = 2$  MV/cm, the as-grown PMN-PT broke down after  $10^6$  cycles, whereas the ion-bombarded PMN-PT remained stable even after  $10^8$  cycles. At  $E = 3$  MV/cm, the as-grown PMN-PT broke down after  $10^2$  cycles and the ion-bombarded PMN-PT remained stable after  $10^6$  cycles.

We studied temperature stability by measuring unipolar hysteresis loops at  $E = 1, 2$ , and  $3$  MV/cm at a temperature range from  $-100^\circ$  to  $200^\circ\text{C}$  (Fig. 3D). Similar to the fatigue behavior, both as-grown and ion-bombarded PMN-PT maintained stable performance at  $E = 1$  MV/cm across the whole temperature range (fig. S10). At  $E = 3$  MV/cm, the ion-bombarded PMN-PT showed excellent temperature stability of energy density ( $\sim 63$  J/cm<sup>3</sup>) and efficiency ( $\sim 80\%$ ) across the entire temperature range. In contrast, the as-grown PMN-PT showed lower energy density ( $\sim 45$  J/cm<sup>3</sup>) and poorer efficiency ( $<60\%$ ) above  $100^\circ\text{C}$ , rendering it unsuitable for high-temperature operation. Typically, the enhancement of  $E_b$  comes at the cost of reduced energy density at the same magnitude of  $E$ , which requires a higher magnitude of  $E$  to be applied and thus limits the merit of higher  $E_b$  (33). This is not the case for ion-bombarded materials because of the simultaneous enhancement of low-field performance (Figs. 1F and 2C) and  $E_b$  (Fig. 3A), which leads to superior high-temperature performance in ion-bombarded PMN-PT relative to as-grown PMN-PT ( $U_d = 67.9$  J/cm<sup>3</sup> and  $\eta = 82.5\%$  versus  $U_d = 38.2$  J/cm<sup>3</sup> and  $\eta = 18.4\%$  at  $3$  MV/cm and  $200^\circ\text{C}$ ).

Because ion bombardment can produce a variety of robust energy storage properties (i.e., energy density, efficiency, leakage current, fatigue resistance, and temperature stability) from intrinsic point defects, it holds promise as a way to improve energy storage performance. Future studies of the creation and control of defects by other processing routes (e.g., thermal treatment) (23, 28) as well as optimization of growth processes with postsynthesis processing are highly desired. Ultimately, this approach could be applied to boost the energy performance of other relaxor-based energy storage capacitors.

## REFERENCES AND NOTES

- B. Chu et al., *Science* **313**, 334–336 (2006).
- H. Pan et al., *Science* **365**, 578–582 (2019).
- H. Palneedi, M. Peddigari, G.-T. Hwang, D.-Y. Jeong, J. Ryu, *Adv. Funct. Mater.* **28**, 1803665 (2018).
- Q. Li et al., *Nature* **523**, 576–579 (2015).
- V. K. Prateek, V. K. Thakur, R. K. Gupta, *Chem. Rev.* **116**, 4260–4317 (2016).
- B. Xu, J. Iñiguez, L. Bellaiche, *Nat. Commun.* **8**, 15682 (2017).
- J. W. McPherson, J. Kim, A. Shanware, H. Mogul, J. Rodriguez, *IEEE Trans. Electron Dev.* **50**, 1771–1778 (2003).
- Z. Sun et al., *Adv. Mater.* **29**, 1604427 (2017).
- L. Zhang et al., *RSC Adv.* **7**, 8388–8393 (2017).
- M. McMillen et al., *Appl. Phys. Lett.* **101**, 242909 (2012).
- L. Yang, X. Kong, Z. Cheng, S. Zhang, *J. Mater. Chem. A* **7**, 8573–8580 (2019).
- Z. Yao et al., *Adv. Mater.* **29**, 1601727 (2017).
- See supplementary materials.
- D. Damjanovic, *Rep. Prog. Phys.* **61**, 1267–1324 (1998).
- S. Saremi et al., *Adv. Mater.* **28**, 10750–10756 (2016).
- B. Mei et al., *APL Mater.* **7**, 111101 (2019).
- S. Saremi, J. Kim, A. Ghosh, D. Meyers, L. W. Martin, *Phys. Rev. Lett.* **123**, 207602 (2019).
- S. Saremi et al., *Adv. Mater. Interfaces* **5**, 1700991 (2018).
- S. Saremi, R. Gao, A. Dasgupta, L. W. Martin, *Am. Ceram. Soc. Bull.* **97**, 16–23 (2018).
- S. Saremi et al., *Phys. Rev. Mater.* **2**, 084414 (2018).
- A. R. Damodaran, E. Breckenfeld, Z. Chen, S. Lee, L. W. Martin, *Adv. Mater.* **26**, 6341–6347 (2014).
- A. Herklotz et al., *Nano Lett.* **19**, 1033–1038 (2019).
- X. Ren, *Nat. Mater.* **3**, 91–94 (2004).
- W. Hu et al., *Nat. Mater.* **12**, 821–826 (2013).
- D. Lee et al., *Adv. Mater.* **24**, 6490–6495 (2012).
- D. Viehland, S. J. Jang, L. E. Cross, M. Wuttig, *J. Appl. Phys.* **68**, 2916–2921 (1990).
- Y. Chiang, D. P. Birnie, W. D. Kingery, *Physical Ceramics* (Wiley, 1997).
- J. F. Scott, C. A. Araujo, B. M. Melnick, L. D. McMillan, R. Zuleeg, *J. Appl. Phys.* **70**, 382–388 (1991).
- W. L. Warren et al., *J. Appl. Phys.* **79**, 9250–9257 (1996).
- J. Robertson, W. L. Warren, B. A. Tuttle, D. Dimos, D. M. Smyth, *Appl. Phys. Lett.* **63**, 1519–1521 (1993).
- Z. Zhang, P. Wu, L. Lu, C. Shu, *Appl. Phys. Lett.* **88**, 142902 (2006).
- S. H. Baek et al., *Science* **334**, 958–961 (2011).
- X. Hao, Y. Wang, L. Zhang, L. Zhang, S. An, *Appl. Phys. Lett.* **102**, 163903 (2013).

## ACKNOWLEDGMENTS

**Funding:** Supported by the U.S. Department of Energy (DOE) Office of Science, Office of Basic Energy Sciences, Materials Sciences and Engineering Division, under contract DE-AC02-05-CH11231 (Materials Project program KC23MP) for the development of novel functional materials. Also supported by the Kwanjeong Educational Foundation (J.K.); DOE Office of Science, Office of Basic Energy Sciences, under award DE-SC-0012375 for the study of ferroelectric materials (S.S.); NSF grant DMR-1708615 (G.V.); Intel Corp. through the FEINMAN program (E.P.); NSF grant DMR-1608938 (P.D.); and NSF grant OISE-1545907 (D.G.). **Author contributions:** J.K. and L.W.M. conceived this study; J.K. performed this study; L.W.M. supervised this study; J.K. fabricated the films; S.S. and M.A. performed ion bombardment; J.K., E.P., P.D., and A.Q. performed the dielectric and ferroelectric measurements; J.K. performed structural characterizations; J.K., G.V. and D.G. fabricated the devices; and J.K. and L.W.M. wrote the manuscript. All authors discussed the results and edited the manuscript.

**Competing interests:** The authors declare no competing interests or patents. **Data and materials availability:** All data are available in the main text or the supplementary materials.

## SUPPLEMENTARY MATERIALS

science.sciencemag.org/content/369/6499/81/suppl/DC1

Materials and Methods

Supplementary Text

Figs. S1 to S11

References (34, 35)

27 January 2020; accepted 4 May 2020

10.1126/science.abb0631

## QUANTUM GASES

# Strongly correlated superfluid order parameters from dc Josephson supercurrents

W. J. Kwon<sup>1,2</sup>, G. Del Pace<sup>2,3</sup>, R. Panza<sup>1,2</sup>, M. Inguscio<sup>1,2,4</sup>, W. Zwerger<sup>5</sup>, M. Zaccanti<sup>1,2</sup>, F. Scazza<sup>1,2,\*</sup>, G. Roati<sup>1,2</sup>

The direct-current (dc) Josephson effect provides a phase-sensitive tool for investigating superfluid order parameters. We report on the observation of dc Josephson supercurrents in strongly interacting fermionic superfluids across a tunneling barrier in the absence of any applied potential difference. For sufficiently strong barriers, we observed a sinusoidal current-phase relation, in agreement with Josephson's seminal prediction. We mapped out the zero-resistance state and its breakdown as a function of junction parameters, extracting the Josephson critical current behavior. By comparing our results with an analytic model, we determined the pair condensate fraction throughout the Bardeen-Cooper-Schrieffer–Bose-Einstein condensation crossover. Our work suggests that coherent Josephson transport may be used to pin down superfluid order parameters in diverse atomic systems, even in the presence of strong correlations.

**W**hen two superfluids or superconductors are weakly coupled through an insulating potential barrier, a dissipationless current  $I_s$  can flow from one to the other, sustained merely by the relative phase difference  $\varphi$  between the two order parameters ( $I, 2$ ). This phenomenon, known as the dc Josephson effect ( $I, 3$ ), represents a paradigmatic manifestation of the macroscopic quantum phase coherence of any condensed state, and it is the basis of many

applications ( $4-7$ ), such as in the field of metrology for high-precision measurements ( $8, 9$ ). A distinctive feature of any Josephson junction

<sup>1</sup>Istituto Nazionale di Ottica del Consiglio Nazionale delle Ricerche (CNR-INO), 50019 Sesto Fiorentino, Italy.

<sup>2</sup>European Laboratory for Nonlinear Spectroscopy (LENs), 50019 Sesto Fiorentino, Italy.

<sup>3</sup>Department of Physics and Astronomy, University of Florence, 50019 Sesto Fiorentino, Italy.

<sup>4</sup>Department of Engineering, Campus Bio-Medico University of Rome, 00128 Rome, Italy.

<sup>5</sup>Physics Department, Technische Universität München, 85747 Garching, Germany.

\*Corresponding author. Email: scazza@leni.unifi.it

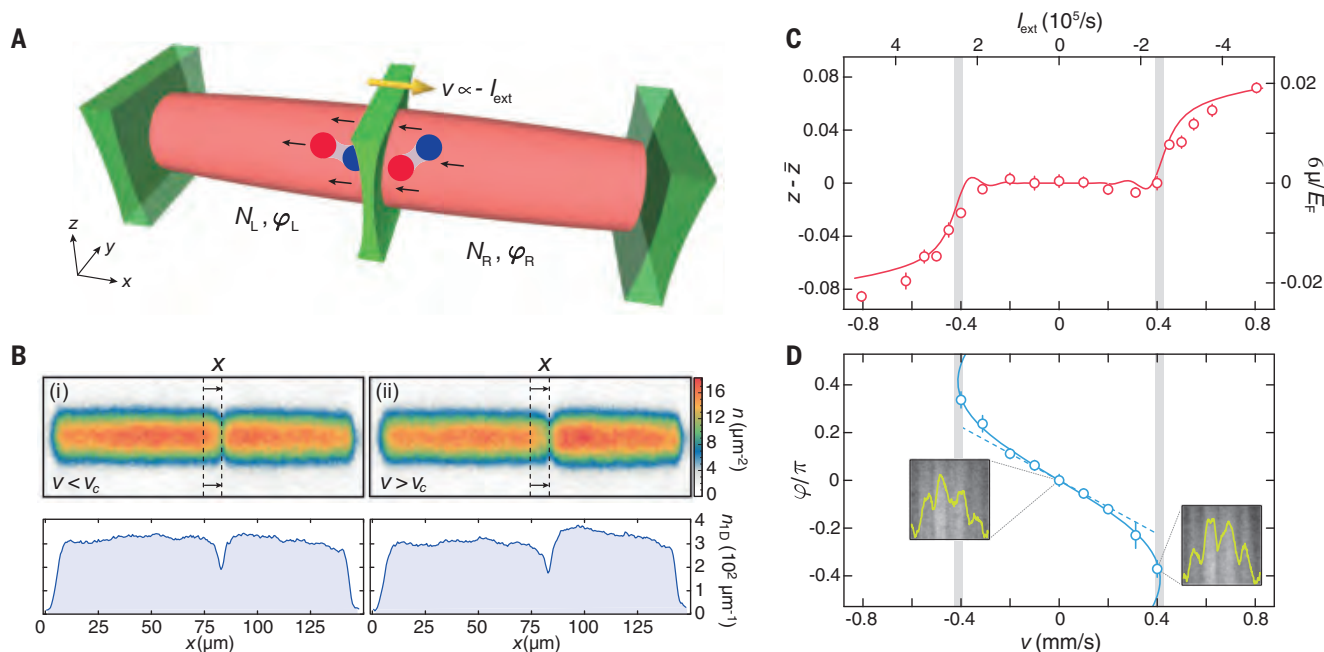


**Fig. 1. Characterization of a current-biased atomic Josephson junction.**

(A) The Josephson junction is realized by weakly coupling two superfluid reservoirs (L, left; R, right) of  $^6\text{Li}$  fermion pairs (paired red/blue circles) through a thin DMD-controlled repulsive barrier. An external current  $I_{\text{ext}}$  is imposed by translating the tunneling barrier at constant velocity  $v$  (yellow arrow). (B) The dynamics are monitored by recording the number imbalance  $z$  through in situ absorption imaging after a total barrier displacement  $\delta x$  (upper panels). Radially integrated density profiles are also shown (lower panels). (i) For currents below a critical value, pairs coherently tunnel through the barrier, maintaining a zero difference in chemical potential between the reservoirs. (ii) Conversely, above the critical current, the superfluid is compressed into the smaller reservoir. (C) Experimental  $I$ - $\Delta\mu$  characteristic of the junction for  $(k_F a)^{-1} \approx 4.2$ ,  $w = 0.95 \mu\text{m}$ , and  $V_0 \approx 0.6E_F \approx 1.8\mu$ , where  $\mu$  is the superfluid bulk chemical potential.

The solid line denotes the RCSJ-model solution fit; the shaded vertical lines represent the value of the extracted  $I_c$  along with its standard confidence interval. The weak oscillatory visible observed in the model just below  $I_c$  stems from small-amplitude plasma oscillations excited by the nonadiabatic ramp-up of the applied current (44). (D) Experimentally determined current-phase relation  $I(\varphi)$  of the junction, recorded under the same conditions as in (C). For each experimental realization,  $\varphi$  is obtained by fitting a matter-wave interference pattern acquired by letting the two reservoirs expand into each other in time of flight (44). Typical interferograms and corresponding integrated profiles are shown in the insets. The solid line is a sinusoidal fit to all data points including a small second-harmonic contribution proportional to  $\sin 2\varphi$ ; the dashed line is a linear fit of the five central data points. Data in (C) and (D) are means  $\pm$  SE over  $\sim 10$  experimental realizations.

is the link between the supercurrent  $I_s$  and  $\varphi$ , namely the current-phase relation  $I_s(\varphi)$  and, associated with it, the existence of a maximum current  $I_c$ . For barriers with sufficiently low transmission, like those originally considered by Josephson (1), the tunneling process can be treated as a perturbation and a simple sinusoidal current-phase relation holds, a simple sinusoidal current-phase relation,  $I_s(\varphi) = I_c \sin(\varphi)$  (2, 10). An externally imposed current  $I_{\text{ext}}$  can flow without establishing any potential drop across the junction only if  $|I_{\text{ext}}| \leq I_c$ , where  $I_c$  is the Josephson critical current. The most striking signature of  $I_c$  is therefore contained in the current-potential characteristic (11, 12). Such a current-voltage ( $I$ - $V$ ) curve is routinely measured in current-biased superconducting Josephson junctions (SJJs), where a zero-voltage branch (the so-called dc branch) at  $|I_{\text{ext}}| \leq I_c$  can be clearly distinguished from a resistive finite-voltage branch at  $|I_{\text{ext}}| > I_c$ . Acting as a precise interferometric probe, Josephson supercurrents offer a unique tool to disclose the nature and the symmetry of superfluid or superconducting order parameters, such as the  $d$ -wave pairing symmetry in cuprate superconductors

(13, 14), and may become fundamental in the quest for Majorana bound states hosted by topological superconducting wires (15, 16).

Supercurrents have been extensively investigated with atomic Bose-Einstein condensates (BECs) (17–26), offering exciting perspectives for atomtronics (27). On the other hand, ultracold Fermi gases offer the unparalleled possibility of exploring superfluid transport from the Bardeen-Cooper-Schrieffer (BCS) limit of weakly bound fermion pairs to a BEC of tightly bound molecules, crossing over the intermediate universal, strongly correlated unitary regime (28). The dynamics of weakly connected fermionic superfluids is fundamentally influenced and complicated by the inherent strong interparticle interactions (29–33), which are also necessary to achieve pair condensation at experimentally accessible temperatures (28). Although the connection between the Josephson current and the superfluid order parameter is theoretically well established in both BCS and BEC limits (34, 35), for crossover superfluids  $I_c$  has been numerically calculated only at the mean-field level (36, 37), and such a connection has not been made explicit. A direct measure

of the Josephson critical current in strongly correlated superfluids is thus highly relevant per se, and it may grant access to the order parameter amplitude—that is, the pair condensate density (38–40)—whose experimental determination has so far been indirect (41–43) and somewhat inconclusive.

Here, we observe the dc Josephson effect by imparting a controlled current through a tunable, nearly ideal Josephson junction connecting two strongly correlated superfluids of ultracold fermionic atoms. Our Josephson junction consists of two superfluid reservoirs comprising  $N_{\text{R,L}} \approx 3.5 \times 10^4$  atom pairs each, weakly coupled through a thin optical barrier (Fig. 1A) (44). The reservoirs are prepared by cooling a balanced mixture of the two lowest hyperfine states of  $^6\text{Li}$  below the condensation temperature at  $T/T_F = 0.06 \pm 0.02$ , measured at unitarity (45, 46), where the superfluid critical temperature is  $T_c/T_F \approx 0.21$  (47). The gas is initially confined into a cigar-shaped harmonic potential, with frequency ratios of about 1:14:12 along the  $x$ ,  $y$ , and  $z$  axes, respectively. Here,  $T_F$  is the Fermi temperature given by  $k_B T_F = E_F$ , where  $k_B$  is the Boltzmann constant,



$E_F \approx \hbar \times 6$  kHz is the Fermi energy of the non-interacting harmonically trapped gas, and  $\hbar$  is the Planck constant. Interactions are parametrized by  $(k_F a)^{-1}$ , where  $a$  is the  $s$ -wave scattering length,  $k_F = \sqrt{2mE_F}/\hbar$  is the Fermi wave vector,  $m$  is the  $^6\text{Li}$  atomic mass, and  $\hbar = \hbar/(2\pi)$ . We tune the scattering length between the two spin states via a broad Feshbach resonance located at 832 G, accessing different superfluid regimes across the BCS-BEC crossover. The repulsive optical barrier at 532 nm propagates along the  $z$  axis and has a Gaussian  $1/e^2$  width  $w \approx 0.95 \pm 0.09$   $\mu\text{m}$  along the  $x$ -direction, unless otherwise specified, whereas it is homogeneous along the  $y$ -direction. Its intensity profile and position are controlled by a digital micromirror device (DMD) whose surface is projected onto the atoms through a high NA  $\approx 0.5$  microscope objective (figs. S1 and S2). To initialize the junction at equilibrium, we initially locate the barrier at the trap center  $x_0$  and raise it to the target potential height  $V_0$  experienced by one atom pair. This creates two identical reservoirs with relative population imbalance  $z = (N_R - N_L)/N \approx 0$ , and correspondingly zero chemical potential difference,  $\Delta\mu = \mu_R - \mu_L$ . Here  $N = N_R + N_L$  is the total pair number and  $\mu$  is the pair bulk chemical poten-

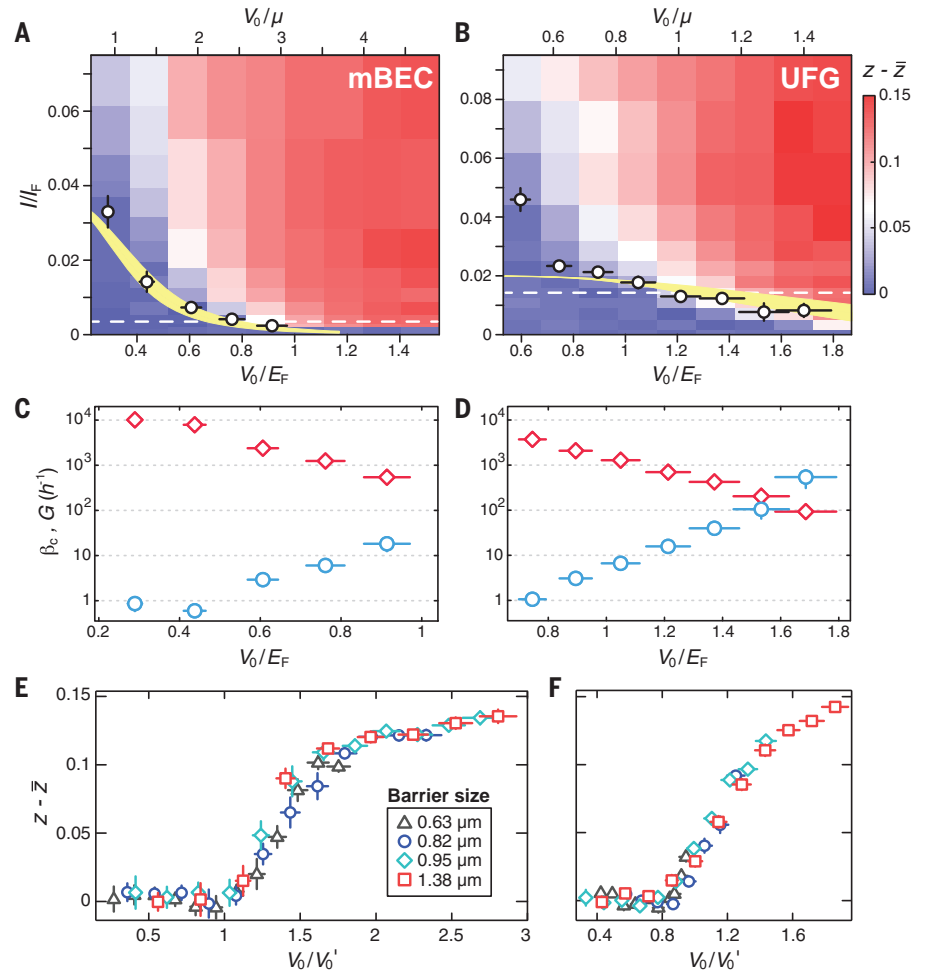
tial. Additionally, two DMD-generated repulsive light sheets select a 140- $\mu\text{m}$ -long central region of the sample (Fig. 1B). These endcaps discard the most dilute, highest-entropy regions of the sample and help to damp out any residual axial sloshing motion, conferring an excellent shot-to-shot stability below 1% to the initially prepared number imbalance  $z$ .

We impose a pair current  $I_{\text{ext}}$  across the junction by setting the optical barrier in relative uniform motion with respect to the superfluid (44, 48), as shown in Fig. 1A. With a constant total barrier displacement  $\delta x \approx 10$   $\mu\text{m}$ ,  $I_{\text{ext}} = (\bar{z}N/2) \times (|v|/\delta x)$ , where  $v$  is the barrier velocity and  $\bar{z} \approx \mp 0.15$  is the imbalance at equilibrium for the final barrier position  $x_0 = \pm \delta x$ . To obtain the current-chemical potential ( $I$ - $\Delta\mu$ ) relation of the junction, we vary  $I_{\text{ext}}$  and use in situ imaging to measure the imbalance  $z$  at time  $t_f = \delta x/|v|$ , when the barrier translation is completed, thus obtaining  $\Delta\mu = (z - \bar{z})E_c N/2$ . Here,  $E_c = 2\partial\mu_L/\partial N_L$  (calculated with  $N_L = N/2$ ) is the effective charging energy of the junction (i.e., the inverse compressibility of the gas), and it reflects the density change between the two reservoirs owing to the particle current through the barrier (35, 48). For  $|I_{\text{ext}}|$  smaller than a critical value  $I_c$ , we observe pairs to

tunnel coherently through the barrier [Fig. 1B, panel (i)], maintaining  $\Delta\mu = 0$  (i.e.,  $z - \bar{z} = 0$ ). Conversely, for  $|I_{\text{ext}}| > I_c$  a finite  $\Delta\mu$  develops, associated with the density increase arising from compression of the smaller reservoir [Fig. 1B, panel (ii)]. Exploiting matter-wave interference between the expanding reservoirs, we can connect the observed pair tunneling to the behavior of the phase difference  $\varphi = \varphi_R - \varphi_L$ . In Fig. 1, C and D, we display typical complete measurements of both the  $I$ - $\Delta\mu$  and  $I$ - $\varphi$  characteristics of our junction for a molecular BEC (mBEC). Albeit with a different current scale, we obtain the same  $I$ - $\Delta\mu$  relation at unitarity and throughout the BEC-BCS interaction crossover (Fig. 2, A and B). The measured current-potential curve closely parallels the typical  $I$ - $V$  characteristics of SJJs in the deep BCS regime (11, 12). In particular, a highly nonlinear  $I$ - $\Delta\mu$  response is clearly visible, with  $\Delta\mu$  exhibiting a zero-resistance plateau for  $|I_{\text{ext}}| < I_c$  (Fig. 1C). The value of  $I_c$  is marked by the sharp onset of a chemical potential difference  $\Delta\mu \neq 0$ , after which the junction displays a resistive behavior. Correspondingly,  $\varphi$  displays a nonlinear monotonic increase, adjusting itself to sustain a supercurrent  $|I_s| = |I_{\text{ext}}| \leq I_c$  (Fig. 1D). For sufficiently large  $V_0$

**Fig. 2. The dc Josephson effect in a tunable, ultracold Josephson junction. (A and B)**

Current-imbalance characteristics for a molecular BEC (mBEC) (A) and a unitary Fermi gas (UFG) (B). Symbols denote the values of  $I_c$  extracted through RCSJ-model fits, normalized to  $I_F \equiv I_{\text{ext}}(v = v_F)$  (i.e., the current associated with a barrier moving at the Fermi velocity  $v_F$ ). The extracted values of  $I_c$  always correspond to barrier motions much slower than the sound velocity (e.g.,  $c \approx 0.35v_F$  at unitarity), as expected for high potential barriers. The vertical error bars denote SE of the fitting combined with uncertainty on  $v_F$ . The yellow shaded regions indicate the calculated  $I_c$  [see (44) for details], considering a 10% uncertainty around the nominal barrier width  $w = 0.95$   $\mu\text{m}$ . Condensate fractions  $\lambda_0$  of 1 and 0.51 are assumed for the mBEC and the UFG, respectively. (C and D) Conductance  $G$  (red diamonds) and Stewart-McCumber parameter  $\beta_c$  (blue circles) as a function of  $V_0/E_F$  for mBEC (C) and UFG (D). (E and F)  $V_0$ -imbalance characteristics of mBEC (E) and UFG (F) obtained for fixed  $I_{\text{ext}}$  [dashed horizontal lines in (A) and (B), respectively] in a mBEC and a UFG for different barrier widths, as indicated. Vertical error bars in (C) to (F) denote SEM; in all panels, horizontal error bars combine the uncertainties in the calibration of  $V_0$  and  $E_F$ .



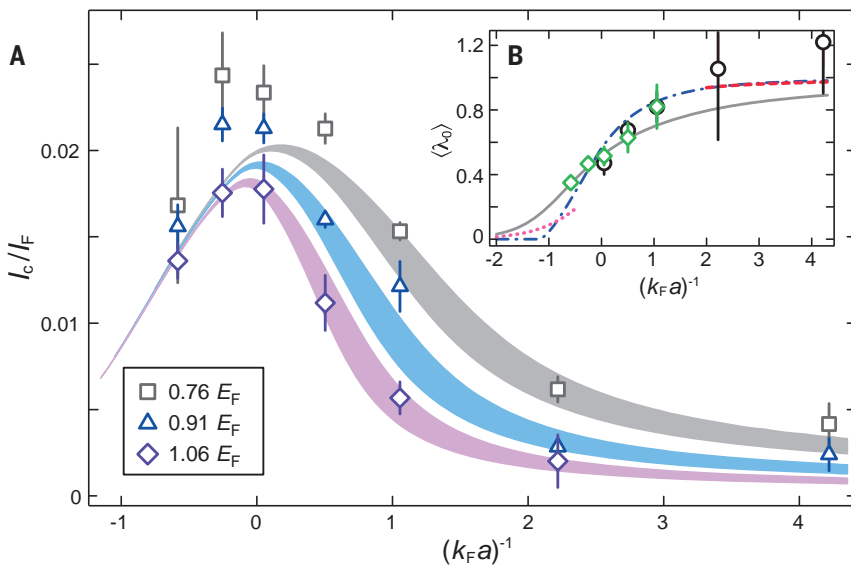


**Fig. 3. Josephson critical current and condensate fraction across the BCS-BEC crossover.** (A) Experimentally determined  $I_c/I_F$  as a function of the interaction strength  $(k_F a)^{-1}$  for three different barrier heights  $V_0$  (symbols). The shaded areas represent the predictions of our analytic model, which use the pair condensate fraction and chemical potential from (45) and account for a 5% uncertainty in the barrier width (44). Error bars are as in Fig. 2, A and B. (B) Total condensate fraction  $\langle \lambda_0 \rangle$  obtained from  $I_c$  through Eq. 3, including all data with  $V_0/\mu > 0.6$  (black circles) or only the  $V_0/E_F \approx 1.06$  dataset (green diamonds). Error bars reflect SE on the experimentally extracted  $I_c$ .  $\langle \lambda_0 \rangle$  values obtained by integrating homogeneous Luttinger-Ward (45) and quantum Monte Carlo results (39) are plotted as a solid gray and dash-dotted blue line, respectively (44). Dotted magenta and dashed red lines represent  $\langle \lambda_0 \rangle$  calculated, respectively, from BCS theory including the Gorkov-Melik-Barkhudarov correction (56) and Bogoliubov quantum depletion for weakly interacting BECs (57).

like that used in Fig. 1, C and D,  $I_s(\varphi) \approx I_c \sin \varphi$ ; this signature has so far been experimentally challenging to observe in degenerate atomic gases (24). These observations unambiguously demonstrate that we access the Josephson dc regime and that the tunneling current observed below  $I_c$  is a Josephson supercurrent. We have directly checked the departure from such a sinusoidal  $I$ - $\varphi$  relation upon decreasing  $V_0$  (10, 36, 49), observing the crossover to a linear current-phase characteristic peculiar to hydrodynamic weak links (24, 44, 49, 50) (fig. S7). Moreover, we find that reversing the direction of the supercurrent across the junction causes the sign of  $\varphi$  to change [i.e.,  $I_s(\varphi) \approx -I_s(-\varphi)$ ], a feature directly associated with the order parameter time-reversal symmetry expected in the present case of  $s$ -wave nonchiral superfluids.

To quantitatively describe the observed  $I$ - $\Delta\mu$  response, we use the resistively and capacitively shunted junction (RCSJ) model widely applied for SJJs (5, 11, 51, 52), namely a lump element circuit model incorporating a capacitive channel  $C$  and a resistive channel  $R$  (fig. S6). The latter opens for  $|I_{\text{ext}}| > I_c$  without affecting the coherent dc Josephson branch, while it incorporates any incoherent currents across the junction that induce a finite  $\Delta\mu$ . The capacitance  $C = 1/E_c$  is provided by self-consistent numerical calculations for crossover superfluids (44, 45). Within the RCSJ model, the dynamics of the junction are described by Kirchhoff's law and the Josephson-Anderson relation:

$$\frac{d^2 \varphi}{d\tau^2} + \sqrt{\frac{1}{\beta_c}} \frac{d\varphi}{d\tau} + \sin \varphi = \frac{I_{\text{ext}}}{I_c}, \quad \dot{\varphi} = -\frac{\Delta\mu}{\hbar} \quad (1)$$

Here,  $\tau = \omega_p t$ , where  $\omega_p = \sqrt{I_c/(\hbar C)}$  is the plasma frequency. Such phase evolution is equivalent

to the motion of a particle with mass proportional to  $C$  and damping proportional to  $G = R^{-1}$  in the tilted washboard potential  $U(\varphi) = \hbar I_c [1 - \cos \varphi - (I_{\text{ext}}/I_c)\varphi]$  (5, 11), and becomes classical for  $\hbar\omega_p \ll \hbar I_c$  (phase regime) as in our case. The Stewart-McCumber parameter (51, 52)  $\beta_c = I_c C/(\hbar G^2) \equiv Q^2$ , where  $Q$  is the quality factor of the junction, determines whether the oscillatory evolution  $\varphi(t)$  is underdamped ( $\beta_c \gg 1$ ) or overdamped ( $\beta_c \ll 1$ ), yielding a hysteretic or nonhysteretic  $I$ - $\Delta\mu$  curve (11), respectively. The RCSJ model excellently captures the experimental  $I$ - $\Delta\mu$  characteristics as shown in Fig. 1C, enabling the extraction of the critical current  $I_c$  and conductance  $G$  as the only fitting parameters. The extracted  $I_c$  values are negligibly sensitive to  $E_c$ , affording a direct and accurate determination of the critical currents.

In Fig. 2, A and B, we display examples of the  $I$ - $\Delta\mu$  curves and the obtained  $I_c$  as a function of  $V_0$  for a mBEC superfluid at  $(k_F a)^{-1} \approx 4.2$  and a unitary Fermi gas (UFG) at  $(k_F a)^{-1} \approx 0$ , respectively. The Josephson critical current is strongly suppressed with increasing  $V_0$  in both regimes because it is proportional to the tunneling amplitude  $|t|$  of pairs between the two coupled condensates (11, 35, 40), which is essentially independent of the strength of the pairing and decreases exponentially with increasing  $V_0 > \mu$ . Figure 2, C and D, shows that  $\beta_c$  and  $G$  exhibit exponential behaviors as a function of  $V_0$  for mBEC and unitary superfluids, respectively. More specifically, we find a quadratic scaling  $G \propto I_c^2$ , in agreement with the prediction for weakly interacting BECs (35), where dissipative normal currents are associated with the emission of Bogoliubov sound modes or localized vortex-like excitations, as observed in previous experiments with crossover superfluids (53). Note that this behavior differs starkly from the linear rela-

tion  $G \propto I_c$  within the Ambegaokar-Baratoff formula (34), typically observed in SJJs, where the normal-state conductance is simply a measure of the barrier transmission probability of single fermions, not necessarily associated with dissipative processes. We also note the wide tunability of the Stewart-McCumber parameter, which increases to values as large as  $\beta_c \sim 10^3$  for the highest  $V_0$  explored in the UFG thanks to a steeper dependence  $\beta_c \propto G^{-3/2}$  when compared to BCS superconductors. In this underdamped regime ( $Q \gg 1$ ), our junction is expected to be highly hysteretic—a promising condition for the observation of Shapiro resonances in the current-potential characteristic under an ac current drive (5, 11).

To gain a precise microscopic understanding of the observed behavior of the Josephson critical current, we rely on the analytic model recently presented in (40). Within such a framework, expected to hold within the tunneling limit for any coupling strength throughout the BCS-BEC crossover, the critical pair current density per unit area can be expressed in terms of a bulk thermodynamic prefactor and the single-pair barrier transmission amplitude. For a homogeneous junction with pair density  $n$ , this reads as

$$\hbar j_c = \frac{\mu n_c}{2k(\mu)} |t(\mu)| \quad (2)$$

where  $k(\mu) = \sqrt{2M\mu}/\hbar$  is the wave vector of a bosonic pair of mass  $M$  and energy  $\mu$ ,  $n_c = n\lambda_0$  is the density of condensed pairs,  $\lambda_0$  is the condensate fraction, and  $|t(\mu)|$  is the transmission amplitude of a single pair at incident energy  $\mu$ . Equation 2 can be extended to the harmonically trapped inhomogeneous case via the local density approximation (LDA) (40, 44), obtaining predictions for the total  $I_c$  as plotted in Fig. 2, A and B. To this purpose, we use the local pair



chemical potential  $\mu(\mathbf{r})$  and condensate fraction  $\lambda_0(\mathbf{r})$  based on nonperturbative Luttinger-Ward results for a zero-temperature homogeneous gas (45), while also accounting for second-harmonic contributions to the current-phase relation (44). We find quantitative agreement with no free parameters, although there are expected discrepancies visible at small  $V_0$  where hydrodynamic transport—not included in Eq. 2—becomes relevant. An additional validation of our model, and specifically of the separation between single- and many-particle properties in Eq. 2, is presented in Fig. 2, E and F. To isolate the barrier transmission contribution, we measure the imbalance  $z - \bar{z}$  as a function of  $V_0$  upon applying a fixed  $I_{\text{ext}}$  at various barrier widths  $w$ . By separately normalizing  $V_0$  to the calculated barrier height  $V_0'$  for which  $I_c = I_{\text{ext}}$  at each value of interaction and  $w$ , all different datasets collapse onto each other. This demonstrates that for fixed interaction strength, the whole trend of  $z - \bar{z}$  (and not only  $I_c$ ) is predominantly determined by the tunneling amplitude  $|t|$ .

We now turn to the measurement of  $I_c$  at varying coupling strength  $(k_F a)^{-1}$ , presented in Fig. 3A for three different fixed barrier heights  $V_0/E_F$ , from which we extract the order parameter amplitude throughout the BCS-BEC crossover. Consistent with previous mean-field simulations (36, 37) and experimental studies of the Josephson plasma frequency (31), all datasets exhibit a nonmonotonic trend of  $I_c$  peaked around unitarity. We find that our model reproduces  $I_c$  for all interaction strengths, especially at the largest  $V_0$ . This agreement demonstrates that the condensate density  $n_c$  (rather than the superfluid density), which quantifies pair long-range coherence (38, 39), represents the key quantity that sets the order parameter amplitude reflected by  $I_c$ . Indeed, the monotonic decrease of  $\mu$  with  $(k_F a)^{-1}$  cannot explain the observed trend of  $I_c$  and is compensated by the increase of the condensate fraction  $\lambda_0$  from exponentially small values in the BCS regime toward unity in the BEC limit (28).

A fairly accurate determination of the total condensate fraction  $\langle \lambda_0 \rangle = N_c/N$ , where  $N_c = \int d^3r n_c(\mathbf{r})$  is the total number of condensed pairs in the trapped superfluid sample, can be obtained by approximating  $I_c$  as

$$\hbar I_c \approx \langle \lambda_0 \rangle \times \int_V d^3r n(\mathbf{r}) \mu(\mathbf{r}) \frac{|t[\mu(\mathbf{r}), V_0]|}{4k[\mu(\mathbf{r})]R_x} \quad (3)$$

(44), where  $R_x$  is the axial Thomas-Fermi radius of the cloud,  $V$  is the total volume of the reservoirs, and  $n(\mathbf{r})$  is the local density of pairs. We have numerically checked that the factorized Eq. 3, fully justified at unitarity within our temperature regime, approximates the  $I_c$  calculated through LDA within a few percent for all interactions explored in our study (44).

From the measured  $I_c$  at several coupling strengths and barrier heights, and by evaluat-

ing the integral in Eq. 3 (44), we obtain  $\langle \lambda_0 \rangle$  throughout the crossover region (Fig. 3B). This is compared with nonperturbative  $T = 0$  predictions of  $\langle \lambda_0 \rangle$  obtained by integrating  $n_c(\mathbf{r}) = \lambda_0(\mathbf{r})n(\mathbf{r})$  based on Luttinger-Ward (45) (solid line) and quantum Monte Carlo simulations (39) (dot-dashed line). As a reference, we also plot the limiting trends of  $\langle \lambda_0 \rangle$  calculated within the Bogoliubov and BCS approximation. We find our data to match the  $T = 0$  predictions quite well within the strongly interacting regime  $|k_F a| > 1$ . In particular, we find  $\langle \lambda_0 \rangle = 0.47 \pm 0.07$  at unitarity, which agrees within its uncertainty with the value  $\lambda_0 = 0.51$  from (45), whereas it is smaller than the mean-field result (54)  $\lambda_0 \approx 0.7$  and smaller than the experimental value obtained at comparable temperatures [see, e.g., (43)] through the rapid-ramp technique (41, 42).

We have experimentally demonstrated the intimate connection between Josephson supercurrents and the complex order parameter in fermionic atom superfluids. Our work reveals that the Josephson critical current represents a reliable quantifier of the condensate density—a fundamental microscopic quantity in any broken-symmetry superfluid state—whose direct determination is typically hindered by strong interactions. An exciting extension will be to study the trend of  $I_c$  and the nature of current-carrying excitations at  $|I_{\text{ext}}| > I_c$  upon approaching the superfluid critical temperature in three- and two-dimensional (possibly homogeneous) Fermi gases. The results of such studies will contribute to a complete thermodynamic description of strongly interacting paired superfluids. Furthermore, our experiments lay the groundwork for exploring exotic current-phase relations in topological or tailored weak links, possibly with an applied ac drive, and may offer a route for unveiling low-temperature condensed phases in atomic simulators of the Fermi-Hubbard model.

## REFERENCES AND NOTES

- B. D. Josephson, *Phys. Lett.* **1**, 251–253 (1962).
- P. W. Anderson, *Lectures on The Many-Body Problems* (Elsevier, 1964), vol. 2.
- K. K. Likharev, *Rev. Mod. Phys.* **51**, 101–159 (1979).
- R. C. Jaklevic, J. Lambe, A. H. Silver, J. E. Mercereau, *Phys. Rev. Lett.* **12**, 159–160 (1964).
- A. Barone, G. Paternò, *Physics and Applications of the Josephson Effect* (Wiley, 1982).
- Y. Sato, R. E. Packard, *Rep. Prog. Phys.* **75**, 016401 (2012).
- S. Datta, *Electronic Transport in Mesoscopic Systems* (Cambridge Univ. Press, 1997).
- R. Pöpel, *Metrologia* **29**, 153–174 (1992).
- J. Clarke, A. I. Braginski, *The SQUID Handbook* (Wiley, 2004), vol. 1.
- F. Bloch, *Phys. Rev. B* **2**, 109–121 (1970).
- M. Tinkham, *Introduction to Superconductivity* (McGraw-Hill, ed. 2, 1996).
- J. T. Anderson, A. M. Goldman, *Phys. Rev. Lett.* **23**, 128–131 (1969).
- D. J. Van Harlingen, *Rev. Mod. Phys.* **67**, 515–535 (1995).
- C. C. Tsuei, J. R. Kirtley, *Rev. Mod. Phys.* **72**, 969–1016 (2000).
- A. Y. Kitaev, *Phys. Uspekhi* **44** (10S), 131–136 (2001).
- L. Jiang et al., *Phys. Rev. Lett.* **107**, 236401 (2011).
- M. Albiez et al., *Phys. Rev. Lett.* **95**, 010402 (2005).
- S. Levy, E. Lahoud, I. Shomroni, J. Steinhauer, *Nature* **449**, 579–583 (2007).
- L. J. LeBlanc et al., *Phys. Rev. Lett.* **106**, 025302 (2011).

- A. Ramanathan et al., *Phys. Rev. Lett.* **106**, 130401 (2011).
- C. Ryu, P. W. Blackburn, A. A. Blinov, M. G. Boshier, *Phys. Rev. Lett.* **111**, 205301 (2013).
- F. Jendrzejewski et al., *Phys. Rev. Lett.* **113**, 045305 (2014).
- S. Eckel et al., *Nature* **506**, 200–203 (2014).
- S. Eckel, F. Jendrzejewski, A. Kumar, C. J. Lobb, G. K. Campbell, *Phys. Rev. X* **4**, 031052 (2014).
- G. Spagnolli et al., *Phys. Rev. Lett.* **118**, 230403 (2017).
- M. Pigneur et al., *Phys. Rev. Lett.* **120**, 173601 (2018).
- C.-C. Chien, S. Peotta, M. Di Ventra, *Nat. Phys.* **11**, 998–1004 (2015).
- M. Randeria, W. Zwerger, M. Zwierlein, *The BCS-BEC Crossover and the Unitary Fermi Gas* (Springer, 2012), pp. 1–32.
- D. Stadler, S. Krinner, J. Meineke, J.-P. Brantut, T. Esslinger, *Nature* **491**, 736–739 (2012).
- D. Husmann et al., *Science* **350**, 1498–1501 (2015).
- G. Valtolina et al., *Science* **350**, 1505–1508 (2015).
- S. Krinner et al., *Proc. Natl. Acad. Sci. U.S.A.* **113**, 8144–8149 (2016).
- M. Lebrat et al., *Phys. Rev. X* **8**, 011053 (2018).
- V. Ambegaokar, A. Baratoff, *Phys. Rev. Lett.* **10**, 486–489 (1963).
- F. Meier, W. Zwerger, *Phys. Rev. A* **64**, 033610 (2001).
- A. Spuntarelli, P. Pieri, G. C. Strinati, *Phys. Rev. Lett.* **99**, 040401 (2007).
- P. Zou, F. Dalfovo, *J. Low Temp. Phys.* **177**, 240–256 (2014).
- C. N. Yang, *Rev. Mod. Phys.* **34**, 694–704 (1962).
- G. E. Astrakharchik, J. Boronat, J. Casulleras, S. Giorgini, *Phys. Rev. Lett.* **95**, 230405 (2005).
- M. Zaccanti, W. Zwerger, *Phys. Rev. A* **100**, 063601 (2019).
- M. W. Zwierlein et al., *Phys. Rev. Lett.* **92**, 120403 (2004).
- C. A. Regal, M. Greiner, D. S. Jin, *Phys. Rev. Lett.* **92**, 040403 (2004).
- M. Horikoshi, S. Nakajima, M. Ueda, T. Mukaiyama, *Science* **327**, 442–445 (2010).
- See supplementary materials.
- R. Haussmann, W. Rantner, S. Cerrito, W. Zwerger, *Phys. Rev. A* **75**, 023610 (2007).
- This corresponds to an entropy per particle  $S/N \approx 0.15 k_B/N$ , where  $S_c \approx 1.6 N k_B$  is the critical entropy for the superfluid transition in a harmonically trapped unitary gas (47).
- R. Haussmann, W. Zwerger, *Phys. Rev. A* **78**, 063602 (2008).
- S. Giovanazzi, A. Smerzi, S. Fantoni, *Phys. Rev. Lett.* **84**, 4521–4524 (2000).
- F. Piazza, L. A. Collins, A. Smerzi, *Phys. Rev. A* **81**, 033613 (2010).
- E. Hoskinson, Y. Sato, I. Hahn, R. E. Packard, *Nat. Phys.* **2**, 23–26 (2006).
- W. C. Stewart, *Appl. Phys. Lett.* **12**, 277–280 (1968).
- D. E. McCumber, *J. Appl. Phys.* **39**, 3113–3118 (1968).
- A. Burchianti et al., *Phys. Rev. Lett.* **120**, 025302 (2018).
- L. Salasnich, N. Manini, A. Parola, *Phys. Rev. A* **72**, 023621 (2005).
- W. J. Kwon et al., <http://doi.org/10.5281/zenodo.3749656>.
- L. Gor'kov, T. Melik-Barkhudarov, *Sov. Phys. JETP* **13**, 1018 (1961).
- S. Giorgini, L. P. Pitaevskii, S. Stringari, *Rev. Mod. Phys.* **80**, 1215–1224 (2008).

## ACKNOWLEDGMENTS

We acknowledge inspiring discussions with E. Demler, L. Mathey, H. Moritz, A. Recati, and J. Tempere. We thank S. Giorgini and G. E. Astrakharchik for providing us with QMC calculations of the condensate fraction across the BCS-BEC crossover, B. Frank for providing us with Luttinger-Ward calculations of the chemical potential and the condensate fraction across the BCS-BEC crossover, and H. Moritz and T. Lompe for careful reading of the manuscript. **Funding:** Supported by European Research Council GA no. 307032 QuFerm2D and no. 637738 PoLiChroM, Fondazione Cassa di Risparmio di Firenze project QuSim2D 2016.0770, and European Union's Horizon 2020 research and innovation program under the Marie Skłodowska-Curie GAs no. 705269 and no. 843303. **Author contributions:** W.J.K., G.D.P., F.S., and G.R. conceived the experiment and built the setup; W.J.K., G.D.P., R.P., and F.S. carried out the measurements and analyzed the data; and W.J.K., M.Z., and W.Z. performed the theoretical modeling. All authors contributed extensively to the discussion of the results and to the writing of the manuscript. **Competing interests:** The authors declare no competing interests. **Data and materials availability:** All data and codes for producing theoretical models shown in this work can be found at (55). Reasonable requests for additional information should be addressed to the corresponding author.

## SUPPLEMENTARY MATERIALS

science.sciencemag.org/content/369/6499/84/suppl/DC1  
Materials and Methods  
Supplementary Text  
Figs. S1 to S9  
References (58–71)

23 August 2019; accepted 27 April 2020  
10.1126/science.aaz2463

## QUANTUM GASES

# An ideal Josephson junction in an ultracold two-dimensional Fermi gas

Niclas Luick<sup>1,2</sup>, Lennart Sobirey<sup>1,2</sup>, Markus Bohlen<sup>1,2,3</sup>, Vijay Pal Singh<sup>4,2</sup>, Ludwig Mathey<sup>4,2</sup>, Thomas Lompe<sup>1,2\*</sup>, Henning Moritz<sup>1,2</sup>

The role of reduced dimensionality in high-temperature superconductors is still under debate. Recently, ultracold atoms have emerged as an ideal model system to study such strongly correlated two-dimensional (2D) systems. Here, we report on the realization of a Josephson junction in an ultracold 2D Fermi gas. We measure the frequency of Josephson oscillations as a function of the phase difference across the junction and find excellent agreement with the sinusoidal current phase relation of an ideal Josephson junction. Furthermore, we determine the critical current of our junction in the crossover from tightly bound molecules to weakly bound Cooper pairs. Our measurements clearly demonstrate phase coherence and provide strong evidence for superfluidity in a strongly interacting 2D Fermi gas.

One of the most notable macroscopic manifestations of quantum mechanics is the dc Josephson effect (1, 2), where a phase difference  $\phi$  between two superconductors separated by a weak link drives a current  $I(\phi)$  without any applied voltage. For an ideal Josephson junction, this current phase relation takes a sinusoidal form  $I(\phi) = I_C \sin(\phi)$  (3), where  $I_C$  is the maximum supercurrent that can flow through the junction. This direct connection between the superfluid current and the phase of the macroscopic wave function makes

Josephson junctions a powerful tool for probing properties of superconductors, providing, for example, clear evidence for the d-wave symmetry of the order parameter in cuprate superconductors (4).

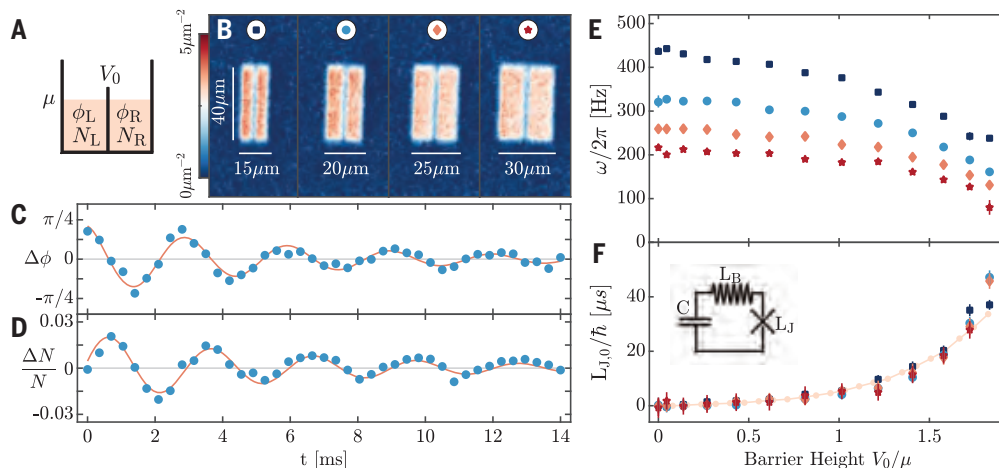
Recently, ultracold quantum gases have been established as ideal model systems to study such strongly correlated two-dimensional (2D) fermionic systems (5–12). However, although pair condensation of fermions has been reported (13), fermionic superfluidity in two dimensions has not been directly observed. Here,

we use a Josephson junction to unambiguously show phase coherence and provide strong evidence for superfluidity in an ultracold 2D Fermi gas. Josephson junctions have already been extensively studied in ultracold quantum gases (14–22), but the ideal sinusoidal current phase relation that directly links the phase difference to the supercurrent across the junction (23–25) has not been observed (26). In this work, we first confirm that our junction follows an ideal current phase relation. This implies that the current across the junction is a supercurrent that is driven by the phase difference between two superfluids. We then proceed to measure the evolution of the critical current of the junction as a function of interaction strength and thereby realize a probe for 2D superfluidity in the crossover from tightly bound molecules to weakly bound Cooper pairs.

For our experiments, we use a homogeneous Fermi gas of  $^6\text{Li}$  atoms in a spin-balanced mixture of the lowest two hyperfine states, trapped in a box potential (27, 28). A strong vertical confinement with trap frequency  $\omega_z/2\pi = 8.8(2)$  kHz ensures that the gas is kinematically 2D with the chemical potential  $\mu$  and temperature  $T$  being smaller than the level spacing  $\hbar\omega_z$ , where  $\hbar$  is the reduced Planck constant. We create a Josephson junction by using a narrow repulsive potential barrier with

**Fig. 1. Josephson oscillations in a homogeneous 2D Fermi gas.**

(A) Sketch of a Josephson junction consisting of two Fermi gases with chemical potential  $\mu$ , particle numbers  $N_L$  and  $N_R$ , and phases  $\phi_L$  and  $\phi_R$  separated by a tunneling barrier with height  $V_0$ . (B) Absorption images of cold atom Josephson junctions. The width of the barrier is held fixed at a waist of  $w = 0.81(6)\mu\text{m}$  while the size  $l_\perp$  of the system is increased. (C and D) Time evolution of the phase difference  $\Delta\phi$  (C) and relative particle number difference  $\Delta N/N$  (D) between the left and right side of the box after imprinting a relative phase difference of  $\phi_0 \approx \pi/4$ . The red lines represent a damped sinusoidal fit. (E) Oscillation frequency as a function of barrier height  $V_0$  for different system sizes [symbols as in (B)], where the error bars denote the  $1\sigma$  fit error. The inductance  $L_B$  and capacitance  $C$  of the bulk system are proportional to the length  $l_\perp$  of the box, and therefore the oscillation frequency decreases with increasing system size for  $V_0 = 0$ . For nonzero values of  $V_0$ , the barrier adds a nonlinear Josephson inductance  $L_J$  to the system and the oscillation frequency decreases as a function of barrier height. (F) Josephson inductance  $L_{J,0}(V_0)$  extracted from the



frequency measurements using an LC circuit model. The Josephson inductances for all system sizes collapse onto a single curve, which shows that the inductance of the junction depends only on the height of the barrier and validates our LC circuit model. We obtain the calibration of the barrier height  $V_0$  by matching the data to a full numerical simulation (light red line with circles) (27). The data are obtained by averaging 20 (B), 42 (C), 130 (D), and 7 [(E) and (F)] individual measurements.

<sup>1</sup>Institut für Laserphysik, Universität Hamburg, Luruper Chaussee 149, 22761 Hamburg, Germany. <sup>2</sup>The Hamburg Centre for Ultrafast Imaging, Universität Hamburg, Luruper Chaussee 149, 22761 Hamburg, Germany. <sup>3</sup>Laboratoire Kastler Brossel, ENS-Université PSL, CNRS, Sorbonne Université, Collège de France, 24 rue Lhomond, 75005 Paris, France. <sup>4</sup>Zentrum für Optische Quantentechnologien, Universität Hamburg, Luruper Chaussee 149, 22761 Hamburg, Germany.

\*Corresponding author. Email: tlompe@physik.uni-hamburg.de

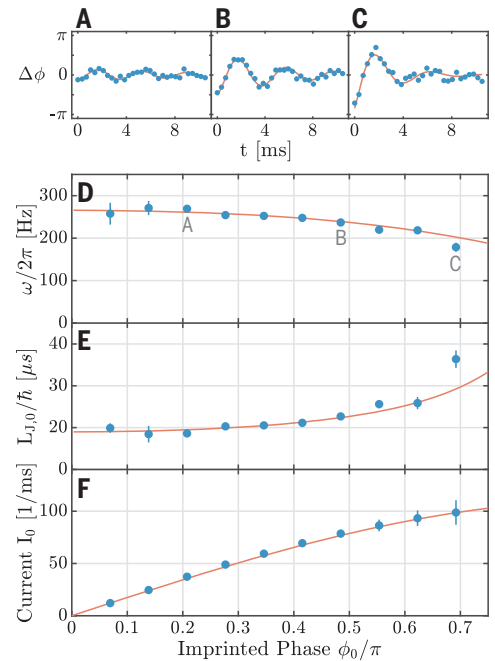


a Gaussian beam waist of  $w = 0.81(6) \mu\text{m}$  to split the system into two homogeneous 2D pair condensates connected by a weak link (Fig. 1, A and B). We imprint a relative phase  $\phi_0$  between the two sides of the junction by illuminating one-half of the system with a spatially homogeneous optical potential for a variable time between 0 and  $20 \mu\text{s}$  (27). We then let the system evolve for a time  $t$  and extract the population imbalance  $\Delta N = (N_L - N_R)$  and the phase difference  $\phi$  between the two sides using either in situ or time-of-flight imaging. A typical Josephson oscillation of a molecular condensate at a magnetic field of  $B = 731 \text{ G}$  (29) and a barrier height of  $V_0/\mu = 1.08(5)$  featuring the characteristic  $\pi/2$  phase shift between imbalance and phase is shown in Fig. 1, C and D. The oscillations are weakly damped with a relative damping of  $\Gamma/\omega = 0.07$ , which, according to a full numerical simulation of our system, can be explained by phononic excitations in the bulk and the nucleation of vortex-antivortex pairs in the junction (fig. S3) (30).

To understand these Josephson oscillations, we use a simple circuit model commonly used to describe superconducting Josephson junctions (21, 31, 32). In this model, we describe our junction as a nonlinear Josephson inductance  $L_J$ , which is connected in series to a linear bulk inductance  $L_B$  and a capacitance  $C$  (Fig. 1F), where the bulk inductance  $L_B$  characterizes the inertia of the gas and the capacitance  $C$  its compressibility. For vanishing Josephson inductance, the model reduces to a linear resonator with frequency  $\omega_s = 1/\sqrt{L_B C} = 2\pi v_s/2l_L$ , which corresponds to the frequency of a sound mode propagating with the speed of sound  $v_s$  across the length  $l_L$  of the system. Introducing a barrier with height  $V_0$  adds a nonlinear inductance  $L_J$  to the system and reduces the oscillation frequency  $\omega$ . Owing to the nonlinearity of the current phase relation, this  $L_J$  depends on the phase difference  $\phi(t)$  across the junction, but for small phase excitations, there is a linear regime where  $L_J[\phi(t)]$  can be approximated by a time-independent Josephson inductance  $L_{J,0}$  and the oscillation frequency is given by  $\omega = 1/\sqrt{(L_B + L_{J,0})C}$ .

To confirm that our physical system is described by this model, we prepare a gas of deeply bound dimers, perform measurements of the oscillation frequency in the linear regime as a function of the barrier height for different system sizes (Fig. 1E), and extract the Josephson inductance  $L_{J,0}$  (Fig. 1F). Because our system has a uniform density, the bulk inductance is given by the simple expression  $L_B = 8m l_\perp/\pi^2 n l_\parallel$ , where  $n$  is the density per spin state,  $m$  is the mass of a  $^6\text{Li}$  atom, and  $l_\parallel$  ( $l_\perp$ ) is the diameter of the box perpendicular (parallel) to the barrier (27). Consequently, the Josephson inductance  $L_{J,0}(\omega) = L_B(\omega_s^2/\omega^2 - 1)$  can be extracted from the frequency

**Fig. 2. Current phase relation.** (A to C) Josephson oscillations through a tunneling barrier with height  $V_0/\mu = 1.51(8)$  at initial phase imprints of  $\phi_0 = 0.14\pi$  (A),  $0.42\pi$  (B), and  $0.62\pi$  (C). The amplitude of the oscillations increases for stronger phase imprints, whereas the frequency is reduced. (D) Oscillation frequency as a function of imprinted phase, where the error bars denote the  $1\sigma$  fit error. The gray labels A, B, and C denote the frequencies obtained from the oscillations shown in (A) to (C). (E) Inductance of the junction calculated from the measured oscillation frequencies. (F) Effective current  $I_0$  through the junction obtained by performing a Riemann sum over the measured values of  $L_{J,0}$  shown in (E) according to  $\partial I/\partial \phi = \hbar/L_J$  (27). Our data are in excellent agreement with the rescaled current phase relation  $I_0 = 2I_C \sin(\phi_0/2)$  expected for an ideal Josephson junction (red lines), where the initial slope  $I_C$  is determined from the first three data points. Each data point in (A) to (C) is obtained by averaging 20 individual measurements.



difference between the Josephson oscillations and the sound mode. Whereas the oscillation frequency is strongly dependent on the size of the box owing to the change in the bulk inductance  $L_B$  and the capacitance  $C$ , the measured Josephson inductance  $L_{J,0}$  should depend only on the coupling between the two reservoirs. As can be seen from Fig. 1F, all measurements of  $L_{J,0}$  versus barrier height collapse onto a single curve regardless of the system size, which confirms that our Josephson junction can be described by an inductor-capacitor (LC) circuit model. For the barrier heights used in our experiments, we also find very good agreement with a full numerical simulation of our system (27).

Next, we probe the fundamental property of Josephson junctions: the nonlinearity of the current phase relation (3, 26). For large phase excitations, the nonlinear current phase relation leads to anharmonic oscillations with an increased oscillation period. Our ability to imprint arbitrary phase differences  $\phi_0$  across the barrier enables us to measure this reduction of the fundamental frequency  $\omega(\phi_0)$  as a probe of the nonlinearity (Fig. 2). To extract the nonlinear response of the current from our measurements of  $\omega(\phi_0)$ , we first calculate  $L_{J,0}[\omega(\phi_0)]$  and then apply the relation  $\partial I/\partial \phi = \hbar/L_J$  to  $L_{J,0}(\phi_0)$  to obtain an effective current  $I_0(\phi_0)$ . For an ideal Josephson junction,  $I_0$  follows a rescaled current phase relation  $I_0(\phi_0) \approx 2I_C \sin(\phi_0/2)$  (27). We find that our measurement is in excellent agreement with this current phase relation, indicating that our junction is an ideal Josephson junction (3, 26, 33). This implies that the current across the junction is

indeed a supercurrent, driven by the phase difference between two superfluids.

Following this result, we can now use our Josephson junction as a probe for 2D superfluidity in the strongly correlated regime. We observe Josephson oscillations over a wide range of interaction strengths, indicating the presence of superfluidity in the entire crossover from tightly bound molecules to weakly bound Cooper pairs (Fig. 3). To quantify the effect of interactions on our system, we extract the critical current  $I_C$  from the frequency of the Josephson oscillations. Because for a fixed barrier height  $V_0$  the change in the critical current would be dominated by the interaction dependence of the chemical potential, we instead maintain a constant  $V_0/\mu = 1.4(2)$  by adjusting the barrier height  $V_0$  for each interaction strength according to a reference measurement of the equation of state (fig. S4). We observe that, within the uncertainty of our measurement, the critical current stays nearly constant, with a tendency toward smaller values of  $I_C$  when approaching the Bardeen-Cooper-Schrieffer (BCS) side of the resonance. Although there is currently no theory available that quantitatively describes a 2D Josephson junction in the whole Bose-Einstein condensate (BEC)-BCS crossover, in the bosonic limit we can calculate the critical current from the condensate density  $n_c$  and the overlap of the condensate wave functions (27, 34). We use this theory to determine the condensate fraction from the measured critical current for interaction strengths  $\ln(k_F a_{2D}) \leq -0.9$  and obtain  $n_c/n = 0.72(8)_{\text{stat.}}^{(+0.1)_{\text{sys.}}}$ , where stat. denotes the statistical error and the

**Fig. 3. Interaction dependence of the critical current.**

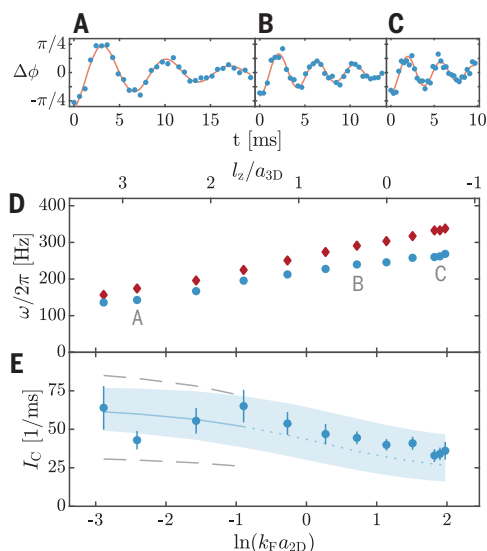
**(A to C)** Josephson oscillations for interaction strengths of  $\ln(k_F a_{2D}) = -2.4$  (A),  $\ln(k_F a_{2D}) = 0.7$  (B), and  $\ln(k_F a_{2D}) = 1.9$  (C), where  $k_F$  is the Fermi wave vector and  $a_{2D}$  is the 2D scattering length as defined in (13, 27). The measurements are performed in the linear regime with constant density  $n = 1.21(9)\mu\text{m}^{-2}$  and relative barrier height  $V_0/\mu = 1.4(2)$ . **(D)** Oscillation frequency for sound (red diamonds) and Josephson (blue dots) oscillations as a function of the 2D interaction parameter  $\ln(k_F a_{2D})$ . The frequency increase of the bare sound mode when going from the molecular to the BCS regime reflects the interaction dependence of the chemical potential. The gray labels A, B, and C denote the frequencies obtained from the oscillations shown in (A) to (C). **(E)** Critical current of the junction extracted from the frequency difference between the sound mode and the Josephson oscillations. The error bars denote the  $1\sigma$  fit error. The blue line is the critical current  $I_C \propto n_c t_{k=0}$  calculated for a condensate fraction of  $n_c/n = 0.72$  and a tunneling amplitude  $t_{k=0}$  obtained from a mean field calculation of the transmission through the barrier (27). To calculate the tunneling amplitude, we approximate our junction with a rectangular barrier with a width  $b = 0.81\mu\text{m}$ , which is a reasonable approximation for the Gaussian barrier used in the experiment. The shaded region denotes the systematic uncertainty resulting from the 15% uncertainty in  $V_0/\mu$ . The dashed gray lines indicate the upper ( $T = 0$ ) and lower ( $T = T_c$ ) bound for the critical current obtained from our theory. Although it is unclear how far into the strongly correlated regime our bosonic theory is quantitatively accurate (27), it reproduces the qualitative behavior of our data across the entire BEC-BCS crossover. Each data point in (A) to (C) is obtained by averaging 42 individual measurements.

systematic error (sys.) arises from the 15% uncertainty in  $V_0/\mu$ . For our homogeneous 2D system, Berezinskii-Kosterlitz-Thouless theory relates the condensate fraction  $n_c/n \propto L^{-\eta}$  to the algebraic decay of phase coherence over the finite size  $L$  of the box, where  $\eta \propto T/n_s$  is the algebraic scaling exponent (35, 36). A measurement of the critical current as a function of system size can therefore be used to extract the algebraic scaling exponent and the superfluid density  $n_s$ , as recently suggested in (37).

Our homogeneous 2D Fermi gas provides an excellent starting point to study the influence of reduced dimensionality on strongly correlated superfluids in the crossover between two and three dimensions. The distinctive combination of reduced dimensionality, uniform density, low entropy, and high-resolution imaging makes our system a perfect platform to observe exotic phases such as the elusive Fulde-Ferrell-Larkin-Ovchinnikov state (38). Finally, our system is ideally suited to investigate whether periodic driving of Josephson junctions can strongly enhance coherent transport, as suggested by experiments with THz-driven cuprate superconductors (39, 40).

## REFERENCES AND NOTES

1. B. D. Josephson, *Phys. Lett.* **1**, 251–253 (1962).
2. P. W. Anderson, J. M. Rowell, *Phys. Rev. Lett.* **10**, 230–232 (1963).



3. A. A. Golubov, M. Y. Kupriyanov, E. Il'ichev, *Rev. Mod. Phys.* **76**, 411–469 (2004).
4. C. Tsuei, J. Kirtley, *Rev. Mod. Phys.* **72**, 969–1016 (2000).
5. B. Fröhlich *et al.*, *Phys. Rev. Lett.* **106**, 105301 (2011).
6. A. T. Sommer, L. W. Cheuk, M. J. H. Ku, W. S. Bakr, M. W. Zwierlein, *Phys. Rev. Lett.* **108**, 045302 (2012).
7. V. Makhlov, K. Martinyanov, A. Turlapov, *Phys. Rev. Lett.* **112**, 045301 (2014).
8. W. Ong, C. Cheng, I. Arakelyan, J. E. Thomas, *Phys. Rev. Lett.* **114**, 110403 (2015).
9. K. Fenech *et al.*, *Phys. Rev. Lett.* **116**, 045302 (2016).
10. D. Mitra, P. T. Brown, P. Schaub, S. S. Kondov, W. S. Bakr, *Phys. Rev. Lett.* **117**, 093601 (2016).
11. A. Mazurenko *et al.*, *Nature* **545**, 462–466 (2017).
12. J. Levinsen, M. M. Parish, in *Annual Review of Cold Atoms and Molecules*, K. W. Madison, K. Bongs, L. D. Carr, A. M. Rey, H. Zhai, Eds. (World Scientific, 2015), vol. 3, chap. 1, pp. 1–75.
13. M. G. Ries *et al.*, *Phys. Rev. Lett.* **114**, 230401 (2015).
14. F. S. Cataliotti *et al.*, *Science* **293**, 843–846 (2001).
15. M. Albiez *et al.*, *Phys. Rev. Lett.* **95**, 010402 (2005).
16. S. Levy, E. Lahoud, I. Shomroni, J. Steinhauer, *Nature* **449**, 579–583 (2007).
17. L. J. LeBlanc *et al.*, *Phys. Rev. Lett.* **106**, 025302 (2011).
18. T. Betz *et al.*, *Phys. Rev. Lett.* **106**, 020407 (2011).
19. G. Spagnolli *et al.*, *Phys. Rev. Lett.* **118**, 230403 (2017).
20. G. Valtolina *et al.*, *Science* **350**, 1505–1508 (2015).
21. A. Burchianti *et al.*, *Phys. Rev. Lett.* **120**, 025302 (2018).
22. C. Ryu, P. W. Blackburn, A. A. Blinova, M. G. Boshier, *Phys. Rev. Lett.* **111**, 205301 (2013).

23. G. Watanabe, F. Dalfvo, F. Piazza, L. Pitaevskii, S. Stringari, *Phys. Rev. A* **80**, 053602 (2009).
24. A. Spuntarelli, P. Pieri, G. C. Strinati, *Phys. Rev. Lett.* **99**, 040401 (2007).
25. F. Ancilotto, L. Salasnich, F. Toigo, *Phys. Rev. A* **79**, 033627 (2009).
26. S. Eckel, F. Jendrzejewski, A. Kumar, C. Lobb, G. Campbell, *Phys. Rev. X* **4**, 031052 (2014).
27. See supplementary materials.
28. K. Hueck *et al.*, *Phys. Rev. Lett.* **120**, 060402 (2018).
29. This corresponds to an interaction strength of  $\ln(k_F a_{2D}) = -2.4$ .
30. Notably, achieving this low damping requires a temperature of  $T/T_F \lesssim 0.03$  (fig. S3), which is far below the predicted critical temperature  $T_c/T_F \approx 0.1$  for 2D superfluidity at this interaction strength (13, 27, 41).
31. J. G. Lee, B. J. McIlvain, C. J. Lobb, W. T. Hill III, *Sci. Rep.* **3**, 1034 (2013).
32. S. Eckel *et al.*, *Phys. Rev. A* **93**, 063619 (2016).
33. We note that achieving a sinusoidal current phase relation requires a barrier deep in the tunneling regime, which is fulfilled for our barrier depth of  $V_0/\mu \approx 1.5$ .
34. M. Zaccanti, W. Zwerger, *Phys. Rev. A* **100**, 063601 (2019).
35. Z. Hadzibabic, J. Dalibard, *Riv. Nuovo Cim.* **34**, 389 (2011).
36. N. V. Prokof'ev, B. V. Svistunov, *J. Exp. Theor. Phys.* **127**, 860–864 (2018).
37. V. P. Singh, N. Luick, L. Sobirey, L. Mathey, arXiv:2002.08375 [cond-mat.quant-gas] (19 February 2020).
38. J. J. Kinnunen, J. E. Baarsma, J.-P. Martikainen, P. Törmä, *Rep. Prog. Phys.* **81**, 046401 (2018).
39. W. Hu *et al.*, *Nat. Mater.* **13**, 705–711 (2014).
40. J.-i. Okamoto, W. Hu, A. Cavalleri, L. Mathey, *Phys. Rev. B* **96**, 144505 (2017).
41. D. Petrov, M. Baranov, G. Shlyapnikov, *Phys. Rev. A* **67**, 031601 (2003).
42. N. Luick *et al.*, Data for “An ideal Josephson junction in an ultracold two-dimensional Fermi gas.” Zenodo (2020); <https://doi.org/10.5281/zenodo.3744797>.
43. N. Luick *et al.*, Simulation script and data for “An ideal Josephson junction in an ultracold two-dimensional Fermi gas.” Zenodo (2020); <https://doi.org/10.5281/zenodo.3786298>.

## ACKNOWLEDGMENTS

We thank K. Hueck and B. Lienau for their contributions during earlier stages of the experiment; T. Enss, A. Recati, and M. Zaccanti for stimulating discussions; and G. Roati and F. Scazza for careful reading of the manuscript and valuable suggestions regarding the interpretation of Fig. 3.

**Funding:** This work was supported by the European Union's Seventh Framework Programme (FP7/2007-2013) under grant agreement no. 335431 and by the DFG in the framework of SFB 925 and the excellence clusters “The Hamburg Centre for Ultrafast Imaging” - EXC 1074 - project ID 194651731 and “Advanced Imaging of Matter” - EXC 2056 - project ID 390715994. M.B. acknowledges support by Labex ICFP of École Normale Supérieure Paris. **Author contributions:** N.L. and L.S. performed the experiments and data analysis with support from M.B. and T.L. V.P.S. and L.M. developed numerical and analytical models and contributed to the interpretation of our experimental data. N.L. and T.L. wrote the manuscript, and L.S. created the figures with input from all authors. T.L. and H.M. supervised the project. All authors contributed to the discussion and interpretation of our results. **Competing interests:** The authors declare no competing interests. **Data and materials availability:** All data presented in this paper and simulation scripts are deposited at Zenodo (42, 43).

## SUPPLEMENTARY MATERIALS

[science.sciencemag.org/content/369/6499/89/suppl/DC1](https://science.sciencemag.org/content/369/6499/89/suppl/DC1)  
Supplementary Text  
Figs. S1 to S4  
References (44–49)

23 August 2019; accepted 7 May 2020  
10.1126/science.aaz2342



## ORGANIC CHEMISTRY

C(sp<sup>3</sup>)-H functionalizations of light hydrocarbons using decatungstate photocatalysis in flowGabriele Laudadio<sup>1\*</sup>, Yuchao Deng<sup>1,2,3\*</sup>, Klaas van der Wal<sup>1</sup>, Davide Ravelli<sup>4</sup>, Manuel Nuño<sup>5</sup>, Maurizio Fagnoni<sup>4</sup>, Duncan Guthrie<sup>5</sup>, Yuhao Sun<sup>2,3</sup>, Timothy Noël<sup>1†</sup>

Direct activation of gaseous hydrocarbons remains a major challenge for the chemistry community. Because of the intrinsic inertness of these compounds, harsh reaction conditions are typically required to enable C(sp<sup>3</sup>)-H bond cleavage, barring potential applications in synthetic organic chemistry. Here, we report a general and mild strategy to activate C(sp<sup>3</sup>)-H bonds in methane, ethane, propane, and isobutane through hydrogen atom transfer using inexpensive decatungstate as photocatalyst at room temperature. The corresponding carbon-centered radicals can be effectively trapped by a variety of Michael acceptors, leading to the corresponding hydroalkylated adducts in good isolated yields and high selectivity (38 examples).

One of the most challenging reactions in organic synthesis is the selective functionalization of C(sp<sup>3</sup>)-H bonds that lack activation by proximal functional groups (1). The conversion of light alkanes to high-value added chemicals has especially been a key objective for the synthetic community in the past decades, yet with limited success so far (2–4). Up to now, strategies to introduce such alkyl fragments into organic scaffolds necessitate prefunctionalization of the hydrocarbons to increase their reactivity (Fig. 1A). Volatile alkanes are typically converted into alkyl electrophiles through halogenation by using chlorine or bromine gas at elevated temperatures (>500°C) or by using light activation (5, 6). These radical chain processes result in low-yielding and unselective transformations, with demands for subsequent energy-intensive and elaborate purification and recycling processes [for the effluent guidelines in the chlorine and chlorinated hydrocarbon manufacturing industry, see (7)]. Despite the apparent drawbacks, these classical halogenation strategies are being carried out on a multi-metric ton scale to prepare a variety of halogenated compounds that are key for the production of most pharmaceuticals, agrochemicals, materials, and other industrial chemicals (8). In synthetic organic chemistry, alkyl halides are widely used as electrophiles in nucleophilic substitution reactions or serve as substrates for elimination reactions to install double bonds regioselectively. Furthermore, alkyl halides

can be easily converted into organometallic reagents, which can be engaged as nucleophiles in a variety of transition metal-catalyzed C-C bond forming reactions (9).

A general synthetic strategy that enables the selective and direct activation of a diverse set of light hydrocarbons under mild reaction conditions remains a challenge, suffering from at least one drawback with regard to substrate scope (10–13), practicality, and selectivity (14). The development of such a transformation would be particularly useful, given the broad availability and the inexpensive nature of these starting materials. Furthermore, the reduction in synthetic steps would allow for streamlined reaction sequences and decreased waste generation. However, we reasoned that two fundamental problems needed to be addressed to succeed: First, a suitable transformation would require the selective cleavage of very strong aliphatic C-H bonds [bond dissociation energy (BDE) = 96.5 to 105 kcal/mol] (Fig. 1B), and second, the handling of these gaseous alkanes presents several technological challenges to bring them into close proximity with a suitable catalyst and reaction partner.

Seeking to address these challenges, we wondered if a photoexcited decatungstate anion (\*[W<sub>10</sub>O<sub>32</sub>]<sup>4-</sup>) could sunder effectively the strong and nonactivated C-H bonds of light alkanes (Fig. 1A). W<sub>10</sub>O<sub>32</sub><sup>4-</sup> is a versatile and inexpensive polyoxometalate-based hydrogen atom transfer (HAT) photocatalyst that can abstract hydrogen atoms from C(sp<sup>3</sup>)-H fragments upon activation by near-ultraviolet (UV) light irradiation (~365 nm) (15–18). The resulting carbon-centered radicals are nucleophilic and might be readily engaged in C-C bond forming reactions, thereby effectively bypassing the requirement for more-elaborate reaction strategies while expanding the synthetic toolbox of available alkyl reagents. To date, W<sub>10</sub>O<sub>32</sub><sup>4-</sup> photocatalysis has enabled a number of synthetically useful C(sp<sup>3</sup>)-H functionalizations, including oxidations (19, 20),

fluorinations (21), arylations (22), and other C-C bond formations (23). However, because of the gaseous nature and the low solubility of light alkanes in organic solvents, we reasoned that the use of flow technology is indispensable to facilitate the gas-liquid decatungstate-mediated processes (Fig. 1C) (24). The short length scales in microflow reactors (typically <1-mm optical path) provide a homogeneous irradiation of the entire reaction medium, allowing for the efficient generation of alkyl radicals (25). Furthermore, by increasing the pressure in the reactor through use of operationally simple back-pressure regulators, the gaseous alkanes can be forced into the liquid phase, increasing the odds of C(sp<sup>3</sup>)-H bond activation through decatungstate photocatalysis (26). Finally, flow processing of these combustible gases can be done safely in microreactors, and the conditions can be readily scaled (27, 28).

Among all volatile alkanes, methane is the hardest one to activate because of high BDE of these C-H bonds (BDE = 105 kcal/mol) (Fig. 1B) (29). However, if we can successfully split methane bonds with decatungstate HAT photocatalysis, cleaving the C-H bond in ethane (BDE = 101 kcal/mol) and other volatile aliphatic feedstock materials, such as propane (BDE = 99 kcal/mol) and isobutane (BDE = 96.5 kcal/mol), should be within reach. Indeed, we carried out trapping experiments with TEMPO (tetramethylpiperidine-1-oxyl), a stable aminoxyl radical, and the trapped adducts of methane, ethane, propane, and isobutane gave credence to the feasibility of our approach (Fig. 1D). Notably, because of the stability of the generated radical and the lower BDE of the C-H bond, high selectivity was observed for the formation of secondary and tertiary C(sp<sup>3</sup>)-O bonds from propane and isobutane, which is in contrast to a recently reported HAT approach using alkoxy radicals (14).

We began our investigation into the proposed C(sp<sup>3</sup>)-H functionalization of light hydrocarbons by exposing isobutane and benzylidenemalonitrile in the presence of tetrabutylammonium decatungstate (TBADT) in acetonitrile:H<sub>2</sub>O (7:1), which provides both good solubility and good reactivity of the photocatalyst, to UV-A light [365-nm light-emitting diodes (LEDs), 60 W]. For a number of substrates, limited solubility was observed upon addition of water. However, this could be circumvented by carrying out the reactions in neat acetonitrile. Furthermore, acetonitrile, despite the relatively low BDE (96 to 97 kcal/mol) of its C-H bonds (30), is also inert under the given HAT reaction conditions. This can be attributed to a polarity mismatch between decatungstate and the C(sp<sup>3</sup>)-H bonds in acetonitrile. All the experiments were carried out in a standardized, commercially available Vapourtec UV-150 photochemical flow reactor, which should enable reproducibility of the results. After careful

<sup>1</sup>Micro Flow Chemistry and Synthetic Methodology, Department of Chemical Engineering and Chemistry, Eindhoven University of Technology, Eindhoven, Netherlands.

<sup>2</sup>School of Physical Science and Technology, ShanghaiTech University, Shanghai 201210, P. R. China. <sup>3</sup>Shanghai Advanced Research Institute, Chinese Academy of Sciences, Shanghai 201210, P. R. China. <sup>4</sup>PhotoGreen Lab, Department of Chemistry, University of Pavia, Pavia 27100, Italy.

<sup>5</sup>Vapourtec, Farnham St Genevieve, Bury St Edmunds, Suffolk IP28 6TS, UK.

\*These authors contributed equally to this work.

†Corresponding author. Email: t.noel@tue.nl

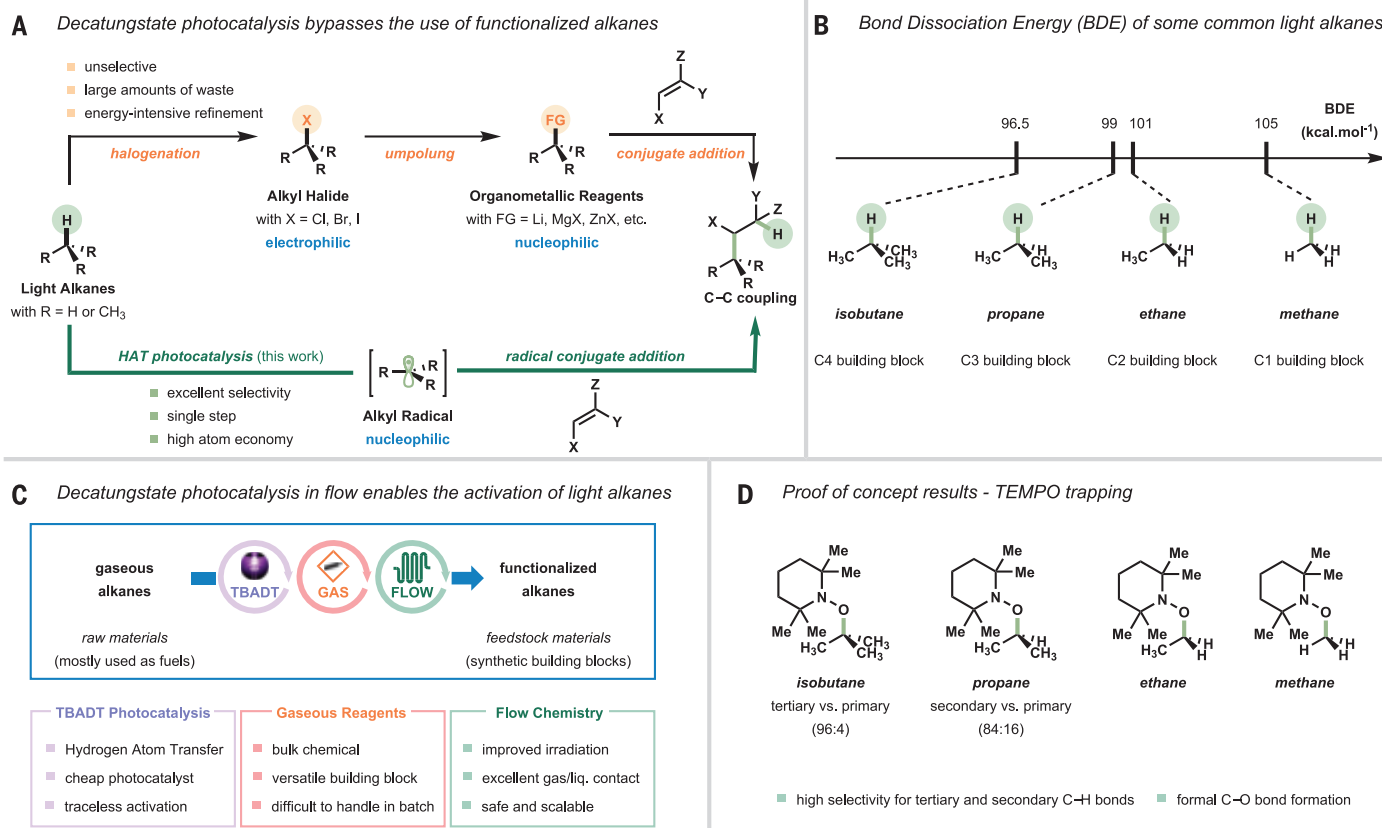


**Fig. 1.** Decatungstate enables the direct C(sp<sup>3</sup>)-H activation of light hydrocarbons. **(A)** Photocatalytic scission of strong C(sp<sup>3</sup>)-H bonds of volatile alkanes allows us to generate nucleophilic alkyl radicals and to bypass the use of halogenated alkanes or organometallic reagents. **(B)** BDE of some common gaseous alkanes (35). **(C)** Conversion of gaseous alkanes into functionalized alkanes by blending TBADT photocatalysis, the use of gases, and flow chemistry. liq., liquid. **(D)** TEMPO trapping experiments showing the feasibility of the outlined strategy of HAT activation of aliphatic substrates (results obtained with GC-MS). Me, methyl.

optimization of the reaction conditions (supplementary materials), we observed that the targeted compound **1** could be obtained in an excellent isolated yield of 91% by using 1 mol % of TBADT as a HAT photocatalyst (Fig. 2). Critical to the success of the reaction was the increase of the reaction pressure up to 10 bar, which results in a complete liquefaction of the gas and thus avoids gas-to-liquid mass transfer limitations. Moreover, 4.3 equivalents of isobutane were used to obtain optimal yields, whereas larger amounts did not lead to a further yield improvement (supplementary materials). Furthermore, classical conjugate addition strategies require transition metal catalysts and prefunctionalized nucleophilic organometallic reagents (31). The stepwise and lengthy procedure to prepare such nucleophilic reagents stands in marked contrast to the single-step HAT activation of gaseous alkanes as shown herein.

With optimized reaction conditions in hand, we next explored the scope of the transformation (Fig. 2). A variety of electronically distinct benzylidenemalononitriles (**1** to **7**) could serve as highly efficient radical traps for the photocatalytically generated carbon-centered

radicals, yielding the targeted hydroalkylated compounds in excellent isolated yields (82 to 93%) and very good selectivity for the installment of a tertiary butyl group [*t*Bu versus isobutyl (*i*Bu): ~96:4]. Halogenated benzylidene malononitrile substrates (**3** to **5**) can be engaged in the transformation as well, providing requisite handles to be converted into diverse organic molecules by using classical cross-coupling strategies. Methyl *trans*- $\alpha$ -cyanocinnamate is another efficient substrate for scavenging tertiary butyl radicals, yielding the targeted compound **8** in 85% isolated yield. Whereas for isobutyl radicals both diastereomers were formed in equal amounts, the trapping of the more sterically demanding tertiary butyl radical resulted in a relatively high diastereomeric ratio (d.r. = 3.1:1). Other traps, such as triethyl ethylenetricarboxylate, *N*-phenylmaleimide, and 3-methylene-2-norbornanone, resulted in the formation of synthetically useful building blocks (**9** to **11**) in good to excellent isolated yields (71 to 90%) and excellent selectivity in favor of the tertiary butyl-appended molecules. Complete endoselectivity was observed for compound **11**, which is consistent with a hydrogen back-donation from the reduced pho-

tocatalyst from the less hindered side of the norbornane moiety (Fig. 3A). We did not observe any significant amount of by-products as detected by gas chromatography-mass spectrometry (GC-MS) analysis (<2%) for a variety of reasons. C-H abstraction from the starting Michael acceptors is not a competitive process, because in most cases, no labile hydrogens are present. Furthermore, C-H cleavage in the alkylated products did not lead to another C-H activation event, in part because of a polarity mismatch (15). TBADT\* has a marked preference for the abstraction of nucleophilic hydrogens and avoids dissociating electrophilic C-H bonds such as those present in  $\alpha$ -position to the electron-withdrawing functional groups. Moreover, despite the presence of labile benzylic hydrogens in some of the products, no by-products are generated, because of a combination of the voluminous size of TBADT and the steric hindrance at those benzylic positions (15). Finally, the presence of an excess of gaseous alkanes prevents hydrogen abstraction from any other organic compound in the reaction mixture.

This protocol was also found to enable the efficient activation of propane, a key constituent



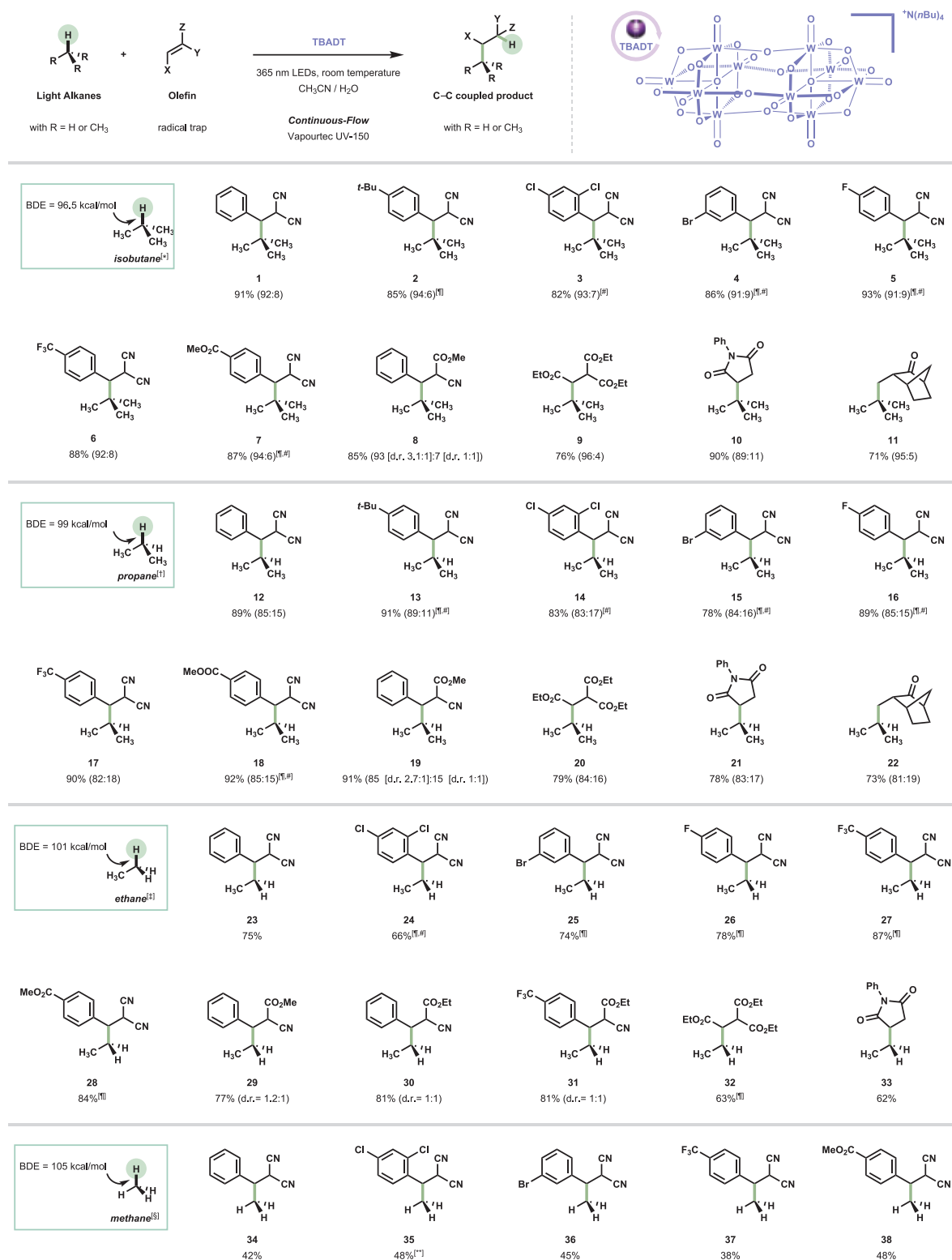


**Fig. 2. Scope of the decatungstate C(sp<sup>3</sup>)-H functionalizations of light hydrocarbons.** All yields are those of isolated products (average of two runs). The reported selectivities are determined with GC-MS. [†]Standard conditions for the decatungstate C(sp<sup>3</sup>)-H functionalizations of isobutane: olefin (1 equiv, 0.1 M), isobutane (4.3 equiv), TBADT (1.0 mol %), CH<sub>3</sub>CN:H<sub>2</sub>O (7:1), 10-bar pressure, 60 W of 365-nm LEDs, 4-hour reaction time, room temperature. Reported selectivity reflects the *t*Bu/*i*Bu ratio. [‡]Standard conditions for the decatungstate C(sp<sup>3</sup>)-H functionalizations of propane: olefin (1 equiv, 0.1 M), propane (4.1 equiv), TBADT (1.0 mol %), CH<sub>3</sub>CN:H<sub>2</sub>O (7:1), 10-bar

pressure, 60 W of 365-nm LEDs, 4-hour reaction time, room temperature. Reported selectivity reflects the *i*Pr/*n*Pr ratio. [§]Standard conditions for the decatungstate C(sp<sup>3</sup>)-H functionalizations of ethane: olefin (1 equiv, 0.1 M), ethane (8 equiv), TBADT (2.0 mol %), CH<sub>3</sub>CN:H<sub>2</sub>O (7:1), 25-bar pressure, 60 W of 365-nm LEDs, 8-hour reaction time, room temperature. [§]Standard conditions for the decatungstate C(sp<sup>3</sup>)-H functionalizations of methane: olefin (1 equiv, 0.02 M), methane (20 equiv), TBADT (5.0 mol %), CD<sub>3</sub>CN:H<sub>2</sub>O (7:1), 45-bar pressure, 150 W of 365-nm LEDs, 6-hour reaction time, room temperature. [¶]C(Michael acceptor) = 0.05 M. [‡]Solvent: neat CH<sub>3</sub>CN. [\*\*\*]Solvent: neat CD<sub>3</sub>CN. Et, ethyl.

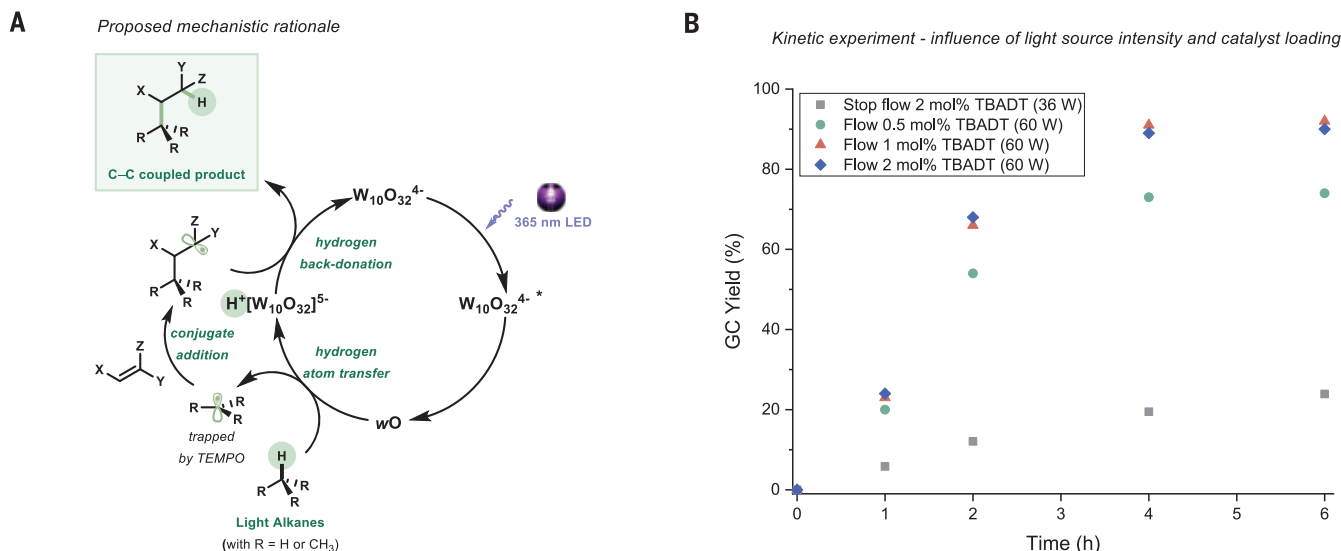


**Fig. 3. Proposed mechanism of the decatungstate C(sp<sup>3</sup>)-H functionalizations of light hydrocarbons.** (A) Proposed mechanistic rationale based on our observations. (B) Importance of photon flux and catalyst loading for the effectiveness of the decatungstate C(sp<sup>3</sup>)-H functionalization of propane.

of liquid petroleum gas. Propyl radicals could be scavenged by a variety of Michael acceptors (**12** to **22**), affording the targeted hydroalkylated compounds in good to excellent isolated yields (73 to 92%). A high selectivity was obtained for the isopropyl derivative (*i*Pr), with selectivities similar to those obtained in the TEMPO trapping experiments [*i*Pr versus *n*-propyl (*n*Pr): ~85:15] (Fig. 1D). The high selectivity in the C-H cleavage is notable despite the low difference in BDE between secondary and primary hydrogens (99 versus 101 kcal/mol) and despite the unfavorable relative abundance (six primary hydrogens versus two secondary ones). With methyl *trans*- $\alpha$ -cyanocinnamate as the substrate, a significant diastereomeric induction was observed for the trapping of the isopropyl radical (d.r. = 2.7:1 versus d.r. = 1:1 for *n*-propyl), showcasing the significance of sterical hindrance in the observed selectivity.

Another notable gaseous hydrocarbon is ethane, which is isolated from natural gas or obtained as a petrochemical by-product of petroleum refining. It is mainly used as a feedstock for ethylene production, required for the fabrication of polyethylene, which accounts for 34% of the total plastics market. Similar to isobutane and propane, ethane could be engaged in the developed C(sp<sup>3</sup>)-H activation protocol using 2 mol % of TBADT and 25 bar of pressure to liquefy the gaseous hydrocarbon. Good isolated yields (62 to 87%) were obtained for a diverse set of hydroethylated compounds (**23** to **33**).

Finally, we turned our attention to the activation of methane, one of the most abundantly available carbon-based feedstocks, using this decatungstate-enabled HAT protocol. Al-

though such a strategy would require cleaving the strongest C(sp<sup>3</sup>)-H bond (BDE = 105 kcal/mol), small changes in the reaction protocol (45-bar pressure and 5.0 mol % TBADT) allowed us to obtain synthetically useful amounts of the corresponding adducts (**34** to **38**, 38 to 48%) in only 6 hours of residence time. Because of the substantially weaker C-H bond of acetonitrile (BDE = 93 kcal/mol) compared with that of methane, the innate selectivity of decatungstate, imparted by the electrophilic nature of its excited state, could be overruled, and substantial amounts of product derived from CH<sub>3</sub>CN activation were observed as well (supplementary materials). This problem could, however, effectively be overcome by using *d*<sub>3</sub>-acetonitrile as a solvent. Investigations to replace this rather exotic solvent with a cheaper and greener alternative are currently ongoing in our laboratory.

A plausible mechanism for the decatungstate C(sp<sup>3</sup>)-H functionalizations of light hydrocarbons is outlined in Fig. 3A. Upon absorption of UV-A light, decatungstate reaches a singlet excited state, which rapidly relaxes to the actual reactive state, wO (**18**). The reactivity of wO originates from the formation of highly electrophilic oxygen centers, which can abstract hydrogen atoms yielding the desired carbon-centered radicals. The power of the light source in combination with a suitable catalyst loading is extremely relevant in photochemical processes (**32**), and this is especially true for the challenging transformation reported herein. As can be seen from Fig. 3B, the activation of propane is particularly slow when a strip of 32-W UV-A LEDs was used. However, the reaction can be boosted by using 60-W UV-A LEDs, requiring only 4 hours to reach full

conversion. For more-challenging transformations, such as the activation of methane, an even stronger light source of 150 W was required to coax the C(sp<sup>3</sup>)-H functionalization process. The nucleophilic carbon-centered radicals subsequently undergo a conjugate addition onto a suitable Michael acceptor. The carbon-centered radicals could be trapped with TEMPO, providing isomeric ratios for propane and isobutane similar to those observed in the final products (Fig. 1D). The catalytic cycle is finally closed by hydrogen back-donation, which affords the targeted hydroalkylated product.

Given the straightforward preparation (**33**) of the photocatalyst and the starting materials and the mild reaction conditions, we believe that the corresponding processes outlined herein can be considered ideal from the vantage point of feedstock upgrading. The ability to directly engage gaseous hydrocarbons as coupling partners in C-C coupling reactions removes the requirement of prefunctionalization and increases the atom efficiency of this important class of transformations. Whereas the throughput of a single microreactor is negligible from a production standpoint, the use of intensified reactors, such as a photo-spinning disk reactor, should enable higher production capacities (**34**).

#### REFERENCES AND NOTES

- J. F. Hartwig, M. A. Larsen, *ACS Cent. Sci.* **2**, 281–292 (2016).
- J. F. Hartwig, *J. Am. Chem. Soc.* **138**, 2–24 (2016).
- H. Li, B.-J. Li, Z.-J. Shi, *Catal. Sci. Technol.* **1**, 191–206 (2011).
- R. H. Crabtree, *J. Chem. Soc., Dalton Trans.* **2001**, 2437–2450 (2001).
- M. Rossberg et al., in *Ullmann's Encyclopedia of Industrial Chemistry* (Wiley, 2006).



6. D. J. Reed, in *Kirk-Othmer Encyclopedia of Chemical Technology*, vol. 6 (Wiley, 2000), pp. 226–253.
7. U.S. Environmental Protection Agency (EPA), *Chlorine and Chlorinated Hydrocarbon Manufacturing Industry* (2004); [www.epa.gov/eg/chlorine-and-chlorinated-hydrocarbon-manufacturing-industry](http://www.epa.gov/eg/chlorine-and-chlorinated-hydrocarbon-manufacturing-industry)
8. R. Lin, A. P. Amrute, J. Pérez-Ramírez, *Chem. Rev.* **117**, 4182–4247 (2017).
9. C. Liu, H. Zhang, W. Shi, A. Lei, *Chem. Rev.* **111**, 1780–1824 (2011).
10. Z. Jin et al., *Science* **367**, 193–197 (2020).
11. G. Chen et al., *Angew. Chem. Int. Ed.* **58**, 17528–17551 (2019).
12. A. Koppaka et al., *Angew. Chem. Int. Ed.* **58**, 2241–2245 (2019).
13. H.-P. Deng, Q. Zhou, J. Wu, *Angew. Chem. Int. Ed.* **57**, 12661–12665 (2018).
14. A. Hu, J.-J. Guo, H. Pan, Z. Zuo, *Science* **361**, 668–672 (2018).
15. D. Ravelli, M. Fagnoni, T. Fukuyama, T. Nishikawa, I. Ryu, *ACS Catal.* **8**, 701–713 (2018).
16. L. Capaldo, D. Ravelli, *Eur. J. Org. Chem.* **2017**, 2056–2071 (2017).
17. M. D. Tzirakis, I. N. Lykakis, M. Orfanopoulos, *Chem. Soc. Rev.* **38**, 2609–2621 (2009).
18. C. Tanielian, *Coord. Chem. Rev.* **178–180**, 1165–1181 (1998).
19. G. Laudadio et al., *Angew. Chem. Int. Ed.* **57**, 4078–4082 (2018).
20. D. M. Schultz et al., *Angew. Chem. Int. Ed.* **56**, 15274–15278 (2017).
21. S. D. Halperin, H. Fan, S. Chang, R. E. Martin, R. Britton, *Angew. Chem. Int. Ed.* **53**, 4690–4693 (2014).
22. I. B. Perry et al., *Nature* **560**, 70–75 (2018).
23. J. J. Murphy, D. Bastida, S. Paria, M. Fagnoni, P. Melchiorre, *Nature* **532**, 218–222 (2016).
24. M. B. Plutschack, B. Pieber, K. Gilmore, P. H. Seeberger, *Chem. Rev.* **117**, 11796–11893 (2017).
25. D. Cambié, C. Bottecchia, N. J. W. Straathof, V. Hessel, T. Noël, *Chem. Rev.* **116**, 10276–10341 (2016).
26. C. J. Mallia, I. R. Baxendale, *Org. Process Res. Dev.* **20**, 327–360 (2016).
27. B. Gutmann, D. Cantillo, C. O. Kappe, *Angew. Chem. Int. Ed.* **54**, 6688–6728 (2015).
28. N. Kockmann, P. Thenée, C. Fleischer-Trebes, G. Laudadio, T. Noël, *React. Chem. Eng.* **2**, 258–280 (2017).
29. N. J. Gonsalus et al., *Chem. Rev.* **117**, 8521–8573 (2017).
30. Y.-R. Luo, *Handbook of Bond Dissociation Energies in Organic Compounds* (CRC Press, 2002).
31. K. Fagnou, M. Lautens, *Chem. Rev.* **103**, 169–196 (2003).
32. H. E. Bonfield et al., *Nat. Commun.* **11**, 804 (2020).
33. D. Ravelli, S. Protti, M. Fagnoni, *Acc. Chem. Res.* **49**, 2232–2242 (2016).
34. A. Chaudhuri et al., *ChemRxiv* [Preprint] (2020).
35. S. J. Blanksby, G. B. Ellison, *Acc. Chem. Res.* **36**, 255–263 (2003).

## ACKNOWLEDGMENTS

We thank F. Gallucci (TU/e) for the kind donation of the light alkanes. **Funding:** We acknowledge financial support from the Dutch Science Foundation (NWO) for a VIDI grant for T.N. (SensPhotoFlow, no. 14150). Y.D.'s stay at the Eindhoven University of Technology was financially supported by the China Scholarship Council (CSC). **Author contributions:** T.N., G.L., and M.F. conceived the idea for this work. G.L., Y.D., and K.v.d.W. carried out the experiments. T.N., Y.S., M.F., and D.R. provided guidance with regard to the catalyst performance and the substrate scope. T.N., M.N., and D.G. provided direction for the flow experiments. T.N. wrote the manuscript with input from all authors. **Competing interests:** M.N. and D.G. both work at Vapourtec, the company that developed the Vapourtec UV-150 used in this study. **Data and materials availability:** All data are available in the main text or the supplementary materials.

## SUPPLEMENTARY MATERIALS

[science.sciencemag.org/content/369/6499/92/suppl/DC1](https://science.sciencemag.org/content/369/6499/92/suppl/DC1)  
Materials and Methods  
Figs. S1 to S13  
Tables S1 to S10  
NMR Data  
References (36–49)

26 February 2020; accepted 6 May 2020  
10.1126/science.abb4688

## SOLAR CELLS

# A piperidinium salt stabilizes efficient metal-halide perovskite solar cells

Yen-Hung Lin<sup>1\*</sup>, Nobuya Sakai<sup>1</sup>, Peimei Da<sup>1</sup>, Jiaying Wu<sup>2</sup>, Harry C. Sansom<sup>1</sup>, Alexandra J. Ramadan<sup>1</sup>, Suhas Mahesh<sup>1</sup>, Junliang Liu<sup>3</sup>, Robert D. J. Oliver<sup>1</sup>, Jongchul Lim<sup>1†</sup>, Lee Aspirtarte<sup>4</sup>, Kshama Sharma<sup>5</sup>, P. K. Madhu<sup>5</sup>, Anna B. Morales-Vilches<sup>6</sup>, Pabitra K. Nayak<sup>1,5</sup>, Sai Bai<sup>7</sup>, Feng Gao<sup>7</sup>, Chris R. M. Grovenor<sup>3</sup>, Michael B. Johnston<sup>1</sup>, John G. Labram<sup>4</sup>, James R. Durrant<sup>2,8</sup>, James M. Ball<sup>1</sup>, Bernard Wenger<sup>1</sup>, Bernd Stannowski<sup>6</sup>, Henry J. Snaith<sup>1\*</sup>

Longevity has been a long-standing concern for hybrid perovskite photovoltaics. We demonstrate high-resilience positive-intrinsic-negative perovskite solar cells by incorporating a piperidinium-based ionic compound into the formamidinium-cesium lead-trihalide perovskite absorber. With the bandgap tuned to be well suited for perovskite-on-silicon tandem cells, this piperidinium additive enhances the open-circuit voltage and cell efficiency. This additive also retards compositional segregation into impurity phases and pinhole formation in the perovskite absorber layer during aggressive aging. Under full-spectrum simulated sunlight in ambient atmosphere, our unencapsulated and encapsulated cells retain 80 and 95% of their peak and post-burn-in efficiencies for 1010 and 1200 hours at 60° and 85°C, respectively. Our analysis reveals detailed degradation routes that contribute to the failure of aged cells.

Two-terminal monolithic perovskite-on-silicon tandem cells appear to be one of the most promising photovoltaic technologies for near-term commercial-scale deployment (*1, 2*). These cells feature a wide bandgap perovskite “top cell” that absorbs in a region of the solar spectrum complementary to that of the silicon “bottom cell,” and such solar cells have been demonstrated with a certified power conversion efficiency (PCE) reaching 29.1% (*3*).

There is often a compromise between achieving high efficiency and long-term stability. The presence of methylammonium (MA) as the A-site cation in the perovskite absorber, which leads to more rapid decomposition under elevated temperature, light exposure, and atmosphere (*4*), can be alleviated by substitution with formamidinium (FA) or compositions of FA and cesium (Cs) (*5–7*). However, the use of MA persists in many recent reports on the highest-

efficiency perovskite cells in the form of the mixed-cation CsFAMA or FAMA perovskites (*8, 9*). Also, the organic hole conductor 2,2',7,7'-tetrakis[*N,N*-di(4-methoxyphenyl)amino]-9,9'-spirobifluorene (Spiro-OMeTAD) and the additives required to deliver high efficiency are detrimental to the stability of perovskite cells (*10–12*) but are often used in the highest PCE single-junction perovskite cells (*9, 12*). Finally, molecular passivation of defects in the perovskite absorber is a common route to increase the solar cell efficiency (*13*) but often introduces additional thermal instabilities. The absorber layers and cells can revert to their unpassivated state after thermal treatment at temperatures as low as 60° to 85°C (*9*).

Thus, efforts are required to simultaneously deliver efficiency enhancements and improve long-term stability. We recently reported that incorporation of an imidazolium-based ionic liquid into positive-intrinsic-negative (p-i-n) perovskite solar cells, which use the triple cation perovskite as the absorber layer and nickel oxide (NiO) as the p-type layer, can improve both efficiency and long-term stability (*14*). However, the best-quality NiO p-type layers require annealing at ~400°C, which makes their integration with Si heterojunction bottom cells challenging, because these bottom cells cannot be processed above 200°C owing to the sensitivity of the amorphous silicon passivation and charge extraction layers. We also found that this imidazolium-based ionic liquid is incompatible with the use of low-temperature processible organic p-type layers. Moreover, we carried out thermal stability tests in nitrogen at 85°C and found that, when using NiO p-type layers, the cells were considerably less stable than cells that use poly(4-butylphenyl-diphenylamine)

<sup>1</sup>Clarendon Laboratory, Department of Physics, University of Oxford, Oxford OX1 3PU, UK. <sup>2</sup>Department of Chemistry and Centre for Plastic Electronics, Imperial College London, London W12 0BZ, UK. <sup>3</sup>Department of Materials, University of Oxford, Oxford OX1 3PH, UK. <sup>4</sup>School of Electrical Engineering and Computer Science, Oregon State University, Corvallis, OR 97331, USA. <sup>5</sup>TIFR Centre for Interdisciplinary Sciences, Tata Institute of Fundamental Research, Hyderabad 500107, India. <sup>6</sup>PVcomB, Helmholtz-Zentrum Berlin für Materialien und Energie GmbH, 12489 Berlin, Germany. <sup>7</sup>Department of Physics, Chemistry and Biology (IFM), Linköping University, 581 83 Linköping, Sweden. <sup>8</sup>Sustainable Product Engineering Centre for Innovative Functional Industrial Coatings (SPECIFIC), College of Engineering, Swansea University, Bay Campus, Swansea SA1 8EN, UK.

\*Corresponding author. Email: [yen-hung.lin@physics.ox.ac.uk](mailto:yen-hung.lin@physics.ox.ac.uk) (Y.-H.L.); [henry.snaith@physics.ox.ac.uk](mailto:henry.snaith@physics.ox.ac.uk) (H.J.S.) †Present address: Graduate School of Energy Science and Technology, Chungnam National University, Yuseong-gu, Daejeon 34134, Republic of Korea.

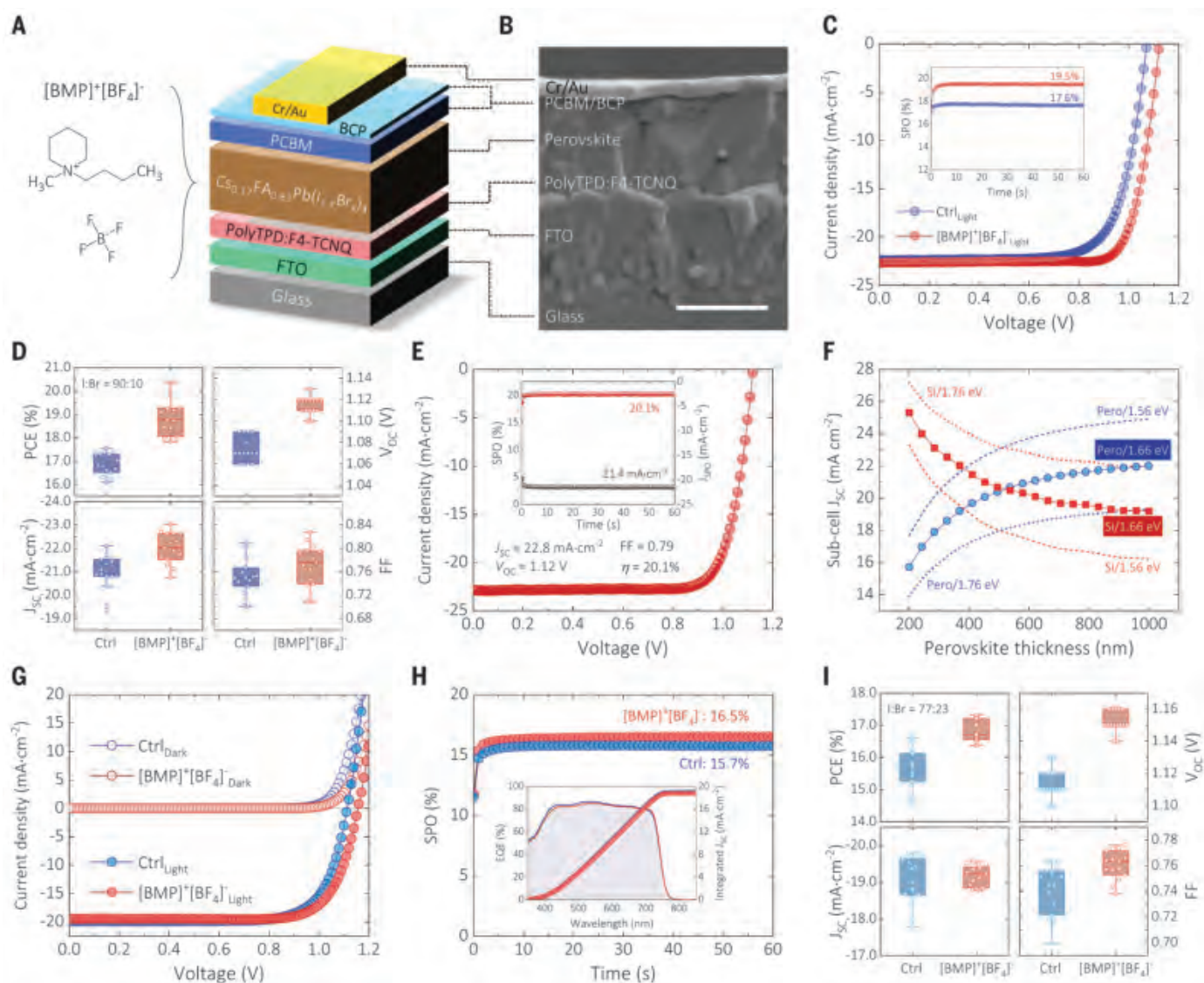


**Fig. 1. Perovskite solar cell characterization.** (A) Schematic of the p-i-n perovskite solar cell and the chemical structure of [BMP]<sup>+</sup>[BF<sub>4</sub>]<sup>-</sup>. BCP, bathocuproine; PCBM, phenyl-C<sub>61</sub>-butyric acid methyl ester; PolyTPD, poly(4-butylphenyl-diphenylamine); F4-TCNQ, tetrafluoro-7,7,8,8-tetracyanoquinodimethane. (B) SEM image of the full device stack made from Cs<sub>0.17</sub>FA<sub>0.83</sub>Pb(I<sub>0.90</sub>Br<sub>0.10</sub>)<sub>3</sub> with 0.25 mol % [BMP]<sup>+</sup>[BF<sub>4</sub>]<sup>-</sup>. Scale bar, 500 nm. (C) J-V characteristics of the representative 0.25 mol % [BMP]<sup>+</sup>[BF<sub>4</sub>]<sup>-</sup> modified Cs<sub>0.17</sub>FA<sub>0.83</sub>Pb(I<sub>0.90</sub>Br<sub>0.10</sub>)<sub>3</sub> and control (Ctrl) devices measured from the forward-bias (FB) to short-circuit (SC) scans under simulated air mass 1.5 sunlight and corresponding SPO. (D) Statistical results of device parameters for Cs<sub>0.17</sub>FA<sub>0.83</sub>Pb(I<sub>0.90</sub>Br<sub>0.10</sub>)<sub>3</sub>-based devices. (E) J-V characteristics for the champion

cell with 0.25 mol % [BMP]<sup>+</sup>[BF<sub>4</sub>]<sup>-</sup> modified Cs<sub>0.17</sub>FA<sub>0.83</sub>Pb(I<sub>0.90</sub>Br<sub>0.10</sub>)<sub>3</sub>. η, power conversion efficiency. (Inset) corresponding SPO and current density measured under SPO (J<sub>SPO</sub>). (F) Modeling of the thickness-dependent subcell J<sub>SC</sub> for perovskite-on-silicon tandem cells with perovskites of different bandgaps. The evolution of perovskite subcell J<sub>SC</sub> is shown in blue, and the corresponding Si subcell J<sub>SC</sub> is shown in red. (G) J-V characteristics of the representative 0.25 mol % [BMP]<sup>+</sup>[BF<sub>4</sub>]<sup>-</sup> modified and control devices using Cs<sub>0.17</sub>FA<sub>0.83</sub>Pb(I<sub>0.90</sub>Br<sub>0.10</sub>)<sub>3</sub>. (H) Corresponding SPO, EQE, and integrated J<sub>SC</sub> for the devices shown in (G). The integrated J<sub>SC</sub> values for the modified and control devices are 18.8 and 19.0 mA·cm<sup>-2</sup>, respectively. (I) Statistical results of device parameters for Cs<sub>0.17</sub>FA<sub>0.83</sub>Pb(I<sub>0.90</sub>Br<sub>0.10</sub>)<sub>3</sub>-based devices.

(polyTPD) as the hole-transport material, which we show in Fig. S1.

In this study, we demonstrate high-performance p-i-n perovskite solar cells using thermally stable CsFA-based lead-halide perovskite absorber layers, low-temperature processed organic charge extraction layers, and the organic ionic solid additive 1-butyl-1-methylpiperidinium

tetrafluoroborate ([BMP]<sup>+</sup>[BF<sub>4</sub>]<sup>-</sup>). The incorporation of [BMP]<sup>+</sup>[BF<sub>4</sub>]<sup>-</sup> into the perovskite absorber suppressed deep trap states, improved performance, and enhanced the operational stability of cells stressed under full-spectrum sunlight at elevated temperatures up to 85°C.

We screened a number of ionic salts as additives for improving the efficiency of perov-

skite solar cells, with the commonality of having a large chemically stable organic cation and a [BF<sub>4</sub>]<sup>-</sup> anion. At low concentrations, [BMP]<sup>+</sup>[BF<sub>4</sub>]<sup>-</sup> (see Fig. 1A for the chemical structure) resulted in a particularly positive influence in photovoltaic performance. We depict the device architecture in Fig. 1A, where polyTPD and [6,6]-phenyl-C<sub>61</sub>-butyric acid



methyl ester (PCBM) were used as the hole-transporting and electron-transporting layers, respectively. The scanning electron microscopy (SEM) image for a representative p-i-n cell based on a perovskite composition of  $\text{Cs}_{0.17}\text{FA}_{0.83}\text{Pb}(\text{I}_{0.77}\text{Br}_{0.23})_3$  and 0.25 mol %  $[\text{BMP}]^+[\text{BF}_4]^-$  (with respect to the Pb content) is shown in Fig. 1B.

To demonstrate the performance enhancement potential of  $[\text{BMP}]^+[\text{BF}_4]^-$ , we fabricated mixed halide perovskites with a low Br content  $\text{Cs}_{0.17}\text{FA}_{0.83}\text{Pb}(\text{I}_{0.90}\text{Br}_{0.10})_3$ , which we have found to be the best composition for maximum efficiency of single-junction cells. In Fig. 1C and fig. S2, we show typical current density-voltage ( $J$ - $V$ ) characteristics for the 0.25 mol %  $[\text{BMP}]^+[\text{BF}_4]^-$  modified and control devices, and the statistical results of the device performance parameters are shown in Fig. 1D. A champion  $[\text{BMP}]^+[\text{BF}_4]^-$  device (Fig. 1E) exhibited an open-circuit voltage ( $V_{\text{OC}}$ ) of 1.12 V, a short-circuit current density ( $J_{\text{SC}}$ ) of  $22.8 \text{ mA cm}^{-2}$ , and a fill factor (FF) of 0.79, resulting in a PCE of 20.1% and a steady-state power output (SPO) of 20.1%. The corresponding external quantum efficiency (EQE) (fig. S3) yielded an integrated  $J_{\text{SC}}$  with a negligible variation ( $\sim 2.5\%$ ) from the measured  $J_{\text{SC}}$ . The addition of  $[\text{BMP}]^+[\text{BF}_4]^-$  in the perovskite light absorber led to very high performance for MA-free single-junction p-i-n perovskite solar cells compared with reports to date (5, 15).

For a perovskite-on-silicon tandem solar cell, balancing the light absorption between the constituent subcells is key to achieving current matching to maximize PCE (16, 17). Following (17), we simulated the evolution of subcell  $J_{\text{SC}}$  values in perovskite-on-silicon tandem cells as a function of absorber layer thickness for perovskite bandgaps of 1.56, 1.66, and 1.76 eV (Fig. 1F). The ideal thickness for a 1.66 eV bandgap was  $\sim 500 \text{ nm}$ , which falls into a common perovskite processing window (15). We also modeled the subcell  $J_{\text{SC}}$  with various bandgaps for a 500-nm perovskite layer (fig. S4), and a 1.66 eV bandgap was also nearly ideal for maximizing energy yield for monolithic perovskite-on-silicon tandem cells deployed in real-world locations (18).

By tuning the I/Br composition, we found that  $\text{Cs}_{0.17}\text{FA}_{0.83}\text{Pb}(\text{I}_{0.77}\text{Br}_{0.23})_3$  perovskite delivered the desired 1.66 eV bandgap, as determined from the derivative of the EQE spectrum, (fig. S5). We optimized the single-junction cells using different  $[\text{BMP}]^+[\text{BF}_4]^-$  concentrations ranging from 0.0 (control) to 0.3 mol %; the device performance parameters from a large batch of cells are summarized in fig. S6. With increasing concentrations of  $[\text{BMP}]^+[\text{BF}_4]^-$ , we observed that  $V_{\text{OC}}$  rose from an average of 1.11 V for the control device to  $>1.16 \text{ V}$  for the 0.3 mol %  $[\text{BMP}]^+[\text{BF}_4]^-$  modified device;  $J_{\text{SC}}$  did not vary appreciably relative to the control. However, on average, the FF increased at low con-

centrations but tended to decrease at higher concentrations of  $[\text{BMP}]^+[\text{BF}_4]^-$ . Thus, devices with 0.25 mol %  $[\text{BMP}]^+[\text{BF}_4]^-$  exhibited the highest PCEs. Characteristic  $J$ - $V$  curves for an optimized 0.25 mol %  $[\text{BMP}]^+[\text{BF}_4]^-$  modified perovskite solar cell and a control device are shown in Fig. 1G, and the corresponding SPOs are shown in Fig. 1H. The corresponding forward and reverse direction  $J$ - $V$  scans are shown in fig. S7. The 0.25 mol %  $[\text{BMP}]^+[\text{BF}_4]^-$  device exhibited a  $V_{\text{OC}}$  of 1.16 V, a  $J_{\text{SC}}$  of  $19.5 \text{ mA cm}^{-2}$ , and a FF of 0.77, yielding a PCE of 17.3%. The control device, which exhibited a lower PCE of 16.6%, had a  $V_{\text{OC}}$  of 1.11 V and a FF of 0.75. The corresponding SPOs were 16.5 and 15.7% for the modified and control devices, respectively. We show a set of statistical results obtained from 15 individual cells of each type in Fig. 1I. The EQE (Fig. 1H, inset) was in good agreement with the  $J_{\text{SC}}$  measured from the  $J$ - $V$  scans (Fig. 1G). With the addition of  $[\text{BMP}]^+[\text{BF}_4]^-$ , the cells generally exhibited an increase in  $V_{\text{OC}}$ , FF, and PCE. The  $J_{\text{SC}}$  was similar or slightly higher with the optimum piperidinium content for all perovskite compositions.

To understand the impact on the optoelectronic characteristics of the perovskite films with the addition  $[\text{BMP}]^+[\text{BF}_4]^-$ , we carried out a series of spectroscopic measurements, including transient photovoltage (TPV) (fig. S8A), charge extraction (fig. S8B), time-resolved photoluminescence (TRPL) (fig. S9A), steady-state

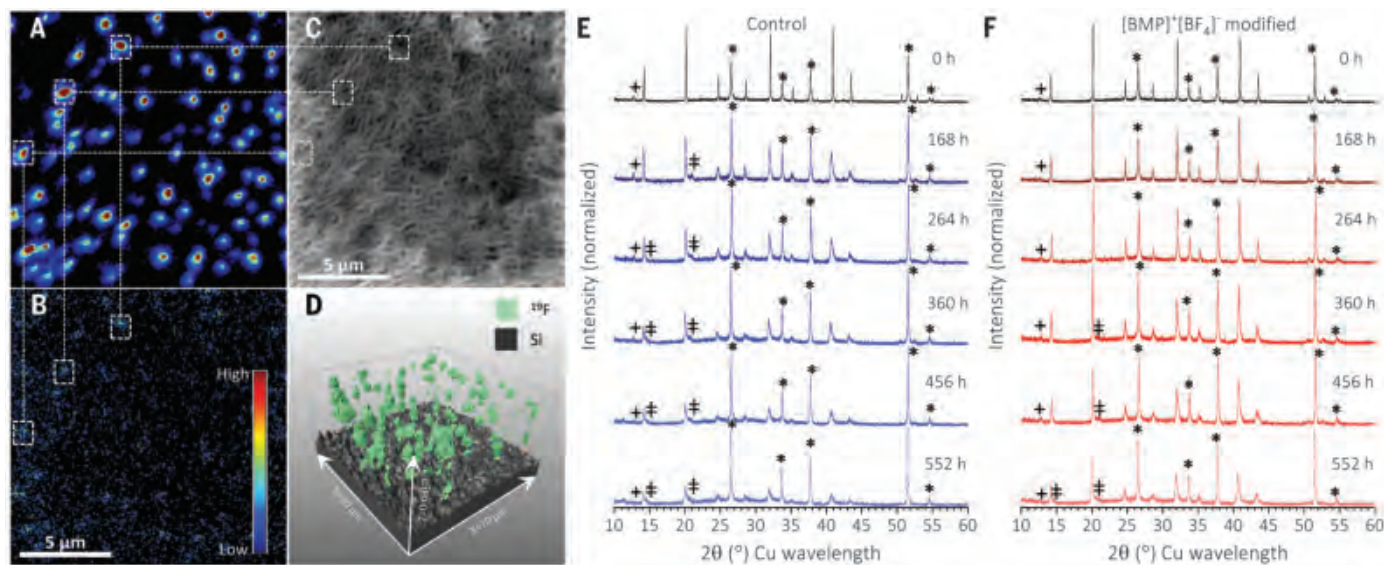


**Fig. 2. High-resolution secondary ion mass spectrometry and x-ray diffraction analysis.** (A and B)  $^{19}\text{F}^-$  and  $^{11}\text{B}^{16}\text{O}_2^-$  ion maps for the F and B distributions toward the top surface of a  $\sim 500\text{-nm}$   $\text{Cs}_{0.17}\text{FA}_{0.83}\text{Pb}(\text{I}_{0.77}\text{Br}_{0.23})_3$  with 0.25 mol %  $[\text{BMP}]^+[\text{BF}_4]^-$  perovskite film. (C) Secondary electron map for the sputtered surface morphology  $\sim 60 \text{ nm}$  below the sample surface. The squares denoted in (A) to (C) are to indicate the corresponding regions of highly localized F and B concentrations. (D) A reconstructed 3D map

(stretched in the  $z$  direction for clarity) showing the distribution of the  $^{19}\text{F}^-$  signals through the perovskite layer. (E and F) XRD series for the gaining of the unencapsulated control and 0.25 mol %  $[\text{BMP}]^+[\text{BF}_4]^-$  modified  $\text{Cs}_{0.17}\text{FA}_{0.83}\text{Pb}(\text{I}_{0.77}\text{Br}_{0.23})_3$  perovskite films, respectively, prepared on FTO glass substrates. The XRD peaks corresponding to  $\text{PbI}_2$  (+ symbol), FTO (asterisk symbol), and the secondary cubic perovskite phase ( $\ddagger$  symbol) are marked. h, hours.

photoluminescence (SSPL) (fig. S9B), and transient photoconductivity (TPC) (fig. S10) on half-complete or complete device structures, and time-resolved microwave conductivity (TRMC) (figs. S11 and S12) and in-plane transient photoconductivity (ip-TPC) (fig. S13) on isolated perovskite films. We found that adding [BMP]<sup>+</sup>[BF<sub>4</sub>]<sup>−</sup> did not compromise charge carrier mobilities (figs. S10B, S12, and S13A). Furthermore, from light intensity-dependent  $V_{OC}$  and charge-extraction measurements of complete devices, we observed a reduced ideality factor and capacitance (or reduced total stored charge density) for the [BMP]<sup>+</sup>[BF<sub>4</sub>]<sup>−</sup> modified devices under low light intensity (fig. S8B). We also observed a slower TRPL decay and more than double the SSPL intensity in the [BMP]<sup>+</sup>[BF<sub>4</sub>]<sup>−</sup> film (fig. S9). These results were consistent with a reduced density of deep trap sites in the [BMP]<sup>+</sup>[BF<sub>4</sub>]<sup>−</sup> modified devices. Further analysis of the optoelectronic and spectroscopic characterizations is provided in the supplementary text section of the supplementary materials.

To reveal how [BMP]<sup>+</sup>[BF<sub>4</sub>]<sup>−</sup> was distributed within the perovskite layer, we used high-resolution nanoscale secondary ion mass spectrometry (nanoSIMS). We present the secondary electron and elemental mapping for the <sup>19</sup>F<sup>−</sup> and <sup>11</sup>B<sup>16</sup>O<sub>2</sub><sup>−</sup> distributions in a Cs<sub>0.17</sub>FA<sub>0.83</sub>Pb(I<sub>0.77</sub>Br<sub>0.23</sub>)<sub>3</sub> perovskite film in Fig. 2, A to C. In Fig. 2A, the <sup>19</sup>F<sup>−</sup> signals show agglomeration and, despite yielding much lower intensities, the <sup>11</sup>B<sup>16</sup>O<sub>2</sub><sup>−</sup> intensity map (Fig. 2B) coincided reasonably well with the <sup>19</sup>F<sup>−</sup> map. We show the three-dimensional (3D) visualization of the entire <sup>19</sup>F<sup>−</sup> dataset in Fig. 2D, where we observed that the <sup>19</sup>F<sup>−</sup> signal originated from roughly spherical regions a few hundred nanometers in diameter that were evenly distributed over the surveyed volume. Both the depth (fig. S14A) and line (fig. S14B) profiles revealed that, in addition to the agglomerates, a small amount of F could be detected throughout the perovskite.

From this nanoSIMS characterization, we deduce that most of the [BMP]<sup>+</sup>[BF<sub>4</sub>]<sup>−</sup> molecules were localized in isolated aggregates that presumably accumulated between the perovskite domains, but small amounts penetrated the entire volume of the film. This distribution differs from that of the imidazolium-based ionic liquid, which we have previously used with NiO p-type layers. For that material, the predominant accumulation of [BF<sub>4</sub>]<sup>−</sup> was at the buried NiO-perovskite interface (14). Presumably, the distribution throughout the entire volume of the perovskite film helped the [BMP]<sup>+</sup>[BF<sub>4</sub>]<sup>−</sup> ionic salt enhance the performance of the cells when we used the poly-TPD organic hole conductor. We attempted to observe interactions between the [BMP]<sup>+</sup>[BF<sub>4</sub>]<sup>−</sup> and the perovskites using solid-state nuclear magnetic resonance (ssNMR) and x-ray photo-

emission spectroscopy (XPS), which we show in the supplementary text and figs. S15 and S16, respectively. However, we observed no discernible differences between the control and modified samples.

We also carried out characterizations to assess the stability of the CsFA perovskite compounds after the addition of [BMP]<sup>+</sup>[BF<sub>4</sub>]<sup>−</sup>. Ultraviolet-visible (UV-vis) absorption spectra (fig. S17) and x-ray diffraction (XRD) patterns (Fig. 2, E and F) were obtained for the [BMP]<sup>+</sup>[BF<sub>4</sub>]<sup>−</sup> modified and control Cs<sub>0.17</sub>FA<sub>0.83</sub>Pb(I<sub>0.77</sub>Br<sub>0.23</sub>)<sub>3</sub> perovskite films aged under simulated full-spectrum sunlight at 60°C in ambient air (relative humidity in the laboratory was ~50%). The absorption edge of the [BMP]<sup>+</sup>[BF<sub>4</sub>]<sup>−</sup> modified sample exhibited a minor change for the first 264 hours (fig. S17A), whereas the control sample exhibited a clear redshift in the absorption edge, which moved from ~750 nm to >775 nm (fig. S17B). This redshift in absorption also coincides with a redshift in the EQE spectrum of complete solar cells aged in a similar manner (fig. S18), indicating that a similar change is occurring, albeit at a slower rate, in the complete devices. The XRD measurements did not reveal any noticeable formation of lead halide (~12.7°) with aging time for both the control (Fig. 2E) and modified (Fig. 2F) samples, which is usually observed during degradation of MA-containing perovskites because of the loss of methylammonium iodide (4). Conversely, a small PbI<sub>2</sub> peak present at 12.7° in both the control and modified films early on disappeared during aging. During the time series, the main perovskite phase peaks broadened (fig. S19) and decreased in intensity, and additional peaks at 14.6° and 20.7°, as well as a low-angle peak at 11.3°, appeared during long aging in the control film.

The broadening of the main phase can be explained by orthorhombic strain. Before aging, we fit the main perovskite phase to an orthorhombic cell in space group *Pnma*, with lattice parameters of  $a = 8.801(1)$  Å,  $b = 8.8329(3)$  Å, and  $c = 12.4940(5)$  Å and a volume of  $971.3(2)$  Å<sup>3</sup> for the control film, and  $a = 8.8146(3)$  Å,  $b = 8.8333(9)$  Å, and  $c = 12.4892(9)$  Å for the modified film with a larger volume of  $972.4(1)$  Å<sup>3</sup>. Both are larger than the orthorhombic perovskite  $\gamma$ -CsPbI<sub>3</sub> [volume =  $947.33(5)$  Å<sup>3</sup>] (19), indicating the mixed CsFA phase. The lowering of symmetry from cubic to orthorhombic was needed to fit the XRD data well (fig. S20). We refined the orthorhombic unit cell across the aging series and defined the orthorhombic strain as  $S$  (%) =  $100 \times \sqrt{\left(\frac{\sqrt{2}a}{\sqrt{2}b} - 1\right)^2 + \left(\frac{\sqrt{2}b}{c} - 1\right)^2 + \left(\frac{\sqrt{2}a}{c} - 1\right)^2}$ , which we show in fig. S21A. The orthorhombic strain in the control and modified films increased at a similar rate; however, the control sample started with a slightly more orthorhombic phase.

The orthorhombic strain was the only sign of change in the XRD pattern for the [BMP]<sup>+</sup>[BF<sub>4</sub>]<sup>−</sup> modified samples at aging times less than 360 hours. Comparison of spectra showed that the orthorhombic strain did not have a large effect on the absorption. The additional peaks at 14.6° and 20.7° appeared for the control sample after the first aging step of 168 hours and for the modified sample between 264 and 360 hours of aging. These peaks were fitted to a cubic unit cell in the *Pm $\bar{3}$ m* space group and could not be fitted with the unit cells of any of the relevant binary halide salts. For the modified sample aged at 360 hours, the cubic unit cell has a volume of  $217(1)$  Å<sup>3</sup>, which is within error of the reported volume of FAPbBr<sub>3</sub> [ $217.45(2)$  Å<sup>3</sup>] (20). The XRD peaks associated with this second phase are indicated with the ‡ symbol in Fig. 2, E and F, and fig. S22.

Segregation of FAPbBr<sub>3</sub> would leave the main phase rich in Cs and I. Iodide enrichment was consistent with the redshift seen in absorption spectra (fig. S17), and the time at which these phases emerged in the XRD patterns coincides with the timing for the redshift. The volume of the main orthorhombic perovskite phase and the secondary FAPbBr<sub>3</sub> perovskite phase both initially increased over time but started to decrease for the control after the 264-hour aging (fig. S21, B and C). This decrease suggests that after the initial separation of FAPbBr<sub>3</sub>, other compositional changes continued, either because of mixing of the halides or external factors. At the same time, the intensity of the main phase peaks decreased, and the decrease was faster in the control sample. The peak at 11.3°, which appeared in the control sample after 456 hours (fig. S23) but was suppressed in the modified sample, was previously ascribed to the nonperovskite yellow hexagonal  $\delta$ -FAPbI<sub>3</sub> phase (21, 22), which can form in the perovskite film when the Cs or FA content is strongly unbalanced (7, 21, 23).

In an attempt to visualize the impurity phases generated during aging, we performed optical microscopy measurements on the fresh and aged control (fig. S24) and [BMP]<sup>+</sup>[BF<sub>4</sub>]<sup>−</sup> modified (fig. S25) Cs<sub>0.17</sub>FA<sub>0.83</sub>Pb(I<sub>0.77</sub>Br<sub>0.23</sub>)<sub>3</sub> perovskite films grown on fluorine-doped tin oxide (FTO) glass. The aged samples were subjected to 500 hours of the same aging environmental parameters that were applied to the XRD samples. The microscope was backlit with a halogen lamp, with optional additional photoexcitation from the front with a 375-nm UV light-emitting diode (LED) to induce photoluminescence. Both the fresh control and [BMP]<sup>+</sup>[BF<sub>4</sub>]<sup>−</sup> modified films appeared orange-red in color and had wrinkled surface characteristic of the antisolvent quenching spin-coating fabrication method (24) and showed no clear difference with or without UV illumination. After aging, the [BMP]<sup>+</sup>[BF<sub>4</sub>]<sup>−</sup> modified films appeared to be predominantly unchanged.



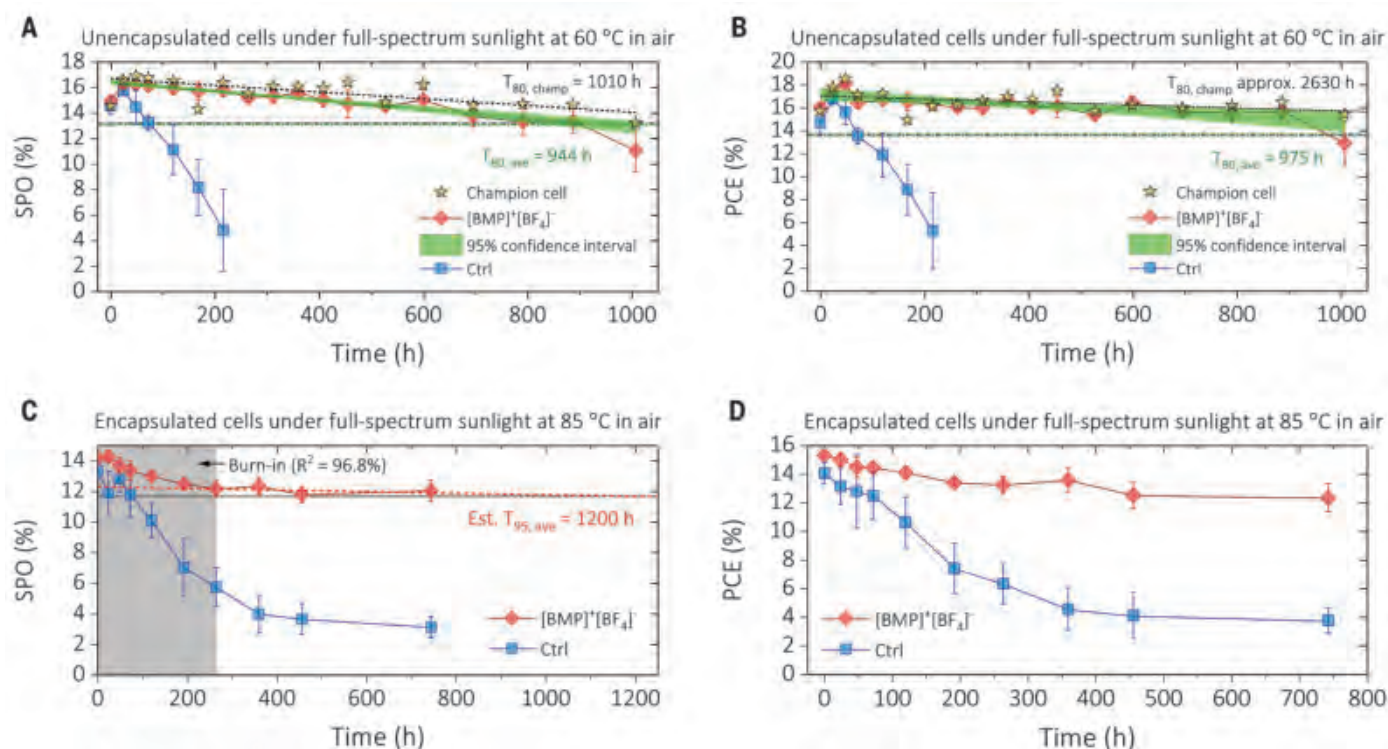


**Fig. 3. Long-term operational stability.** (A) Evolution of SPOs of unencapsulated 0.25 mol % [BMP]<sup>+</sup>[BF<sub>4</sub>]<sup>-</sup> modified and control (Ctrl) Cs<sub>0.17</sub>FA<sub>0.83</sub>Pb(I<sub>0.77</sub>Br<sub>0.23</sub>)<sub>3</sub> perovskite solar cells (eight cells for each condition), aged under full-spectrum sunlight at 60°C in ambient air. The 95% confidence interval for the SPOs of the modified devices is shown as a green band. The champion cell with the [BMP]<sup>+</sup>[BF<sub>4</sub>]<sup>-</sup> additive is indicated with yellow stars, and the black dotted line is a guide to the eye. The intersections between the data points and the black and green dashed-dotted lines show  $T_{80, \text{champ}}$  for the champion cell and  $T_{80, \text{ave}}$  for eight individual

cells, respectively. (B) Corresponding PCEs for (A). (C) Evolution of SPOs of encapsulated 0.25 mol % [BMP]<sup>+</sup>[BF<sub>4</sub>]<sup>-</sup> modified and control Cs<sub>0.17</sub>FA<sub>0.83</sub>Pb(I<sub>0.77</sub>Br<sub>0.23</sub>)<sub>3</sub> cells aged under full-spectrum sunlight at 85°C in ambient air (six cells for each condition). The early burn-in region (~264 hours) is determined using a linear model (coefficient of determination  $R^2 = 96.8\%$ ). The intersection between the linear extrapolation for the data (red dashed line) and black dotted line estimated the lifetime for 95% of the post-burn-in SPO (Est.  $T_{95, \text{ave}}$ ) from six individual cells. (D) Corresponding PCEs for (C). In all figures, the error bars denote standard deviations.

In contrast, for the control films, we observed a strong darkening in color and the appearance of large dark domains. Upon UV illumination, these dark domains emitted blue light. The blue emission was consistent with these regions containing some wider gap impurity phase material, most likely the non-perovskite hexagonal  $\delta$ -FAPbI<sub>3</sub> phase (21, 22). In addition to these coarse features, we observed numerous white or yellow bright spots in images of the aged control samples (fig. S24, C to F). From SEM images of the same samples, which we present in fig. S26, we confirmed that these bright spots were pinholes in the film. The presence of these pinholes in the aged control films, which were absent from the [BMP]<sup>+</sup>[BF<sub>4</sub>]<sup>-</sup> modified films, was a key difference. The addition of [BMP]<sup>+</sup>[BF<sub>4</sub>]<sup>-</sup> appeared to have prevented the formation of the blue-emitting impurity phase, inhibited FAPbBr<sub>3</sub> impurity phase growth, and strongly suppressed pinhole formation (fig. S26D).

We investigated the operational stability of Cs<sub>0.17</sub>FA<sub>0.83</sub>Pb(I<sub>0.77</sub>Br<sub>0.23</sub>)<sub>3</sub>-based perovskite solar cells aged at open-circuit condition under full-

spectrum sunlight at elevated temperatures in ambient air (relative humidity in the laboratory was ~50%). We first examined the stability of unencapsulated devices aged at 60°C. The average SPOs and PCEs obtained from eight individual devices for each condition are shown in Fig. 3, A and B, respectively, and the evolution of the device parameters is plotted in fig. S27. For both the [BMP]<sup>+</sup>[BF<sub>4</sub>]<sup>-</sup> modified and control devices, we observed a positive light-soaking effect that enhanced the SPO and PCE values by ~2% absolute during the first few days of aging, whereas the average SPO and PCE of the control devices dropped below the initial performance after 72 hours and continuously decreased to ~5% absolute efficiency after 216 hours. The efficiency of the [BMP]<sup>+</sup>[BF<sub>4</sub>]<sup>-</sup> modified devices improved over the first few hundred hours, likely because of the photobrightening effect (25) resulting from passivation of defects in the perovskite film via reaction with photogenerated superoxide and peroxide species (26).

Our [BMP]<sup>+</sup>[BF<sub>4</sub>]<sup>-</sup> modified devices remained highly operational, decreasing to 80% of the

peak SPO and PCE ( $T_{80, \text{ave}}$ ) within an average time of 944 and 975 hours, respectively. We observed that the  $V_{\text{OC}}$  remained beyond its initial level for >1000 hours at close to 1.2 V (fig. S27A). The unencapsulated devices appear to be much more stable than the isolated perovskite films aged under the same conditions. This is likely because of the PCBM and BCP electron extraction layer and the CrAu electrode partially encapsulating the perovskite film, by inhibiting ingress of atmosphere and loss of degradation products (10, 27–29). Our champion [BMP]<sup>+</sup>[BF<sub>4</sub>]<sup>-</sup> device exhibited the measured and estimated lifetimes through a linear extrapolation for 80% of the peak SPO and PCE (i.e.,  $T_{80, \text{champ}}$ ) of 1010 and 2630 hours, respectively (30). The difference in  $T_{80, \text{champ}}$  between SPO and PCE originates from non-negligible hysteresis in the  $J$ - $V$  scans from the aged samples (fig. S28). We benchmark our stability results against the long-term stability data from the literature (table S1). Most stability studies are performed on encapsulated cells or cells in an inert atmosphere. Previous reports from unencapsulated cells in ambient

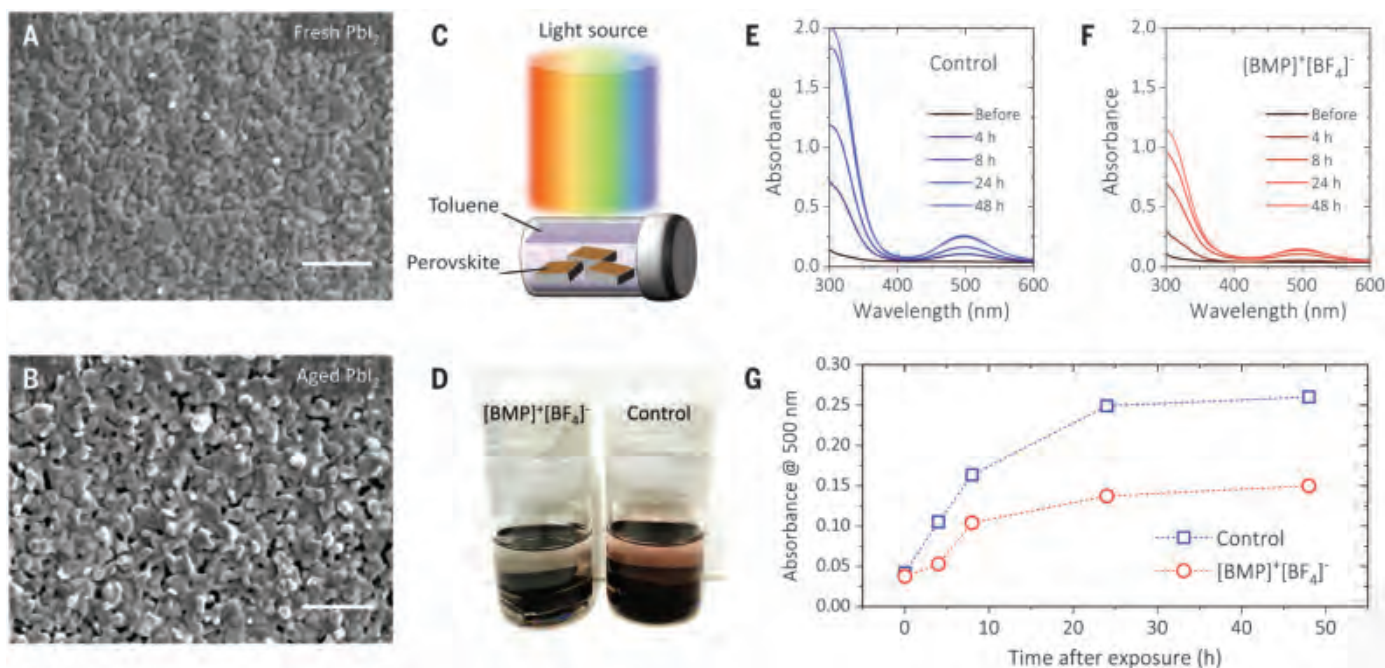


**Fig. 4. Iodine-loss analysis of  $\text{PbI}_2$  and perovskite films.** (A and B) Top-surface SEM images of  $\text{PbI}_2$  films: (A) fresh and (B) aged under  $\sim 0.32$  suns white LED illumination at  $85^\circ\text{C}$  in a nitrogen-filled glove box for 6 hours. Scale bars,  $1\ \mu\text{m}$ . (C) Schematic of the iodine-loss experimental setup: Vials filled and sealed in nitrogen, containing perovskite films fully submerged in toluene, were exposed to full-spectrum sunlight at  $60^\circ\text{C}$  in

ambient air. (D) Photo of the sealed vials with the control and 0.25 mol %  $[\text{BMP}]^+[\text{BF}_4]^-$  additive modified  $\text{Cs}_{0.17}\text{FA}_{0.83}\text{Pb}(\text{I}_{0.77}\text{Br}_{0.23})_3$  perovskite samples, taken after 4 hours of light and heat exposure. (E and F) Ten UV-vis absorbance spectra recorded for the toluene solution taken from the (E) control and (F)  $[\text{BMP}]^+[\text{BF}_4]^-$  vials at different aging times. (G) Evolution of absorbance recorded at 500 nm.

atmosphere have delivered  $T_{80}$  of  $\sim 100$  hours under similar aging conditions (14), or similar  $T_{80}$  lifetimes, but at  $25^\circ\text{C}$  in Colorado at a relative humidity of 15%, dropping to  $\sim 30$  hours at  $70^\circ\text{C}$  (12).

To explore the stability of our cells under higher elevated temperatures, we sealed them in a nitrogen atmosphere with glass cover slides and UV-cured epoxy resin and aged the encapsulated devices under full-spectrum sunlight at  $85^\circ\text{C}$  in air. Figure S29 shows the evolution of the device parameters. The  $J-V$  scans for the champion  $[\text{BMP}]^+[\text{BF}_4]^-$  device at different aging stages are shown in fig. S30. At this temperature, a clear burn-in effect was observed in the SPOs (Fig. 3C) and PCEs (Fig. 3D) for both the  $[\text{BMP}]^+[\text{BF}_4]^-$  modified and control devices. The SPO of the control devices decreased rapidly to  $<6\%$  absolute efficiency after 264 hours, whereas the modified devices retained an operational SPO of  $\sim 12\%$  absolute over the aging period. We estimated the lifetime of 1200 hours at 95% of the post-burn-in efficiency ( $T_{95,\text{ave}}$ ), using a linear extrapolation of the post-burn-in SPO (Fig. 3C) (14, 30).

Much variation in aging conditions for perovskite solar cells occurs between laboratories, so it is not feasible to compare results directly. With respect to our previous best-in-class, the  $T_{80}$  lifetime of our unencapsulated

cells at  $60^\circ\text{C}$  in this study is  $\sim 7$  times longer (14). The post-burn-in  $T_{95,\text{ave}}$  SPO lifetime of our encapsulated cells at  $85^\circ\text{C}$  was 1200 hours, three times longer than our previous best-in-class cells, which were stressed at  $75^\circ\text{C}$  and gave a  $T_{95,\text{ave}}$  of  $\sim 360$  hours (14). Considering that we would expect about a twofold increase in the degradation rate with a  $10^\circ\text{C}$  increase in temperature (31), the cells in this study appear to degrade at approximately one sixth the speed.

To elucidate the degradation mechanism in complete cells, we carried out XPS analysis on the unencapsulated device stacks, absent of electrodes, before and after a 300-hour light-soaking aging process at  $60^\circ\text{C}$ . The XPS spectra of the core levels relevant to the perovskite elements were measured, and full peak positions, spectra, and fittings can be found in figs. S31 to S33 and table S2. Subtle differences between the  $[\text{BMP}]^+[\text{BF}_4]^-$  and control devices were observed in the C 1s, N 1s core levels, but these additional peaks correspond to the presence of  $[\text{BMP}]^+[\text{BF}_4]^-$ . The I  $3d_{5/2}$  core levels for both the  $[\text{BMP}]^+[\text{BF}_4]^-$  and control devices show that aging resulted in the emergence of an additional peak at  $\sim 620$  eV next to the main peak at  $\sim 618$  eV, which is attributed to  $\text{I}^-$ . This peak at the higher binding energy could correspond to either the formation of  $\text{IO}_2^-$ , which

has been observed in methylammonium lead triiodide (32), or to the formation of methyl iodide (33).

The Pb 4f core level spectra demonstrated a clear difference between the aged devices with and without  $[\text{BMP}]^+[\text{BF}_4]^-$ . In the aged control devices, we observed two peaks at 138.0 and 139.1 eV (Pb  $4f_{7/2}$ ), whereas in the devices with  $[\text{BMP}]^+[\text{BF}_4]^-$  we only observed one peak at 137.8 eV. The peaks at  $\sim 138$  eV correspond to the presence of  $\text{Pb}^{2+}$ , while the peak at 139.1 eV corresponds to  $\text{PbO}_x$ . This result suggests that, when aged, the control devices formed lead oxide, which is a product formed from a photooxidative degradation process (34). The addition of  $[\text{BMP}]^+[\text{BF}_4]^-$  inhibited lead oxidation.

To understand how  $[\text{BMP}]^+[\text{BF}_4]^-$  can improve the stability of the perovskite film, we first review the mechanisms that have been proposed to explain the photoinduced degradation processes of metal halide perovskites. The role of oxygen and moisture has been extensively discussed, in particular for MA-containing perovskites (35–37). However, for perovskite films prepared in inert atmosphere and encapsulated, photodegradation is still observed. A key factor in the photodegradation is the generation of  $\text{I}_2$  under illumination, which has been observed experimentally



via a range of analytic methods, including electrochemistry (38), optical absorption (38), and mass spectrometry (39). The detrimental role of  $I_2$  has been established for silver electrodes (40) but also directly upon the perovskite (41).

Several mechanisms have been proposed to explain the generation of  $I_2$ . They have in common the capture of a hole by an iodide ion ( $I^-$ ), with  $I^-$  being either in its lattice site ( $I_i^x + h^+ \rightarrow I_i^\bullet$  in Kröger-Vink notation) (26, 42), as an interstitial ion from a Frenkel pair ( $I_i + h^+ \rightarrow I_i^\bullet$ ) (43), or becoming interstitial upon hole capture ( $I_i^x + h^+ \rightarrow I_i^\bullet + V_i^\bullet$ ) (38). To generate gaseous iodine ( $I_2$ ), two neutral atoms ( $I_i^\bullet$  or  $I_i^\bullet$ ) need to diffuse and combine. Owing to the ability to release iodine from the surface of the film, and the likelihood of a higher vacancy density at the surface than in the bulk of the grains, this process is more likely to happen at the surface of the grains, leading to the release of iodine and the generation of a pair of iodide vacancies ( $2V_i^\bullet$ ).

The exact nature of the detrimental effect of  $I_2$  on the perovskite is still under debate (41). Fu *et al.* investigated these effects in detail and found that  $PbI_2$  was more prone to degradation than the perovskite itself and that voids were left in the films of  $PbI_2$  upon prolonged exposure to light and heat (44). We repeated Fu *et al.*'s experiments for the photodegradation of  $PbI_2$  at elevated temperatures under light in a nitrogen atmosphere (figs. S34 and S35) and confirmed the observed generation of lead (fig. S36) and pinholes in the films (Fig. 4, A and B). Although slower than for  $MA^{+}$ -containing perovskites, this degradation pathway was also observed in FACs perovskites, indicating that the  $I_2$  generation process is related to the lead-halide framework.

We confirmed a faster release of  $I_2$  from our control perovskite films versus the  $[BMP]^+ [BF_4]^-$  modified films during light soaking, from UV-vis absorption spectrum of toluene, after exposing toluene-submersed films to light and heat (Fig. 4, C to G) (38, 41). The presence of voids (or pinholes, Fig. 4B) in the  $PbI_2$  films (and control perovskite films, fig. S26) after aging can be explained by the loss of volume during  $I_2$  release, upon conversion to metallic lead. The presence of  $PbO_x$  in the degraded unencapsulated devices (fig. S32) is also consistent with the formation of metallic lead, with subsequent oxidation to  $PbO_x$  or  $Pb(OH)_2$  in ambient air, which both have a much higher density than the perovskite.

In light of this degradation mechanism, we discuss the stabilization induced by the ionic additive. For degradation to occur, hole-trapping is likely to require interstitial  $I^-$  (43), and two neutral interstitial iodine atoms need to diffuse together and combine to form  $I_2$ . Therefore, this reaction could be slowed by either reducing the overall density of Frenkel defects (iodide

vacancies and/or interstitial pairs) or by reducing the diffusivity of interstitials. As with most crystalline materials, defect densities are usually highest on the crystal surface (45). Therefore, we would expect the interstitials or Frenkel defects to mostly diffuse around the surfaces of the polycrystalline domains, where the highest density of defects exists.

If crystallization in the presence of  $[BMP]^+ [BF_4]^-$  leads to reduced Frenkel defect densities, then this would have the effect of reducing the number of sites available for iodide oxidation. Furthermore, if  $[BMP]^+ [BF_4]^-$  adsorbs to these surface defects, it is likely to block or inhibit the further migration of such defects, slowing down the diffusivity of interstitial iodide or neutral iodine interstitials, reducing the rate of  $I_2$  formation. Finally,  $[BMP]^+ [BF_4]^-$  does appear to reduce the amount of residual  $PbI_2$  in the films, by improving the crystallization (as indicated in Fig. 2). Because  $I_2$  generation occurs preferentially at  $PbI_2$  sites (44), minimizing the amount of residual  $PbI_2$  may play a crucial role.

## REFERENCES AND NOTES

- W. Chen *et al.*, *Adv. Mater.* **30**, e1800515 (2018).
- T. Leijtens, K. A. Bush, R. Prasanna, M. D. McGehee, *Nat. Energy* **3**, 828–838 (2018).
- The National Renewable Energy Laboratory, Best Research-Cell Efficiency Chart; [www.nrel.gov/pv/cell-efficiency.html](http://www.nrel.gov/pv/cell-efficiency.html).
- S. N. Habisreutinger, D. P. McMeekin, H. J. Snaith, R. J. Nicholas, *APL Mater.* **4**, 091503 (2016).
- D. P. McMeekin *et al.*, *Science* **351**, 151–155 (2016).
- G. E. Eperon *et al.*, *Energy Environ. Sci.* **7**, 982–988 (2014).
- J.-W. Lee *et al.*, *Adv. Energy Mater.* **5**, 1501310 (2015).
- M. Saliba *et al.*, *Energy Environ. Sci.* **9**, 1989–1997 (2016).
- Q. Jiang *et al.*, *Nat. Photonics* **13**, 460–466 (2019).
- S. N. Habisreutinger *et al.*, *Nano Lett.* **14**, 5561–5568 (2014).
- Y. Hou *et al.*, *Science* **358**, 1192–1197 (2017).
- J. A. Christians *et al.*, *Nat. Energy* **3**, 68–74 (2018).
- S. N. Habisreutinger, N. K. Noel, H. J. Snaith, R. J. Nicholas, *Adv. Energy Mater.* **7**, 1601079 (2017).
- S. Bai *et al.*, *Nature* **571**, 245–250 (2019).
- S. H. Turren-Cruz, A. Hagfeldt, M. Saliba, *Science* **362**, 449–453 (2018).
- E. Köhnen *et al.*, *Sustain. Energy Fuels* **3**, 1995–2005 (2019).
- L. Mazzarella *et al.*, *Adv. Energy Mater.* **9**, 1803241 (2019).
- M. T. Hörantner, H. J. Snaith, *Energy Environ. Sci.* **10**, 1983–1993 (2017).
- R. J. Sutton *et al.*, *ACS Energy Lett.* **3**, 1787–1794 (2018).
- S. Govinda *et al.*, *J. Phys. Chem. C* **122**, 13758–13766 (2018).
- W. Rehman *et al.*, *Energy Environ. Sci.* **10**, 361–369 (2017).
- Z. Li *et al.*, *Chem. Mater.* **28**, 284–292 (2016).
- C. Yi *et al.*, *Energy Environ. Sci.* **9**, 656–662 (2016).
- K. A. Bush *et al.*, *ACS Energy Lett.* **3**, 1225–1232 (2018).
- D. W. deQuilettes *et al.*, *Nat. Commun.* **7**, 11683 (2016).
- J. S. W. Godding *et al.*, *Joule* **3**, 2716–2731 (2019).
- K. A. Bush *et al.*, *Nat. Energy* **2**, 17009 (2017).
- M. Kaltenbrunner *et al.*, *Nat. Mater.* **14**, 1032–1039 (2015).
- R. Prasanna *et al.*, *Nat. Energy* **4**, 939–947 (2019).
- M. V. Khenkin *et al.*, *Nat. Energy* **5**, 35–49 (2020).
- H. J. Snaith, P. Hacke, *Nat. Energy* **3**, 459–465 (2018).
- G. Rajendra Kumar *et al.*, *Phys. Chem. Chem. Phys.* **18**, 7284–7292 (2016).
- X. L. Zhou, F. Solymosi, P. M. Blass, K. C. Cannon, J. M. White, *Surf. Sci.* **219**, 294–316 (1989).
- Y. X. Ouyang *et al.*, *J. Mater. Chem. A* **7**, 2275–2282 (2019).
- R. Brenes, C. Eames, V. Bulović, M. S. Islam, S. D. Stranks, *Adv. Mater.* **30**, e1706208 (2018).
- Z. Andaji-Garmaroudi, M. Anaya, A. J. Pearson, S. D. Stranks, *Adv. Energy Mater.* **10**, 1903109 (2020).
- N. Aristidou *et al.*, *Nat. Commun.* **8**, 15218 (2017).
- G. Y. Kim *et al.*, *Nat. Mater.* **17**, 445–449 (2018).
- Z. N. Song *et al.*, *Sustain. Energy Fuels* **2**, 2460–2467 (2018).
- Y. Kato *et al.*, *Adv. Mater. Interfaces* **2**, 1500195 (2015).
- S. Wang, Y. Jiang, E. J. Juarez-Perez, L. K. Ono, Y. Qi, *Nat. Energy* **2**, 16195 (2016).
- J. Verwey, J. Schoonman, *Physica* **35**, 386–394 (1967).
- S. G. Motti *et al.*, *Nat. Photonics* **13**, 532–539 (2019).
- F. Fu *et al.*, *Energy Environ. Sci.* **12**, 3074–3088 (2019).
- A. Pimpinelli, J. Villain, *Physics of Crystal Growth* (Cambridge Univ. Press, 2010).

## ACKNOWLEDGMENTS

Y.-H.L. thanks N. Noel and W. Li from the University of Oxford (UK) for the discussion on the effect of ionic molecules on perovskites and for assisting with ssNMR sample preparation and optical microscopic imaging, respectively. J. Liu acknowledges the assistance of J. Marrow from the University of Oxford (UK), who provided access to the Avizo software packages to perform 3D virtualization of the nanoSIMS data. **Funding:** This work was supported by the U.K. Engineering and Physical Sciences Research Council (EPSRC) grants EP/S004947/1 and EP/P006329/1. J. Liu and C.R.M.G. are grateful for support for the nanoSIMS facility from EPSRC under grant EP/M018237/1. S.M. is grateful for the support of the Rhodes Scholarship (India and Worcester). R.D.J.O. gratefully acknowledges the Penrose Scholarship for funding his studentship. **Author contributions:** Y.-H.L. and H.J.S. conceived of the concept, designed the experiments, analyzed the data, and wrote the manuscript. H.J.S. supervised and guided the project. Y.-H.L. performed the fabrication, optimization, and characterization of the perovskite films and solar cells. Y.-H.L. conducted optical microscopy measurements. Y.-H.L. and N.S. conducted UV-vis, XRD, and FTIR characterization and analysis. N.S. performed SEM characterization and material analysis. P.D. and S.B. screened ionic additives and conducted early assessments for single-junction cells. Y.-H.L. and P.D. performed cell thermal-stability measurement on p-type layers. J.W. conducted CE, TPV, and TPC and analyzed the data with J.R.D. H.C.S. conducted analysis on XRD results to deduce degradation mechanism with Y.-H.L. and N.S. A.J.R. performed XPS characterization and analyzed the data with Y.-H.L. and N.S. S.M. performed numerical modeling. J. Liu conducted nanoSIMS characterization and analyzed the results with Y.-H.L., P.K.N., and C.R.M.G. R.D.J.O. conducted EQE measurements and analyzed the data with M.B.J. J. Lim conducted ip-TPC characterization. L.A. and J.G.L. performed TRMC characterization. K.S. and P.K.M. performed ssNMR and analyzed the data with P.K.N. A.B.M.-V. and B.S. contributed to the planning of the experiments to tune the bandgap of the perovskite solar cells and optical modeling. B.W. contributed to degradation mechanism analysis. J.M.B. set up  $N_2$  aging system, characterized the EQE spectrum of aged devices, and evaluated spectrum mismatch factors. Y.-H.L. analyzed the data with H.J.S. F.G. provided suggestions for ionic additives. All authors discussed the results and contributed to the writing of the paper. **Competing interests:** H.J.S. is a cofounder, chief scientific officer, and a director of Oxford PV Ltd. Oxford University has filed a patent related to the subject matter of this manuscript. **Data and materials availability:** All data needed to evaluate the conclusions of the paper are present in the paper or the supplementary materials.

## SUPPLEMENTARY MATERIALS

[science.sciencemag.org/content/369/6499/96/suppl/DC1](https://science.sciencemag.org/content/369/6499/96/suppl/DC1)  
Materials and Methods  
Supplementary Text  
Figs. S1 to S36  
Tables S1 to S2  
References (46–80)

10 November 2019; accepted 5 May 2020  
10.1126/science.aba1628

## HIV

# Number of HIV-1 founder variants is determined by the recency of the source partner infection

Ch. Julián Villabona-Arenas<sup>1,2</sup>, Matthew Hall<sup>3</sup>, Katrina A. Lythgoe<sup>3</sup>, Stephen G. Gaffney<sup>4</sup>, Roland R. Regoes<sup>5</sup>, Stéphane Hué<sup>1,2</sup>, Katherine E. Atkins<sup>1,2,6\*</sup>

During sexual transmission, the high genetic diversity of HIV-1 within an individual is frequently reduced to one founder variant that initiates infection. Understanding the drivers of this bottleneck is crucial to developing effective infection control strategies. Little is known about the importance of the source partner during this bottleneck. To test the hypothesis that the source partner affects the number of HIV founder variants, we developed a phylodynamic model calibrated using genetic and epidemiological data on all existing transmission pairs for whom the direction of transmission and the infection stage of the source partner are known. Our results suggest that acquiring infection from someone in the acute (early) stage of infection increases the risk of multiple-founder variant transmission compared with acquiring infection from someone in the chronic (later) stage of infection. This study provides the first direct test of source partner characteristics to explain the low frequency of multiple-founder strain infections.

**S**exual transmission of HIV-1 results in a viral diversity bottleneck due to physiological barriers as well as viral or cellular constraints that prevent most genetic variants within the source partner from establishing onward infection (1–3). Indeed, this diversity bottleneck results in around three-quarters of new infections being founded by a single genetic variant (4–9). The extent of genetic diversity transmitted to a new partner is a crucial determinant in understanding the efficacy of putative vaccines and may shed light on the transmission of drug resistance to treatment-naïve individuals.

The factors leading to the diversity bottleneck during sexual transmission can be broadly categorized as those determined by the source partner, such as viral load and viral diversity available for transmission (10); those determined by the recipient partner, such as target cell type and availability in the genital or rectal mucosa [e.g., (3, 11, 12)]; and those connected with viral characteristics, such as glycosylation profiles and cell tropism [reviewed in (13)]. Whereas the impact of the recipient partner and the characteristics of transmitted founder variants have been widely discussed, little is known about how the source partner affects the viral diversity bottleneck. Modeling work suggests that the infection stage of the source partner at the point of onward trans-

mission may be a key driver in determining the number of transmitted variants (14). However, there is currently no empirical evidence to suggest how the infection stage of the source partner influences the viral diversity bottleneck. This gap has arisen because studies are routinely conducted without information on the partner from whom infection was acquired. Phylogenetic analyses now offer a possible solution to this impasse.

Phylogenetic trees are representations of the ancestral relationships of organisms, with the tips of the tree representing those that are sampled, the internal nodes representing their inferred common ancestors, and the branches the evolutionary pathways between these actual and inferred individuals. When phylogenetic trees are constructed using sequence data from both partners in an HIV transmission pair, the relationship between the evolutionary histories of both sets of viral samples may reflect epidemiological relationships between the two individuals (15–17). Previous modeling studies have suggested that the evolutionary histories of the viral populations in both partners can provide important information, such as the direction of transmission (15) and the number of transmitted founder variants (18). For such histories, each putative transmission pair can be classified into one of three “topology classes” that define the evolutionary relationship between the viral populations of the two partners: monophyletic-monophyletic (MM, where the sequences from each partner form separate groups), paraphyletic-monophyletic (PM, where the sequences from one partner are embedded in the sequences from the second partner), or a combination of paraphyletic and polyphyletic (PP, where sequences from both partners are interspersed) (Fig. 1A). The number of monophyletic clusters in a PM (one) or PP (more than one) tree can be interpreted as the minimum number of transmitted founder

variants. In practice, however, many factors may influence epidemiological interpretations from phylogenetic trees, such as sampling times, sampling density of the viral populations, and phylogenetic signal (19, 20).

Here, we present a data-driven phylodynamic approach to overcome these empirical and methodological issues to evaluate the impact of the source partner’s infection stage and route of exposure on the HIV diversity bottleneck (Fig. 1, B and C). We first retrieved all available genetic and epidemiological information from published HIV sexual transmission pairs where the direction of transmission is known, and we kept for further analysis those pairs for whom transmission could be classified as having occurred in the source partner’s acute stage ( $\leq 90$  days after his/her infection) or chronic stage (later than 90 days after his/her infection). After further stratifying pairs into heterosexual (HET) and men who have sex with men (MSM) risk groups, we found a significant difference in the timing of transmission between the two risk groups. Specifically, 10 of 36 MSM pairs were the result of acute-stage transmission, compared with 1 of 76 HET pairs (Fig. 2).

We then performed Bayesian phylogenetic tree reconstruction on the genetic sequences of the transmission pairs and classified the topology class of each tree in the posterior distribution as MM, PM, or PP. The most likely topology class was PM (65% and 61% for HET and MSM, respectively), but with a higher number of PP trees in the MSM group ( $P = 0.056$ ) (Fig. 2). This result has previously been described as indicative of a higher number of founder variants for MSM (18). However, when we stratified the topology class by whether the source partner was in the acute or chronic stage of infection at the time of transmission, our results indicate that the infection stage of the source is the primary driver for any observed differences in topology class. Specifically, there is no difference between the HET and MSM groups in the PM/PP topology class ratio when transmission occurs in the chronic stage of infection ( $P = 0.570$ ). Note that only one HET transmission occurred during the acute stage, and the topology class for this pair is PP. These results remained qualitatively consistent when we analyzed data only from the 66% of transmission pairs for whom the posterior trees gave a certainty of over 95% for the most frequent topology class (fig. S3). These results indicate that infection stage of the source partner, and not risk group per se, may influence the diversity bottleneck at transmission.

To test whether these empirical findings are indicative of a smaller diversity bottleneck in the chronic stage of HIV infection, we developed a phylodynamic framework in which we simulated the epidemiological characteristics of each HET and MSM transmission pair, the

<sup>1</sup>Department of Infectious Disease Epidemiology, Faculty of Epidemiology and Population Health, London School of Hygiene and Tropical Medicine, London, UK. <sup>2</sup>Centre for Mathematical Modelling of Infectious Diseases, London School of Hygiene and Tropical Medicine, London, UK. <sup>3</sup>Big Data Institute, Nuffield Department of Medicine, University of Oxford, Oxford, UK. <sup>4</sup>Department of Biostatistics, Yale School of Public Health, New Haven, CT, USA. <sup>5</sup>Institute of Integrative Biology, Department of Environmental Systems Science, ETH Zurich, Zurich, Switzerland. <sup>6</sup>Centre for Global Health, Usher Institute of Population Health Sciences and Informatics, University of Edinburgh, Edinburgh, UK.

\*Corresponding author. Email: katherine.atkins@ed.ac.uk



**Fig. 1. Methods schematics.**  
(A) Phylogenetic tree topology classes of known transmission pairs previously used as proxies for calculating the minimum number of founder variants transmitted to the recipient. Trees of both MM and PM classes suggest a minimum of one founder variant, whereas trees of class PP suggest multiple founder variants, with the minimum number of founder variants being the number of recipient clades embedded in PP trees (here shown as two). (B) Pipeline of phylodynamic analysis (LANLdb, Los Alamos National Laboratory HIV Sequence Database), where teal represents data or analysis output and white represents methods and analysis. An example of a standardized transmission timeline for a known source-recipient pair is provided in (C). (C) Schematic of the transmission pair model simulation that shows the transmission and sampling timelines. The simulated number of virus particles transmitted to the index case and the source and recipient partners ( $n_I$ ,  $n_S$ , and  $n_R$ , respectively) are shown on the transmission events timeline.

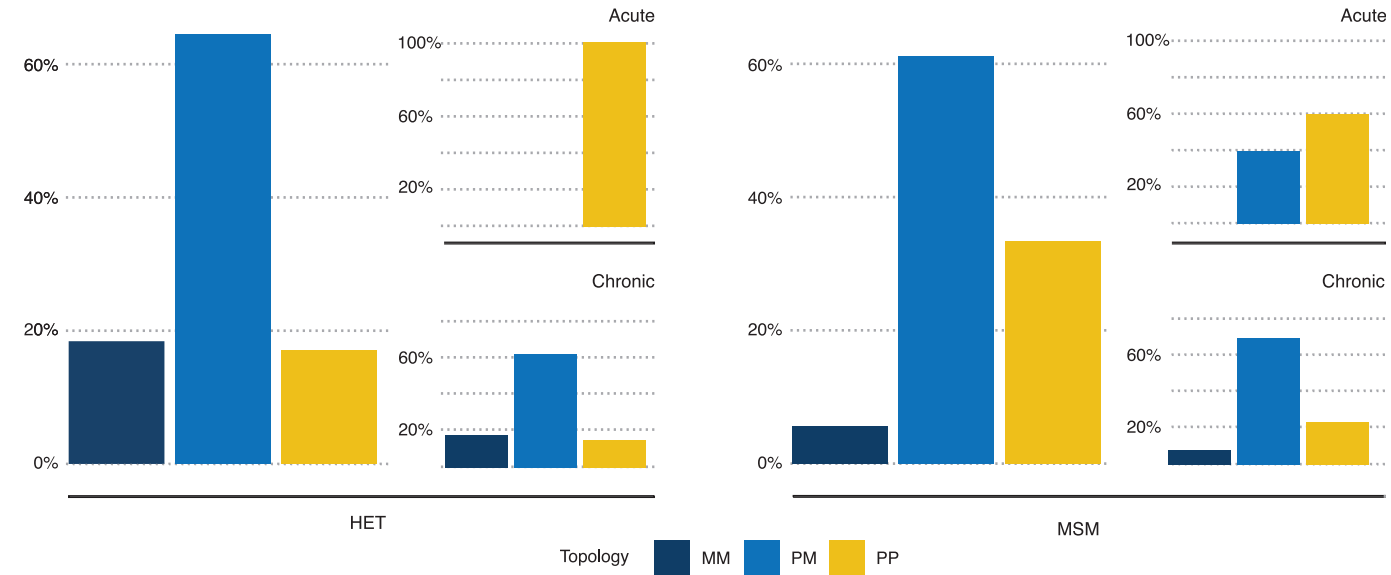


**Fig. 2. Phylogenetic findings from the empirical transmission pairs.** Percentages of phylogenetic tree topology classes (MM, PM, and PP), where each tree topology class is classified as the most frequent topology class of each posterior distribution per transmission pair. Results are stratified by risk group (76 HET pairs and 36 MSM pairs) and infection stage of the source partner at transmission (11 acute pairs defined as  $\leq 90$  days after infection and 101 chronic pairs defined as  $> 90$  days after infection).

timing of the virus sampling, the transmission of virus particles, and the within-host genetic evolution in both the source and recipient (Fig. 1B). Specifically, using the epidemiological information from the transmission pairs, we simulated phylogenies under a coalescent model before generating genetic sequences from these simulations and performing maximum likelihood (ML) phylogenetic reconstruction on these simulated sequences. We classified each of these simulated trees as MM, PM, or PP and determined the frequency of each topology class (i.e., the fraction of simulated trees classified as MM, PM, and PP) for each simulated transmission pair across all the simulated sequences. However, as we could not directly observe the number of virus particles that were transmitted between source and recipient, we repeated the simulation of phylogenetic trees for each transmission pair under a range of plausible virus particle numbers transmitted. By fitting the simulation output topology class frequencies to the topology class distribution from the empirical phylogenetic trees using maximum likelihood inference, we then determined the most likely number of transmitted virus particles for each transmission pair and used this best-fit model for further analysis. Note that two or more virus particles may have the same genetic sequence and would constitute a single founder variant (or haplotype), as discussed below. Further, because the analysis is conditioned

on extant lineages, we use the term “founder variants” to describe those transmitted variants for which we found detectable viral lineages; thus, we ignored variants that were transmitted but whose lineages had become extinct.

Our fitting procedure selected a best-fit model that clearly delineated transmission pairs between whom one virus particle was transmitted (75% of pairs) and those between whom more than one virus particle was transmitted (25% of pairs) (Fig. 3A). Although there is a high degree of confidence in the result when one particle was transmitted, there is often uncertainty around the exact number when multiple particles were transmitted (Fig. 3A). We found that acute-stage transmissions are more likely to lead to multiple-particle infections than are chronic-stage transmissions (73% versus 20%;  $P = 0.0005$ ). The topology class of the simulated phylogenetic trees is strongly influenced by the number of virus particles transmitted (Fig. 3B). PM trees were more commonly found in the pairs that were better described by a model with a single transmitted virus particle (81%), whereas PP trees appeared more often when multiple particles were likely to have been transmitted (86%).

For each transmission pair, we then simulated the genetic sequences of the transmitted viral population under the best-fit virus particle model and calculated the most likely number of founder variants for each transmission pair (i.e., the number of distinct haplotypes).

The median number of founder variants transmitted across all pairs was 1 (range, 1 to 11) (Fig. 4A). Using the full distribution of the number of transmitted founder variants for each pair, we also calculated the probability that a single founder variant was transmitted to the respective recipient. Our results suggest that across all pairs in both risk groups, the mean probability of observing one founder variant is 0.73. Stratifying by risk group, we found that there is a higher probability that one founder variant founds HET infections than MSM infections (a mean of 0.83 versus 0.69) (Fig. 4B). However, these risk group differences mostly disappear when we stratify the results by the infection stage of the source. For example, when only chronic-stage transmissions are considered, there is no difference in the probability of one founder variant for MSM transmissions versus HET transmissions (means of 0.84 versus 0.76;  $P = 0.398$ ), and the pairwise diversity at transmission is similar between both groups (Fig. 4C). By contrast, when we stratified solely by infection stage of the source partner, we found that transmission during the acute stage had a much lower probability of one founder variant than during the chronic stage (means of 0.44 versus 0.82), with a higher median number of founder variants transmitted, when only the most likely number of founder variants for each pair was considered (two versus one) (Fig. 4A). Nonetheless, if multiple-founder variant transmission does occur, our results suggest that the

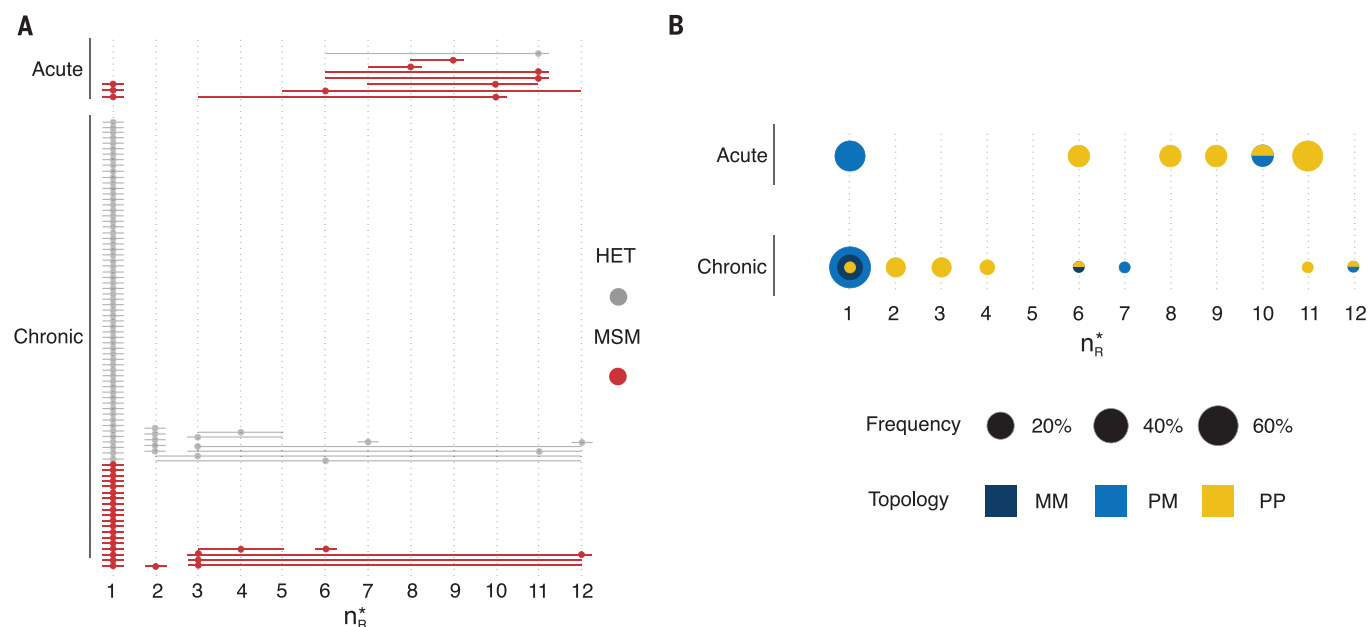


**Fig. 3. Estimated numbers of transmitted virus particles for the 112 transmission pairs.** The estimates of transmitted virus particles for each transmission pair were calculated by choosing the model simulation that generated a phylogenetic tree topology class distribution (i.e., the number of MM, PM, and PP trees constructed from the simulated genetic sequences) that best matched the topology class distribution from the phylogenetic trees constructed from

the empirical genetic sequences. **(A)** Maximum likelihood number of virus particles founding recipient infections,  $n_R^*$ , for each pair (stacked points) with 95% confidence intervals (lines) grouped by stage of infection (acute, 11 pairs; chronic, 101 pairs) and risk group (76 HET and 36 MSM). **(B)** Maximum likelihood number of virus particles founding recipient infections, colored by topology class, of the phylogenetic tree constructed from the simulated genetic sequences.



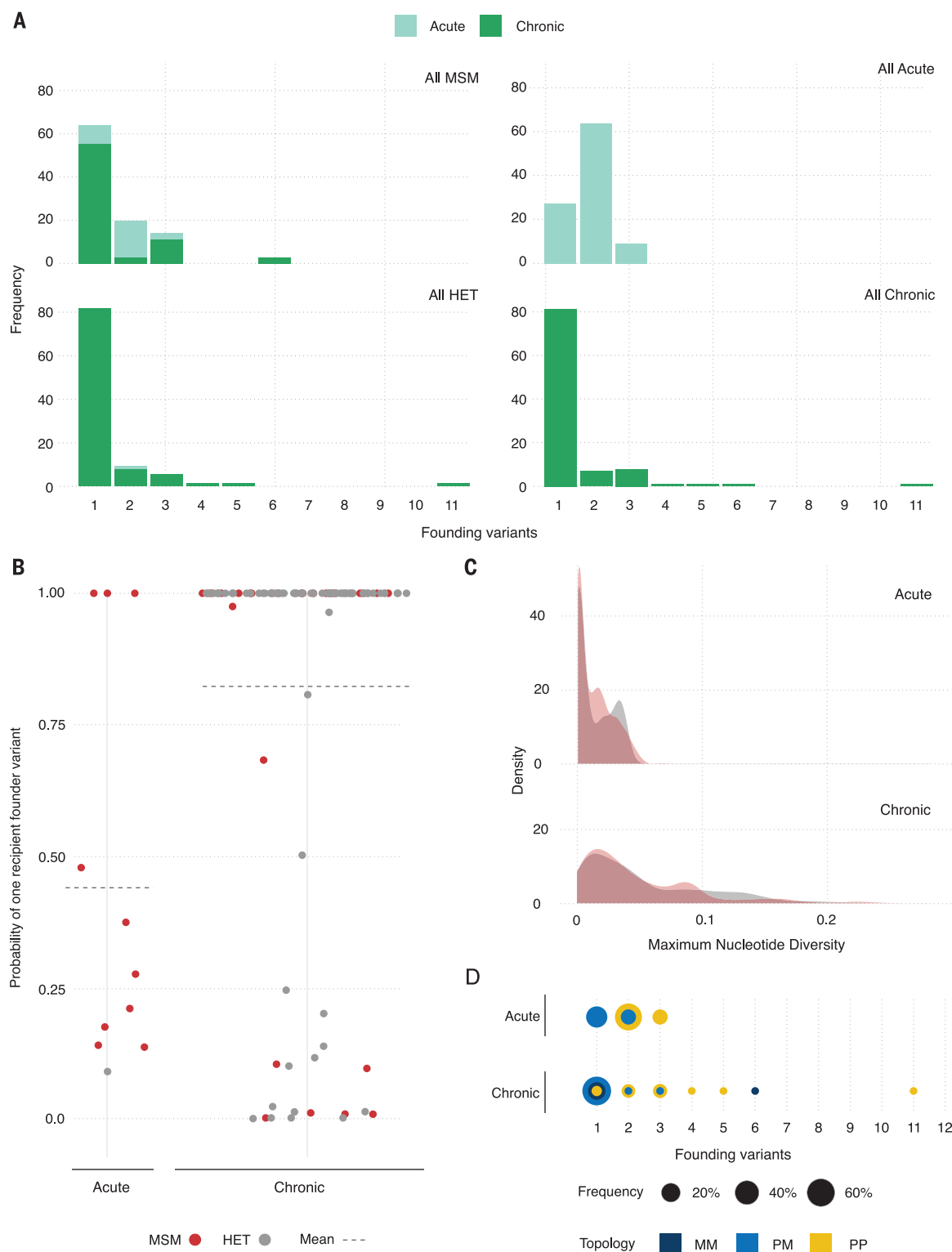


**Fig. 4. Phylogenetic findings from the calibrated simulations.** (A) Frequency of number of transmitted founder variants for transmission pairs either by risk group (left) or by infection stage of source partner at transmission (right). The number of multiple founder variants is calculated as the modal simulated value. (B) Probability of one founder variant in the recipient for each pair stratified by infection stage of the source partner at

transmission. (C) Probability density distribution of maximum diversity (proportion of sites that differ) in the recipient partner across all simulations with more than one haplotype stratified by infection stage of the source at transmission. (D) Number of founder variants, colored by topology class, of the phylogenetic tree constructed from the best-fit model of the simulated genetic sequences.

number of founder variants is higher during chronic-stage transmission, consistent with the higher diversity measured during this later stage of infection (Fig. 4C).

From these results, therefore, there is approximately double the chance of multiple-founder variant transmission during acute-stage infection across both risk groups (relative risk = 0.54). When we assumed that transmission risk is weighted toward early transmission such that half of all index case-to-source partner transmissions occur after 90 days of index case infection, this leads to qualitatively similar results (supplementary materials). Similarly, calibrating the simulation model to bootstrapped samples rather than Bayesian posterior distributions leads to similar results (supplementary materials).

Our results suggest that there is an association between tree topology class and multiple-founder variant transmission, with 95% of MM and PM trees being due to one founder variant (Fig. 4D). However, the number of embedded recipient clades is not always a proxy for the minimum number of founder variants transmitted. For example, in chronic-stage transmission, 11% of PP topology class trees were due to single-founder variant transmission (Fig. 4D). We stress that a PP topology class outcome not only may occur as a result of multiple genetically distinct virus populations founding recipient infections but also may reflect a lack of phylogenetic signal in the data; for instance, the sampled sequence lengths that gave rise to PP trees were on average shorter than those for MM ( $P = 0.096$ ) and PM ( $P = 0.004$ ). Across both infection stages, we found that if MM, PM, or PP was assigned as the most likely tree topology class, then 92, 96, and 15% of transmissions, respectively, were due to a single founder variant.

We have used a combination of empirical data and phylodynamic model simulation to evaluate the role of infection stage at transmission and route of transmission on the number of virus variants transmitted during sexual HIV exposure. This has allowed three important advances on previous work. First, it is the first empirically based study that fits a model to data to understand the role of the source partner in multiple-founder variant transmission. Second, although we have used a previously developed topology classification of phylogenetic trees to understand HIV transmission pairs, we have extended this methodology by calibrating a phylodynamic model to empirical data. This new approach provides a means to validate the previously untested assumption that the number of embedded recipient partner lineages in a phylogenetic tree directly corresponds to the minimum number of founder variants transmitted. Third, our phylodynamic model explicitly incorporates virus particle number and the identity of genetic sequences. This

advance produces results that contrast with previous work, which showed that the number of founder variants had little impact on the topology class of the phylogenetic tree when only overall genetic diversity, rather than sequence identity, was tracked (15).

The relative importance of acute and chronic stages of HIV infection in determining both the number of virus particles and the number of founder variants transmitted is consistent with results from a recent modeling study (14). However, our study found higher proportions of infections initiated by multiple founder variants overall during these two stages. This difference is likely due to the assumptions related to how the stages of infection are defined as well as the relative importance of transmission during late infection. Specifically, the previous modeling study found that two-thirds of multiple-founder variant transmission occurs during the pre-AIDS stage of infection, which is assumed to involve both a high viral load and high haplotype diversity. If later stages of infection account for disproportionately less transmission, then the previous model would predict higher proportions of multiple-founder variant transmission in both the acute and chronic stages of infection, and this would be more consistent with empirical estimates from our analysis. By contrast, our study is agnostic about the relative importance of early and late transmission and does not differentiate between the chronic and a pre-AIDS stage of infection, which cannot easily be identified through analysis of empirical data.

Data from four of the MSM transmission pairs in this study have previously been used to estimate the number of variants founding infection with a combination approach of single-genome amplification (SGA), direct amplicon sequencing, and mathematical modeling (7). Our results broadly agree with this previous analysis, with both analyses suggesting that two recipients were infected with one founder variant and one recipient was infected with multiple founder variants (our analysis suggests a mean of two to three founder variants, and the previous analysis suggested three founder variants). There was disagreement with results from a fourth recipient, for whom a single founder variant was 13% probable in this study (with a mode of two founder variants) but considered the most likely outcome in the previous analysis. Small differences between the two studies likely arise because our study used sequence data from both partners to evaluate the transmission of multiple founder variants to the recipient partner. These extra data can be used to parameterize a mathematical model that accounts for the evolutionary relationship between the virus samples from both partners, rather than relying solely on accumulating diversity. Specifically, neglecting the extent of genetic similarity be-

tween the source and recipient virus samples might misattribute borderline cases of diversity accumulation.

Our study finds a median of 1 founder variant and a maximum of 11, with little difference between HET and MSM risk groups. When only multiple-founder variant transmissions are considered, our study finds a median of two to three founder variants. These values are consistent with a previous pooled analysis based on results from four analyses that used the current gold standard SGA combination approach (9), as described above.

At present, the genetic determinants of HIV-1 disease progression are not clear. However, even small differences between genotypes can have important clinical outcomes. For instance, single polymorphisms can affect replication capacity (21) or can lead to primary non-nucleoside reverse transcriptase inhibitor resistance with different amino acid changes at the same position conferring equivalent levels of resistance (22).

Previous studies have disagreed over the extent to which the elevated risk of transmission during the acute stage of infection [reviewed in (23)] is driven by increased viral load, elevated per particle transmission probability, or other behavioral factors, such as high rates of sex partner change or concurrent partnerships (24–29). Here, although we find strong evidence to support the fact that acute-stage transmissions are characterized by more virus particles and variants founding infection, this result alone cannot disentangle virus- and host-related drivers of elevated transmission. For example, the higher number of variants being transmitted during acute infection could arise if the number of transmissible variants declines as infection progresses or because there are more opportunities for multiple variants to found infection due to increased viral load (14, 30). However, our study can shed light on the eight-fold increased per-exposure risk of infection that has been found for MSM transmission relative to HET transmission (31, 32). In particular, the lack of differences in both the number of virus particles and the number of founder variants that establish infection after transmission from a chronically infected source in HET and MSM suggest that the observed heightened acquisition risk for MSM could in part be due to sampled MSM individuals being more likely to be in the acute stage at the time of transmission (14, 27). Whether MSM partners are more likely to be sampled earlier in infection because of sampling procedures or because MSM are indeed more likely to transmit during early infection is unclear. Although this observation raises the possibility that the role of sexual risk group in itself may have less of an impact on the transmission of multiple-founder variant probability, from a pragmatic perspective, if more MSM infections are indeed



caused by acute-stage transmissions, then the evolutionary and epidemiological impacts on public health will be the same irrespective of the mechanism.

There are two primary limitations to acknowledge. First, our model assumes a single transmission event between each source and recipient partner. Without detailed knowledge of the transmission pairs, we cannot distinguish between multiple infections each with a single founder variant and a single infection with multiple founder variants; if for some pairs the former were true, then this might suggest an elevated transmission rate during the acute stage, as has been observed previously (28, 29). Second, our phylodynamic framework does not account for the effects of selection and recombination. Specifically, selection, such as that for viruses that use the CCR5 co-receptor (33), is thought to occur at the point of transmission, although the strength may be dependent on the route of transmission (34).

Our study finds that the transmission of multiple HIV-1 founder variants is determined by infection stage of the source partner, with transmission of more founder variants of HIV-1 in acute infection than in chronic infection. These findings stress that epidemiological or clinical analysis of known transmission pairs should account for potential mediation by stage of transmission when evaluating the effect of sexual risk group.

## REFERENCES AND NOTES

1. J. L. Geoghegan, A. M. Senior, E. C. Holmes, *Proc. Biol. Sci.* **283**, 20160727 (2016).
2. S. M. Kariuki, P. Selhorst, K. K. Arien, J. R. Dorfman, *Retrovirology* **14**, 22 (2017).
3. K. Talbert-Slagle *et al.*, *PLOS Pathog.* **10**, e1004092 (2014).
4. B. F. Keele *et al.*, *Proc. Natl. Acad. Sci. U.S.A.* **105**, 7552–7557 (2008).
5. J. F. Salazar-Gonzalez *et al.*, *J. Virol.* **82**, 3952–3970 (2008).
6. M.-R. Abrahams *et al.*, *J. Virol.* **83**, 3556–3567 (2009).
7. H. Li *et al.*, *PLOS Pathog.* **6**, e1000890 (2010).
8. S. Gnanakaran *et al.*, *PLOS Pathog.* **7**, e1002209 (2011).
9. D. C. Tully *et al.*, *PLOS Pathog.* **12**, e1005619 (2016).
10. K. A. Lythgoe, C. Fraser, *Proc. Biol. Sci.* **279**, 3367–3375 (2012).
11. B. F. Keele, J. D. Estes, *Blood* **118**, 839–846 (2011).
12. L. R. McKinnon, R. Kaul, *Curr. Opin. HIV AIDS* **7**, 195–202 (2012).
13. M. Sagar, *J. Infect. Dis.* **210** (suppl. 3), S667–S673 (2014).
14. R. N. Thompson *et al.*, *Virus Evol.* **5**, vey038 (2019).
15. E. O. Romero-Severson, I. Bulla, T. Leitner, *Proc. Natl. Acad. Sci. U.S.A.* **113**, 2690–2695 (2016).
16. O. Ratmann *et al.*, *Nat. Commun.* **10**, 1411 (2019).
17. C. Wymant *et al.*, *Mol. Biol. Evol.* **35**, 719–733 (2018).
18. T. Leitner, E. Romero-Severson, *Nat. Microbiol.* **3**, 983–988 (2018).
19. R. Rose *et al.*, *J. Infect. Dis.* **220**, 1406–1413 (2019).
20. A. B. Abecasis, M. Pingarilho, A.-M. Vandamme, *AIDS* **32**, 543–554 (2018).
21. D. B. A. Ojwach *et al.*, *J. Virol.* **92**, e00811-18 (2018).
22. R. W. Shafer, J. M. Schapiro, *AIDS Rev.* **10**, 67–84 (2008).
23. W. C. Miller, N. E. Rosenberg, S. E. Rutstein, K. A. Powers, *Curr. Opin. HIV AIDS* **5**, 277–282 (2010).
24. E. M. Volz *et al.*, *PLOS Med.* **10**, e1001568, discussion e1001568 (2013).
25. J. P. Hughes *et al.*, *J. Infect. Dis.* **205**, 358–365 (2012).
26. R. H. Gray *et al.*, *Lancet* **357**, 1149–1153 (2001).
27. T. D. Hollingsworth, R. M. Anderson, C. Fraser, *J. Infect. Dis.* **198**, 687–693 (2008).
28. S. E. Bellan, J. Dushoff, A. P. Galvani, L. A. Meyers, *PLOS Med.* **12**, e1001801 (2015).
29. T. D. Hollingsworth, C. D. Pilcher, F. M. Hecht, S. G. Deeks, C. Fraser, *J. Infect. Dis.* **211**, 1757–1760 (2015).
30. K. A. Lythgoe, A. Gardner, O. G. Pybus, J. Grove, *Trends Microbiol.* **25**, 336–348 (2017).
31. M.-C. Boily *et al.*, *Lancet Infect. Dis.* **9**, 118–129 (2009).
32. R. F. Baggaley, R. G. White, M.-C. Boily, *Int. J. Epidemiol.* **39**, 1048–1063 (2010).
33. M. Beretta *et al.*, *AIDS* **32**, 1917–1926 (2018).
34. J. M. Carlson *et al.*, *Science* **345**, 1254031 (2014).
35. Ch. J. Villabona Arenas, K. Atkins, S. Gaffney, AtkinsGroup/TransmissionPairs, Version v1.0, Zenodo (10 May 2020); <http://doi.org/10.5281/zenodo.3819343>.

## ACKNOWLEDGMENTS

**Funding:** C.J.V.-A. and K.E.A. were funded by an ERC Starting Grant (award number 757688) awarded to K.E.A. K.A.L. was supported by The Wellcome Trust and The Royal Society grant no. 107652/Z/15/Z. M.H. was funded by The HIV Prevention Trials Network (grant number H5R00701.CR00.01) and The Bill and Melinda Gates Foundation (grant number OPP1175094). **Author contributions:** K.E.A. conceived the study. C.J.V.-A., M.H., K.A.L., S.H., and K.E.A. designed the study. C.J.V.-A. performed the experiments and analyzed the data. C.J.V.-A., M.H., K.A.L., S.H., and K.E.A. interpreted the data. S.G.G. created new software used in the study. K.E.A. and C.J.V.-A. drafted the manuscript, with critical revisions from M.H., R.R.R., K.A.L., and S.H. All authors approved the final version of the manuscript. **Competing interests:** The authors declare no competing interests. **Data and materials availability:** All code and data are available at Zenodo (35).

## SUPPLEMENTARY MATERIALS

[science.sciencemag.org/content/369/6499/103/suppl/DC1](https://science.sciencemag.org/content/369/6499/103/suppl/DC1)  
Materials and Methods  
Supplementary Text  
Figs. S1 to S5  
Data S1 to S4  
References (36–47)  
MDAR Reproducibility Checklist

12 December 2019; accepted 11 May 2020  
10.1126/science.aba5443

# 10 ways that Science Careers can help advance your career

1. Register for a free online account on **ScienceCareers.org**.
2. Search thousands of job postings and find your perfect job.
3. Sign up to receive e-mail alerts about job postings that match your criteria.
4. Upload your resume into our database and connect with employers.
5. Watch one of our many webinars on different career topics such as job searching, networking, and more.
6. Download our career booklets, including Career Basics, Careers Beyond the Bench, and Developing Your Skills.
7. Complete an interactive, personalized career plan at “my IDP.”
8. Visit our Employer Profiles to learn more about prospective employers.
9. Research graduate program information and find a program right for you.
10. Read relevant career advice articles from our library of thousands.

Visit **ScienceCareers.org**  
today — all resources are free



**ScienceCareers**

FROM THE JOURNAL SCIENCE  AAAS

SCIENCECAREERS.ORG



By Shalini Arya

# A child of the slums

I scrambled up a ladder to the tin roof of our house, clutching a book about the evolution of animals. I was 10 years old, and I'd just finished cooking dinner for my entire family—a task that was my daily responsibility. From my perch, I could look out at the slum where we lived in a small town in India. But that wasn't what drew me to the roof: We didn't have any lamps in our house, so I needed sunlight to read my book. I didn't know it at the time, but that study routine was my ticket to a career as a scientist.

My father—a laborer—didn't let me attend school initially. I was always jealous of my younger brother when he set off to school each day. So, one day, when I was 5 years old, I followed him and hid under the teacher's desk. She noticed me and sent me home. But the next day, she called my father and told him that he should put me in school. Much to my delight, my father said yes.

I had a passion for learning, and—despite the hunger pangs I went to school with most days—I quickly shot to the top of my class. When I was 10 years old, my father sent me to a better school outside our neighborhood, one that was mostly attended by students from wealthier families. I was at the top of the class there, too. But I was treated poorly by classmates who saw me as a child of the slums. I also suffered from embarrassment during biology labs because I was very short—due to malnutrition, I suspect—and I had to stand on a chair to see into the microscope.

When I graduated from high school, I wanted to become an engineer. My father was eager for me to attend university, but he told me I couldn't study engineering because it was for boys; he said I should study food science instead. My initial reaction was that food science was the last thing I wanted to study. After a childhood preparing meals for my family, there was nothing I hated more than cooking.

I enrolled in a food science program anyway, and I quickly discovered that food science wasn't so bad after all. It was a real science—something akin to chemistry—that involved hypothesis testing and experimentation. Soon enough, I was hooked.

While attending university, I lived in a hostel near campus, paying my tuition and living expenses with the help of student loans my father secured for me as well as my side job as a research assistant. My room had a lamp, and I was thankful every night that I had light to study under—



**“I hope others can take inspiration from my story and realize ... they, too, can persevere.”**

something I have learned to never take for granted.

In the years that followed, I received a Ph.D. in food engineering and was appointed to a faculty position—milestones that felt far removed from my beginnings in the slums. But shortly thereafter, I began a collaboration that brought me back to my roots. I worked with a company that wanted to tackle malnutrition in India's slums. When representatives from the company first approached me, they said, “You'd need to go to the slums and talk with people”—thinking that I'd never done that before. “That's no problem,” I replied. “I grew up in the slums.”

As part of my work with the company, I modified the ingredients in a traditional Indian flatbread called

chapati, which I'd made every day growing up. I realized it was the perfect vehicle to introduce more nutrition into the diet of poor people, because it was a staple eaten at every meal. I experimented with the ingredients and landed on a recipe that replaced wheat flour with cheap, locally grown grains that contain more minerals, protein, and dietary fiber.

Other researchers laughed at me when I started to work on chapati because they didn't think there'd be much science, or innovation, associated with it. But I've since proved them wrong. My work has won numerous national and international awards, and companies, nonprofit organizations, and government agencies have all sought my expertise.

In my life, I've faced poverty, hunger, and discrimination. But I didn't let them hold me back. I pushed through the obstacles and learned lessons from them that helped propel me forward. I hope others can take inspiration from my story and realize that—despite the challenges they may be facing—they, too, can persevere. ■

Shalini Arya is an assistant professor at the Institute of Chemical Technology in Mumbai, India.



*Science Webinars* help you keep pace with emerging scientific fields!

Stay informed about scientific breakthroughs and discoveries.

Gain insights into current research from top scientists.

Take the opportunity to ask questions during live broadcasts.



Get alerts about upcoming free webinars.

**Sign up at: [webinar.sciencemag.org/stayinformed](https://webinar.sciencemag.org/stayinformed)**



# SARS-CoV-2 Research Solutions

## Supporting Research and Discovery

**ProMab Biotechnologies** offers multiple solutions for SARS-CoV-2 (COVID-19) research and development. From ready-to-use antibody, protein, and molecular diagnostic reagents to reliable CDMO services, utilize an established platform to aid your next breakthrough.

### SARS-CoV-2 RT-qPCR Detection Kit



ProMab Biotechnologies' SARS-CoV-2 RT-qPCR Detection Kit detects the presence of three highly specific COVID-19 nucleocapsid (N) primers with Fam probe pairs, and a Human RNASE P primer with probe for internal control.

### SARS-CoV-2 IgG ELISA Kit



ProMab Biotechnologies COVID-19 (SARS-CoV-2) IgG ELISA Kit has been optimized for the qualitative detection of nucleocapsid protein specific IgG antibodies and is available for research use only.

*These SARS-CoV-2 detection kits are not approved by the FDA and are available for research use only.*

### SARS-CoV-2 Research Reagents

Product Name	E. coli	HEK293	CHO	Yeast	Baculovirus	mAb	pAb
Spike protein 1 (S1) His tag			✓	✓			
Spike protein 1 (S1) Lentivirus particles		✓					
Spike protein 1 (S1) Pseudovirus particles							
S1 Receptor Binding Domain (RBD) His tag	✓	✓	✓			✓	
S1 Receptor Binding Domain (RBD) Biotinylated with His tag		✓					
S1 Receptor Binding Domain (RBD) Human Fc tag		✓	✓				
S1 Receptor Binding Domain (RBD) Cell surface display		✓		✓			
Nucleocapsid Protein Full Length His tag	✓	✓			✓		✓
Nucleocapsid Protein Full Length Human Fc tag		✓					
Nucleocapsid Protein Fragment 1 His tag	✓						
Nucleocapsid Protein Fragment 2 His tag	✓						
Nucleocapsid Protein Fragment 3 His tag	✓					✓	
Angiotensin-Converting Enzyme 2 (ACE2) Human Fc tag		✓	✓				
Angiotensin-Converting Enzyme 2 (ACE2) Biotinylated with human Fc tag		✓					
Angiotensin-Converting Enzyme 2 (ACE2) His tag			✓	✓			
Angiotensin-Converting Enzyme 2 (ACE2) Human Fc tag with RFP				✓			
Angiotensin-Converting Enzyme 2 (ACE2) Cell surface display		✓		✓			
Angiotensin-Converting Enzyme 2 (ACE2) Lentivirus with GFP		✓					
SARS-CoV S glycoprotein [CR3022] Antibody		✓		✓			
SARS-CoV S glycoprotein [CR3022] Antibody			✓				

Many more products in development. For custom inquiries, contact us today!

Discover more | [www.promab.com](http://www.promab.com)



2600 Hilltop Dr, Building B, Richmond, CA 94806

1.866.339.0871 | [info@promab.com](mailto:info@promab.com)